

# **Therapeutic Design for Nasal Powder Delivery**

Mohammed Ali Haider Farouq

University of Strathclyde

Department of Chemical and Process Engineering

A thesis presented for the degree of Doctor of Philosophy

May 2024

This thesis is the result of the author's original research. It has been composed by the author and has not been previously submitted for examination which has led to the award of a degree.

The copyright of this thesis belongs to the author under the terms of the United Kingdom Copyrights Acts as qualified by University of Strathclyde Regulation 3.50. Due acknowledgement must always be made of the use of any material contained in, or derived from, this thesis.

Signed: Mohammed Ali Haider Farouq

Date: 20/5/24

## Acknowledgements

First and foremost, I would like to praise Allah SWT for blessing me with the opportunity to undertake a PhD, and giving me the strength and courage to complete this thesis. This thesis represents the work of the past 4 years of my life, it was a long journey, filled with highs and lows that helped shape who I am today. I would like to take the opportunity to thank the people who made this journey possible. I must start by thanking the IBioIC/BBSRC CTP for the funding that enabled this research to be conducted, and my academic supervisors Dr. Paul Mulheran and Dr. Valerie Ferro. The advice, guidance and experience of my academic supervisors has been invaluable throughout my PhD, both professionally and personally, and I am grateful for them granting me the opportunity to pursue a PhD.

Thanks to ARCHIE-WeSt HPC for facilitating the computational work I carried out. Further thanks to Dr. Karina Kubiak-Ossowska for her guidance, help throughout the project, and being there for all matters 'ARCHIE-WeSt'. I would not have been able to complete this project without the help and expertise of the team at CMAC including Dr. Thomas McGlone, Dr. Kenneth Smith, Dr. Aruna Prakash and several others to whom I express my apologies for not mentioning personally. Further thanks to Ian Harrison and Bukhtiar Ahmed at Alchemy Pharmatech, my industrial partners, for their help and support in this project.

The management of my medical condition was very important in the completion of my studies, and I would like to thank all the healthcare professionals involved in my care. Thanks also to Christopher Service and the staff at PureGym Shawlands, and Alexander Brand and the staff at Glasgow club for their support in allowing me to work on my exercise programmes, which are an important part of managing my condition. A further mention to Christopher Service, Jordan Macdonald, Stephen Barrie, Emma Walker, Amanda Fisher, Jamie Sturrock, Melissa Macdonald and Martin Brown at PureGym Shawlands for their emotional support in addition to the physical. They were a family to me, and our interactions made Glasgow seem like home away from home, which made it a bit easier to turn up for work when I was struggling during particularly difficult times. Last, but by no means least, I am

incredibly grateful to my parents Malik Farouq and Nobeela Farouq, and sisters Aisha and Noor for their support and prayers throughout this journey.

## Contents

|   |           |
|---|-----------|
| <b>Acknowledgements</b> .....   | ii        |
| <b>Figures</b> .....  | vii       |
| <b>Tables</b> .....   | x         |
| <b>Abbreviations</b> .....  | xi        |
| <b>Publications</b> .....   | xv        |
| <b>Abstract</b> .....   | xvi       |
| <b>Chapter One: Introduction</b> .....                                    | 1         |
| <b>1.1. Vaccine Types</b> .....   | <b>2</b>  |
| 1.1.1. Toxoid Vaccines .....  | 3         |
| 1.1.2. Live Attenuated Vaccines .....                                     | 3         |
| 1.1.3. Inactivated Vaccines .....   | 4         |
| 1.1.4. Subunit Vaccines.....  | 5         |
| 1.1.5. Viral Vector Vaccines .....  | 6         |
| 1.1.6. mRNA Vaccines .....  | 7         |
| <b>1.2. Vaccines and COVID-19</b> .....                                   | <b>8</b>  |
| <b>1.3. Drawbacks to Conventional Vaccination</b> .....                   | <b>10</b> |
| <b>1.4. IN Vaccines</b> .....   | <b>10</b> |
| <b>1.5. IN Vaccines and COVID-19</b> .....                                | <b>11</b> |
| <b>1.6. Project Aims</b> .....  | <b>12</b> |
| <b>Chapter Two: Therapeutics</b> .....                                    | 15        |
| <b>2.1. Coronaviruses</b> .....   | <b>16</b> |
| 2.1.1. Structure and Function of SARS-CoV-2.....                          | 17        |
| 2.1.2. Therapeutic Targets.....   | 18        |
| <b>2.2. NPs</b> .....   | <b>20</b> |
| 2.2.1. The Role of NPs in Vaccines .....                                  | 20        |
| 2.2.2. Therapeutic Applications of Adjuvants .....                        | 23        |
| <b>Chapter Three: Methodology</b> .....                                   | 33        |
| <b>3.1. Molecular Simulation</b> .....                                    | <b>34</b> |
| <b>3.2. MD</b> .....  | <b>34</b> |
| 3.2.1. Integration Algorithms, Constraint Solvers, and Water Models ..... | 35        |
| 3.2.2. Thermostats, Barostats and Forcefields .....                       | 37        |
| 3.2.3. NAMD and Visual Molecular Dynamics.....                            | 41        |

|  |            |
|--|------------|
| <b>3.3. Laboratory Techniques .....</b>  | <b>42</b>  |
| 3.3.1. Spray Drying and Characterisation of The Sample.....                    | 42         |
| 3.3.2. Spray-dried Sample Imaging .....  | 46         |
| 3.3.3. NPs Characterisation.....   | 48         |
| 3.3.4. Design of Experiments.....  | 50         |
| <b>Chapter Four: Model SpA Systems.....</b>                                    | <b>52</b>  |
| <b>4.1. SpA .....</b>  | <b>53</b>  |
| <b>4.2. Materials and Methods.....</b>   | <b>56</b>  |
| 4.2.1. Surface Models .....  | 56         |
| 4.2.2. MD Simulations .....  | 57         |
| <b>4.3. Results and Discussion.....</b>  | <b>61</b>  |
| 4.3.1. Structural Stability .....  | 61         |
| 4.3.2. Angles Between Neighbouring $\alpha$ -helices in Simulation.....        | 80         |
| 4.3.3. Ramachandran Plots.....   | 85         |
| <b>4.4. Conclusions.....</b>   | <b>88</b>  |
| <b>Chapter Five: Model SARS-CoV-2 RBD Systems .....</b>                        | <b>90</b>  |
| <b>5.1. Introduction.....</b>  | <b>91</b>  |
| <b>5.2. Materials and Methods.....</b>   | <b>95</b>  |
| 5.2.1. Surface Models .....  | 95         |
| 5.2.2. MD Simulations of S1 Subunit .....                                      | 96         |
| 5.2.3. MD Simulations of S1 Subunit with His-Tag .....                         | 98         |
| <b>5.3. Results and Discussions .....</b>                                      | <b>100</b> |
| 5.3.1. Adsorption of the S1 Subunit and S1 Subunit with a His-Tag .....        | 100        |
| 5.3.2. Further Discussion of Adsorption Simulations on Negative Surfaces ..... | 124        |
| <b>5.4. Conclusions.....</b>   | <b>129</b> |
| <b>Chapter Six: Dry-Powder Vaccine Formulation.....</b>                        | <b>131</b> |
| <b>6.1. Introduction.....</b>  | <b>132</b> |
| <b>6.2. Materials and Methods.....</b>   | <b>132</b> |
| 6.2.1. Initial Spray Drying Runs .....   | 132        |
| 6.2.2. DoE Spray Drying Parameters.....  | 136        |
| 6.2.3. Mastersizer 3000.....   | 138        |
| 6.2.4. Morphologi G3.....  | 138        |
| 6.2.5. SEM .....   | 138        |
| 6.2.6. ZP.....   | 139        |
| 6.2.7. DLS.....  | 139        |

|   |            |
|---|------------|
| <b>6.3. Results and Discussion.....</b>                                     | <b>139</b> |
| 6.3.1. Initial Spray Drying Runs .....                                      | 139        |
| 6.3.2. Further Production Runs Incorporating NPs .....                      | 143        |
| <b>6.4. Conclusions .....</b>   | <b>151</b> |
| <b>Chapter Seven: Conclusions &amp; Perspectives .....</b>                  | <b>153</b> |
| <b>7.1. Scope for IN Vaccines .....</b>                                     | <b>154</b> |
| <b>7.2. Development of a Dry-Powder IN Vaccine for COVID-19 .....</b>       | <b>154</b> |
| <b>7.3. Future Directions: Proof of Concept Dry-Powder IN Vaccine .....</b> | <b>156</b> |
| <b>Bibliography .....</b>   | <b>159</b> |
| <b>Appendix .....</b>   | <b>187</b> |

## Figures

|   |       |
|---|-------|
| <b>Figure 2.1:</b> Diagram showing the structural proteins of the SARS-CoV-2 virus.....   | 18    |
| <b>Figure 2.2.</b> Interaction between the ACE2 receptor and the S protein RBD.....   | 19    |
| <b>Figure 2.3:</b> A diagram showing drug loading options in NPs targeted drug delivery..                                       | 21    |
| <b>Figure 2.4:</b> Images of prepared mesoporous silica nanoparticles.....  | 26    |
| <b>Figure 2.5:</b> A diagram showing the process of making mesoporous silica nanoparticles.....                                 | 27    |
| <b>Figure 3.1:</b> A representation of the conventional spray-drying process.....   | 43    |
| <b>Figure 3.2:</b> A diagram showing the optical setup for a laser diffractor.....  | 45    |
| <b>Figure 3.3:</b> A typical SEM column showing internal sample-beam interactions.....  | 46    |
| <b>Figure 4.1:</b> The SpA structure illustrated using VMD.....   | 53    |
| <b>Figure 4.2:</b> The structure of Staphylococcal sortase A.....   | 54    |
| <b>Figure 4.3:</b> Images showing the protein close to surface, and close to image.....   | 59    |
| <b>Figure 4.4:</b> RMSD of SpA in simulations.....  | 62-64 |
| <b>Figure 4.5:</b> Adsorption of SpA on the oxygen rich silica surface.....   | 66    |
| <b>Figure 4.6:</b> Representative snapshots showing the Lys37 and Lys34 residues.....   | 67/68 |
| <b>Figure 4.7:</b> Adsorption of SpA on the positively charged silica surface.....  | 72    |
| <b>Figure 4.8:</b> Adsorption of SpA on the hydrophobic gold surface.....   | 76    |
| <b>Figure 4.9:</b> The angles between the $\alpha$ -helix pairs in water, silica surface, and Au (111) surface simulations..... | 81-84 |
| <b>Figure 4.10:</b> Ramachandran plots of SpA in water, silica surface and Au (111) surface simulations.....                    | 86/87 |
| <b>Figure 5.1:</b> Adsorption of IgG1 onto two different SAMs on a gold surface.....  | 91    |
| <b>Figure 5.2:</b> The S1 subunit structure illustrated using VMD.....  | 93    |
| <b>Figure 5.3:</b> The S1 subunit modified with a His-Tag, illustrated using VMD.....   | 94    |



|   |         |
|---|---------|
| <b>Figure 5.4:</b> The RMSD and RMSF of S protein RBD and His-Tag S Protein RBD in the water simulations.....   | 101     |
| <b>Figure 5.5:</b> The structure overlaps after 100ns simulation in water of the tagless protein and tagged protein.....  | 102     |
| <b>Figure 5.6:</b> The RMSD and RMSF of S protein RBD and His-Tag S Protein RBD in the siloxide silica surface simulations.....   | 104     |
| <b>Figure 5.7:</b> Representation of the S1 subunit with the positively charged hydrophilic lysine and arginine residues concentrated in the centre of the protein.....   | 106     |
| <b>Figure 5.8:</b> Adsorption of the S1 subunit on oxygen rich silica surface.....  | 107     |
| <b>Figure 5.9:</b> Adsorption of His-Tag modified S1 subunit on oxygen rich silica surface.....   | 110     |
| <b>Figure 5.10:</b> The RMSD and RMSF of S protein RBD and His-Tag S Protein RBD in the silicon undercoordinated silica surface simulations.....  | 113     |
| <b>Figure 5.11:</b> Adsorption of the S1 subunit on the silicon rich silica surface.....  | 114     |
| <b>Figure 5.12:</b> The RMSD and RMSF of S protein RBD and His-Tag S Protein RBD in the SAMs terminated silica surface simulations.....   | 120     |
| <b>Figure 5.13:</b> Adsorption of His-Tag modified S1 subunit on COOH silica surface...   | 122     |
| <b>Figure 5.14:</b> The Hydrogen Bonds and Radius of Gyration for the tagless protein on siloxide silica surface, tagged protein siloxide silica surface and tagged protein COOH silica surface adsorption simulations..... | 126     |
| <b>Figure 6.1:</b> The concept of rotary atomisation.....   | 133     |
| <b>Figure 6.2:</b> The spray dryer calibration curve for the Buchi B290 mini spray dryer..  | 134     |
| <b>Figure 6.3:</b> The spray dryer calibration curve for the new tubing.....  | 135     |
| <b>Figure 6.4:</b> SEM images for the second spray-drying runs.....   | 141/142 |
| <b>Figure 6.5:</b> Size distribution of COOH SiNPs and SiNPs measured by DLS.....   | 144     |
| <b>Figure 6.6:</b> SEM images of COOH SiNPs and SiNPs.....  | 145     |

|   |     |
|---|-----|
| <b>Figure 6.7:</b> Zeta potential data for COOH SiNPs and SiNPs.....      | 146 |
| <b>Figure 6.8:</b> Particle size data for samples for the third runs..... | 149 |
| <b>Figure 6.9:</b> SEM images for samples 1 and 6.....                    | 150 |

## Tables

|  |     |
|--|-----|
| <b>Table 2.1:</b> A list of coronaviruses found in humans and the illness they cause.....  | 17  |
| <b>Table 4.1:</b> SpA dipole moment on the three different surfaces.....   | 74  |
| <b>Table 4.2:</b> RMSD summary in Water, Au (111) surface, and silica surface simulations.....   | 79  |
| <b>Table 4.3:</b> Anchoring residues upon SpA adsorption on the three model surfaces.....  | 80  |
| <b>Table 5.1:</b> A list of residues in the S1 subunit that were protonated to run the His-Tag modified S1 subunit simulations at pH6.....     | 98  |
| <b>Table 5.2:</b> A list of the adsorbed residues in the final adsorption state of each stable adsorption simulation on negative surfaces..... | 127 |
| <b>Table 6.1:</b> A list of the materials used in the laboratory work and their abbreviations.....   | 135 |
| <b>Table 6.2:</b> The spray-dryer parameters used in the first two spray drying runs.....  | 136 |
| <b>Table 6.3:</b> The two levels of the four factors that have the most effect on the experimental spray drying set up.....                    | 137 |
| <b>Table 6.4:</b> The experimental runs obtained from DoE ran in Minitab v19.0.....  | 137 |
| <b>Table 6.5:</b> Particle size data gathered from the Mastersizer 3000.....   | 140 |
| <b>Table 6.6:</b> Particle size data gathered from the Mastersizer 3000.....   | 140 |
| <b>Table 6.7:</b> Particle size data gathered from the Morphologi G3.....  | 143 |
| <b>Table 6.8:</b> Particle size data gathered from the Morphologi G3.....  | 148 |

## Abbreviations

- 3CL<sup>pro</sup>** - Chymotrypsin-like Cysteine Protease
- ACE2** - Angiotensin-converting Enzyme 2 Receptor
- AFM** – Atomic Force Microscopy
- ALA** - Alanine
- ALUM** – Aluminium Hydroxide Salts
- ASN** – Asparagine
- ASP** – Aspartic Acid
- AuNPs** – Gold Nanoparticles
- BSA** – Bovine Serum Albumin
- BSE** – Backscattered Electrons
- CFA** – Complete Freund’s Adjuvant
- CMSNPs** – Colloidal Mesoporous Silica Nanoparticles
- CNPs** – Cyclodextrin Nanoparticles
- COOH SiNPs** – Carboxyl SAMs Terminated Silica Nanoparticles
- COVID-19** – Coronavirus Disease 2019
- CpG ODNs** – CpG Oligodeoxynucleotides
- DLS** – Dynamic Light Scattering
- DoE** – Design of Experiments
- DOX** – Doxorubicin
- DOX-MSNPs** – Doxorubicin Mesoporous Silica Nanoparticles
- DOX-Z-MSNPs** – Doxorubicin Zwitterionic Mesoporous Silica Nanoparticles
- E Protein** – Envelope Protein
- ELS** – Electrophoretic Light Scattering
- EMA** – European Medicines Agency
- EtOH** - Ethanol
- FCC** – Face-centred Cubic Crystal
- FDA** - United States Food and Drug Administration
- FF** – Forcefield

**GLN** - Glutamine  
**HDLs** - High Density Lipoproteins  
**HE** - Haemagglutinin-acetylerase Receptor  
**HIS** – Histidine  
**HIS-TAG** – Histidine Tag  
**HIV** – Human Immunodeficiency Virus  
**HPC** – High-performance Computer  
**HSP** – Protonated Histidine  
**IEP** – Iso-Electric Point  
**IN** – Intranasal  
**LDV** – Laser Doppler Velocimetry  
**L-J** – Lennard Jones  
**LM** – Alpha Lactose Monohydrate  
**LNPs** – Lipid Nanoparticles  
**LYS** - Lysine  
**LYZ** – Lysozyme  
**M Protein** – Membrane Protein  
**MC** – Monte Carlo  
**MD** – Molecular Dynamics  
**MET** - Methionine  
**MHDA** - 16-mercaptohexadecanoic Acid  
**MHRA** - United Kingdom Medicines and Healthcare Products Regulatory Agency  
**M<sup>Pro</sup>** – Main Protease  
**MPL** – Monophosphoryl Lipid A  
**MS** – Molecular Simulation  
**MSNPs** – Mesoporous Silica Nanoparticle  
**MUO** - 11-mercapto-1-undecanol  
**N Protein** – Nucleocapsid Protein  
**NAMD** – Nanoscale Molecular Dynamics

**N7-MTase** - Guanine N7-methyltransferase  
**NLRP3** – Protein 3  
**NPs** – Nanoparticles  
**NVE** – Microcanonical Energy Ensemble  
**NPT** – Microcanonical Pressure Ensemble  
**NVT** – Microcanonical Temperature Ensemble  
**ORFs** – Open Reading Frame  
**OVA** - Ovalbumin  
**PBC** – Periodic Boundary Conditions  
**PDB** – Protein Data Bank  
**PDI** – Polydispersity Index  
**PDMA** – Polydimethylacrylamide  
**PE** – Potential Energy  
**PEI** – Cationic Polymer Coating  
**PHE** - Phenylalanine  
**PL<sup>pro</sup>** - Papain-like Protease  
**PME** – Particle Mesh Ewald  
**Polio** – Poliomyelitis  
**QCM** – Quartz Crystal Microbalance  
**RA** – Rheumatoid Arthritis  
**RBD** – Receptor Binding Domain  
**RdRp** - RNA-dependent RNA Polymerase  
**RMSD** – Root Mean Square Deviation  
**RMSF** – Root Mean Square Fluctuations  
**RMTEM** – Rotary Metal Shadowing Transmission Electron Microscopy  
**RoG** – Radius of Gyration  
**ROS** – Reactive Oxygen Species  
**RPM** – Rotations Per Minute  
**rProtA** – Cysteine Tagged Recombinant Protein A

**rProtG** – Cysteine Tagged Recombinant Protein G

**S Protein** – Spike Protein

**SAMs** – Self-assembled Monolayers

**SARS-CoV-2** – Severe Acute Respiratory Syndrome Coronavirus 2

**saRNA** - Self-amplifying RNA

**SE** – Secondary Electrons

**SEM** – Scanning Electron Microscope

**SiNPs** – Silica Nanoparticles

**SOP** – Standard Operating Procedure

**SpA** – Staphylococcus Protein A

**SPC** – Single Point Charge

**SPR** – Surface Plasmon Resonance

**SR-B1** - HDL-scavenger Receptor B Type 1

**Tagged Protein** – His-Tag Modified S1 Subunit

**Tagless Protein** - S1 Subunit Without a His-Tag

**TMPRSS2** - Transmembrane Protease Serine 2

**TYR** – Tyrosine

**VAL** - Valine

**VdW** – Van der Waals Forces

**VMD** – Visual Molecular Dynamics

**Z-MSNPs** – Zwitterionic Mesoporous Silica Nanoparticle

**ZP** – Zeta Potential

## Publications

**Farouq, M.A.H. et al.** (2022a) 'The Role of Antibodies in the Treatment of SARS-CoV-2 Virus Infection, and Evaluating Their Contribution to Antibody-Dependent Enhancement of Infection'. *Int J Mol Sci*, 23 (11).

**Farouq, M.A.H. et al.** (2022b) 'Functionalisation of Inorganic Material Surfaces with Staphylococcus Protein A: A Molecular Dynamics Study'. *Int J Mol Sci*, 23 (9).

**Farouq, M.A.H. et al.** (2021) 'Biomolecular interactions with nanoparticles: applications for coronavirus disease 2019'. *Current Opinion in Colloid & Interface Science*, 54 101461.



## Abstract

Coronavirus disease 2019 (COVID-19) is an infectious disease caused by the severe acute respiratory syndrome coronavirus 2 (SARS-CoV-2) virus. The response to the pandemic saw widespread diagnostic testing, and the development of vaccines at speed, with global distribution ahead of emergency regulatory approval.

Antibody conjugation with nanoparticles (NPs) through Staphylococcus Protein A (SpA) can be used a platform for the development of new diagnostics, and Molecular Dynamics (MD) simulations were used to investigate SpA for its potential as an antibody conjugation agent with model NPs. The simulations showed the model negatively charged silica surface produced favourable SpA adsorption, that facilitated the binding of antibodies at the Fc region to functionalise the system. The SpA was blocked on both sides when it bound to the model gold surface, and the SpA receptor binding domain (RBD) is blocked on the model positive silica surface. Overall, these results indicate SpA is a promising agent to guide the development of a new diagnostic for COVID-19.

The initial aim was to develop a novel diagnostic for COVID-19. However, after the withdrawal of my original industrial partner, and the project workplan change with my new industrial partner, it was decided to pursue the development of a dry-powder intranasal (IN) vaccine. Therefore, the aim of this thesis is to design a dry-powder IN vaccine for COVID-19, by studying the SARS-CoV-2 RBD interactions with model NPs. The SARS-CoV-2 RBD and SARS-CoV-2 RBD with histidine tag (His-Tag) were studied by MD simulations with model silica NPs (SiNPs) and model carboxyl terminated SiNPs (COOH SiNPs). The MD simulations indicate SARS-CoV-2 RBD binds preferentially on the model SiNPs and SARS-CoV-2 RBD with His-Tag binds preferentially to the model COOH SiNPs. These model systems were used to guide the experimental production of a dry-powder IN vaccine for COVID-19.

The simulations guided the laboratory work, where a spray-dryer was used along with other characterisation equipment for the production, and analysis of a dry-powder IN vaccine formulation for COVID-19. Alpha lactose monohydrate spheres, used as the excipient in the dry-powder IN vaccine formulation, were successfully spray-dried to

the required size. Despite the overall unsuccessful attempt at IN vaccine production for COVID-19, this project has opened up many possibilities for the future, as the MD simulations showed the NPs are suitable for a vaccine formulation, and the experimental component of this project also contributed to the development of an IN vaccine.

# Chapter One: Introduction

*“What is not started will never get finished”*

*Johann Wolfgang von  
Goethe*

The emergence of severe acute respiratory syndrome coronavirus 2 (SARS-CoV-2), a previously unknown coronavirus, caused global chaos. Hospitals were overwhelmed with patients, and economies affected as the global response saw the adoption of social distancing, face masks and lockdowns. Researchers made it their priority to diagnose and treat coronavirus disease 2019 (COVID-19), and the initial aim of this project was to design a new diagnostic for COVID-19, using antibody conjugation with Staphylococcus Protein A (SpA). However, COVID-19 diagnostic tests rapidly became commonplace, with RT-PCR tests effectively scaled up, and new antigen tests also introduced.

Vaccines for the virus were also developed at speed, and they were successfully rolled out in different vaccination programmes. However, the current vaccines for COVID-19 pose several challenges, and there is a need for alternative mucosal vaccines that would primarily target respiratory surfaces. The aim of this thesis is to design a dry-powder intranasal (IN) vaccine for COVID-19, by targeting the SARS-CoV-2 receptor binding domain (RBD), which causes COVID-19. This chapter begins by introducing vaccines, discussing different types of vaccines, assessing their key features and components, and looking at some COVID-19 vaccines. Dry-powder IN vaccines are then introduced, their clear advantages over conventional vaccines are explored, and current attempts at IN vaccines for COVID-19 are assessed. The chapter concludes with a summary of key points pinpointing the motivation for this work, and a description of the contents of subsequent chapters.

## **1.1. Vaccine Types**

A vaccine is a biological preparation that provides active acquired immunity to a particular infectious or malignant disease (Pollard and Bijker, 2021). The formulation contains an agent that resembles a disease-causing microorganism, which is often made from weakened or dead forms of the microbe, its toxins or one of its surface proteins (World Health Organisation, 2020). The agent stimulates the body's immune system to recognise it as a threat and destroy it. It also creates ability for the immune system to destroy any related threat in future encounters (World Health Organisation, 2020). There are several types of vaccine, and they are detailed below.

### **1.1.1. Toxoid Vaccines**

Toxoid vaccines use inactivated toxins to suppress toxic effects of these bacterial-released proteins, rather than targeting the bacteria itself (Yadav *et al.*, 2014). These vaccines are effective at preventing certain toxin-mediated diseases such as tetanus or diphtheria. For instance, the harmful toxin produced by the bacterium *Clostridium tetani* causes painful muscle contractions, causing the neck and jaw muscles to lock, making it hard to open the mouth or swallow (Moynan *et al.*, 2018). Diphtheria, caused by *Corynebacterium diphtheria*, is a highly contagious bacterial disease causing inflammation of the mucous membranes, and the formation of a false membrane in the throat that hinders breathing and swallowing (Hadfield *et al.*, 2000). In toxoid vaccines, the toxin is purified from the bacterial cell culture and then inactivated via chemical treatment with formalin. For immunisation purposes, the inactive, harmless form of the toxin known as the ‘toxoid’ generates an immune response, building long lasting immunity to the particular disease (Yadav *et al.*, 2014), and boosters are often given every 10 years for ongoing immunity. However, toxoid vaccines are only useful for diseases caused by certain toxin-producing bacteria (Angsantikul *et al.*, 2018), as other pathogens do not produce toxins.

### **1.1.2. Live Attenuated Vaccines**

Using one of the earliest methods of eliciting a protective immune response, a live attenuated vaccine contains an ‘attenuated’ or weakened pathogen, inducing an immune response for the target pathogen, to develop long-term immunity (Yadav *et al.*, 2014). The actual pathogen is weakened sufficiently, but retains the epitopes key to recognition by the immune system. As this vaccine type contains an actual, live pathogen, it delivers strong immunity and booster shots are not always needed (Aaby *et al.*, 2023), it is also the closest treatment to a live infection. The pathogen may be attenuated by introducing it into an unfamiliar host in a process known as ‘passaging’, or by growing it through tissue culture. The former relies on the principles of genetic variability and mutation, as the strain evolves in the new host, the pathogen becomes well acquainted to the new host, making it harmless to the original recipient (Hanley, 2011). Attenuation through cell culture relies on the same principle. The pathogen is

repeatedly ‘passaged’ through cell lines, forcing replication and putting it under increased pressure to adapt to the different environment, thus weakening the pathogen and reducing its efficacy, but keeping it strong enough to elicit an immune response (Bankamp *et al.*, 2008).

An example of a live-attenuated vaccine is the rotavirus vaccine, Rotarix ®. Rotavirus is a highly infectious gastric organism affecting mainly babies and young children, with symptoms including fever, stomach ache, diarrhoea and vomiting (Anderson and Weber, 2004). Development of this vaccine involved obtaining a virus isolated from an infected child and serially passaging it through primary African Green Monkey Kidney (AGMK) cells; this was carried out 26 times, and then a further 7 times in a serially passaged AGMK cell line (Bernstein *et al.*, 1998). To determine the attenuation of the virus, studies were conducted in adults, followed by children with a rotavirus infection (Bernstein *et al.*, 1998).

Live attenuated vaccines demonstrate durable immunity against a disease because they are as close to the active, wild-type virus, and therefore, can usually immunise after a single dose, not always requiring boosters (Aaby *et al.*, 2023). On the other hand, live attenuated vaccines cannot be safely given to people who are immunocompromised, as they would not be able to fight the attenuated pathogen and could develop serious illness as opposed to developing immunity (Torresi and Kollaritsch, 2013). These vaccines cannot be given to pregnant women too, as pregnancy weakens the immune system and increases the risk of the vaccine making its way to the developing foetus, which could cause serious damage to the unborn child (Bozzo *et al.*, 2011, Torresi and Kollaritsch, 2013). Furthermore, the vaccines pose logistical problems when it comes to transport and delivery in some countries, as they are only effective when kept and stored at controlled temperature. They also need security to prevent theft/diversion of the vaccine (Kartoglu *et al.*, 2020).

### **1.1.3. Inactivated Vaccines**

It is also possible to produce inactivated vaccines, which generally have poorer immunogenicity than live attenuated vaccines. Inactivated vaccines involve killing a pathogen in the process, or altering it so that it cannot replicate. When the vaccine is

administered, the ‘inactivated’ pathogen is strong enough to initiate an immune response, yet cannot cause disease (Lopez *et al.*, 2023). However, as the pathogen cannot replicate in the host cell, the immunity provided is not as strong as live attenuated vaccines, and multiple booster doses are needed for ongoing immunity (Louten, 2016). Inactivated vaccines are usually more stable in long-term storage than live attenuated vaccines, and do not need a cold chain, making them more accessible to store/transport, and readily available to use (Dumpa *et al.*, 2019). The vaccines may be safer than live vaccines as the pathogen is essentially inactive, and unlikely to mutate into a harmful form (Louten, 2016).

Commonly, whole live pathogens are collected from animal cell cultures and then ‘inactivated’ using heat or formalin; there are currently several licensed inactivated vaccines available on the market. Poliomyelitis (Polio) is an infectious disease that is spread by the faecal-oral route, and symptoms of polio include fever, paralysis and muscle pain (Mehndiratta *et al.*, 2014). An example of an inactivated vaccine is the Inactivated Polio Vaccine (Salk, 1953), which is produced by wild-type poliovirus strains of each serotype that have been inactivated with formalin. The vaccine is often given as a combination along with diphtheria, tetanus and acellular pertussis vaccines. There is no risk of ‘reversion’ with inactivated vaccines, as opposed to live vaccines, and inactivated vaccines can also be freeze-dried for ease of transport (Louten, 2016). On the other hand, production of inactivated vaccines can be relatively expensive because of the treatment processes involved in inactivating the pathogen (Fu *et al.*, 2022); this is an important consideration for mass vaccine manufacture.

#### **1.1.4. Subunit Vaccines**

A subunit vaccine is formulated from a component of a pathogen, so they do not contain whole pathogens, but rather a protein and/or a polysaccharide from a pathogen, that has been carefully studied using *in silico* methods to identify if it initiates a strong immune response (Goodswen *et al.*, 2023). There are three main types of subunit vaccines:

- Polysaccharide vaccines target an immune response to pathogenic bacteria encased in a chain of polysaccharide found in the pathogen capsule (i.e. the cell walls of some bacteria), and this develops responses against the surface of the bacteria, killing the pathogen in the process (Mandell, 2012).
- Conjugate vaccines also have a polysaccharide component, but the weak polysaccharide antigen is bound to a strong protein antigen. The polysaccharide-conjugated protein complex boosts the immune response, and helps in forging strong immune memory (Granoff *et al.*, 2013).
- Protein-based vaccines contain isolated proteins from pathogens. The immune response is usually instigated by a surface protein of the pathogen, or against a secreted toxin, and the antigen used in the vaccine is a very specific part of or derived from the pathogen.

Subunit vaccines may be produced from the original pathogen or recombinantly. Hepatitis B is a viral liver infection spread through blood, semen and vaginal fluids, and symptoms of hepatitis B include high temperature, sickness and diarrhoea (Liang, 2009). The hepatitis B vaccine, Recombivax HB ®, is an example of a recombinant protein-based subunit vaccine, which is produced using yeast cells.

The biggest advantage of subunit vaccines is their safety. For instance, the organism in live attenuated vaccines can undergo changes in their genetic material, which can cause a harmless version of a pathogen to revert to the original virulent pathogen (Hanley, 2011). There is no such risk with subunit vaccines, and this is particularly helpful for immunocompromised individuals or pregnant women, who cannot take live vaccines. However, despite their safety and efficacy, the immunity initiated by subunit vaccines is weaker than live vaccines, and multiple booster doses are needed (Chellasamy *et al.*, 2021). Finally, subunit vaccines need to be engineered to contain several antigens, as preparing a vaccine with just one epitope will not be enough to provide effective immunity (Heidary *et al.*, 2022).

### **1.1.5. Viral Vector Vaccines**

A viral vector vaccine uses a harmless virus to deliver genetic code to host cells. Their key differentiator is that they do not actually contain antigens, but instead a modified



virus to deliver genetic code of the antigen into human cells (Deng *et al.*, 2022). The mass production of the antigen triggers an immune response, and the vaccine ‘mimics’ infection with a real pathogen. The principle relies on the ability of viruses to survive and replicate by invading and hijacking host cells, except the vaccine ‘acts’ as the virus and delivers genetic code to host cells to generate the antigen. The double advantage of vector vaccines is that they stimulate a strong cellular immune response by T cells, as well as stimulating the production of antibodies by B cells (Gavi). Most viral vector vaccines only need one administration, as they induce strong immunity. However, booster doses maybe needed for ongoing immunity (Deng *et al.*, 2022, Kanokudom *et al.*, 2022). On the other hand, disadvantages of viral vector vaccines include a more complicated manufacturing process and an increased risk of genomic integration (Li *et al.*, 2020). An example of a viral vector vaccine distributed on a vast global scale is the COVID-19 Oxford-AstraZeneca vaccine (Falsey *et al.*, 2021) (**See section 1.2**). The viral vector maybe used as a platform for treating cancer (Larocca and Schlom, 2011, University of Oxford, 2021). Imlygic® (Ferrucci *et al.*, 2021), which employs similar technology to that found in viral vector vaccines, is available as a treatment for certain people with melanoma skin cancer, where cancer cannot be removed by surgery.

#### **1.1.6. mRNA Vaccines**

mRNA vaccines use mRNA (encoding a specific pathogenic protein) encapsulated in organic nanoparticles (NPs), and most commonly lipid NPs (LNPs) to induce immunity (Reichmuth *et al.*, 2016). LNPs are readily integrated in medicines due to their high biocompatibility, low toxicity, ability to cross membranes and seamless integration with hydrophobic/hydrophilic drugs (Syama *et al.*, 2022, Ghasemiyeh and Mohammadi-Samani, 2018). Once the LNPs reaches the host cell, the cell machinery follows the encapsulated mRNA instructions and produces the target protein, which is then displayed on the cell surface and eventually triggers an immune response (Pardi *et al.*, 2018). Upon future exposure to the pathogen, memory immune cells rapidly trigger the relevant antibody production to fight the threat (Reichmuth *et al.*, 2016). This is probably one of the newest and most exciting developments in recent vaccine technology, and the biggest advantage of this approach is the ability of large-scale

vaccine manufacture at speed (Rosa *et al.*, 2021), as conventional vaccines can take months, or even years to develop. The most significant example of this type of vaccine is the Pfizer-BioNTech COVID-19 vaccine (Polack *et al.*, 2020) (see **section 1.2**), which saw a highly successful global roll out, and is estimated to have saved around 110,000 lives in 2021 (Fujimura, 2022). The Moderna COVID-19 vaccine (Wang *et al.*, 2020) only took seven weeks from design, manufacture and shipment (World Economic Forum, 2021). However, although the early efficacy data of these vaccines is positive, the long-term effects are still unknown (World Economic Forum, 2021) and the data is not representative of long-term efficacy and side effects (Anand and Stahel, 2021). On the other hand, the requirement for a cold-chain remains with mRNA vaccines (Fahrni *et al.*, 2022), making storage and distribution challenging. The mRNA vaccine technology is fairly recent, and has so far been studied for a few viral diseases, including influenza (Arevalo *et al.*, 2022), zika (Essink *et al.*, 2023), rabies (Li *et al.*, 2022) and cytomegalovirus (Clinical Trials Arena, 2021). Aside from vaccines, mRNA technology has also been studied to initiate an immune response against specific cancer cells (Qin *et al.*, 2022).

## **1.2. Vaccines and COVID-19**

NPs can open up a variety of administration routes beyond injection. For example, liposomes can be designed for ingestion, protecting the drug from the acidic environment of the digestive tract to release it within the gastrointestinal tract and to relevant immune structures (Daraee *et al.*, 2016). The obvious target for the SARS-CoV-2 virus is the Spike (S) protein (see **Section 2.1.2**) found on the surface of the virus, and the mRNA-based vaccine developed by BioNTech in collaboration with Pfizer targets this. The vaccine was approved by the United States Food and Drug Administration (FDA), the United Kingdom Medicines and Healthcare products Regulatory Agency (MHRA) and the European Medicines Agency (EMA), demonstrating an estimated efficacy of 95% (Mahase, 2020b) (Polack *et al.*, 2020). As described above, another mRNA-based vaccine targeting the S protein was also developed at speed by Moderna, a United States based biotech firm (Wang *et al.*, 2020). Phase 3 clinical trials demonstrated 94.1% efficacy in preventing COVID-19 (Mahase, 2020a, Baden *et al.*, 2020). The Moderna vaccine was also approved by the

FDA for emergency use, and by the MHRA and EMA. The viral vector Oxford-AstraZeneca COVID-19 vaccine (Falsey *et al.*, 2021) was also developed very quickly to help combat the COVID-19 pandemic, and was globally rolled-out at scale, with emergency approval by the MHRA and EMA. The vaccine uses a modified, replication-deficient chimpanzee adenovirus as a vector, from which essential replication genes were deleted and replaced with a gene encoding the S protein (Arashkia *et al.*, 2021, Watanabe *et al.*, 2021). A tissue plasminogen activator (tPA) leader sequence was also used to increase immunogenicity (Arashkia *et al.*, 2021, Watanabe *et al.*, 2021). A phase 3 clinical trial demonstrated that the vaccine had 64.3% efficacy in preventing COVID-19 (Falsey *et al.*, 2021), and it was rolled out at speed, as part of the immediate response to the COVID-19 pandemic.

McKay (McKay *et al.*, 2020) investigated the vaccine potential of a self-amplifying RNA (saRNA) molecule encoding the S protein, encapsulated within LNPs, and a high concentration of SARS-CoV-2 specific antibody titres was observed in mice. When compared to the results from a natural immune response in recovered COVID-19 human patients, the vaccine resulted in higher antibody titres, which were able to neutralise both a pseudo and wild type SARS-CoV-2 virus. Furthermore, there was no observation of Antibody-dependent Enhancement (McKay *et al.*, 2020), which could result in enhanced respiratory disease and acute lung injury after respiratory virus infection. This is a common concern when developing antibody dependent vaccines, which could reverse amplify the infection (Arvin *et al.*, 2020).

saRNA is a newer type of RNA vaccine which contains a viral replication enzyme (replicase), which allows the target antigen to multiply (Ballesteros-Briones *et al.*, 2020). The saRNA enters the host cell, translates the replicase, making a negative copy of the mRNA. The mRNA strand is used by the replicase to synthesise more saRNA, while simultaneously binding to a sub-genomic promoter in the negative strand (Bloom *et al.*, 2021, Blakney, 2021). This synthesises sub-genomic mRNA at a 10-fold greater concentration than genomic RNA, encoding the viral antigen more effectively and making a more efficient vaccine (Blakney, 2021, Bloom *et al.*, 2021).

### **1.3. Drawbacks to Conventional Vaccination**

Vaccination is one of the most powerful, and in the long-term, cost-effective health care interventions, preventing 4-5 million deaths per annum, and working effectively in all age groups (World Health Organisation, 2019). However, traditional delivery is by needle, and this is a major drawback which influences uptake and effective delivery of vaccination programmes. Firstly, there is increased chance of transmission of blood-borne pathogens (Kuehnert and Cardo, 2000). Secondly, the safety of these vaccines maybe compromised due to unsafe use, resulting in needlestick injury. Thirdly, the fear of needles is a real concern for children and adults, and one which deters people and reduces vaccine uptake (Freeman *et al.*, 2021). Therefore, it is crucial to explore new vaccines that will overcome some, if not all the barriers faced by needle administration, and provide a better scope for delivery.

There are several alternative delivery methods which may be considered a ‘safer’ alternative to needles. Mucosal immunisation involves delivery of the drug to mucosal membranes such as the oral, nasal, pulmonary or vaginal/rectal membranes (Huang *et al.*, 2022a, Song *et al.*, 2004), and there are advantages and disadvantages to each. Oral delivery has been proven to be extremely challenging due to deactivation of the vaccine in the gastrointestinal tract, resulting in low bioavailability (Homayun *et al.*, 2019). Vaginal or rectal delivery results in poor patient compliance and low retention time caused by poor adsorption (ClinicalGate, 2015). The nasal mucosa is often the first point of contact for inhaled pathogens, and it is better to administer vaccines via the nasal mucosal surface to induce local mucosal immunity to prevent infectious agents from entering the host (Erdő *et al.*, 2018).

### **1.4. IN Vaccines**

IN vaccines act as a ‘first entry block’. This means, the pathogen is blocked from entering the nose, while the vaccine acts on the mucosal surface by inducing local microbial-specific immune responses (Ramvikas *et al.*, 2017). As the nasal mucosa is often the first point of contact for inhaled pathogens, administering vaccines via the nasal mucosal surface effectively prevents infectious agents from entering the host (Erdő *et al.*, 2018). The IN administration route for vaccine delivery also allows easy

administration, is non-invasive (Degenhard *et al.*, 2015), and it may allow self-administration, as demonstrated by a self-administration trial of an IN influenza vaccine (Burgess *et al.*, 2015). A pharmaceutical powder formulation is a solid dosage form which contains a mixture of finely divided drugs in combination with an excipient, and the tuneable properties of powdered drug formulations mean they are currently used in a wide variety of formulations, ranging from ointments and pastes to suppositories (Bartels *et al.*, 2021). Powder properties can be adjusted to develop a formulation that yields several advantages over liquid formulations for use in IN vaccine design include: the reduction of the powdered formulation to a very fine state, increasing adsorption, and enhancing therapeutic activity (Henriques *et al.*, 2022, Tiozzo Fasiolo *et al.*, 2018). Furthermore, nasal powders have increased stability without the use of preservatives, a prolonged residence time, better storage stability and enhanced protection at mucosal surfaces (Chavda *et al.*, 2021). By adding a dry-powder adjuvant to the formulation, it can induce specific mucosal and systemic antibody responses (Awate *et al.*, 2013).

### **1.5. IN Vaccines and COVID-19**

For COVID-19, nasal administration is an attractive proposition since the virus primarily enters the host by breathing in virion particles, and therefore, providing protection at the site of infection would be beneficial. One existing flu vaccine, FluMist (FluMist Quadrivalent, 2022) is sprayed into the patient's nose where the weakened virus induces mucosal, as well as systemic immunity (Mantis *et al.*, 2011). This means that the immunised patient has two layers of defence against the virus, and reduced likelihood of being able to carry and transmit the virus. Nanoparticulate systems could similarly be administered through inhalation or nasal spray, providing an attractive administration route with potential for greater protection for the patient, and more feasible storage conditions for healthcare providers (Kafetzis *et al.*, 2023).

Successful development of a COVID-19 IN vaccine will overcome the aforementioned problems associated with conventional vaccines, as well as providing effective mucosal immunity. The results from trials of current IN vaccines for COVID-19 have so far been mixed, with a clear indication that for an IN vaccine to work effectively, a

tailor-made formulation for IN administration is required. Researchers from the University of Oxford reported Phase 1 clinical trial data studying the safety and efficacy of an IN vaccine (University of Oxford, 2022) using the same formulation as the viral vector vaccine (Falsey *et al.*, 2021, University of Oxford, 2022) that was previously licensed for emergency use (**see Section 1.2**). The researchers reported mucosal antibody responses in a few participants and weaker systemic immune responses when compared to intramuscular vaccination (Slomski, 2022). Intravacc has an ongoing trial for an IN subunit COVID-19 vaccine booster (Intravacc, 2022), and the phase 1 clinical trial concluded on 15/1/24 (UK date) (ID: NCT05604690). Another experimental IN vaccine from Blue Lake Biotechnology provided strong protection against COVID-19 according to preliminary results from a Phase 1 clinical trial (ID: NCT04954287). Hyderabad based Bharat BioTech (Bharat Biotech, 2022) have developed an IN vaccine, which has been licensed for use as a primary vaccine and as a booster (Bharat Biotech, 2022). The vaccine, administered through the nose in the form of liquid drops, overcomes many of the problems associated with conventional vaccines. However, administration of the vaccine still stimulates the reflex action of sneezing or initiating a runny nose (Bharat Biotech, 2022). Therefore, the challenge of developing a dry-powder IN vaccine for COVID-19, one that will overcome the problems associated with traditional vaccines, liquid formulation IN vaccines, as well as limiting side-effects and maximising patient comfort, remains.

## **1.6. Project Aims**

The initial plan was to conjugate anti-SARS-CoV-2 antibodies to NPs, guided by Molecular Dynamics (MD) simulations, and use those studies to develop a new diagnostic for COVID-19. However, following the withdrawal of ‘The Antibody Company’ as my industrial sponsor, and the IBioIC CTP requirement of working with an industrial partner, I am now working on vaccine development with my new industrial partner, Alchemy Pharmatech. This study is sponsored by Alchemy Pharmatech, Manchester, and will use a MD-designed formulation for delivery of a dry-powder with their IN delivery device, Naltos. The main aim of this study is to investigate an IN vaccine for COVID-19, while targeting the significant unmet need of a dry powder IN vaccine that overcomes the aforementioned issues with traditional

vaccines, and those with currently licensed IN COVID-19 vaccines. MD simulations will be carried out to optimise antigen and inorganic NPs formulations, followed by experimental work starting with spray-drying lactose carrier particles in the 20-25 micrometres range, as it is the Naltos device particle size requirement, then incorporating silica NPs (SiNPs), and finally SiNPs with the S protein RBD. The thesis is presented as the following chapters:

- Chapter one (the current chapter) is an introduction to the topic, and sets the scope for the dissertation.
- Chapter two is a literature review, giving further background information relevant to experimental/MD simulation work carried out in this thesis. The chapter builds on chapter one to provide a deeper understanding as to why the work in this thesis was pursued.
- Chapter three covers the theory behind the instrumentation and methods used in this thesis, both for the experimental and computational work.
- Chapter four describes MD simulations to study the interaction of SpA with different model NPs to establish its suitability for designing a new diagnostic. In this study, SpA was modelled on three surface models (SiO<sub>2</sub> Siloxide, SiO<sub>2</sub> Silicon-undercoordinated, and Au (111)) to study adsorption and the predicted stability of the protein/NPs systems. The interactions of SpA with common model inorganic NPs developed an initial understanding of the protein-NPs systems for integration into a new diagnostic following the antibody conjugation route.
- Chapter five describes use of MD simulations to study the interaction of SARS-CoV-2 S protein RBD with model SiNPs and model carboxyl terminated SiNPs (COOH SiNPs). MD simulations were carried out to establish the structural stability of S protein RBD with the NPs, and to provide a good prediction as to their behaviour in practice, where these systems will be constructed experimentally. SARS-CoV-2 was chosen as the model for the dry-powder IN vaccine due to its relevance at the time, and to address the ongoing need for a dry-powder IN vaccine for COVID-19.

- Chapter six uses the MD studies to attempt production of a dry-powder IN vaccine formulation. In this part of the study, a dry powder IN vaccine formulation was constructed which consisted of lactose spheres, along with S protein RBD conjugated to SiNPs and COOH SiNPs, with the aim of formulating a dry-powder vaccine formulation consisting of the S protein RBD with SiNPs and lactose excipient.
- Chapter seven evaluated the work carried out by drawing conclusions, giving general perspectives and outlining scope for future work.



## Chapter Two: Therapeutics

*“Everything is theoretically impossible until it is done”*

*Robert A. Heinlein*

The current vaccines for COVID-19 present several challenges (see **Section 1.3**), and it is important to review and establish the best way to approach the development of new vaccines for COVID-19. SARS-CoV-2 consists of several different antigens, and with each antigen acting differently, this opens up a range of possibilities for new vaccines. We can also assess different materials, and determine how they may be used in conjunction with the target antigen, to optimise the design of potential new approaches.

## **2.1. Coronaviruses**

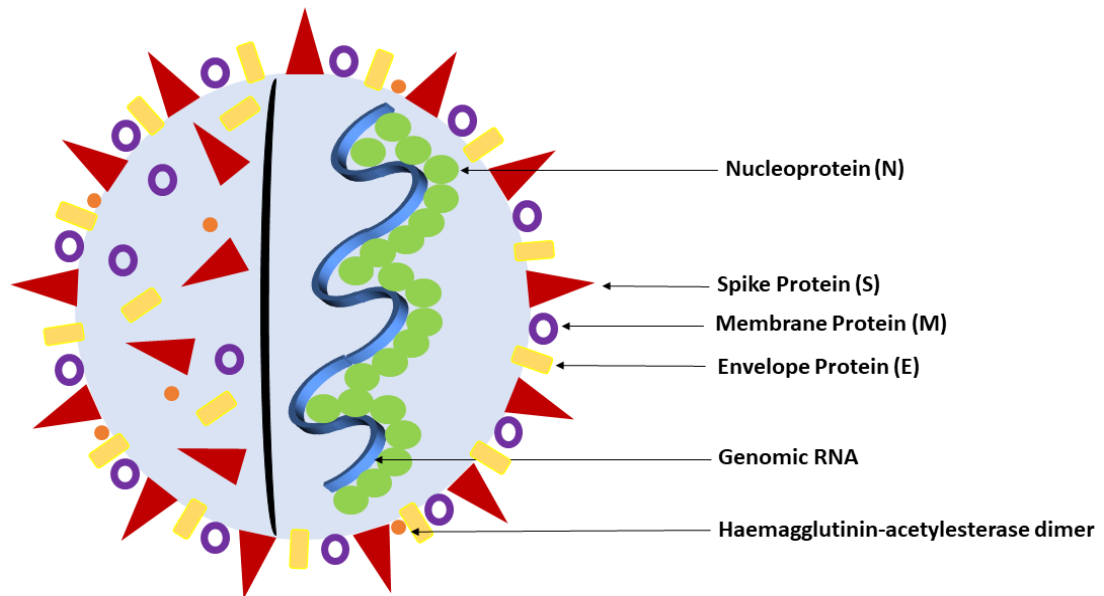
Coronaviruses are a family of viruses that can affect both animals and humans and which generally cause mild to moderate upper-respiratory tract illnesses in humans (Hu *et al.*, 2021). The coronavirus genome consists of RNA, which can constantly change and adapt, and these mutations may have been the root of the emergence of the COVID-19 pandemic (Harvey *et al.*, 2021), although natural mutation as opposed to a laboratory-derived source is still controversial (Yee *et al.*, 2021). There are seven coronaviruses that have been found in humans to date (**Table 2.1**), and four of them cause symptoms such as those seen with a common cold. The other three coronaviruses cause more severe illness, which in many cases can be fatal. These coronaviruses are SARS-CoV (emerged in Nov 2002), MERS-CoV (emerged in 2012) and SARS-CoV-2 (emerged in 2019) (National Institute of Allergy and Infectious Diseases, 2022).

**Table 2.1:** A list of coronaviruses found in humans and the illness they cause (Chen *et al.*, 2020) (Liu *et al.*, 2021).

| Coronavirus       | Illness  |
|-------------------|--|
| SARS-CoV-2 (2019) | COVID-19   |
| SARS-CoV (2003)   | SARS   |
| MERS-CoV (2012)   | MERS   |
| HCoV-NL63 (2004)  | Cough, fever, inspiratory stridor  |
| HCoV-229E (1965)  | Headache, nasal discharge, sneezing, sore throat, general malaise  |
| HCoV-OC43 (1967)  | Sore throat, coryza, general malaise   |
| HKU1 (2005)       | Cough, nasal congestion, rhinorrhoea, fever, sputum, sore throat, chills, postnasal discharge, tonsillar hypertrophy |

### 2.1.1. Structure and Function of SARS-CoV-2

The causative agent of the COVID-19 pandemic (Vox, 2021), was a previously unidentified coronavirus strain, denoted as SARS-CoV-2 (Cucinotta and Vanelli, 2020). SARS-CoV-2 (**Figure 2.1**) is spread predominantly from person to person, by droplets generated when an infected person coughs, sneezes or expels air through the mouth. Infection may also occur by touching contaminated surfaces, and then touching the face without first washing hands. The faecal-oral route may also be a source of transmission for the virus (Mohan *et al.*, 2021). The basic symptoms include fever, cough, shortness of breath, fatigue, and loss of taste and/or smell, and dependent on factors such as infection level, age, ethnicity, and strain of virus, the symptoms may be extended to include headaches, coughing up of blood from the lungs (haemoptysis) (Casey *et al.*, 2020), or diarrhoea, highlighting the severity of the virus, which can be fatal (Hanley *et al.*, 2020).



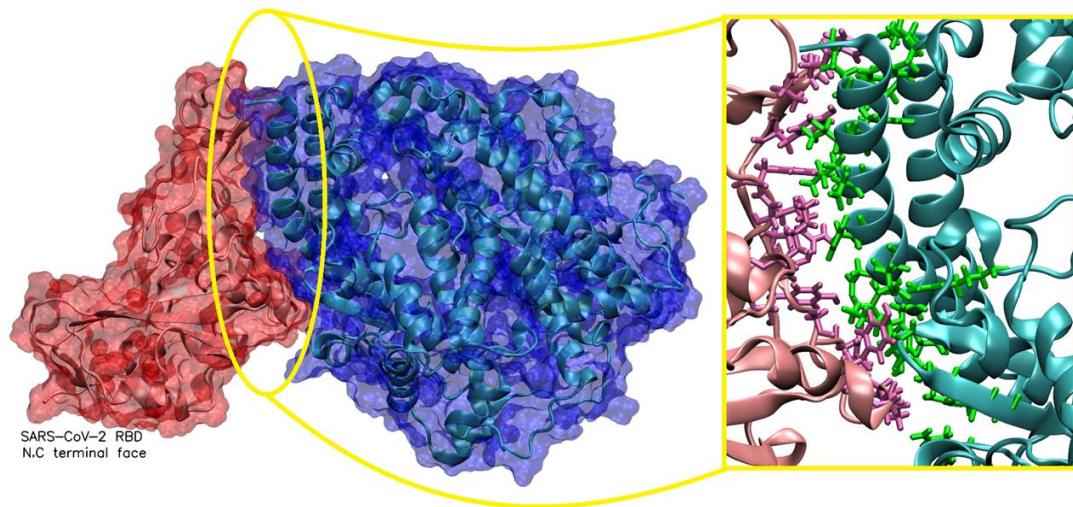
**Figure 2.1:** Diagram showing the structural proteins of the SARS-CoV-2 virus (Farouq *et al.*, 2021). Created using PowerPoint for Microsoft 365.

Analysis of the genomic sequence of SARS-CoV-2 (Wu *et al.*, 2020) shows there are at least six open reading frames (ORFs), which are segments of an RNA molecule that can be translated, allowing production of four main structural proteins: the S protein, Envelope (E) protein, Membrane (M) protein, and Nucleocapsid (N) protein. There is also the viral haemagglutinin-acetyesterase (HE) glycoprotein receptor, as illustrated in **(Figure 2.1)**. The M and E proteins are involved in virus morphogenesis and assembly (Schoeman and Fielding, 2019), while the N protein protects the RNA at the core of the virus, and the S protein is on the outside, and the entry point of the virus into host cells. As well as COVID-19, the S protein has also been linked with causing cardiovascular disease by damaging cardiac pericytes, which are mural cells supporting the maintenance and repair of the vasculature in the heart (Avolio *et al.*, 2021, Chen *et al.*, 2015, Imig, 2022).

### **2.1.2. Therapeutic Targets**

The S protein is an important therapeutic and diagnostic target, as it is responsible for entry into and infiltration of the host cell. It is a homotrimer with two domains, S1 and S2 on each monomer. Analysis of these monomers shows they are highly glycosylated

(Andersen *et al.*, 2020), protecting the protein from the biological environment and allowing evasion from the host immune system.



**Figure 2.2.** Interaction between the ACE2 receptor (Blue) and the S protein RBD (Red). Inset shows key interacting residues between the ACE2 receptor (Farouq *et al.*, 2021). The crystal structure was obtained from the Protein Databank entry 6M0J.pdb (Lan *et al.*, 2020). The crystal structure was viewed and analysed using Visual Molecular Dynamics 1.9.1 (Humphrey *et al.*, 1996).

The S1 subunit contains the RBD that binds to the peptidase domain of angiotensin-converting enzyme 2 (ACE2) (**Figure 2.2**), a cellular receptor expressed on several cell types in human tissues, that allows entry of SARS-CoV-2 into the cell (Lam *et al.*, 2020). Upon cell entry, two ORFs, 1a and 1b, translate to two polypeptides (1a and 1ab) which further encode two proteases, the main protease ( $M^{\text{pro}}$ ), which is also known as the chymotrypsin-like cysteine protease ( $3\text{CL}^{\text{pro}}$ ), and papain-like protease ( $\text{PL}^{\text{pro}}$ ) (Shin *et al.*, 2020). These represent significant therapeutic targets, since inhibition of these will stop production of proteins that are critical to viral transcription and replication (Gui *et al.*, 2017, Selvaraj *et al.*, 2020, Grottesi *et al.*, 2020). The S1 subunit allows entry of the virus into the host cell, and inhibition of this will block the protein from interacting with the ACE2 receptor (Nayak, 2020). Another potential target for vaccine development is transmembrane protease serine 2 (TMPRSS2) found on host cells (Mollica *et al.*, 2020). It cleaves the S protein into its subunits to enable cell entry, and inhibition of this process may prevent the initial entry of the virus.

NsP12 is a RNA-dependent RNA polymerase (RdRp) which plays a critical role in the assembly of the entire RNA polymerase replicative machinery, and is a key enzyme mediating the synthesis of all viral RNA molecules (Mishra and Rathore, 2021), making it a potential target. In addition, guanine N7-methyltransferase (N7-MTase), found at the C-terminal of SARS-CoV-2 nsP14, is crucial for exonuclease activity (Ogando *et al.*, 2020). Inhibition of this target could interfere with enzyme catalysis, and prevent capping of the 5'-ends of viral genomic RNA and sub-genomic RNA, that is crucial in SARS-CoV-2 evasion of the host immune response (Pearson *et al.*, 2021). This is because failure of RNA capping leads to viral RNA degradation and interference with the viral replication cycle (Selvaraj *et al.*, 2020).

High density lipoproteins (HDLs) are particles consisting of several proteins which transport all fat molecules around the body. HDL-scavenger receptor B type 1 (SR-B1) is a cell surface HDL receptor, which has been shown to facilitate ACE2-dependent entry of SARS-CoV-2, and further enhance uptake and increase the rate of virus entry (Wei *et al.*, 2020). Wei (Wei *et al.*, 2020) also suggested that blockage of the cholesterol binding site on the S1 subunit or treatment with SR-B1 antagonists inhibits HDL enhanced SARS-CoV-2 infection. Therefore, SR-B1 could also potentially be a target for vaccine design. Patel (Patel *et al.*, 2020) also suggested HE as a target to inhibit the virus invasion mechanism.

The residues responsible for the interaction between the S protein and the ACE2 receptor have been investigated by Veeramachaneni (Veeramachaneni *et al.*, 2020). This information is important for designing any medicine, since the residues required for interaction with the target should remain free to bind to the therapeutic molecule, to allow effective inhibition. Their analysis has identified the key residues that interact with the ACE2 receptor (see **Figure 2.2**).

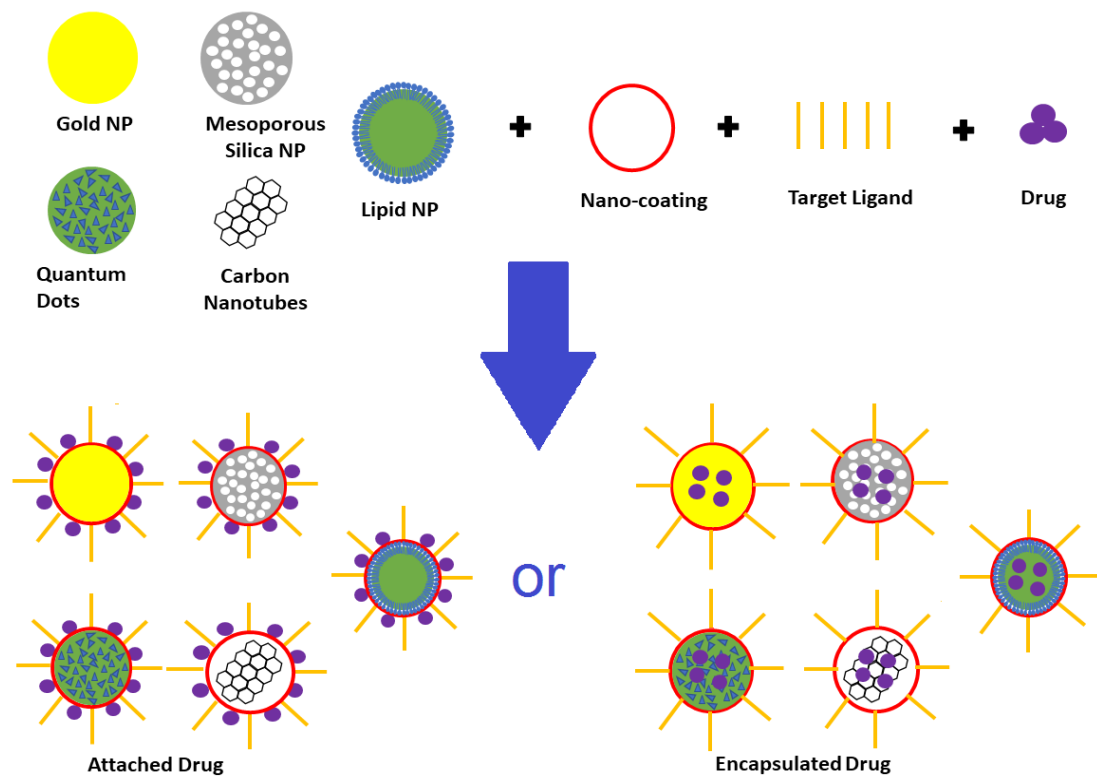
## **2.2. NPs**

### **2.2.1. The Role of NPs in Vaccines**

NPs are very small materials with a dimension between 1 and 100 nm. Their key physicochemical properties include a high surface area to volume ratio, solubility, surface topology/morphology and controllable aggregation, making them suitable for

application in a variety of commercial and domestic sectors including electronics, catalysis, environment, imaging, energy, automotive and healthcare (Khan *et al.*, 2019).

Pharmaceutical nanotechnology is the development of therapeutic materials and devices at a nanometre scale, and there are several advantages to exploiting NPs in drug delivery. These include, but are not limited to: (i) improvement in the solubility of certain drugs; (ii) controlled, sustained release of drugs for a long-term effect; (iii) reduction of the side effects of some drugs; (iv) targeting of specific cells; (v) administration routes; and (vi) delivery of drugs in a secure manner, so that they are protected from degradation in the body and can effectively reach the target cells intact (Gelperina *et al.*, 2005). NPs can display efficient adsorption of proteins, drugs molecules, and a variety of other chemical compounds. Therefore, NPs can carry a varied cargo load (Mitchell *et al.*, 2021), making them efficient not only for drug delivery, but also diagnostic and therapeutic applications.



**Figure 2.3:** A schematic diagram showing drug loading options in NP targeted drug delivery (Farouq *et al.*, 2021). Created using PowerPoint for Microsoft 365

The key properties of NPs (**Figure 2.3**) make them ideal for a variety of effective drug delivery systems. They can be porous or even hollow, and are often amenable to surface chemistry modification. Proteins adsorbed on NPs normally form a dynamic corona, and the conformational changes associated with the adsorption influence the overall *in vivo* bioreactivity (Oh *et al.*, 2018). The nature of NPs can influence the folding and unfolding properties of the protein, and by tuning the properties of the NPs, it can open new prospects in producing biologically active molecules. Thus, understanding the properties of the corona is essential (Treuel and Nienhaus, 2012). The interactions between NPs and a particular protein can utilise a noncovalent route, with the solvent having a critical role to facilitate the interaction (Treuel and Nienhaus, 2012). Consequently, it is vital to utilise a solvent *in vitro* that mediates the same interactions *in vivo* (Bresme *et al.*, 2009).

The biodegradation of NPs also requires attention, as uniform bio-distribution kinetics and sustained drug release are key elements in the drug design process. Absorption, distribution, metabolism and excretion are pharmacokinetic features linking directly to the nature and profile of these systems, and it is therefore crucial to account for all these factors when designing a nanoparticulate therapy (Patil *et al.*, 2020).

Adjuvants are compounds used to boost an immune response, and are particularly useful where vaccines do not naturally promote a strong immune response (Awate *et al.*, 2013). This is especially true for many vaccines developed in the modern era as they contain just a small component of the pathogen. On the other hand, vaccines designed with a weakened or live “wild” virus or bacteria can yield a strong, protective, immune response.

Adjuvants are particularly important for IN delivery due to the low affinity of most antigens with the epithelium, and the rapid clearance of antigens by mucociliary removal (Jiao and Zhang, 2019). Therefore, in addition to enhanced immunogenicity in the mucosal area, the addition of vaccine adjuvants to IN vaccines increases the magnitude and durability of antiviral immunity (Jiao and Zhang, 2019, Coffman *et al.*, 2010). Mucosal adjuvants must therefore be robust, as a strong mucosal response requires adjuvants capable of exerting their effects under the harsh conditions often found in mucosal tissues (low pH, high-density microbiota, sparse lymphoid cells)



(Freytag and Clements, 2015). Particulate adjuvants such as microspheres, nanospheres or microparticles, and various polymers used to encapsulate antigens, have been used as carriers or adjuvants for mucosal vaccines. Therefore, several substances have been described for IN delivery, many of which demonstrate great potential for use in humans.

For instance, CTA1DD is a nontoxic cholera toxin derivative, hybridised with a fragment of SpA (Eriksson *et al.*, 2004). CTA1DD adjuvanted vaccines effectively induced antibody responses and prevented influenza virus infection and transmission after IN administration (Bernasconi *et al.*, 2021). Chitosan, which is a natural derivative of  $\alpha$ -chitin, has promising mucoadhesive and immune-stimulatory properties leading to prolonged local retention time and enhanced mucosal adsorption (Wen *et al.*, 2011, Shim and Yoo, 2020). A chitosan adjuvanted, inactivated mutant, diphtheria toxoid CRM197 vaccine generated high levels of neutralising antibodies in humans after IN administration (Mills *et al.*, 2003). Also, a norovirus vaccine adjuvanted with chitosan and monophosphoryl lipid A (MPL), showed no signs of vaccine-related serious adverse effects (Clinical trial number: NCT00806962) (El-Kamary *et al.*, 2010) and induced strong antigen-specific humoral responses (Clinical trial number: NCT00973284) (Atmar *et al.*, 2011).

### **2.2.2. Therapeutic Applications of Adjuvants**

#### Aluminium Salts

Aluminium salts were initially used in the 1930s, 1940s and 1950s with the diphtheria and tetanus vaccines (Centre for Disease Control and Prevention, 2022). The mode of action these mineral agents employ in enhancing the efficacy of vaccines has been widely discussed (HogenEsch, 2002, Marrack *et al.*, 2009, HogenEsch, 2013), and several different mechanisms have been suggested. The antigen depot effect is when the antigen is released slowly, providing continuous stimulation to the immune system and amplifying the immune response triggered by a vaccine (Awate *et al.*, 2013). The antigen-adjuvant complex disintegrates, and the insoluble adjuvant keeps the antigen at the injection site. Antigen presenting cells navigate the bloodstream to the local

nymph nodes, where the antigen is presented to T cells (Brewer *et al.*, 2018). Aluminium salt adjuvants could enhance vaccine action by this phenomenon (Marrack *et al.*, 2009, He *et al.*, 2015). Alternatively, the aluminium salt adjuvants may act by stimulation of cytokine and chemokines, the enhancement of antigen uptake and presentation, and the promotion of antigen transport to draining lymph nodes (Awate *et al.*, 2013). Cytokines are peptides produced by a variety of cells, and are especially important in the immune system (Arango Duque and Descoteaux, 2014). There have been suggestions that aluminium salts work heavily in activating intracellular recognition receptor signalling pathways involving the NACHT, LRR and PYD domains-containing protein 3 (NLRP3) (Franchi and Núñez, 2008, Eisenbarth *et al.*, 2008, Kool *et al.*, 2008a). Activation of NLRP3 also releases potent inflammatory cytokines such as IL-1 $\beta$  and IL-18, which direct the host response (Franchi and Núñez, 2008).

Aluminium salts could be linked to the production of uric acid (Thakkar *et al.*, 2018b, Kool *et al.*, 2008b), excessive production of which may cause accumulation in the kidneys, leading to the formation and deposition of stones (El Ridi and Tallima, 2017). In current products, aluminium salts are attached to antigens using physical adsorption. This means any kind of physical strain to the product can break the bonds, making the vaccine ineffective, so the utmost care must be taken during formulation to ensure a good balance between product stability and efficacy (D'Amico *et al.*, 2021). Aluminium hydroxide salts (alum) are used as effective adjuvants in vaccines, and elicit a strong Th2 immune response (Ulanova *et al.*, 2001, Brewer *et al.*, 1999) in mice. Alum was found to act as a powerful and unique adjuvant when added to a nasal influenza vaccine in mice (Sasaki *et al.*, 2021). The vaccine worked by the release of IL-33 from alveolar epithelial cells, which stimulates production of IgA through a Th2 immune response (Sasaki *et al.*, 2021). IL-33 is from the IL-1 superfamily of cytokines, and can function both as a traditional cytokine and as a nuclear factor regulating gene transcription (Miller, 2011), meaning it is an important protein in cell-signalling. A dry powder vaccine, adjuvanted with insoluble aluminium salt was found to initiate both specific mucosal and systemic immune responses (Thakkar *et al.*, 2018a).

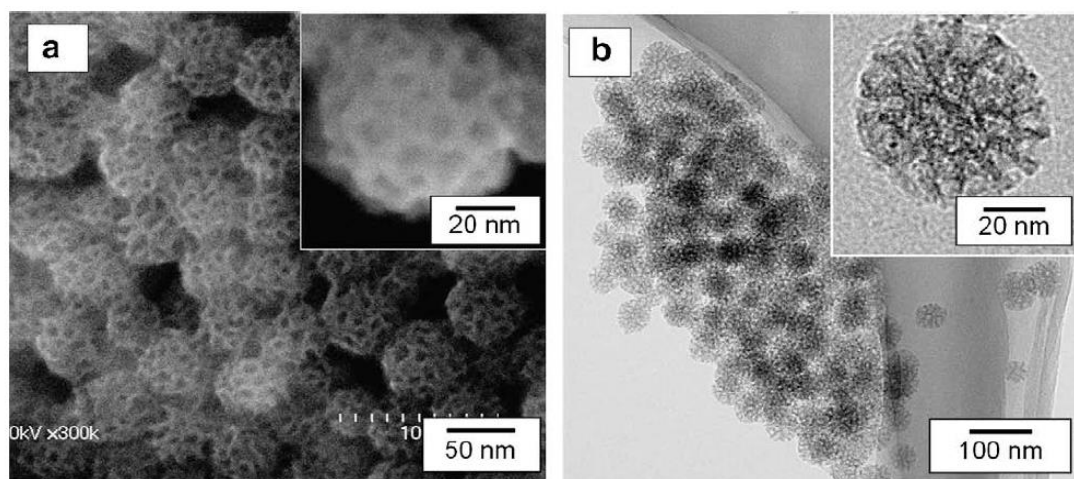
The AS03 immunological adjuvant is an oil-in-water emulsion composed of squalene, polysorbate 80, and alpha-tocopherol (vitamin E), used in various vaccine products including the A/H1N1 pandemic flu vaccine (Pandemrix ®) manufactured by GlaxoSmithKline (GSK) (GSK, 2009a, GSK, 2009b). Several mouse and human studies have demonstrated that the vaccine triggers a transient innate immune response, although additional mechanisms are also likely to be involved (Pulendran *et al.*, 2021). The vaccine was associated with increased risk of narcolepsy, a chronic sleep disorder, in young children (Miller *et al.*, 2013, Nohynek *et al.*, 2012). The successor to AS03, AS04, consists of aluminium hydroxide and MPL, it is commonly used in the HPV-16/18 AS04-adjuvanted vaccine (Cervarix ®) (Le Tallec *et al.*, 2009, Apter *et al.*, 2015, Angelo *et al.*, 2014). The MPL component of this formulation increases nuclear factor NF- $\kappa$ B and cytokine production, while the aluminium hydroxide component increases the efficiency of the immune response (Didierlaurent *et al.*, 2009).

Despite aluminium salt adjuvants being commonplace in many vaccines, there are several disadvantages to their use, giving scope for further research and development. Firstly, a vaccine prepared with aluminium salts involves binding of the antigens with the adjuvant, and in order to maintain high efficacy of this formulation, the vaccines must be kept in cold-chain (2-8°C) storage during transport (Thakkar *et al.*, 2017, Fortpiet *et al.*, 2018). In practical terms, this is a challenging requirement, as even a slight deviation from the ideal temperature can lead to freeze damage, resulting in drastically altered colloidal composition of the aluminium salts and irreversible cluster formation (Rybczynska *et al.*, 2020), and leading to loss of stability and efficacy of the vaccine (Fortpiet *et al.*, 2018, Rybczynska *et al.*, 2020). The accidental exposure of the vaccines to freezing temperatures means their safety is compromised and they must be discarded, not only contributing significantly to medical product waste, but also wasting time and resources used to produce and transport the vaccine (Thielmann *et al.*, 2019, Das *et al.*, 2020, Lloyd *et al.*, 2015). Thin-film freeze-drying can be used to convert aluminium salt-adjuvanted vaccines from a liquid dispersion to a dry powder without causing particle aggregation or decreasing immunogenicity (Thakkar *et al.*, 2017). However, despite the best efforts to produce and transport these vaccines, temperature deviations still occur due to several reasons including: faulty refrigerators,

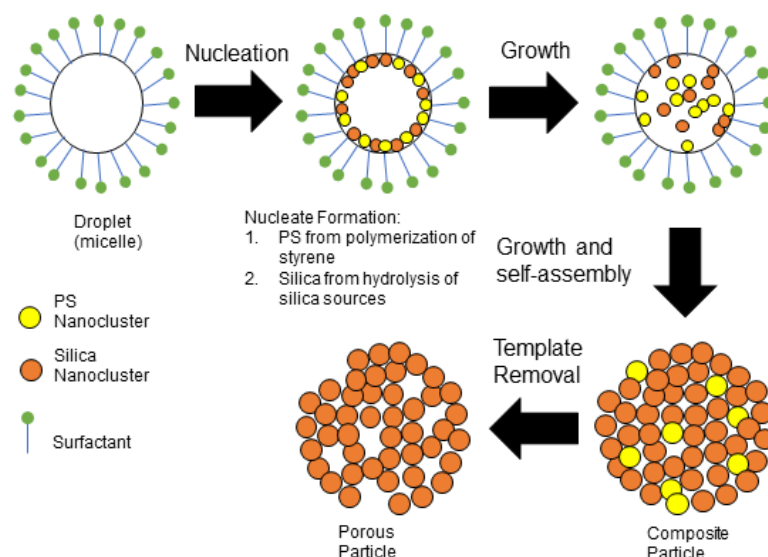
loss of power needed to operate the refrigerators and a poor understanding of maintaining the required temperature (Kumru *et al.*, 2014).

### SiNPs

SiNPs are amorphous materials that are highly versatile. They show promise for a variety of applications due to their properties which include high biocompatibility, hydrophobicity, systemic stability, and resistance to pH changes (Roy *et al.*, 2003). These combined factors make these materials useful for a variety of applications in drug delivery and nanomedicine, e.g. SiNPs have previously been investigated as a vaccine platform against human immunodeficiency virus (HIV) (Thalhauser *et al.*, 2020). A particularly interesting feature of SiNPs is the ability to functionalise them with different coatings, and Xia (Xia *et al.*, 2009) demonstrated that cationic polymer (PEI) coated SiNPs significantly increased their bioavailability.



**Figure 2.4:** a) Scanning Electron Microscope, b) Transmission Electron Microscope images of mesoporous SiNPs (MSNPs). The inset image shows a high resolution electron microscope image of a single particle, highlighting the tuneable pore size (Nandiyanto *et al.*, 2009).



**Figure 2.5:** A diagram showing the process of making mesoporous NPs. Their porous structure can host a variety of molecules, making them ideal candidates for drug delivery. Figure adapted from (Nandiyanto *et al.*, 2009).

SiNPs exist in non-porous and mesoporous forms (**Figures 2.4 & 2.5**). Colloidal mesoporous SiNPs (CMSNPs) were investigated for their adhesion with polydimethylacrylamide (PDMA) (Kim *et al.*, 2017). The polymer and linker in PDMA is comparable to the extracellular matrix, and several different NPs with varying pore and particle diameters and concentrations were prepared, with the NPs evaluated for wound healing in mouse skin, as well as their degradation rate (Kim *et al.*, 2017). The results were compared with conventional suture and treatment with non-mesoporous NPs, and the CMSNPs were significantly more adhesive than the non-mesoporous equivalent. The CMS-C50 NPs, with an average diameter of 50 nm, and a pore diameter and specific pore volume of 6.45nm and 1.79 cm<sup>3</sup>/g were found to absorb the largest amount of polymer at any given concentration (Kim *et al.*, 2017).

The interactions of particles with cell membrane phospholipids can cause the release of hydrophobic drugs (Lu *et al.*, 2007), and studying the rate of cellular uptake of these mesoporous SiNPs (MSNPs) is therefore important. By attaching a fluorescent dye to the MSNPs, confocal microscopy can be used to visualise their movements, and fluorescent dye molecules fluorescein isothiocyanate and rhodamine B isothiocyanate

were attached to the surfaces of particles, with visible cellular uptake with normal and cancerous cell lines (Lu *et al.*, 2007). The robustness, coupled with tunable pore size, high biocompatibility, and cargo of a variety of drug molecules, means that MSNPs have potential to adapt as drug delivery systems for cancer treatment (Mohamed Isa *et al.*, 2021, Pasqua *et al.*, 2016). Zwitterionic MSNPs (Z-MSNPs) were prepared by the inclusion of carboxylic groups (with pH-dependent negative charge) and quaternary amine groups (pH-dependent positive), so that the release of the drug encapsulated within the structure depended on the interaction with the environment (Khatoon *et al.*, 2016). When in contact with aqueous matrix, these NPs form a hydration layer on their surface via electrostatic interactions, leading to prolonged blood circulation in the body, and enhanced cellular uptake in tumour cells (Khatoon *et al.*, 2016). These properties make Z-MSNPs exciting and with unparalleled potential for use as nanocarriers in drug delivery (Estephan *et al.*, 2011, Cao *et al.*, 2010). Z-MSNPs were tested with doxorubicin (DOX), a chemotherapy drug used to treat cancer. DOX was not readily released from the Z-MSNPs under standard blood conditions (pH 7.4), but release of DOX was shown to favour mildly acidic conditions (Khatoon *et al.*, 2016). Overall, DOX-Z-MSNPs showed higher anti-tumour efficacy than standard DOX or DOX-MSNPs (Khatoon *et al.*, 2016). These results also demonstrate Z-MSNPs as a promising candidate for cancer therapy and other biomedical applications.

However, there are several disadvantages to SiNPs for drug delivery. Firstly, they may be toxic; this toxicity stems from their high surface area to volume ratio, which can affect cellular interactions in organisms (Saikia *et al.*, 2018, Zhao *et al.*, 2011). The toxicity in NPs is also associated with the surface SiOH groups (Slowing *et al.*, 2009). Secondly, SiNPs may lead to the production of reactive oxygen species (ROS). ROS are chemically volatile radicals, and their instability makes them very reactive with tissues, resulting in cell death (Lehman *et al.*, 2016). The HO\* radical in particular is one of the most volatile species, and ROS can cause a variety of damage to DNA, cell membranes, and in some cases even initiate cancer (Fu *et al.*, 2014).

There are two subsets of T-lymphocyte cells, CD4<sup>+</sup> T helper cells and CD8<sup>+</sup> cytotoxic T cells. CD4<sup>+</sup> T cells differentiate into Th1 and Th2 cells, and Th1 cells drive the immune response towards a cell-mediated response, while Th2 cells promote a

humoral response. While CD8<sup>+</sup> cells directly kill virus-infected cells. Many conventional vaccines produce either a Th1 or Th2 mediated immune response, and there is a clear need for a robust, non-toxic and effective adjuvant that can induce coproduction of immune responses with no or minimal side effects. SiNPs may act as vaccine adjuvants and Hepatitis B virus core virus like particles were found to adsorb onto commercially available SiNPs. These complexes then induced strong Th1-biased immune responses in mice (Skrastina *et al.*, 2014). In a separate study, SiNPs were found to enhance adjuvant immune activity when used in combination with other inorganic vaccine delivery vectors. SiNPs with layered double hydroxide core-shell NPs were synthesised to deliver DNA vaccines and activate macrophages. It promoted the expression of IFN- $\gamma$ , IL-6, MHC II and CD86, displaying an enhanced immune response in mice (Wang *et al.*, 2014).

### Gold NPs

Gold NPs (AuNPs) have been investigated against the influenza A virus to combat mutations which caused the virus to become resistant to existing anti-viral drugs (Kim *et al.*, 2020). AuNPs are particularly promising because of their properties which include: chemical inertness, a large surface area to volume ratio and the simplicity of integrating them in synthetic processes (Yeh *et al.*, 2012, Cao-Milán and Liz-Marzán, 2014). Their large surface area is particularly helpful in SpA functionalisation, providing a good interface for SpA-IgG binding. A spin-off using AuNPs (Liu *et al.*, 2019), was studied, where citrate-capped AuNPs, and their conjugation with cysteine-tagged recombinant Protein A (rProtA) and Protein G (rProtG) was investigated. The resulting conjugates were characterised by Surface Plasmon Resonance (SPR) spectroscopy, Dynamic Light Scattering (DLS), Electrophoretic Light Scattering (ELS) and Rotary Metal Shadowing Transmission Electron Microscopy (RMTEM) (Liu *et al.*, 2019). The data was cross analysed and the rProtA-AuNPs complex exhibited stronger binding properties towards IgG. In addition, there was a larger size distribution and a distinct build-up of protein corona around the AuNPs, indicating protein absorption (Liu *et al.*, 2019). Binding isotherms, which are curves resulting from the measurement of a solid-liquid equilibrium interaction at constant temperature, indicated a 4-fold higher binding strength of rProtG on AuNPs than

rProtA. However, the rProtA-AuNPs conjugate displayed significantly higher binding capacity (Liu *et al.*, 2019). Given their aforementioned properties, several types of AuNPs may be adapted and used as adjuvants in vaccines. The immune response to the envelope protein of the West Nile virus was compared with nanorods, nanocubes, and 40nm/20nm nanospheres. The immune response was found to be the best with 40nm nanospheres, however, nanorods induced the secretion of proinflammatory cytokines IL-1 $\beta$  and IL-18 more effectively (Niikura *et al.*, 2013). TNF- $\alpha$  is an inflammatory cytokine produced by macrophages/monocytes during acute inflammation (Idriss and Naismith, 2000), and the nanospheres and nanocubes were found to increase TNF- $\alpha$ , monocytes IL-6/IL-12, and glycoprotein GM-CSF (Niikura *et al.*, 2013). AuNPs are more effective as antigen carriers and adjuvants when combined with other immune response stimulants, most commonly Complete Freund's Adjuvant (CFA) and CpG oligodeoxynucleotides (CpG ODNs) (Dykman and Khlebtsov, 2017, Dykman *et al.*, 2018), with unmethylated CpG motifs found to be particularly effective immunostimulants (Weiner *et al.*, 1997). AuNPs coupled with CpG ODNs effectively enhanced intracellular penetration of NPs into macrophages and significantly increased the secretion of proinflammatory cytokines TNF- $\alpha$  and IL-6. Furthermore, the immunostimulatory effect of AuNPs conjugated to CpG ODNs is higher than the equivalent concentration of CpG ODNs (Chen *et al.*, 2014, Zhang and Gao, 2017). Javadi (Moshref Javadi *et al.*, 2022) assessed the immunogenicity of AuNPs-conjugated RBD protein coupled with CFA to establish its efficacy as a possible vaccine candidate for COVID-19 in BALB/c mice. Two formulations, one with RBD protein only and another with AuNPs-conjugated RBD protein were tested and both formulations displayed short-term humoral immunity mediated by IgM antibodies. However, the AuNPs-conjugated RBD formulation gave stronger shorter and longer-term immunity mediated by IgG and IgM antibodies, producing TNF- $\alpha$  and IFN- $\gamma$  cytokines. These results indicate the RBD protein only vaccine is promising for short-term immunity, while the AuNPs-adjuvanted vaccine was promising for long-term immunity (Moshref Javadi *et al.*, 2022).



### Silver NPs

Silver NPs (AgNPs) have also been investigated for their anti-viral activity against Peste des petits ruminants virus, which depends on the NPs interaction with the virion surface (Khandelwal *et al.*, 2014). These NPs may also lead to better anti-viral activity when used in conjunction with bronchodilators in the lungs (Subhasish, 2020). The immunological adjuvant effect of AgNPs was investigated *in vivo* and *in vitro* with model antigens ovalbumin (OVA) and bovine serum albumin (BSA) (Xu *et al.*, 2013). The formulation was administered to mice and AgNPs were found to enhance production of antigen-specific IgG. Furthermore, the AgNPs induced Th2-biased immune responses, and *in vivo* assays showed increased peritoneal leukocytes, MHC II molecules on the macrophage surface and TNF- $\alpha$  and IFN- $\gamma$  levels, indicating AgNPs act as adjuvants by the activation of peritoneal leukocytes, particularly macrophages (Xu *et al.*, 2013). In a separate study, the efficacy of an AgNPs-adjuvanted influenza vaccine formulation was demonstrated in a mouse model (Sanchez-Guzman *et al.*, 2019), with the inclusion of AgNPs resulting in a reduction of viral loads and prevention of excessive lung inflammation following influenza infection. The AgNPs also enhanced specific IgA secreting plasma cells and antibody titres, indicating successful Th2/IgA mediated mucosal immunity (Sanchez-Guzman *et al.*, 2019).

### Cyclodextrin NPs

Cyclodextrin NPs (CNPs) are cyclic oligosaccharides with a hydrophilic outer surface and a lipophilic central cavity (Garrido *et al.*, 2020, Gadade and Pekamwar, 2020). These NPs maybe particularly useful due to their physical properties with polar hydroxy groups oriented specifically, allowing increased solubility and decreased toxicity of the associated drug. Garrido (Garrido *et al.*, 2020) suggested the use of cyclodextrins against COVID-19. Therapeutic cancer vaccination requires the activation of antigen-specific cytotoxic T lymphocytes. These are poorly stimulated by conventional vaccines, and immunisation of mice with peptide-loaded CNPs showed increased cytokine-producing CD8<sup>+</sup> T cells (Geisshüsler *et al.*, 2022). However, this study focused on eliciting CD8<sup>+</sup> responses, and an efficient immune

response needs a balanced CD8<sup>+</sup> and CD4<sup>+</sup> T-cell response, which could be achieved by utilising longer peptide sequences in the formulation. This study highlights the potential of CNPs as a vaccine platform which may be investigated for a range of diseases, and ultimately trialled in humans (Geisshüsler *et al.*, 2022).

### NPs for COVID-19

NPs can be readily constructed with a similar size to a virus, and may interact with proteins associated with the SARS-CoV-2 virus, disrupting viral replication and disease prognosis (Sportelli *et al.*, 2020). Tabish (Tabish and Hamblin, 2020) explored the multivalent nature of nanomedicines and how this may be particularly useful in the fight against COVID-19. Multivalent NPs have several advantages over standard monovalent drugs, including a high density of binding sites on individual NPs, the ability to form multivalent ligand receptor pairs, multi-fold RNA hybridisation, and the transformation of inactive NPs into multivalent conjugates (Tabish and Hamblin, 2020). Multivalency works through receptor-mediated endocytosis (Gao *et al.*, 2005), and Hassanzadeh (Hassanzadeh, 2020) suggested the use of multivalent NPs against COVID-19. Given the similarities in size of synthetic NPs and SARS-CoV-2, they could be particularly useful for investigation with drug repurposing, enhancing properties of existing drugs and compounds against COVID-19. However, caution is required, since SARS-CoV-2 may induce a hyperinflammatory response, driven by a dysregulated macrophage response (Merad and Martin, 2020). Therefore, it is important to look at the properties of any material to make sure it does not interact negatively *in vivo*.

Given the aforementioned studies, there are several types of NPs that have been investigated for their therapeutic properties, either to deliver drugs, or as vaccine adjuvants. SiNPs (used in this work) have several features which make them effective for therapeutic applications (see **Section 2.2.2**), and there are several human studies (Zanoni *et al.*, 2021, Phillips *et al.*, 2014, Kharlamov *et al.*, 2015, Meola *et al.*, 2021, Tan *et al.*, 2014) which indicate their potential, and are promising in work towards making therapeutics incorporating SiNP, or indeed other NPs, readily available on the market.

## Chapter Three: Methodology

*“Science is magic that works”*

*Kurt Vonnegut*

### **3.1. Molecular Simulation**

Molecular Simulation (MS) utilises computers with a variety of theoretical and experimental models to help solve scientific problems that would be difficult to accomplish through experimental methods alone (van Gunsteren *et al.*, 2018). MS has been used as an important tool by many researchers to expand understanding of systems and processes, and by building up a mathematical model, outcomes can be predicted (van Gunsteren *et al.*, 2018). The recent rise in computational power has made simulations easier to run, and has seen MS establish itself as an increasingly important tool in research. There are two main branches of MS techniques: Monte Carlo (MC), and MD. MC builds up many models of potential results, giving a range of values and calculating results by extensive random sampling; these results are displayed in the form of probability data charts (Harrison, 2010). The random sampling of molecules allows all possible outcomes to be viewed as a result of variables, which can be changed in the system. Therefore, it is possible to build up an approximation of uncertainty in a system, and allow necessary changes to influence the result. MC is used in a variety of fields for research and risk management (Suhobokov, 2007). In this project MD simulations have been chosen to study biomolecular interactions, and to shape the experimental work.

### **3.2. MD**

MD allows direct analysis of the physical movement of atoms and molecules in a system over time. The major advantage of MD over MC is that it allows the study of real time, precise interactions, giving a true dynamic representation of the system (Hollingsworth and Dror, 2018). MD results in a trajectory, which is a collection of sequential snapshots representing atomic position over time (Likhachev *et al.*, 2016). The trajectory is computed numerically by solving the Newton's equations of motion for the system, allowing access to interactions that would otherwise be impossible to observe, such as changes in protein dynamics and structural changes that occur upon interaction with different systems (Durrant and McCammon, 2011). Furthermore, the versatility of MD in allowing the study of a variety of systems, while observing

relationships and real-time interactions in the systems, has led to the growth of MD as a commonly used simulation technique (Hospital *et al.*, 2015).

### **3.2.1. Integration Algorithms, Constraint Solvers, and Water Models**

MD simulations numerically solve Newton's equations of motion, and there are general algorithms available to solve such equations. For instance, the fourth order Runge-Kutta method (Ramos and Vigo-Aguiar, 2007), or any of the other higher-order predictor/corrector methods come with limitations including an increased computation cost and an instability in dealing with long simulations of multi-particle systems (Ramos, 2019). In MD simulations, higher-order integration algorithms are not necessary for several reasons. Firstly, only an algorithm that will specifically solve Newton's laws is required, to ensure the correct statistical ensembles are generated, while energy is conserved (MSI, 1998). Secondly, the increased accuracy of higher-order algorithms does not allow a proportional increase of the timestep due to the stiff nature of the interatomic forces at short distances (Babicheva *et al.*, 2022). The timestep limits the length of MD trajectories and the simulation, as too large timesteps can cause a simulation to become unstable due to the energy in the system increasing rapidly with time, allowing the atoms move freely. Therefore, it is important to regulate the timestep of a simulation, as a proportional increase will yield simulations and trajectories with quality data. Finally, the algorithm should place minimal load on computer memory, while allowing use of a large timestep (Winger *et al.*, 2009). The Verlet algorithm (Verlet, 1967) is a 3<sup>rd</sup> order, symplectic integrator, with three algorithms; The Basic Verlet, Leapfrog Verlet and Velocity Verlet algorithms. Phase space is a mathematical concept that represents all possible states of a system, and it is important to use a symplectic integrator in MD simulations as it gives a conservative system, where the set of position and momentum statepoints remain constant in the system for the duration of simulation, conserving the overall momentum. Otherwise, using a non-symplectic integrator in MD simulations will give a dissipative system, resulting in increased motion of species and a decrease in momentum, as energy is lost through motion. The Velocity Verlet algorithm (Verlet, 1967, Swope *et al.*, 1982) generates a sequence of 'images' for the particle coordinates and velocities, following

the same order as the Basic Verlet algorithm, which makes it fast and accurate while preserving linear and angular momentum. The algorithm is also time reversible, this, and the aforementioned properties make it the most widely used integration algorithm and it was also used in this work.

A constraint solver satisfies bond geometry constraints in protein and peptide MD simulations, allowing efficient simulations by neglecting motion along some degrees of freedom, either translational, rotational or vibrational (López-Villellas *et al.*, 2023). Therefore, the use of constraint solvers in MD simulations reduces the time required to compute the high-frequency movements in simulation, or else, finding the equilibrium state between the protein, water and ions would use much more computational power (López-Villellas *et al.*, 2023). Explicit or implicit constraint solvers maybe used, with the former needing more computational power, resulting in an inefficient simulation (Simuleon, 2021). Therefore, implicit-force constraint solvers increase the overall efficiency of the simulation. The SHAKE algorithm was first developed for satisfying bond geometry constraints during MD simulations (Ryckaert *et al.*, 1977). The method was then further developed to handle any holonomic constraint (Ciccotti and Ryckaert, 1986), and the SHAKE algorithm is commonly used to satisfy bond geometry constraints during MD simulations without significantly affecting the accuracy of simulations. The SHAKE algorithm was also used in this work.

Several water models can be used in MD simulations. The TIP3P model uses water molecules with three sites of interaction at two hydrogen atoms and one oxygen atom, and it is a simple water model which saves computational power. It is therefore the most commonly used water model in simulation (Izadi and Onufriev, 2016), and was also used in this work. Using a more complex water model, such as the TIP4P or TIP5P maybe be more accurate (Ji *et al.*, 2012), but would require significantly more computational power. The single point charge (SPC) model maybe more computationally efficient (Ji *et al.*, 2012). A measure to improve simulation efficiency is to use an implicit solvent model. Using an implicit solvent water model means instead of adding all the individual water molecules explicitly, and running many calculations simultaneously, water is treated as a continuous medium surrounding the

solute, which reduces computational load and increases simulation efficiency (Liu *et al.*, 2017). Although an implicit solvent speeds up the calculations, this comes at the expense of some of the simulation details as it considerably decreases the number of particles it tracks for a system (Al Qaraghuli *et al.*, 2018). Therefore, an explicit solvent model was used in these simulations to ensure as much of the simulation detail and data is available.

### 3.2.2. Thermostats, Barostats and Forcefields

MD simulations are usually computed in one of three thermodynamic ensembles. The Microcanonical (NVE) where number of particles (N), the system volume (V), and the energy (E) are kept approximately constant. The Canonical (NVT), where N, V and the temperature (T) are kept approximately constant or Isothermal-Isobaric (NPT), where N, the system pressure (P) and T are kept approximately constant (CompChems, 2022). T is a statistical quantity which has to be expressed as a function of position and momenta of all particles in the system, and for a system containing enough atoms, the temperature can be estimated from the kinetic energy (Bormashenko, 2020). The NVT and NPT ensembles are the most practically relevant as experimentally, it is far easier to control the temperature of a system than it is to control energy.

A thermostat is therefore an algorithm used in MD simulations to regulate the simulation temperature (Hünenberger, 2005). There are several thermostat algorithms available to use, and in this work, the Langevin thermostat was used, which is a stochastic method most commonly used with Nanoscale Molecular Dynamics (NAMD) and most MD software packages. The Langevin Equation (eq 3.1) regulates the temperature while changing the way in which velocities are updated:

$$m\dot{v} = F(x) - \gamma v + \sqrt{\frac{2\gamma K_B T}{m}} R(t) \tag{3.1}$$

Where  $m$  is the mass,  $v$  is the velocity,  $F$  is the force,  $\gamma$  is the friction coefficient,  $K_b$  is the Boltzmann constant,  $T$  is the temperature and  $R(t)$  is a random number drawn from a univariate Gaussian random process (Phillips *et al.*, 2005). Newton's equations of motion are modified by adding appropriate dissipative and fluctuating forces, and the system randomly assigns new velocities based on the Maxwell-Boltzmann distributions for the target temperature, slowing down the system kinetics, but reaching the desired temperature (eq 3.1).

A barostat is a pressure control algorithm used in MD simulations that adjusts the volume of the simulated system by scaling the coordinates of each atom in a system by a small factor (Braun *et al.*, 2019). This also changes the size of the system, but ensures the desired pressure is reached in simulation. There are several barostats available to use, and the Langevin piston Nose-Hoover method, which is a combination of the Nose-Hoover constant pressure method (Martyna *et al.*, 1994), and piston fluctuation control implemented using Langevin dynamics (Feller *et al.*, 1995) was used in this work.

The potential energy (PE) is the energy of the object which depends purely on the position of the object in space, and PE is associated with several different forces that act on the object concerned. PE can be divided into covalent forces and non-bonded interactions, and this is simplified with the following equation:

$$PE = E_{\text{Bonded}} + E_{\text{Non-bonded}}$$

Where

$$E_{\text{Bonded}} = E_{\text{Bond}} + E_{\text{Angle}} + E_{\text{Dihedral}}$$

And

$$E_{\text{Non-bonded}} = E_{\text{Electrostatic}} + E_{\text{VDW}}$$

(3.2)



In forces defined by forcefields (FF),  $E_{\text{bonded}}$  interactions refer to all two, three and four atom interactions in the system, while  $E_{\text{Non-bonded}}$  refers to all the electrostatic and Van der Waals (VDW) interactions in the system (Theoretical and Computational Biophysics Group, 2002).

A FF is a collection of interatomic potentials defining the forces between particles given their positions at a particular point in time (Guvench and MacKerell, 2008) (**eq 3.2**), and every FF includes interatomic interactions based on parameters suited to the system. Non-bonded terms use the most computational power, and VDW forces are usually calculated using the Lennard-Jones (L-J) potentials. Therefore, it is crucial to select the correct FF for a system to ensure correct parameterisation to a system and effectively cover all the interactions, while delivering effective performance. The Charmm-27 FF covers most protein interactions and was used in this work (Vanommeslaeghe *et al.*, 2010).

In MD simulations, the atoms in a system are modelled as interacting balls with a defined radius and no directional properties. The radius of the ‘ball’ depends mainly on the atomic properties, and charge is setup on a particular atom, and remained fixed on all species in all simulations in this thesis. Simple harmonic oscillation can be described as an oscillatory motion in which the acceleration of the particle at any position is directly proportional to the displacement from the mean position. This principle can be explained by Hooke’s law (**eq 3.3**):

$$F(x) = -kx \tag{3.3}$$

Where  $F$  is the spring force,  $k$  is the spring constant and  $x$  is the spring compression, and  $-kx$  is the restoring force.

The equation of motion is given by Newton’s second law (**eq 3.4**):

$$\Sigma F_x = -kx = ma_x \tag{3.4}$$

Where  $\Sigma F_x$  is the sum of forces in x direction, k is the spring constant, x is the spring compression,  $-kx$  is the restoring force, m is the mass and  $a_x$  is the acceleration in x direction. This equation can be solved for acceleration (**eq 3.5**) to provide the basis for simple harmonic motion:

$$a_x = -k/mx \quad (3.5)$$

In simulation, bonds and angles are treated as harmonic oscillators, they are modelled virtually and treated as ‘springs’, so there is no bond formation or destruction, independent of the distance between the bonded and non-bonded atoms.

$$U_{el} = \sum_{i>j} \frac{q_i q_j}{4\pi\epsilon_0 r_{ij}} \quad (3.6)$$

The simple Coulomb equation gives the total Coulomb interaction energy, where  $q_i$  and  $q_j$  are the amount of charge on ionic pairs,  $\epsilon_0$  is the dielectric permittivity of vacuum and  $r_{ij}$  is the interatomic separation (Theoretical and Computational Biophysics Group, 2002). This links both to Coulomb and VdW forces, which are crucial to the simulation and disappear rapidly as the distance between the molecules increases; the nature of the electrostatic forces in simulation is formulated by the simple Coulomb equation (**eq 3.6**). As the electrostatic force loses its value slower than the L-J potential, which gives a stronger interaction, using a defined cut-off may therefore not be the best idea, as the strength of the interaction may fluctuate. Particle Mesh Ewald (PME) is a method for computing full electrostatics in a system. As the electrostatics of the simulation can be attractive or repulsive dependent on charge, PME divides the long-range interaction into two parts: a short-range contribution and a long-range contribution and the basic idea of PME is to replace the direct summation of interaction energies between point particles.

The VdW force is the sum of the attractive and repulsive forces between atoms due to dispersion forces, irrespective of covalent bonds or electrostatic interactions between ions or charged atoms. These can be defined by the following equation:

$$U_{vdW} = (-\epsilon_{\min}) \left[ \left( \frac{R_{\min}}{r_{ij}} \right)^{12} - 2 \left( \frac{R_{\min}}{r_{ij}} \right)^6 \right] \quad (3.7)$$

Where  $\epsilon_{\min}$  is the minimum dispersion energy,  $r_{ij}$  is the interatomic separation and  $R_{\min}$  is the distance at which the particle-particle PE is zero. VdW forces are relatively weak when compared to covalent bonds or electrostatic interactions, but collectively, they play an important role in simulation. VdW forces are described by the L-J potential (eq 3.7). The L-J potential approaches zero rapidly as the  $r_{ij}$  increases, meaning the VdW forces usually shift to be zero past the L-J cutoff radius (Theoretical and Computational Biophysics Group, 2002).

### 3.2.3. NAMD and Visual Molecular Dynamics

NAMD is a MD code designed for high-performance simulation of large biomolecular systems, with features ranging from constant temperature and pressure control methods, to more advanced simulation methods such as free energy calculations and enhanced sampling via replica exchange (Theoretical and Computational Biophysics Group, 2013). NAMD can be used on supercomputers with many nodes in parallel to simulate large systems with millions of atoms (Theoretical and Computational Biophysics Group, 2013).

Several options may be modified to reduce computational cost and increase the efficiency of simulations. NAMD has options that control the way non-bonded interactions are calculated, and the simplest non-bonded interaction is VdW (Blamey *et al.*, 2017). The L-J cut-off is the local interaction distance common to both electrostatic and VdW calculations, and in NAMD, VdW interactions are always

truncated at the L-J cut-off distance (Theoretical and Computational Biophysics Group). In general, a higher L-J cut-off will give a more accurate simulation. However, for best results, the L-J cut-off which validates a FF should be used.

Periodic Boundary conditions (PBC) are a set of boundary conditions which allow simulations to mimic an infinite system by allowing particles to become enclosed in a unit cell, and being replicated to infinity by periodic translations (Cheatham *et al.*, 1995). The use of PBC in simulation means a relatively small system can be used to obtain detailed results to explain the corresponding experimental data. The simulation timestep holds the dynamic data for a molecule for a single step in a simulation trajectory and maybe altered in a way to improve simulation efficiency. A larger timestep, for example 2fs instead of 1fs ensures phase space can be sampled more rapidly, saving on computational power (NanoMedic, 2021). However, it is important to exercise caution as too large a timestep can cause the simulation to become unstable as the energy increases rapidly with time (Löfgren *et al.*, 2022).

Visual Molecular Dynamics (VMD) is a molecular modelling and visualisation software package, with features ranging from visualising MD simulations to extensive exploitation of biomolecules to generate images (Humphrey *et al.*, 1996, Theoretical and Computational Biophysics Group). VMD allows a large quantity of trajectory data to be loaded, which is particularly helpful when analysing trajectories.

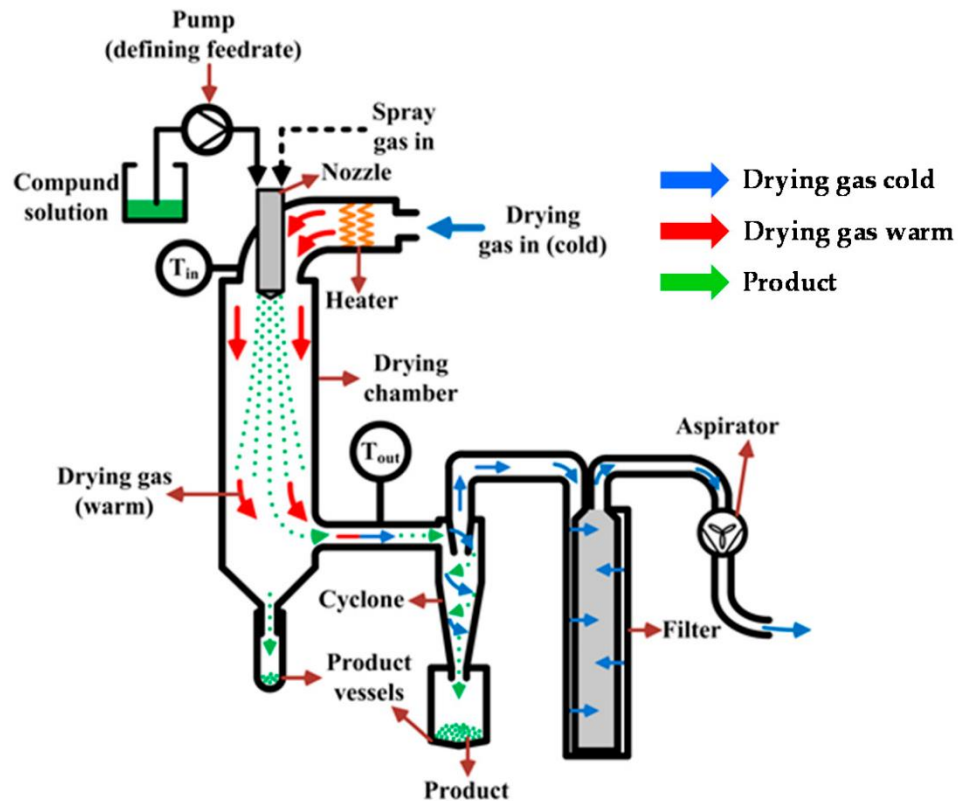
### **3.3. Laboratory Techniques**

#### **3.3.1. Spray Drying and Characterisation of The Sample**

##### Spray drying

Spray drying is a method of changing a liquid to a dry powder by atomising the solution and drying it with a hot gas (Daniel *et al.*, 2017). The solution is sprayed into droplets, and then the rapidly evaporating droplets are dried into powder by a mixture of hot gas, temperature and pressure (Gohel *et al.*, 2009). The method is used commercially across the food and pharmaceutical industries, and the heated drying medium may consist of hot air or nitrogen gas, though the use of nitrogen is preferred

as it allows the safe drying of organic solvents and reduces oxidation in the product (Gaspar, 2014).



**Figure 3.1:** A schematic representation of the conventional spray-drying process (Piñón-Balderrama *et al.*, 2020).

All spray dryers use a spray nozzle or atomiser head to disperse the liquid into a controlled particle size, and a blast of hot gas dries the particles into a free-flowing powder, with the size of the final particles dependent on the type of nozzle used to disperse the solution (Both *et al.*, 2020) (**Figure 3.1**). There are two main types of spray-dryer and the most common type, a single-effect spray dryer, consists of a single source of drying gas at the top of the chamber with the hot gas blown in co-current as the sprayed liquid, resulting in fine dried particles. Counter current spray dryers, which spray the hot gas in the opposite direction to the sprayed liquid, are also available (Julián *et al.*, 2017), and these maybe more thermally efficient (Feeco). However, single-effect spray dryers may result in poor powder flow and a low-quality powder.

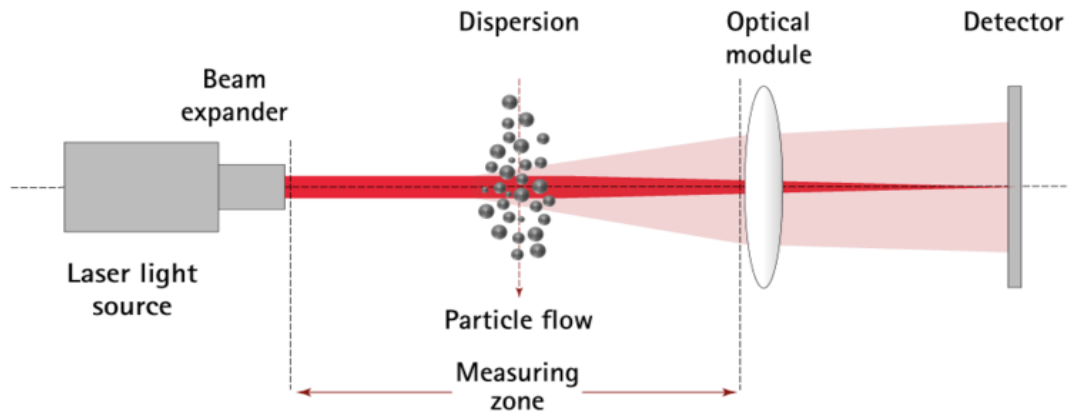
Newer, multiple-effect spray dryers overcome this limitation by operating through two steps, the first drying occurs as with single effect spray dryers, and the second drying with an integrated static bed at the bottom of the chamber. The spray dryer used in this work was the single-effect Buchi B290 mini spray dryer.

### Laser Diffraction

Laser diffraction spectroscopy uses diffraction patterns of a laser beam to measure the dimensions of a particle. In most laser diffractors, a laser beam is passed through an object at speed, resulting in a quick measurement, and although practically there is a particle size limit of ~0.1-10000  $\mu\text{m}$ , objects can range from hundreds of nanometres to several micrometres in size (Rawal and Patel, 2018). The range of particle size measurement can be extended by using multiple laser light wavelengths. The basic principle of laser diffraction relies on the measurement of the angles from the intensity of the light scattered as the beams pass through the sample. When the laser beam is fired at larger particles, the light is scattered at smaller angles, while firing the beam at smaller particles scatters the light at larger angles (Rawal and Patel, 2018). The measured data is then analysed to calculate the size of the particles using the Mie theory of light scattering.

$$I = I_0 \frac{1 + \cos^2 \theta}{2R^2} \left( \frac{2\pi}{\lambda} \right)^4 \left( \frac{n^2 - 1}{n^2 + 2} \right)^2 \left( \frac{d}{2} \right)^6 \quad (3.8)$$

The Rayleigh approximation (**eq 3.8**), where  $I$  is the intensity of the scattered radiation,  $\theta$  is the scattering angle,  $R$  is the distance to the particle,  $\lambda$  is the wavelength of light under consideration,  $n$  is the refractive index of the particle and  $d$  is the diameter of the particle (Seinfeld and Pandis, 2006).



**Figure 3.2:** A schematic diagram showing the optical setup for a laser diffractor (Sympatec).

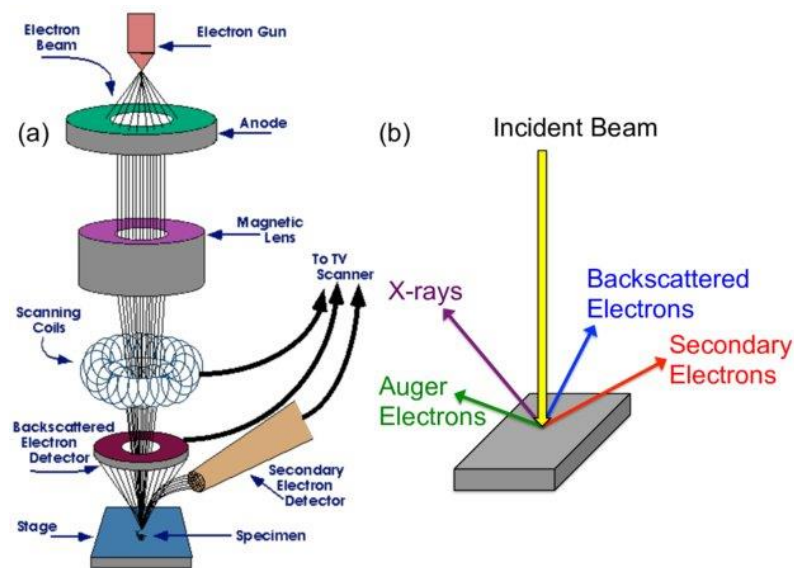
The Mie theory is a complete mathematical-physical theory of the scattering of the electromagnetic wave by a sphere, requiring knowledge of the real refractive index and imaginary component of both the sample being measured, along with the refractive index of the dispersant (Singh and Soni, 2019). The real refractive index defines where the exiting light will focus and spread, while the imaginary component is an indication of the intensity of the refracted light. If the imaginary component is very low, the intensity of refraction will be high. The imaginary component is especially relevant to particle size, and as it is not known or defined, and selection of the correct value is based on compensation values from predicted light scattering particle size distribution. For instance, very small ( $< 1$  micrometre), transparent, and not highly absorbing particles have a very short light path and absorption does not occur, so the imaginary term can be assumed to be zero (MicroTrac). Particle size increase is proportional to the imaginary component, but it results in a weak secondary effect of negligible or insignificant importance as the imaginary component is not defined (MicroTrac). A notable feature of the Mie theory is Mie resonances, which account for varied particle sizes that scatter the beam particularly strongly or weakly. This is in contrast to the Rayleigh scattering approximation (eq 3.8), which describes the elastic scattering of light by primarily small particles (Farafonov *et al.*, 2011). A simplified approach to measuring data is to use the Fraunhofer approximation of the Mie theory, which does not require the aforementioned data for the sample. However, the Fraunhofer approximation can only provide accurate

data for larger particles (Chen *et al.*, 2017a). The two laser diffractors used in this work are the Mastersizer 3000, and the Sympatec HELOS (**Figure 3.2**).

### 3.3.2. Spray-dried Sample Imaging

#### Scanning Electron Microscope

A Scanning Electron Microscope (SEM) is a type of electron microscope that uses electrons to scan the surface of a sample to produce an image (Golding *et al.*, 2016). SEMs have been developed over the years to become powerful and versatile tools for characterisation as they can work with very small materials (Golding *et al.*, 2016). The wavelength of electrons is smaller than light, so the resolution of SEMs is far superior to that of conventional light microscope images (ThermoFisher, 2019).



**Figure 3.3:** a) A typical SEM column, and b) sample-beam interactions within a SEM (ThermoFisher, 2019).



The electrons are generated at the top of the column by the source, and these are then emitted and attracted to a positively-charged anode (**Figure 3.3**). The main column and all internal components must be under vacuum, so as to prevent any interference when testing to avoid any contamination of the sample (ThermoFisher, 2019). Additionally, the column being under vacuum means the electrons are not able to collide with the gas atoms in air, resulting in a higher resolution image (ThermoFisher, 2019). Another key element of the apparatus is the electromagnetic coils, these are used to control the path of electrons and two types of lenses are used to achieve this. The condenser lens converges the electron beam, defining the size of the electron beam, and directly affecting the resolution of the image produced. The beam is then passed along a second lens, the objective lens, which focuses the beam onto the sample (**Figure 3.3**) (ThermoFisher, 2019).

Once the beam strikes the sample, it generates several types of electrons, and the SEM commonly uses two types of electrons to form an image (ThermoFisher, 2019), backscattered (BSE) or secondary electrons (SE). BSE are formed from the primary electron beam and are reflected back after elastic interactions between the beam and the sample (**Figure 3.3**), while SE originate from the atoms of the sample and are a direct result of inelastic interactions between the electron beam and the sample (ThermoFisher, 2019) (**Figure 3.3**). The aforementioned events also affect the image produced, BSE images show a higher sensitivity to differences in atomic number, which increases with a brighter image, whereas, SE provides more detail about the sample surface (ThermoFisher, 2019). The electrons are detected by a solid-state detector, placed above the sample to maximise BSE collection (**Figure 3.3**). Commonly, an Everhart-Thornley detector is used for SEs (ThermoFisher, 2019). A low voltage is applied to the faraday cage with a scintillator inside, attracting the low energy SEs to it. This is an important differentiator as the other higher energy electrons are not attracted to the scintillator. The scintillator builds to a high positive voltage, attracting the incoming electrons to it and once the electrons collide with the scintillator, they convert to light photons. The light photons are guided by total internal reflection, and the photons travel outside the vacuum chamber to a photomultiplier for amplification, forming a 3D image of the sample (ThermoFisher, 2019). The SEM used in this work is the Hitachi TM-4000-plus.

### Morphologi G3

The Morphologi G3 is a particle shape analysis and size measurement instrument which uses static image analysis to analyse samples (Malvern Panalytical, 2021, Müller *et al.*, 2015). The sample is placed in the dry powder dispersion system, and then automatically dispersed and analysed for its statistical data. Images of the sample complement the statistical data, and recalibration of the image analysis system between runs ensures accurate images (American Pharmaceutical Review). The storage of a custom made Standard Operating Procedure (SOP) also speeds up subsequent analyses as the operational parameters do not need to be inputted every time (American Pharmaceutical Review).

### **3.3.3. NPs Characterisation**

#### DLS

DLS is a technique used to determine the size distribution of small particles in solution. The Brownian motion is the random movement of particles due to bombardment by the surrounding solvent molecules, and the larger the particle, the slower the Brownian motion, meaning smaller molecules move further and quicker (Trueman *et al.*, 2012). The Stokes-Einstein equation (eq 3.9) is used to calculate the particle size in DLS:

$$d(x) = k_b T / 3\pi n x \quad (3.9)$$

Where  $d(x)$  is the translational diffusion coefficient,  $k_b$  is the Boltzmann constant,  $T$  is the temperature,  $n$  is the viscosity and  $x$  is the size of the assumed spherical particles (Sympatec). The translational diffusion coefficient establishes the correlation between the variables, and the particle diameter measured in DLS refers also to the particle movement in solution, which is why it is called the hydrodynamic diameter (Zheng *et al.*, 2016). The translational diffusion coefficient depends not only on the size of the particle

‘core’, but also on several other factors such as: ionic strength of the medium; particle surface structure and non-spherical particles (Malvern Panalytical, 2010).

DLS measures the speed at which particles diffuse due to their Brownian motion by measuring the rate at which the scattered light fluctuates. A monochromatic light source, usually a laser beam, is shot through a polariser and through the sample (Stetefeld *et al.*, 2016). All the molecules in the sample are hit by the light, and they all diffract the light in different directions. The diffracted light can interfere constructively or destructively, and the process is repeated at short time intervals, and the resulting ‘speckle patterns’ are analysed by an autocorrelator which compares the light intensity at each spot over time (Stetefeld *et al.*, 2016). The Malvern Nano ZS was used for the DLS analysis.

### Zeta Potential

Zeta Potential (ZP) is the potential difference between particles and the surrounding liquid medium. It is one of the fundamental parameters that affect stability, and measurement of the ZP gives a detailed insight into the dispersion, aggregation and flocculation of molecules (Joseph and Singhvi, 2019). Measuring and understanding the surface potential of NPs in solution is an important tool for understanding these interactions, and predicting/improving the long-term stability of a colloidal dispersion. The data can be used to improve a variety of formulations including pharmaceuticals, dispersions, emulsions and to improve water treatment processes (Nobbmann *et al.*, 2010, Barhoum *et al.*, 2018). The PE of the interactions involved in ZP can be defined by the following equation:

$$V_{repulsion} = \frac{Aa^2\zeta^2}{R} e^{-s/r_D}$$

(3.10)

Where A is a constant, a is the particle radius,  $\zeta$  is the ZP, R is the distance between particle centres,  $r_D$  is the thickness of the electric double layer and s is the distance between the surfaces of two particles (Atkins and de Paula, 2006). In colloidal

dispersions with a low ZP value, other attractive forces can overcome the charge repulsion, leading the molecules to aggregate (eq 3.10). When a particle is dissolved or dispersed in a solution, the functional groups on its surface react with the surrounding medium, creating a surface charge which attracts oppositely charged ions (Pal *et al.*, 2020, Ouyang *et al.*, 2021). In colloidal systems, dispersed particles have two layers of oppositely charged ions on the surface called the stern (ions strongly bound) and diffuse (ions loosely bound) layers (Bücker *et al.*, 2019). The ZP is the voltage at the edge of the diffuse layer, where the particles meet the surrounding liquid, and if the charge of the NPs falls below a certain level, the colloid will start to flocculate, conjugate and eventually sediment, which further emphasises the importance of maintaining the ideal ZP to yield the optimum experimental results (Bücker *et al.*, 2019). The ZP was measured using the Malvern Nano ZS, with folded capillary zeta cells used for the sample. The folded capillary zeta cells are a disposable poly-carbonate cell with gold-plated copper electrodes (Malvern Panalytical, 2013). The gold-plated copper electrodes conduct the outside field into the sample, allowing measurement of the ZP. The copper electrodes are gold plated for inertness, however, the thin gold film may blacken overtime as it interacts with aqueous compounds during sample measurements (Malvern Panalytical, 2013).

### **3.3.4. Design of Experiments**

Design of Experiments (DoE), is a process optimisation method which involves designing a task, all while accounting for the variation caused by simultaneous factors (Weissman and Anderson, 2015). DoE falls into the applied statistics field, and helps with planning, conducting, analysing and interpreting tests, while allowing evaluation of the factors affecting the output to control the process (Jankovic *et al.*, 2021). All possible combinations of factors affecting an experiment (full factorial) or only a portion of the possible combinations (fractional factorial) can be investigated, and multiple input factors may be manipulated simultaneously, allowing DoE to account for every single interaction and covering all combinations that might otherwise be missed when experimenting by changing one factor at a time (Jankovic *et al.*, 2021). The key concepts in creating a designed experiment include blocking, randomisation, and replication (Clifton Young,

1996). Randomisation refers to the order in which the trials of an experiment are performed, and a randomised sequence helps eliminate effects of unknown or uncontrolled variables (Clifton Young, 1996). When randomising a factor is too costly, blocking enables partial randomisation of the process by carrying out all of the trials with one setting of the factor, and then all the trials with the other setting. Replication is repetition of a complete experimental setup to ensure reliability in results (Clifton Young, 1996). Therefore, a repetitive approach, consisting of three steps to gaining the necessary information is utilised. Firstly, a screening design narrows the field of variables under assessment. Secondly, a ‘full factorial’ design studies responses of every factor levels and zones in on where the process is likely optimised. Finally, a response surface is designed to model the response, and we can evaluate the process and make changes as required (ASQ).

The biggest advantage of DoE is being able to strategically plan and execute experiments, as many experimental setups use a ‘one factor at a time’ approach. This approach is highly inefficient for mainly two reasons. Firstly, it leads to a large number of runs, some of which may not be needed, and secondly, interactions between the factors are not considered, which may have a bearing on whether the experiment is successful (Czitrom, 1999). A well performed DoE provides answers that would be impossible to obtain with a ‘one factor at a time approach’ by allowing establishment of the key factors in a process. DoE also gives the perfect settings which deliver acceptable performance and bring about less variation in the results (ASQ).

A fractional factorial design, using Minitab v19.0, was used in this work.

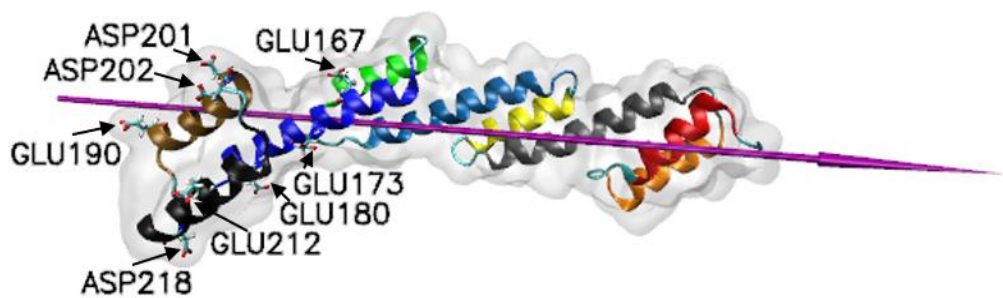
## Chapter Four: Model SpA Systems

*“If we knew what we were doing, it would not be called research, would it?”*

*Albert Einstein*

## 4.1. SpA

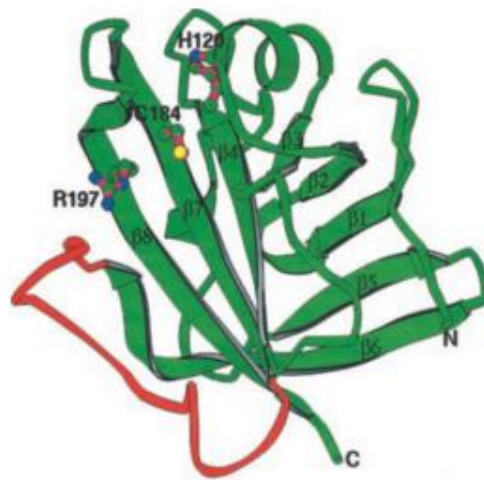
Studying protein adsorption on biomaterials is important in modern medicine and biotechnology (Hlady and Buijs, 1996), since it can indicate whether a biomaterial is suitable for a therapeutic application (Serpooshan *et al.*, 2015). Ascertaining the suitability of materials, and how they interact with proteins, is the first step towards the development of new diagnostics. SpA (**Figure 4.1**) is a 42 kDa bacterial protein produced by *Staphylococcus aureus* (*S. aureus*). The high affinity of SpA for the Fc fragment of antibodies makes it an interesting candidate for biotechnologies.



**Figure 4.1:** The SpA structure (5H7A.pdb) illustrated using VMD 1.9.1 (Humphrey *et al.*, 1996). The protein is indicated as a ghost surface, and the secondary structural  $\alpha$ -helices are coloured as follows. Helix 1: red ribbons (close to the N terminus), helix 2: orange, helix 3: grey, helix 4: yellow, helix 5: light blue, helix 6: green, helix 7: dark blue, helix 8: brown, helix 9: black (close to the C terminus). The purple needle indicates the dipole moment. The key Glu and Asp residues that interact with the Fc fragment of antibodies are indicated in the ‘liquorice’ representation.

SpA is a crucial part of *S. aureus* as it helps the bacteria suppress the host B-cell immune response, preventing damage to the bacteria (Kobayashi and DeLeo, 2013). B-cells are a type of white blood cell which function in the humoral immunity component of the immune response. They mount a response against bacteria and viruses by secreting antibodies, which are highly specific to pathogens and lock onto their surface to allow destruction by other immune cells (Hoffman *et al.*, 2016). SpA functions as an antibody binding protein, primarily binding to IgG type antibodies,

through the Fc region because it recognises both the second and third constant domains (Graille *et al.*, 2000). The binding interactions of SpA with IgG1, IgE and IgG3 have been studied by conducting MD simulations, and the binding free energy decomposition calculated using the Molecular Mechanics Poisson-Boltzmann Surface Area (MM/PBSA) method (Huang *et al.*, 2011). SpA was shown to interact with IgG1 through ‘hotspots’ via hydrophobic interactions involving the F132, Y133, H137, E143, R146 and K154 residues for SpA, and I253, H310, Q311, D315, K317, E430, N434 residues for IgG1 (Huang *et al.*, 2011).



**Figure 4.2:** The structure of Staphylococcal sortase A, the enzyme which binds SpA to the cell wall (Zong *et al.*, 2004).

SpA is bound to the cell wall of *S. aureus* by sortase A (**Figure 4.2**) which is an enzyme catalysing the cell wall sorting reaction involving linkage of a Thr residue to a Gly residue in the peptidoglycan cross bridge (Ilangoan *et al.*, 2001). The release of SpA from the bacterial cell wall has been studied extensively, and this is an important consideration because of the importance of SpA in commercial use. LytM is a secreted glycyl-glycine endopeptidase of *S. aureus* which cuts the cross-bridges of staphylococcal peptidoglycan and releases SpA into the cellular medium. It was found that LytM released significantly more SpA into the cellular medium than the mutant version of LytM (Becker *et al.*, 2014). Furthermore, the release of SpA from the



bacterial cell wall may be influenced by bacterial growth (Wang *et al.*, 2022, Becker *et al.*, 2014).

SpA has previously been studied for use as a vaccine candidate, and the effectiveness of this approach relies on its ability to block the immune response (Kobayashi and DeLeo, 2013). However, such promise has only been observed in mice, and the approach to using SpA in vaccines is still under development. SpA suppression of B-cells is also fundamental in the progression of some auto-immune diseases. Rheumatoid Arthritis (RA) is an auto-immune condition where the immune system produces IgG which attacks the synovial tissues in multiple joints (Navegantes *et al.*, 2017), leading to swollen and painful joints with stiffness over a prolonged period of time (Bullock *et al.*, 2018). An immunoabsorption treatment device containing SpA (Furst *et al.*, 2000) and ultrapure SpA (PRTX-100) (Gemma *et al.*, 2017) has previously been investigated as a treatment for RA. Furthermore, SpA is also a target for drug delivery, and targeting SpA with monoclonal antibodies significantly decreased *S. aureus* colonisation in the mouse nasopharynx and intestinal tract (Chen *et al.*, 2019).

NPs have been studied computationally for their integration in diagnostics and therapeutics (Ramezanpour *et al.*, 2016), and SpA has been previously studied as a treatment for autoimmune diseases (Navegantes *et al.*, 2017, Gemma *et al.*, 2017). SpA binding to antibodies through the Fc region allows extraction of antibodies, while keeping the Fab site free to allow antigen binding (Kobayashi and DeLeo, 2013), enabling the study of SpA for the development of new diagnostics and therapeutics. However, for this concept to succeed, it is crucial to understand how SpA interacts with different inorganic materials, since this will determine whether SpA maintains its functionality when adsorbed.

The aim of this chapter is to use MD simulations to investigate the interactions of SpA with model inorganic materials, and establish if the interaction of the protein with the materials is optimal for integration in diagnostics. This work is a preliminary study that could be further used to develop a COVID-19 diagnostic by aiming to conjugate anti-SARS-CoV-2 antibodies to NPs. However, this antibody conjugation route was

not pursued following the withdrawal of ‘The Antibody Company’ as the industrial sponsor for this project. A new industrial partner, Alchemy Pharmatech was found, and the direction of the project changed to developing a dry-powder IN vaccine formulation for COVID-19, that could be used with their ‘Naltos’ nasal delivery device. The work in this chapter is based on a published paper ‘Functionalisation of Inorganic Material Surfaces with Staphylococcus Protein A: A Molecular Dynamics Study’ (Farouq *et al.*, 2022). The Protein Data Bank (PDB) file (5H7A.pdb) consists of nine  $\alpha$ -helices, with helices 7-9 containing the Fc binding region. Although this PDB structure has some residues missing at the N-terminal end, this is not expected to affect protein function or behaviour in simulation, as the residues making up the body of the protein and the Fc binding region are present.

## **4.2. Materials and Methods**

### **4.2.1. Surface Models**

**SiO<sub>2</sub>:** The model SiO<sub>2</sub> slab employed in the simulations is neutral, but it has an intrinsic dipole moment across it that does not change during the simulation; the slab is created from an  $\alpha$ -cristobalite structure and the material was modelled as ions fixed in space (Patwardhan *et al.*, 2012). Due to the 3D periodicity of the simulation cell, an electric field is induced through the simulation box (Kubiak-Ossowska *et al.*, 2013), so that the electrostatic environment above the slab mimics that expected above a negatively charged silica surface. The slab dimension was 103 Å x 199 Å x 13 Å, with 17280 atoms, yielding two surfaces; an SiO<sub>2</sub> surface with siloxide groups at the top of the slab and undercoordinated Si species at the bottom. The Charmm-27 force-field parameters for the surface were used according to Patwardhan (Emami *et al.*, 2014). The SiO<sub>2</sub> surface with siloxide groups at the top mimics the negatively charged surface encountered experimentally at pH7 (Patwardhan *et al.*, 2012), and the surface with under-coordinated Si species exposed mimics a positively charged surface. The positive surface is not encountered in practice, except perhaps at very low pH, and is therefore not a realistic model but nevertheless provides an interesting model structure to explore SpA adsorption at a hypothetical positively charged material surface. These variants of the model silica surface represent SiNPs.

**Au (111):** Adsorption to the model Au (111) surface was explored by creating a slab of face-centered cubic crystal (fcc) Au oriented with the (111) direction aligned the z-axis of the simulation cell. The model Au had no partial charges (and so no electric field has been introduced). The atoms of the Au (111) model surface were also fixed in space to represent a slab of 98 Å x 196 Å x 15 Å, with 13824 Au atoms, and the Charmm-27 force-field parameters for Au were used following Heinz *et al.* (Feng *et al.*, 2011, Heinz *et al.*, 2009, Heinz *et al.*, 2008). This model surface represents AuNPs.

#### 4.2.2. MD Simulations

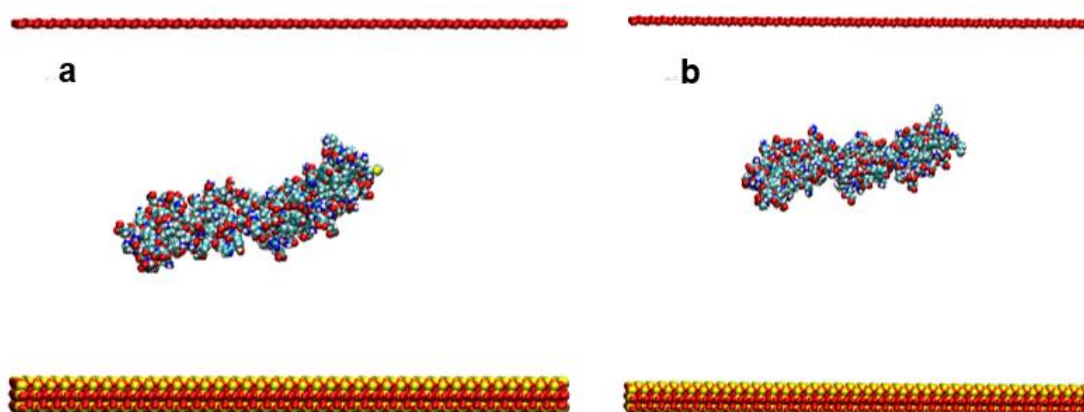
The protein obtained from the PDB structure was not modified in any way, despite missing 33 residues at the N-terminal end. This is because the protein binds to the Fc region of antibodies through residues on the C-terminal, and those residues are all present. The simulations were computed at pH 7 as at the time, there was no indication of where this diagnostic would be used, and whether pH needed to be adjusted accordingly. The NAMD 2.12 package (Phillips *et al.*, 2005) was utilised along with the Charmm-27 force-field, and the simulation results were analysed with VMD 1.9.1 (Humphrey *et al.*, 1996). The simulation was performed in three stages (Kubiak-Ossowska *et al.*, 2016). The first stage consisted of adding water and ions to the simulation cell that contained the static protein as obtained from the PDB structure, followed by water and ion minimisation of 1000 steps and a subsequent 100 ps run in the NVT ensemble with an integration time-step 1 fs, at a target temperature of 300K and a pressure of 1 atm. The second stage of the system preparation used the complete system (protein, water and ions), with energy minimisation for 10,000 steps followed by NVT equilibration for 300 ps. Finally, the production trajectory was performed, which consisted of an initial 10 ns run, extended to 100 ns with a 2fs time-step at 300 K in the NVT ensemble. PBC were used along with the SHAKE algorithm: the PBC create copies of the simulation cell in all directions, creating a continuous surface for the protein to adsorb onto. The L-J cut-off distance for the VdW interactions was set at 12 Å, and the PME summation was used to describe the electrostatic Coulomb interactions (Essmann *et al.*, 1995). Only the production trajectories have been analysed in detail.

### Protein in Water

The crystal structure of Protein A obtained from the PDB entry 5H7A.pdb contained four repeat modules, from which one (C) was used in the simulations. A single SpA unit contains 221 amino acids (3,001 atoms), and the net protein charge at pH 7 is -11e. SpA was initially simulated with just water and ions, and then with the model crystal slabs included. The dipole moment changes due to protein flexibility in simulation, and is an important indicator in studying charge distribution and interaction of a protein with model surfaces. The protein was initially solvated in a rectangular box that extended at least 12 Å from the structure, and the TIP3P (Jorgensen *et al.*, 1983) (Neria *et al.*, 1996) model was used describe the water molecules. The system was neutralised by adding NaCl salt at ionic strength  $2 \times 10^{-2}$  M (16 Na<sup>+</sup> and 5 Cl<sup>-</sup>), making the system better representative of experimental conditions. The system comprised 46357 atoms (SpA: 3001 atoms; Water: 43338; Ions: 21), and the initial simulation in water showed the protein is stable, so it was further simulated with the surface models.

### Protein, Water and SiO<sub>2</sub> surfaces

The protein was placed ~80 Å above the siloxide-rich surface (the protein surface distance varied between 80-83 Å), and solvated in a rectangular water box (TIP3P model) extending at least 40 Å in the z axis (~96415 water molecules), giving a system with ~310,000 atoms.



**Figure 4.3:** a) simulation setup where the protein is placed closer to the surface than the image, the resulting system is wider and shorter, which could restrict protein movements, b) simulation setup where the protein is placed closer to the image than the surface, this results in a narrower system, forcing the protein to freely diffuse upwards.

The protein was therefore closer to the image of the SiO<sub>2</sub> slab (**Figure 4.3**), meaning further away from the surface, and this larger system was employed to allow the protein time to diffuse and re-orientate before adsorbing to the surface. The electric field that runs in the -z-direction between the top of the SiO<sub>2</sub> slab to bottom of its image (across the water-protein space) is screened by NaCl: 288 Na<sup>+</sup> ions to screen the siloxide-rich surface, and 277 Cl<sup>-</sup> ions to screen the positive Si-rich surface. Sufficient ions were added through trial and error to shield both of the surfaces, and the additional 11 Na<sup>+</sup> ions neutralise the system, as the protein has a charge of -11 at pH 7. There was a distance of 5 Å from the solute, and between ions.

A further system was set up with the SiO<sub>2</sub> undercoordinated silicon termination surface, the protein was positioned ~40 Å above the surface (the protein surface distance varied between 40-43 Å) and solvated in a rectangular box (TIP3P model), extending at least 60 Å (~87332 water molecules) in the z axis, giving a system with ~260,000 atoms. The net protein charge was -11 e, so the system was charge neutralised by the addition of NaCl salt (288 Na<sup>+</sup>, 277 Cl<sup>-</sup>). The protein was placed closer to the surface than the image in this simulation (**Figure 4.3**), following a standard simulation setup. It was only when adsorption was difficult to obtain on the

siloxide surface in a standard setup, was the protein moved further from the surface and closer to the image. Throughout the simulation, the silica atoms were kept immobile to make the model surface as representative of NPs as possible.

#### Protein, Water and Au (111) surface

The protein was positioned  $\sim 20$  Å above the Au (111) surface (the protein surface distance varied between 18-21 Å), and solvated in a rectangular box (TIP3P model) extending at least 30 Å in the z axis ( $\sim 48500$  water molecules), resulting in a system with  $\sim 160,000$  atoms. The net protein charge was -11 e, so the system was charge neutralised by the addition of NaCl salt at ionic strength  $2 \times 10^{-2}$  M (mol/L), which is at a suitable ionic strength for studying these interactions with surfaces. The addition of ions also makes the system better representative of practical conditions. Throughout the simulation, the gold surface atoms, as with the silica surface atoms, were kept immobile so they could not move, and the protein was placed in four different orientations above the surface. The positioning of the protein was related to default in two systems, and the N terminus was flipped to the opposite side in the remaining two. Therefore, there were four 100ns trajectories named SpA\_on\_gold1 to SpA\_on\_gold4. SpA\_on\_gold4 gave the adsorption trajectory analysed further, because it gave the most consistent adsorption to the surface.

The protein was placed at a different distance away from the surface in every system, along with a different water box and ionic concentration. This was done to optimise adsorption conditions for the protein on each model surface. Generally, on the silica surfaces, the protein was placed further from the surface and more water was also added to the systems, when compared with the Au (111) model surface, to improve chances of adsorption by free diffusion of the protein.

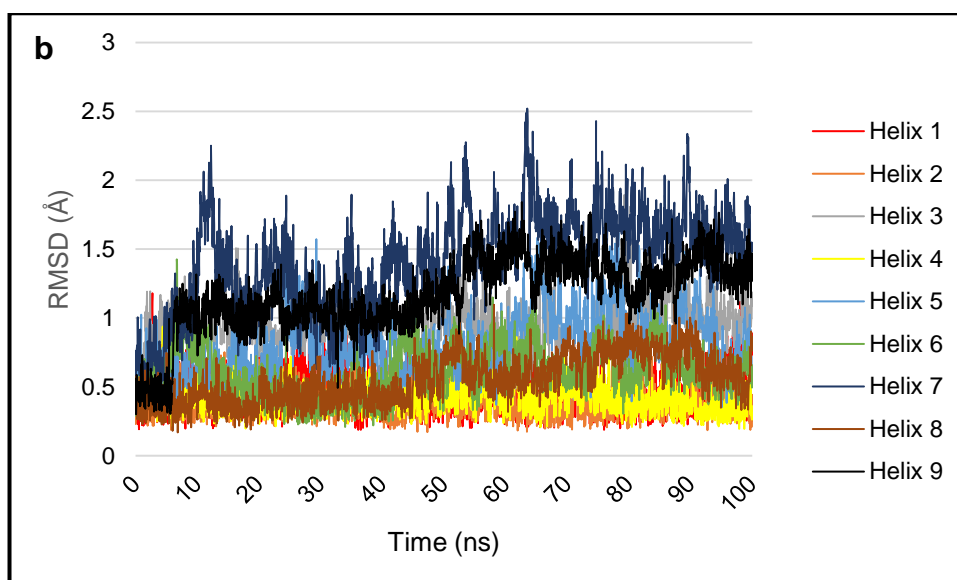
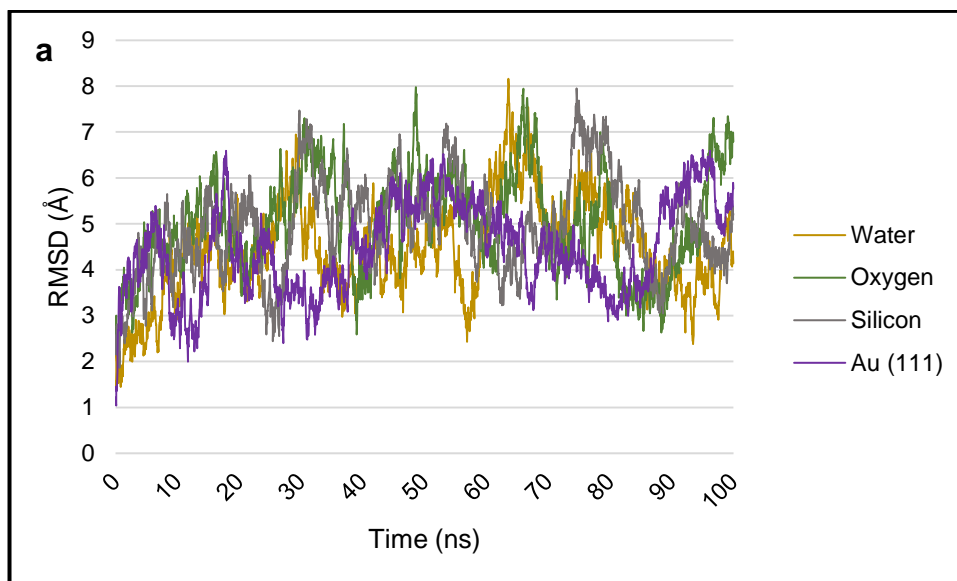
## 4.3. Results and Discussion

### 4.3.1. Structural Stability

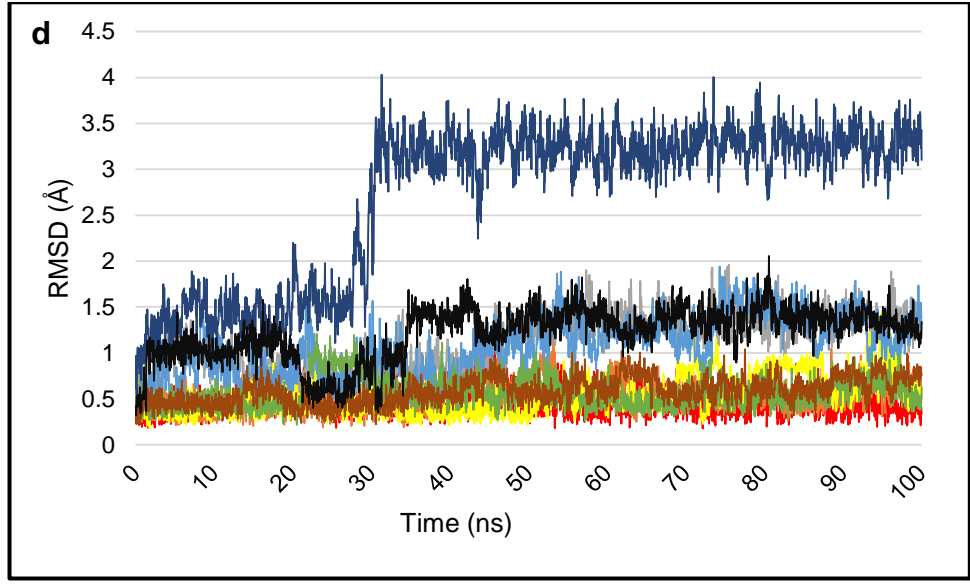
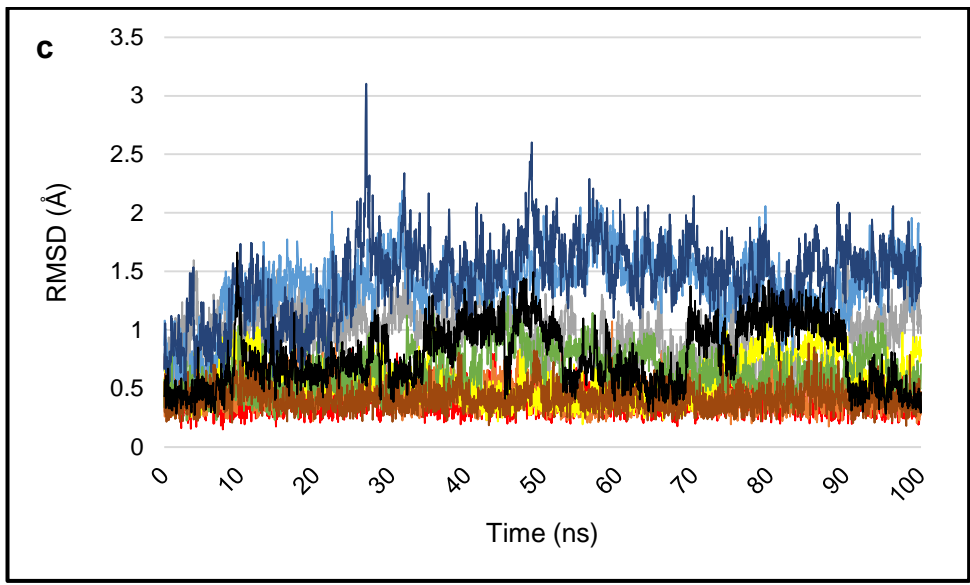
#### Simulation in water

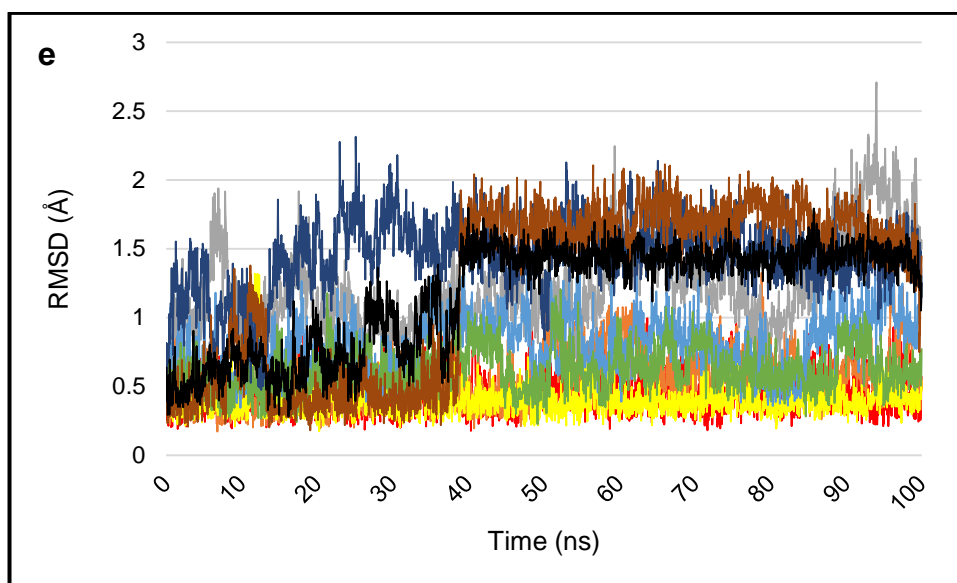
The SpA in water system was simulated for 100 ns and the Root Mean Square Deviation (RMSD) is reported in **Figure 4.4a**. The RMSD is a measure of the average deviation of a molecular structure from the reference structure, and the smaller the RMSD, the similar the structures and more stable the molecule in question is (Kufareva and Abagyan, 2012). The RMSD initially increases to 3 Å, indicating a structural change as the protein is solvated. The RMSD for the whole protein fluctuated between ~3-7 Å throughout the simulation, demonstrating its stability in these simulations (there is no consistent growth in the RMSD and no observable unfolding). This shows that the model protein structure is stable, and is good enough for assessment of its adsorption behaviour and interactions with model surfaces. The key binding sites of the protein, which bind to the Fc fragment of antibodies, maintain their structural integrity throughout the duration of simulation, this is crucial for SpA binding to antibodies, conjugated to NPs.

The fluctuations can mainly be attributed to flexing between the  $\alpha$ -helices in the protein, which tend to be linked together by short flexible loops (see **Figure 4.1**). The relative stability of the  $\alpha$ -helices can be analysed by studying the RMSD for each  $\alpha$ -helix separately, overlapping each in turn with its structure at  $t = 0$  ns. The results are also presented in **Figure 4.4b**, where it can be seen that  $\alpha$ -helix 4 is the most stable in the simulation with an average RMSD of 0.35 Å, while  $\alpha$ -helix 7 is the least stable, reaching a maximum of 2.5 Å at 65 ns and averaging 1.5 Å through the course of simulation. Consistent bending of  $\alpha$ -helix 7 is visible in the simulation.  $\alpha$ -helices 8 and 9, the other two with the glutamic acid and aspartic residues involved in binding to the Fc fragment of antibodies, also show good stability. It will be particularly interesting to examine how SpA interacts with the model surfaces, observe changes in the angles between the  $\alpha$ -helices, and explore whether the structural stability remains similar to that in the bulk water simulation.









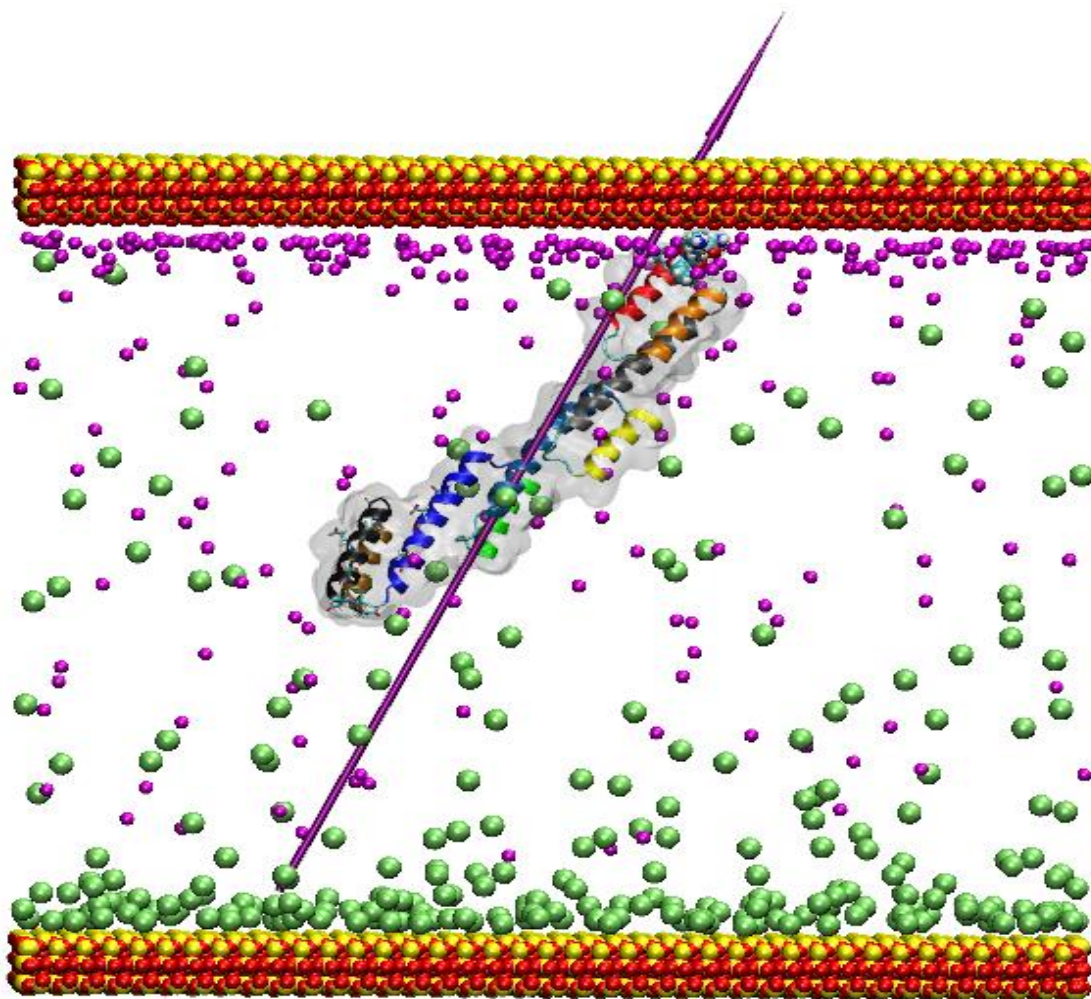
**Figure 4.4:** a) full protein RMSD of SpA, the water simulation is shown in gold, the silica siloxide simulation is shown in dark green, the silica undercoordinated simulation is shown in dark grey, and the Au (111) simulation is shown in purple, b) RMSD for the individual  $\alpha$ -helices of SpA in the water simulation, c) RMSD for the individual  $\alpha$ -helices of SpA in the silica siloxide simulation, d) RMSD for the individual  $\alpha$ -helices of SpA in the silica undercoordinated simulation, e) RMSD for the individual  $\alpha$ -helices of SpA in the Au (111) simulation. The  $\alpha$ -helices colour scheme is same as Figure 4.1.

#### SiO<sub>2</sub> Siloxide Surface Simulation

SpA has an overall negative charge of  $-11e$  in the simulations, so based on simple electrostatics there is a net force driving the protein away from the surface. Since the system is designed to have an electric field above the siloxide-rich surface, the electric field would force it towards the positive surface. However, the surface electric field is screened by the ions in solution, and the protein experiences a fluctuating electric field when it is closer than the Debye screening length from the surface (Kubiak-Ossowska *et al.*, 2016). Furthermore, the charge distribution across the protein surface is not uniform, meaning a negatively charged protein can approach close to a negatively charged surface, and if it is oriented in a preferred way with positively charged regions

exposed to the surface, adsorption is possible (Kubiak and Mulheran, 2009, Kubiak-Ossowska *et al.*, 2016, Stroud *et al.*, 2019).

Adsorption, where the residues have a close approach, strong interactions with the surface and strong interaction with the ions shielding the surface, is observed on the siloxide rich surface with the residues Lys34 and Lys37 (positively charged, strongly hydrophilic), along with Asn36 (neutral, strongly hydrophilic) and Met33 and Phe 35 (neutral, hydrophobic). The residues anchor the protein to the surface, leaving the Fc binding regions, found between  $\alpha$ -helices 7-9, freely moving and exposed to solution (see **Figure 4.5**).

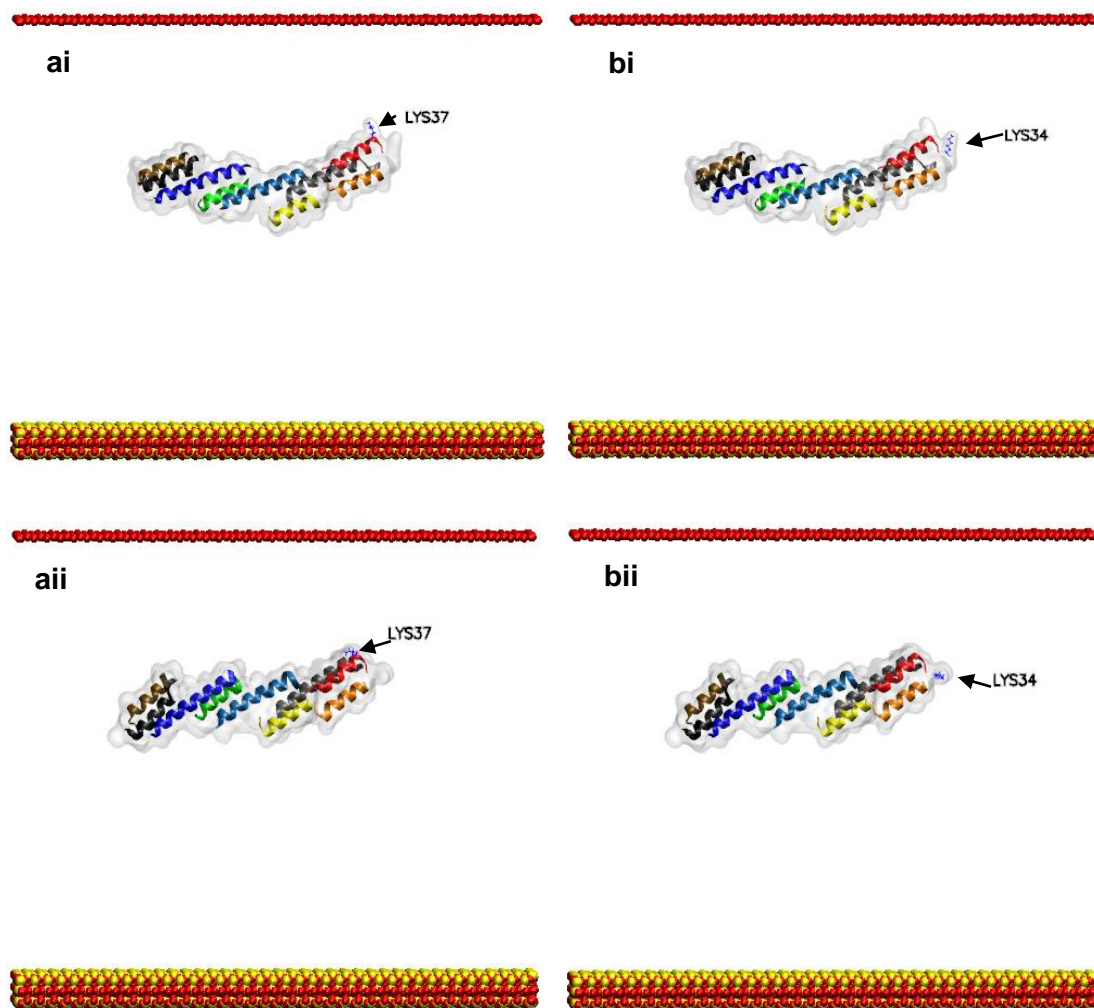


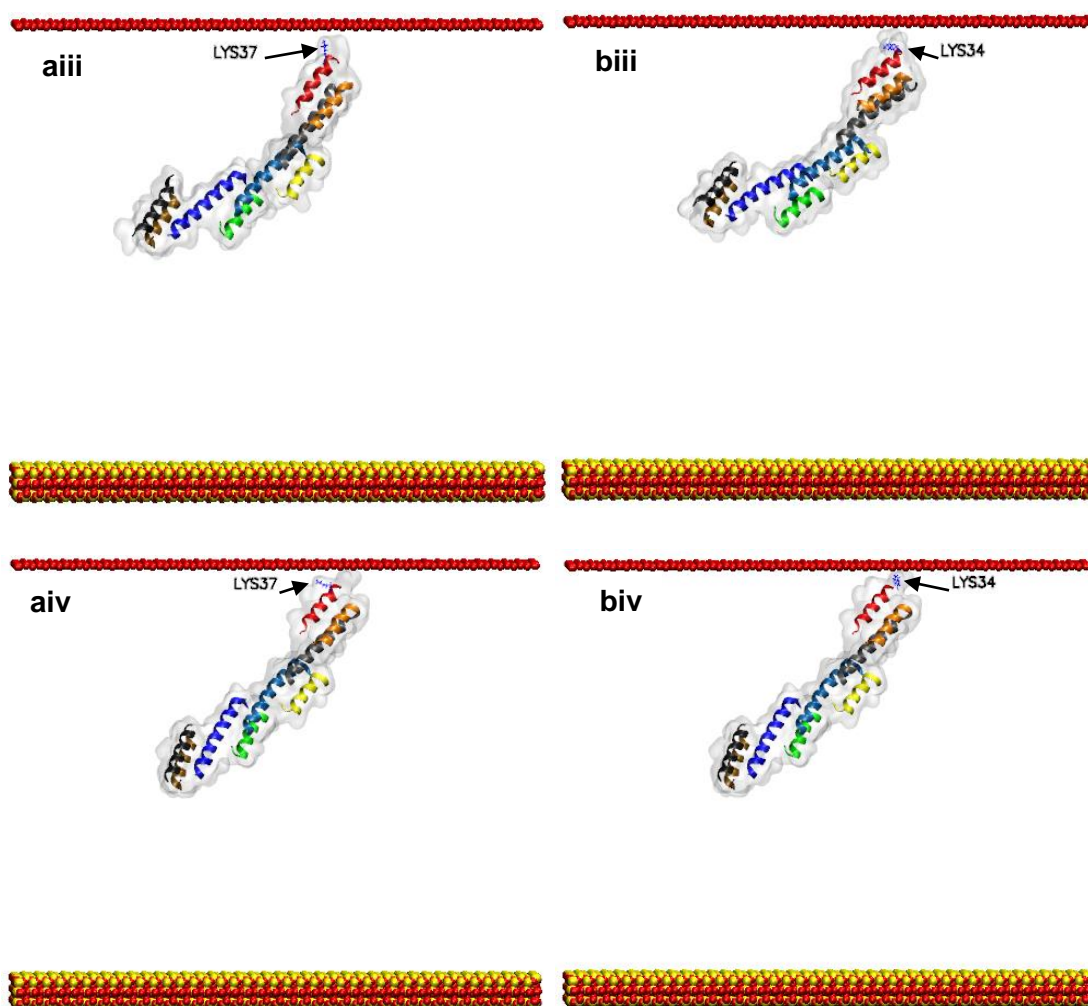
**Figure 4.5:** Adsorption of SpA on the oxygen rich surface. The protein colour scheme follows that in Figure 4.1. The outer layer of oxygen atoms in the silica model surface is shown as red spheres,  $\text{Cl}^-$  ions are shown as lime VdW spheres, and  $\text{Na}^+$  as magenta. The adsorbing residues are also shown as VdW representation. The purple needle indicates the dipole moment, and water molecules are not shown for clarity.

The  $\text{Na}^+$  ions are attracted to the  $\text{O}^-$  siloxide surface, forming a diffuse layer that screens the electric field. There is a persistent electric field that can steer the adsorption of SpA and five key residues anchor the protein to the surface, three of which are neutral and two are positive. The residues leading the protein adsorption penetrate the water layers, opening a path through the ion layer for adsorption to occur. This

phenomenon is particularly visible with the positive Lys residues, which reach out for the surface; this is particularly noticeable with Lys34.

On positive surfaces, the electric field causes rotational and translational motion of the protein, leading to adsorption. However, in adsorption on the negative surface, the protein approaches the surface several times without adsorbing, diffusing close to the surface due to the effective screening of the surface by the  $\text{Na}^+$  ions. This is because adsorption on the negative surface for an overall negative protein is a rare event. Furthermore, due to a complicated electric field, the protein is not steered towards a particular adsorption site, as it fluctuates between attraction with the ions and repulsion from the surface. The protein movements are also influenced by the water box. During this time, there is no preferential orientation of the protein to encourage anchoring.





**Figure 4.6:** Representative sequential snapshots showing ai) the Lys37 sidechain at 25ns, aii) the Lys37 sidechain at 50ns, aiii) the Lys37 sidechain at 77.32ns, when it first starts to form contacts with the surface, aiv) the Lys37 sidechain at 100ns, when the residue is firmly bound to the surface, bi) the Lys34 sidechain at 25ns, bii) the Lys34 sidechain at 50ns, biii) the Lys34 sidechain at 80.24ns, when it first starts to form contacts with the surface, biv) the Lys34 sidechain at 100ns, when the residue is firmly bound to the surface.

However, at 77.32 ns in the production trajectory, the Met33 and Lys37 side-chains extend and almost make direct contact (come within the relevant VdW radii, defined as the closest distance of two equal, non-covalently bound atoms) with the surface. Lys34 is the next residue to adsorb to the surface at 80.24 ns, and the positive charge on the Lys side-chains explains the attraction to the negative surface. The Lys34 and Lys37 residues extend their side-chains to penetrate the water layer at the silica surface, displacing the water molecules and creating strong anchors to the surface, and it appears that after a weak initial binding, the residues bound firmly on the surface as the simulation progresses (**Figure 4.6**). The formation of an ordered water layer at ionic surfaces has also been demonstrated previously (Kubiak-Ossowska *et al.*, 2016, Kubiak and Mulheran, 2009, Mulheran *et al.*, 2016). The adsorption in this simulation is electrostatically driven, so that the dipole moment of the SpA is oriented towards the O-rich surface.

The RMSDs reported in **Figures 4.4a and 4.4c** show the stability of the protein and the individual  $\alpha$ -helices. The protein appears to have similar stability to that in bulk solution (**Figure 4.4a**). Again,  $\alpha$ -helix 7 is the least stable, with a peak RMSD of 3 Å at 28 ns (see **Figure 4.4c**). However, it is clear that lower-index  $\alpha$ -helices (so at the N-terminus side) respond to the adsorption processes at around 80 ns, but these are nearest to the silica surface. At the opposite end of the protein,  $\alpha$ -helix 8 is the most stable, with a starting RMSD of 0.2 Å, reaching a maximum of 0.9 Å at 88 ns.  $\alpha$ -helix 9 also shows good stability, although its RMSD fluctuates the most. This is important because it means the end of the protein containing the binding sites is unaffected by the surface adsorption, behaving in a similar way to the protein in bulk solution.

Most importantly, the simulation demonstrates adsorption to the siloxide-rich silica surface, as found experimentally by the adsorption of peptides to negative SiNPs (Patwardhan *et al.*, 2012), and leaves the SpA's Fc binding region free and exposed to the solution. In this sense, the protein orientates itself in an ideal manner due to the role that the electrostatics plays above the charged surface. There are several unsuccessful 100ns trajectories, and only one successful adsorption trajectory in a 100 ns period. This further highlights such an adsorption event is rare in a 100 ns timescale because the interacting bodies possess identical charge, and adsorption requires

favourable local fluctuations of the electric field, as well as a bigger system than the other simulations.

The adsorbed state appears to be stable, and a 100ns trajectory extension to this simulation shows the protein remains anchored to the surface in its initial orientation, as dictated by the electrostatics, slightly diffusing on the surface, indicating low likelihood of desorption. There was also no significant change to the position of SpA, and this observation is encouraging as it suggests there is scope for further adsorption simulations of the protein at different points on the surface, and to assess whether the protein being placed in a different position will have an effect on adsorption/desorption.

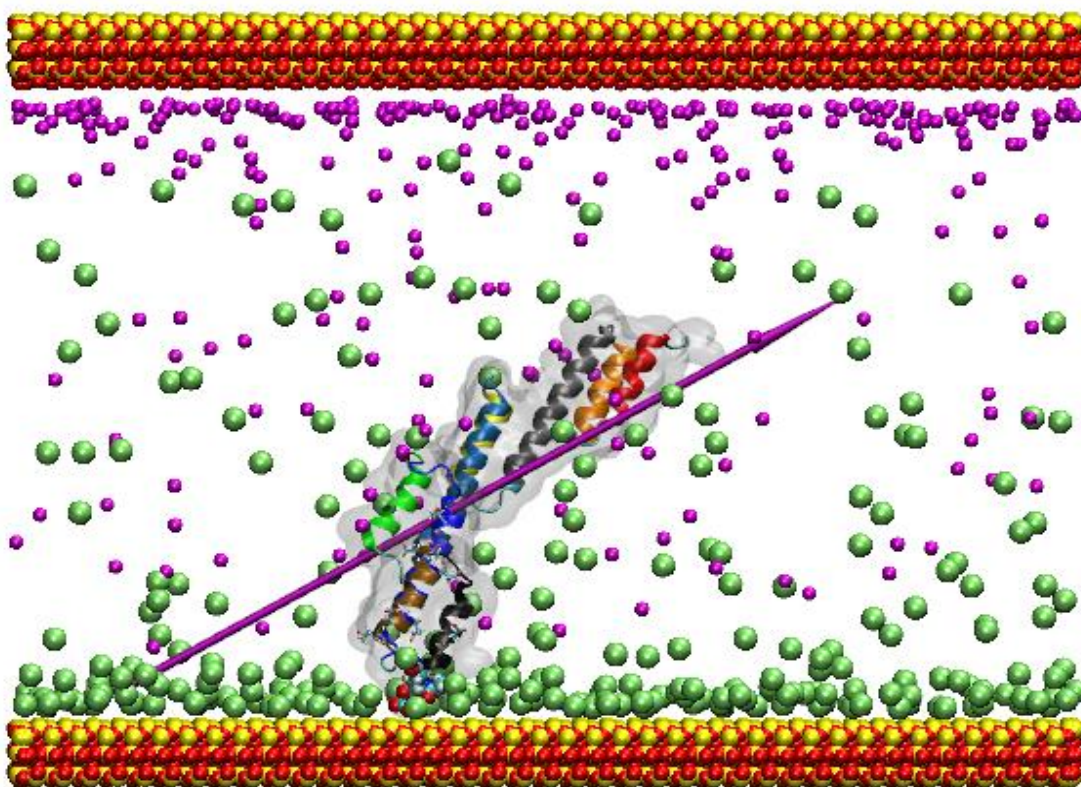
#### SiO<sub>2</sub> Under-coordinated Surface Simulation

The model silica slab used in the adsorption simulations presents both an oxygen-rich and a silica-rich surface to the solution. The latter creates a model positively charge surface on which SpA adsorption can be explored, and the electric field above the surface, while fluctuating due to the movement of the screening Cl<sup>-</sup> ions, readily pulls the negatively charged protein towards it. Due to the polarising effect created by charged surfaces in the model SiO<sub>2</sub> slab, the Na<sup>+</sup> and Cl<sup>-</sup> ions were attracted to the oppositely charged surfaces, which partially screens the force field beyond the Debye length. So even though the positive surface has a layer of negative Cl<sup>-</sup> ions, adsorption is easily achieved due to net protein charge (-11e). After several attempts, the trajectory with the most consistent and stable protein adsorption to the surface was analysed further.

The starting orientation of the protein in this simulation is such that the Fc binding sites are not directly facing the surface, and the protein is in a side-on conformation. During the first few nanoseconds of simulation, the SpA long axis changes orientation, so as to align its dipole moment with the electric field imposed by the charged surfaces, before stabilising in its movements and adsorbing to the surface. The positively charged surface attracts the Cl<sup>-</sup> ions and creates a diffuse screening, and adsorption in



this simulation is supported by three neutral residues which interact with the surface for the duration of the simulation. The ‘anchoring’ residues involved in the adsorption are Ala221 (neutral, hydrophobic), Ala219 (neutral, hydrophobic), and Gln220 (neutral, strongly hydrophilic), all localised in  $\alpha$ -helices 7-9, which is the Fc binding region (**Figure 4.7**). The trajectory shows these anchoring residues have increased mobility prior to adsorption, as they diffuse close to the surface, eventually stabilising once anchored to the surface. The residues display weak binding to the surface in the early stages of adsorption, and as the simulation progresses, they strengthen their grip to the surface by further disruption of the water layer formation at the surface. The attraction of the protein to the surface is driven by the overall negative charge on the protein, as opposed to specific residues, and the overall negative charge attracts it to the positive surface below the diffuse Cl<sup>-</sup> layer. The whole adsorption event is slow as the protein this time fluctuates between attraction with the negative Cl<sup>-</sup> ion layer and the positive surface, and the protein movements are also influenced by the water box, meaning the protein freely diffuses for a long time before adsorption. This is despite adsorption on the positive surface not being a rare event, as negative protein adsorption to a positive surface would be expected.



**Figure 4.7:** Adsorption of SpA on the positively charged surface. The colour scheme is same as Figure 4.5. The purple needle indicates the dipole moment, and water molecules are not shown for clarity.

This also explains why only the anchoring residues, and no others remain adsorbed to the surface for the duration of simulation, and although the simulation is for 100ns, this is unlikely to change if the simulation is extended as the adsorption state seems stable. Due to electrostatics driving adsorption on the model SiO<sub>2</sub> slab, it is reasonable to expect an increased presence of negatively charged residues on the side of the protein which is in contact with the positive surface. However, most of the observed residues on the protein binding side are in fact neutral, meaning in addition to a complicated electric field with several charges pulling the protein, other factors such as pH and hydrophobicity could also have a bearing on the protein behaviour (Antosiewicz and Długosz, 2020, Mücksch and Urbassek, 2014). Due to the orientation of protein as it adsorbs, the Fc binding residues are directed towards the








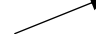



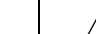




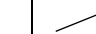
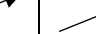
surface and so are not free to interact with the solution. Crucially, it is an important observation because integration of the SpA in new technology will only really be effective if the Fc binding sites are kept free, allowing interaction of SpA with the antibody, leading to facile and efficient conjugation that enables the antibody to further bind to its target with its exposed Fabs.

Consequently, SpA adsorption to positively charged surfaces and NPs is not favourable, while adsorption to negatively charged ones is. As mentioned previously, the model SiO<sub>2</sub> surface creates an electric field, and positively charged residues are attracted towards the negative surface, while negatively charged residues are attracted to the positive surface. Subsequently, the protein may unfold as the residues are pulled by opposing forces. The electric field in the charged simulation system can be easily managed by increasing the number of ions accordingly, as the ions form a layer of opposing charge on the surface, screening the electric field over the Debye length and reducing the forces pulling the protein. As a result, the system setup is a compromise between retaining some electric field as it influences adsorption kinetics, ensuring the protein retains its integrity, while also considering the effect of ionic strength in slowing down MD simulations, which ultimately may slow down the rate of adsorption (Mulheran *et al.*, 2016). However, as the surface charge must be neutralised in order to represent the electrostatic environment above the surface, the bulk ionic strength is not expected to have a noticeable impact on the adsorption process. Therefore, and accounting for the aforementioned factors, the ionic concentration was much higher in the simulation systems with the model SiO<sub>2</sub> surface slab than the Au (111).

Adsorption also occurred on the SiO<sub>2</sub> undercoordinated surface faster than the siloxide-rich surface, and this could be explained by the electric field, which may stimulate the protein movement towards the surface. The atoms in the silica surfaces are densely packed, and this means both the anchoring residues and ions are present at well-defined distances from the surface, which is determined from the VdW volume of the atoms. As with many fully atomistic MD simulations, the present work is focused on the first 100 ns or so of protein adsorption on a surface, which is the first stage of adsorption, but not the final stable state which can be different, as suggested by previous work (Kubiak-Ossowska and Mulheran, 2012). Nevertheless, the

structural stability of SpA in the simulations was similar to previous work (Alonso and Daggett, 2000). Furthermore, in the case of the charged surfaces, the electrostatics will tend to keep the protein oriented in the same way as it adsorbs, suggesting that the conclusions from the simulations provide good indicators of long-term behaviour too, as indicated by the siloxide surface adsorption, which was extended by 100ns.

**Table 4.1:** SpA dipole moment at various stages of adsorption on the three different surfaces. 0 = starting position, D1/D2 = Protein movements in solution, pre-adsorption, abs = at the time of adsorption, 10/20 = 10/20 ns post-adsorption. The arrows indicate the direction of the dipole moment vector. The upwards direction is normal to the surface for the Si-rich surface, so that the surface normal points in the downwards direction for the O-rich surface. Numbers in the following row indicate the value of the dipole in Debye.

|  | 0   | D1  | D2  | abs  | 10  | 20  |
|--|---|---|---|--|---|---|
| <b>Au (111) surface</b>                    |  |  |  |  |  |  |
| <b>Dipole moment (Debyes)</b>              | 883   | 941   | 928   | 850  | 980   | 973   |
| <b>Silica siloxide-rich surface</b>        |  |  |  |  |  |  |
| <b>Dipole moment (Debyes)</b>              | 883   | 971   | 902   | 1066   | 1036  | 993   |
| <b>Silica under-coordinated Si surface</b> |  |  |  |  |  |  |
| <b>Dipole moment (Debyes)</b>              | 882   | 947   | 942   | 1055   | 1027  | 1175  |

The SiO<sub>2</sub> slab used to create the model silica surfaces has an intrinsic dipole moment across it; the atoms were fixed in space, so that the siloxide groups were on the top and

under-coordinated Si species at the bottom. Therefore, when adsorption was driven by a long-range electric field above a positive surface, the adsorption is rapid and specific. In the first stages of the simulation, the dipole moment of the protein quickly aligns (**Table 4.1**) with the electric field and in all simulations the protein flexes in a way to orient its dipole moment perpendicularly to, and away from the under-coordinated surface.

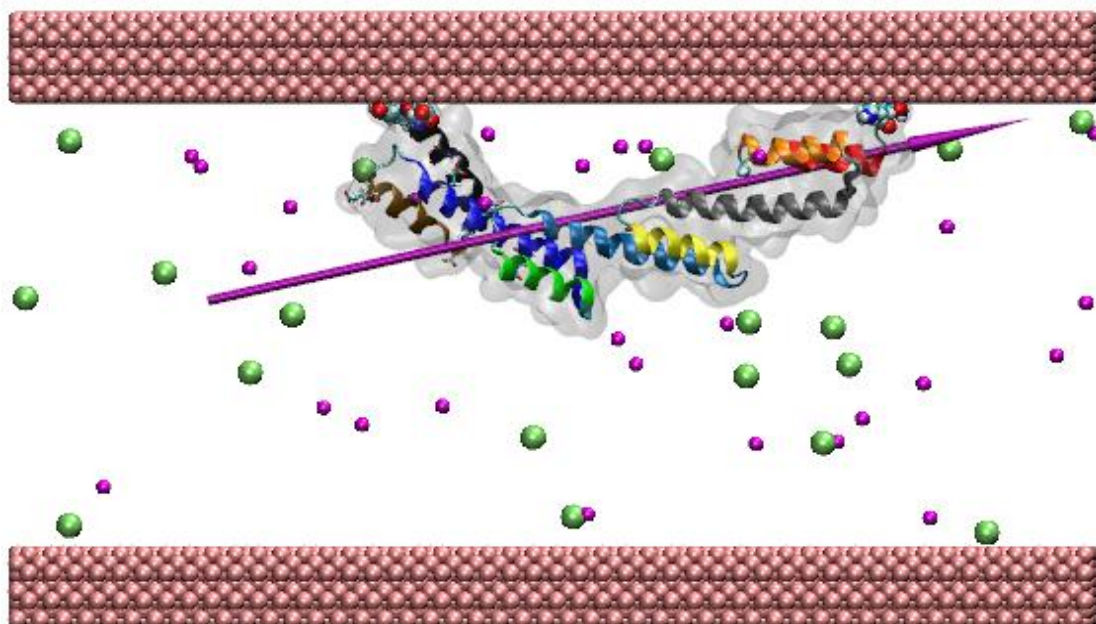
Studying the  $\alpha$ -helix stability in this system,  $\alpha$ -helix 7 is the most unstable, with a peak RMSD of 4 Å at 31 ns, it increases in value at 30 ns. This is down to the fluctuations of the flexible loops in the structure, linking to a subset of atoms in the helix, and causing divergence in the backbone RMSD. In terms of stability,  $\alpha$ -helix 8 is very stable, peaking at 0.9 Å after 45 ns, followed closely by  $\alpha$ -helix 9 which peaks at 1.5 Å (55 ns) (**Figure 4.4d**). As it turns out, even the  $\alpha$ -helices of interest are generally stable in this simulation, although the antibody binding region is blocked.

Previous work involving protein adsorption on the SiO<sub>2</sub> surface has revealed roles for many residues. Adsorption of BSA on the SiO<sub>2</sub> siloxide surface was also reported (Kubiak-Ossowska *et al.*, 2016), and it was found that in the final adsorption state there are several interacting residues at the protein-silica interface, of which Lys plays a significant anchoring role in a similar way to found here (see **Table 4.3**). The importance of charged residues in adsorption to the silica surface has been widely noted, in particular the positively charged Lys and Arg residues (Mathé *et al.*, 2013).

#### Au (111) Surface Simulation

Adsorption on the Au (111) surface is expected to be slow and non-specific, and it is difficult to predict *a priori* which parts of the protein may bind stronger. This is because even though the protein has a positive dipole moment, this surface is neutral. Therefore, the interactions on the Au (111) surface are not driven by charge, but by hydrophobicity and influenced by VdW forces. Adsorption on a hydrophobic surface occurs due to dehydration of the surface. This is because water closest to the surface initially has a reduced entropy, but as the simulation progresses, displacement of the surface water into the bulk solution increases its enthalpy and entropy, as the water forms hydrogen bonds with the surrounding water molecules.

Adsorption to the model hydrophobic gold surface provides no orientation preference for the protein dipole. Since this aligns to the long axis of the protein (see **Figure 4.8**), and the protein tends to lie parallel to the surface plane to maximise the short-range interactions with it, the dipole also tends to be parallel to the gold surface (**Table 4.1**), also maximising water displacement from the surface. The initial orientation of the protein was in a side on conformation, and in the adsorption trajectory, one end of the protein (towards the C-terminus) adsorbs first, followed later by the adsorption of the opposite end of the protein. The final adsorbed conformation is shown in **Figure 4.8**.



**Figure 4.8:** Adsorption of SpA on the hydrophobic gold surface. The colour scheme is the same as in Figure 4.5, and the gold atoms are shown as pink VdW spheres (defined in VMD 1.9.4). The purple needle indicates the dipole moment, and water molecules are not shown for clarity.

Adsorption is influenced by the water box, ionic strength of the system, hydrophobicity of the interacting residues relevant to the hydrophobic surface, and entropic/enthalpic effects. However, the protein seems to follow a non-specific Brownian motion in the bulk solution until the first adsorption event in this simulation occurred at 27.88 ns, this is by Ala221, which is neutral and hydrophobic. This initial interaction on the Au

(111) surface occurs at the active binding site of the protein to antibodies, which is evidence of the expected arbitrary adsorption on the Au (111) surface. This is followed by the adsorption of Gln220 (neutral, strongly hydrophilic) at 51.28 ns, and Asp218 (neutral, strongly hydrophilic) at 63.08 ns. The adsorption for the other residues on the non-binding side involves Lys34 (positively charged, strongly hydrophobic) at 84.08 ns and Met33 (neutral, hydrophobic) at 88.6 ns. The presence of Met33 in the list of residues interacting with Au (111) is particularly noteworthy as it is a sulphur containing residue. This is crucial in cysteine, which is the preferential binding site for gold in proteins (Buglak and Kononov, 2020), and dependent on the accessibility, it may be able to play a further role in sulphur-gold interactions, although potential covalent bonding of this type is not considered in these simulations.

Note that of these key residues that adsorb to the Au (111) surface, Ala221, Gln220 and Asp218 are located on the Fc binding side of the protein. Although the Ala221 and Gln220 residues are not involved in Fc binding, their interaction with the gold surface impacts those residues that are involved. It is also worth noting that the non-specific adsorption on the model hydrophobic surface is likely to encourage the protein to lie parallel to the surface plane, so that the availability of the Fc binding residues will always be restricted to some extent. The SpA maintains a good degree of mobility on the surface after the anchoring event, with a stable adsorption state and the protein only slightly diffusing on the surface. There is a structured layer of water at the model Au (111) surface, penetrated by the SpA residues, which break through the layer to interact directly with the surface; this phenomenon has previously been observed with metal surface models (Tavanti *et al.*, 2017, Palafox-Hernandez *et al.*, 2014, Penna *et al.*, 2014, Hughes *et al.*, 2017). The side of the protein facing the model Au (111) surface contains mostly uncharged, hydrophilic residues, as expected since adsorption is driven by water displacement, resulting from entropic/enthalpic effects.

The RMSD for the protein in the system is relatively stable. All the  $\alpha$ -helices in the protein maintain their structural integrity with an average RMSD value of 1.5 – 2 Å.  $\alpha$ -helix 3 is slightly higher, suggesting more movement for that part of the protein. The most stable  $\alpha$ -helix in simulation with the gold surface is  $\alpha$ -helix 4, starting at 0.25 Å and consistently maintaining its value throughout, and peaking at 1.3 Å (12 ns).

Although  $\alpha$ -helix 4 was not specifically kept free, consistent stability is a good sign nonetheless.  $\alpha$ -helix 7 shows improved stability in this simulation compared to the water box simulation, starting at 0.7 Å and ending at 1.3 Å, although it is consistently above 1 Å after 13 ns and hits a high of 2.3 Å at 25 ns.  $\alpha$ -helix 8 displays instability relative to the simulation in water, hitting a high of 2.1 Å at 67 ns, and at 40 ns, this jumps up significantly. This is an indication of the flexible loops moving together in the active region of the protein.  $\alpha$ -helix 9 is slightly more stable, starting at 0.3 Å and finishing at 1.4 Å, with a peak of 1.8 Å at 60 ns (**Figure 4.4e**). The RMSD values (**Table 4.2**) show SpA maintains the highest structural integrity on the Au (111) surface, and this can be attributed to VdW interactions, which influence adsorption. VdW interactions become important when adjacent atoms come close enough, so that their outer electron clouds briefly interact. Therefore, the interactions are short range, relatively weak, and not as specific or as strong as electrostatic interactions, though they can still be strong collectively (Reilly and Tkatchenko, 2015). These collective factors do not affect the protein structure as much as they do in adsorption driven by electrostatics, as seen with the silica siloxide rich surface. This also explains why SpA maintains its structural integrity on the Au (111) surface; the VdW interactions are strong at a short distance, and the SpA has more time to adjust and find local energetic minima. Simulations on the two SiO<sub>2</sub> surfaces (**Table 4.2**) show the biggest structural changes for the full protein and for individual  $\alpha$ -helices. This links primarily to the electrostatic interactions on the SiO<sub>2</sub> surfaces, which are strong and long range (York *et al.*, 1993), so that adsorption is directed and specific. Furthermore, the charge on SpA is not spread evenly across the structure (Lee *et al.*, 2021), so there are positive and negative patches that can distort the protein's tertiary structure in the electric field above the charged surfaces (Zhou and Pang, 2018).



**Table 4.2:** RMSD summary in Water, Au (111), SiO<sub>2</sub> O<sup>-</sup>, SiO<sub>2</sub> Si<sup>+</sup> simulations.

| Simulation                        | RMSD Values in Simulation |          |                                 |                                  |                  |          |                                 |                                  |                    |          |                                 |                                  |
|-----------------------------------|---------------------------|----------|---------------------------------|----------------------------------|------------------|----------|---------------------------------|----------------------------------|--------------------|----------|---------------------------------|----------------------------------|
|                                   | Start (Å) – 0 ns          |          |                                 |                                  | End (Å) – 100 ns |          |                                 |                                  | Max RMSD Value (Å) |          |                                 |                                  |
|                                   | Water                     | Au (111) | SiO <sub>2</sub> O <sup>-</sup> | SiO <sub>2</sub> Si <sup>+</sup> | Water            | Au (111) | SiO <sub>2</sub> O <sup>-</sup> | SiO <sub>2</sub> Si <sup>+</sup> | Water              | Au (111) | SiO <sub>2</sub> O <sup>-</sup> | SiO <sub>2</sub> Si <sup>+</sup> |
| <b><math>\alpha</math>-helix1</b> | 0.2                       | 0.2      | 0.29                            | 0.2                              | 1                | 0.3      | 0.2                             | 0.2                              | 1.1                | 1        | 0.88                            | 1.4                              |
| <b><math>\alpha</math>-helix2</b> | 0.32                      | 0.3      | 0.23                            | 0.4                              | 1                | 0.33     | 0.2                             | 0.6                              | 0.95               | 1.3      | 1.07                            | 1.2                              |
| <b><math>\alpha</math>-helix3</b> | 0.33                      | 0.35     | 0.6                             | 0.7                              | 1                | 1.35     | 1                               | 1.2                              | 1.4                | 2.7      | 1.7                             | 1.9                              |
| <b><math>\alpha</math>-helix4</b> | 0.3                       | 0.25     | 0.3                             | 0.3                              | 0.35             | 0.25     | 1                               | 0.5                              | 0.75               | 1.3      | 1.1                             | 1.4                              |
| <b><math>\alpha</math>-helix5</b> | 0.5                       | 0.4      | 0.6                             | 0.5                              | 0.8              | 1.3      | 1.4                             | 1.5                              | 1.6                | 1.48     | 2.2                             | 1.8                              |
| <b><math>\alpha</math>-helix6</b> | 0.3                       | 0.35     | 0.3                             | 0.4                              | 0.6              | 0.5      | 0.6                             | 0.4                              | 1.4                | 1.1      | 1.2                             | 1.2                              |
| <b><math>\alpha</math>-helix7</b> | 0.5                       | 0.7      | 0.6                             | 0.6                              | 1.7              | 1.3      | 1.5                             | 3.6                              | 2.5                | 2.3      | 3                               | 4                                |
| <b><math>\alpha</math>-helix8</b> | 0.3                       | 0.3      | 0.2                             | 0.2                              | 0.7              | 1.5      | 0.2                             | 0.5                              | 1                  | 2.1      | 0.9                             | 0.9                              |
| <b><math>\alpha</math>-helix9</b> | 0.5                       | 0.3      | 0.3                             | 0.5                              | 1.3              | 1.4      | 0.3                             | 1.1                              | 2.1                | 1.8      | 1.4                             | 1.5                              |
| <b>Full Protein</b>               | 1                         | 1        | 3                               | 2                                | 4                | 5.8      | 6.3                             | 5.1                              | 7.8                | 6.5      | 8                               | 8                                |

Due to the lack of an electric field, adsorption on the Au (111) was slower and non-specific, and it is worth noting, hydrophobic residues rather than hydrophilic residues are responsible for anchoring on the hydrophobic surface. This is despite hydrophobic residues mainly being in the core of the polypeptide chain of a protein (Kovacs *et al.*, 2006), as explained by the hydrophobic effect. Adsorption is initiated by a hydrophobic residue, followed by hydrophilic residues, and once the protein is adsorbed, the protein unfolds on the surface, facilitated by dehydration of the surface, and allowing exposure of the hydrophobic residues in the core. There is also be an entropic element influencing this phenomena, as protein unfolding increases its conformational entropy (Dyakin and Uversky, 2022). Another interesting observation is that most of the residues that anchor the Au (111) surface are polar uncharged and hydrophobic, this could explain the reduced mobility of the SpA on the Au (111) surface once adsorbed, as it has increased interactions between the hydrophobic anchoring residues and the Au (111) surface. Furthermore, it is worth considering previous work using similar surfaces, and the key residues observed in those simulations. The adsorption of amino acids and surfactants on a model Au (111) surface were studied (Feng *et al.*, 2011), and of the key anchoring residues found in the simulations (see **Table 4.3**), Gln and Met were found to be in the strongest binding

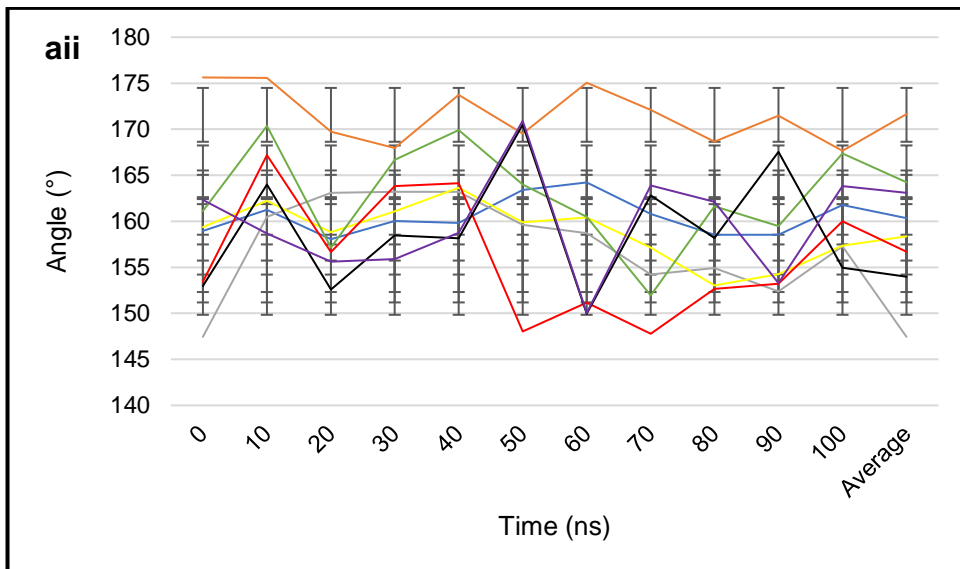
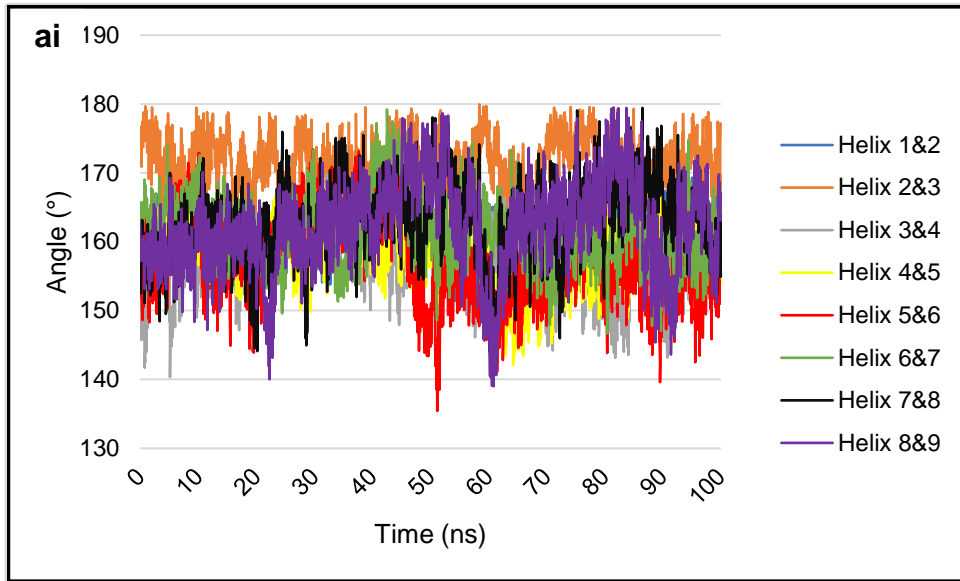
group, with Lys having intermediate strength, supporting the stability of the adsorbed state.

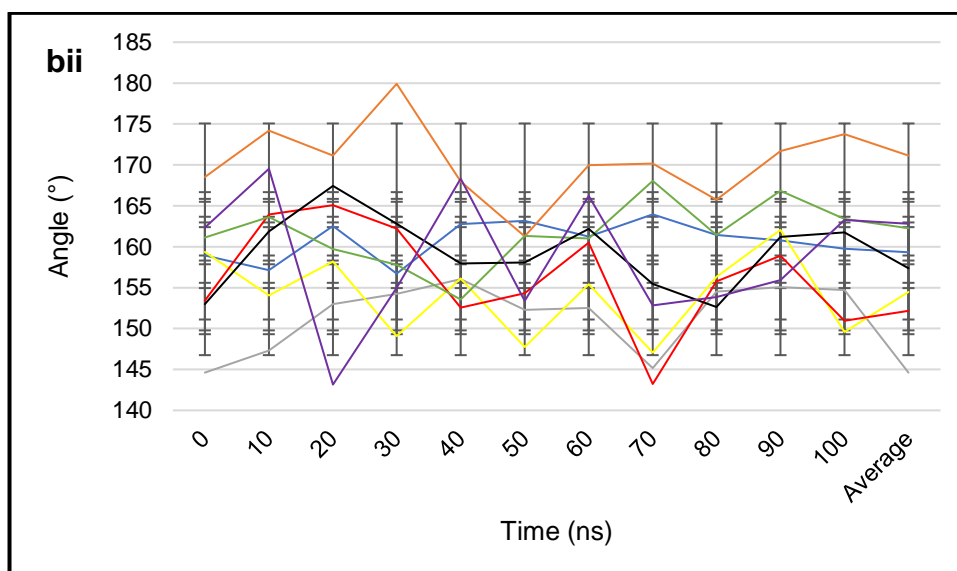
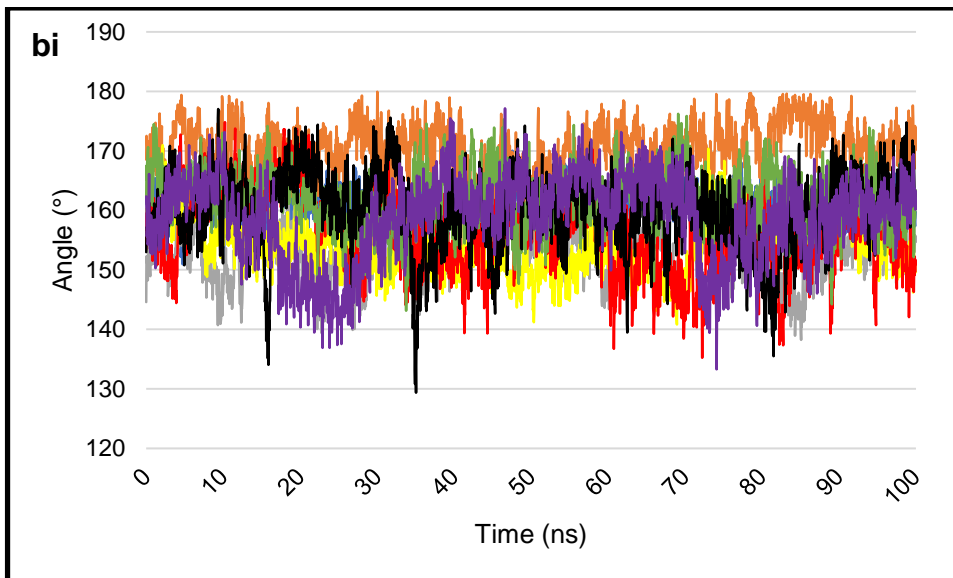
**Table 4.3.** Residues in contact with the surface (anchoring residues) in the final stages of SpA adsorption on the three model surfaces.

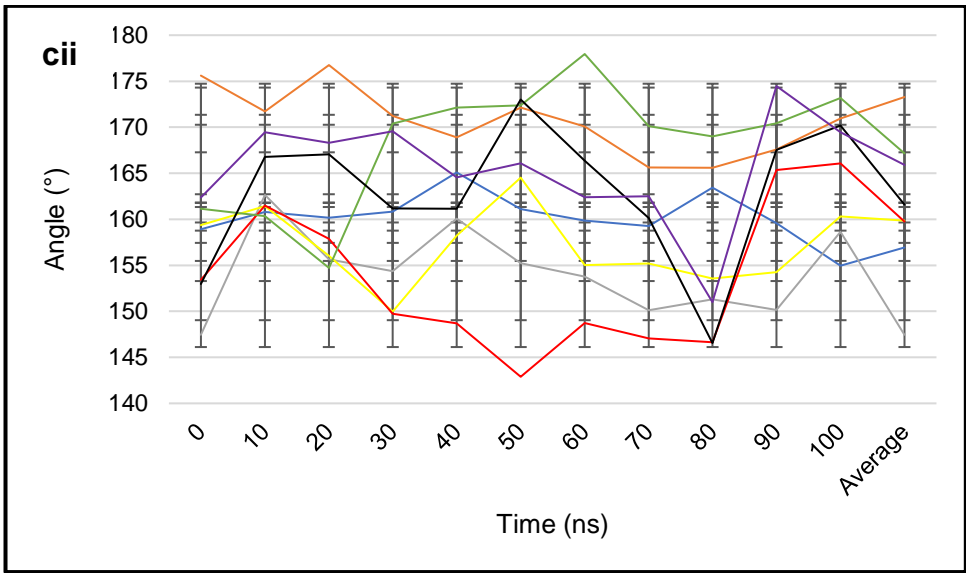
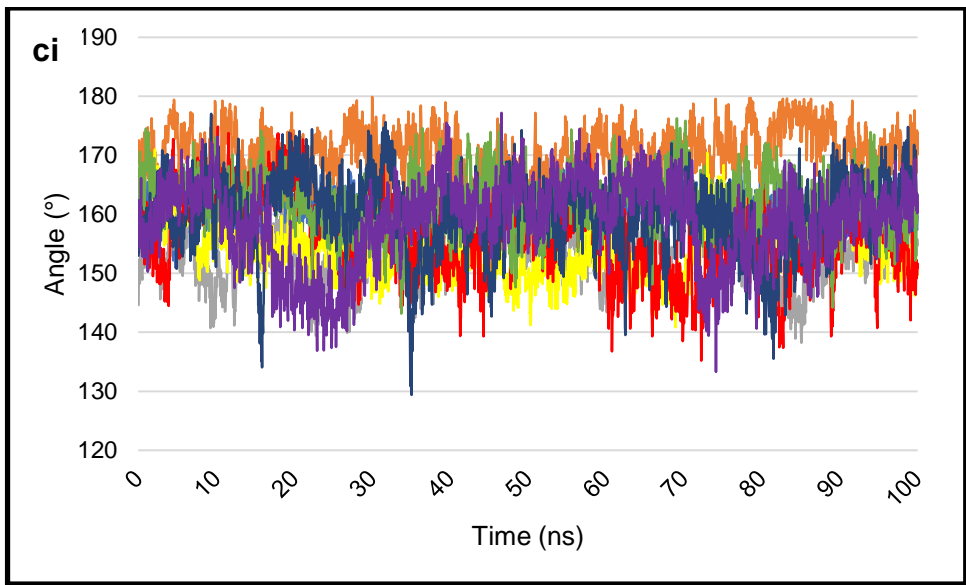
| Surface        | Adsorbing Residues                   |
|----------------|--------------------------------------|
| Au (111)       | Ala221, Gln220, Asp218, Met33, Lys34 |
| Silica O-rich  | Met33, Lys34, Phe35, Asn36, Lys37    |
| Silica Si-rich | Ala221, Gln220, Ala219               |

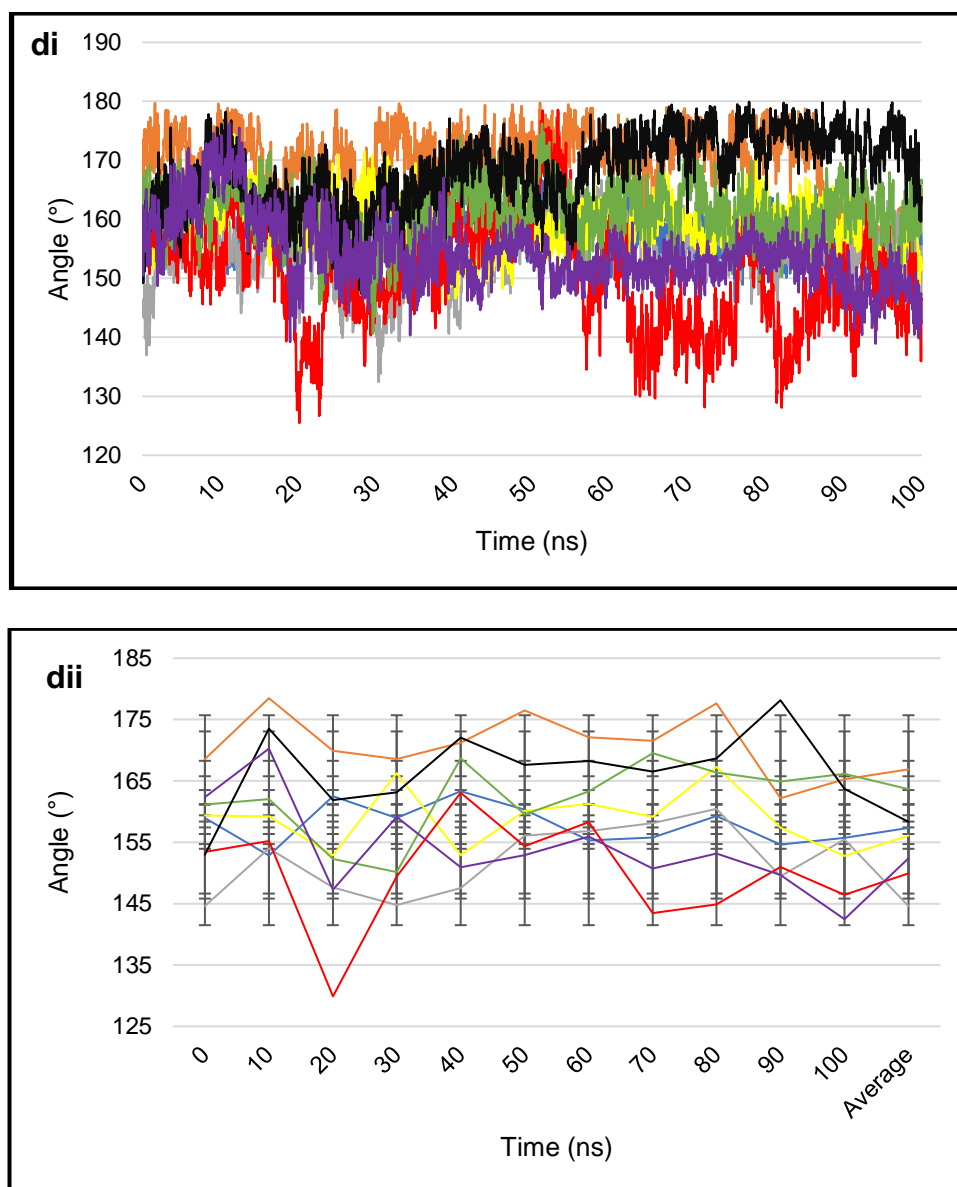
#### **4.3.2. Angles Between Neighbouring $\alpha$ -helices in Simulation**

The protein has nine  $\alpha$ -helix structures linked by loop regions, and all consecutive helices are aligned anti-parallel to each other. This is an interesting observation, as visibly, the protein structure moves in unison and the  $\alpha$ -helices stay closely linked throughout, pointing to strong hydrogen bonding, which is optimal in anti-parallel structures. The protein maintains a low RMSD value throughout the simulations, indicating good stability and similarity to the original structure.









**Figure 4.9:** The angles between the  $\alpha$ -helix pairs in ai) water, bi) silica siloxide, ci) silica under-coordinated, di) Au (111) simulations. The angles between the  $\alpha$ -helix pairs every 10ns in aii) water, bii) silica siloxide, cii) silica under-coordinated, dii) Au (111) simulations, these figures also contain the average angle in simulation, and standard deviations showing the spread of data.

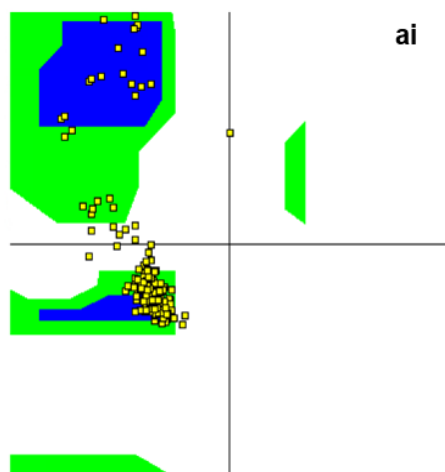
The angles between the long axes of the neighbouring helices throughout the simulations are given in **Figures 4.9ai, 4.9bi, 4.9ci and 4.9di**. There is clear uniformity, and the angles are close to (but below)  $180^\circ$  across all simulations, this could be attributed to the nature of the vectors being in opposite directions because of

the helix packing. The behaviour of the protein in the bulk water simulation (**Figure 4.9ai**), where there is no surface to guide protein movement, allows observation of the natural protein behaviour. Adsorption to the model charged surfaces (**Figures 4.9bi and 4.9ci**) do not show significantly different fluctuations in the inter-helix angles, again confirming the structural stability of the protein adsorbed to these surfaces.

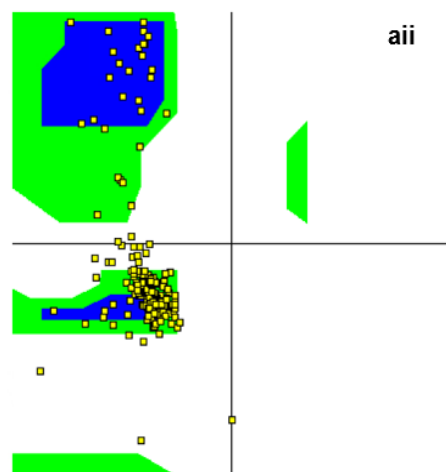
In the Au (111) simulation, greater fluctuation of some of the inter-helix angles is observed (**Figure 4.9di**). It is particularly visible in the angle between helices 5&6, where the angle is regularly  $\sim 130^\circ$  between 65-85 ns. This seems to accommodate the adsorption of both ends of the protein to the surface (see **Figure 4.8**); the overall bending of the protein is permitted by hinging movements between the helices, which themselves retain rather rigid structures. In the same simulation, helices 8&9 generally maintain a lower angle of  $\sim 150^\circ$  when compared to the bulk water simulation, where it is  $\sim 170^\circ$ . The angle every 10 ns of simulation, the average angle over 100 ns of simulation, and the spread of data is shown for every simulation in **Figures 4.9aii, bii, cii and dii**.

### 4.3.3. Ramachandran Plots

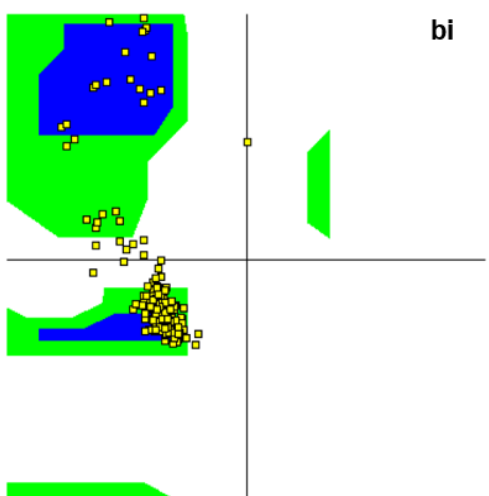
The Ramachandran plot (Ramachandran *et al.*, 1963) is a 2d plot of the  $\phi$ - $\psi$  torsion angles of the protein backbone, and provides a simple view of the conformation of a protein (Ramachandran *et al.*, 1963). The distribution of backbone dihedral angles (**Figure 4.10**) in a protein relevant to the observed and the experimental distribution of residues are highlighted. These graphs are powerful assets for quality control and assessment of the suitability of protein structure in biochemistry (Hooft *et al.*, 1997). The graphs show the  $\phi$ - $\psi$  angles clustered into distinct regions, with each region corresponding to alpha helix, or beta sheet, with the residues visible as being in sterically 'allowed' or 'disallowed' conformations. There are four basic types of Ramachandran plots, depending on the stereo-chemistry of the amino acid: generic, glycine, proline, and pre-proline (MacArthur and Thornton, 1991). The generic and proline Ramachandran plots are now well understood (Ho *et al.*, 2003), but the glycine and pre-proline Ramachandran plots are not.



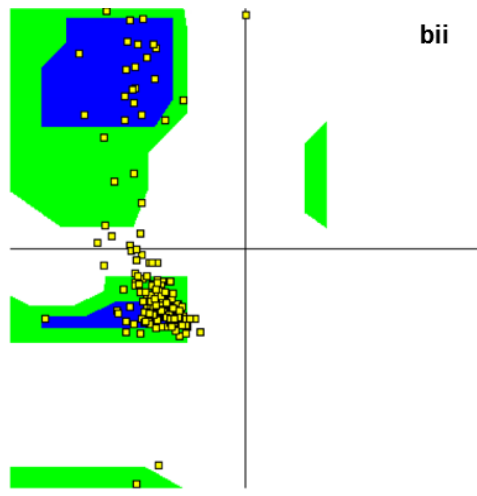
ai



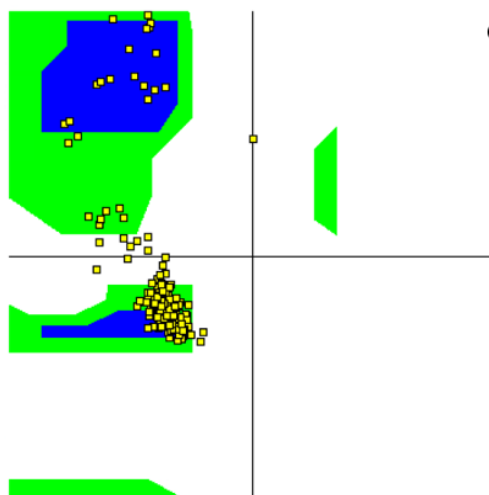
aii



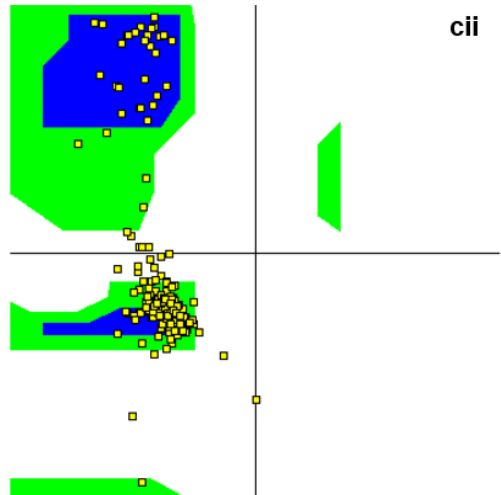
bi



bii

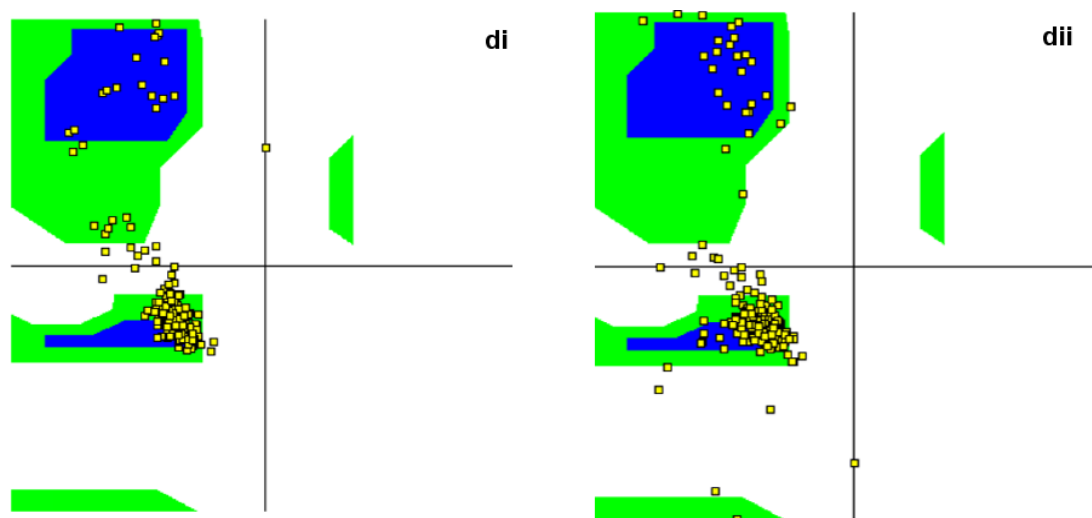


ci



cii





**Figure 4.10:** a) Ramachandran plots of SpA in water i) at 0 ns, ii) after 100 ns; b) Ramachandran plots of SpA simulation with SiO<sub>2</sub> siloxide surface i) at 0 ns, ii) after 100 ns; c) Ramachandran plots of SpA simulation with SiO<sub>2</sub> undercoordinated surface i) at 0 ns, ii) after 100 ns; d) Ramachandran plots of SpA simulation with Au (111) surface i) at 0 ns, ii) after 100 ns. The blue indicates alpha helix, green indicates beta sheet and the yellow squares indicate residues. The presence of most of the residues on the blue area shows SpA is a helical protein, and a few residues on white indicate they are in an ‘forbidden’ conformation.

Ramachandran plots were computed for four simulations: SpA in water (**Figure 4.10a**), on SiO<sub>2</sub> Siloxide surface (**Figure 4.10b**), on SiO<sub>2</sub> Undercoordinated surface (**Figure 4.10c**) and on Au (111) surface (**Figure 4.10d**). The Ramachandran Plots confirm all previous observations. Structurally, SpA is further highlighted as a helical protein with no observed protein unfolding, this is the same as what was previously observed from the protein structure and its stability in simulation trajectories, where it maintained its structure. Furthermore, the Ramachandran plots indicate good stability of the protein upon adsorption to the surfaces, and there seems to be little change in the protein secondary structure as the simulation proceeds. Finally, there are little to no residues at the “disallowed” regions, which is further validation of the simulation quality.

#### 4.4. Conclusions

The model SiO<sub>2</sub> slab with an electric field across the water/protein space, and a model Au (111) slab without an electric field both highlight the effect of different factors affecting protein adsorption. The three fully atomistic MD simulations of SpA at different model surfaces provide an interesting insight into protein dynamics at the solid/liquid interface. In the present study, the effect of surface chemistry on the adsorption mechanism of SpA was investigated, and the following conclusions can be drawn.

Firstly, when adsorption was driven by a long-range electric field above a positive surface, as seen with the under-coordinated silica surface model, the adsorption was found to be direct and specific, and the dipole moment of the protein quickly aligns with the electric field in the early stages of simulation, while the anchoring residues interact specifically with the surface. Similarly, adsorption to the negatively charged siloxide surface required the protein to re-orientate above the surface, which it is able to do due to the screening of the electric field by the diffuse layer of counter ions in solution.

Secondly, SpA has a large negative charge (-11e) at pH7, yet can still adsorb to the negatively charged silica surface due to the distribution of positively and negatively charged residues on the protein, and the capacity of a larger system in allowing the protein to diffuse and adsorb freely. Furthermore, the protein remains functional upon adsorption on the Siloxide surface and available for subsequent binding to the Fc region of antibodies.

Thirdly, the adsorption on the uncharged Au (111) surface was relatively slow and non-specific, and the interactions are therefore short-range in nature, with no preferred protein orientation, other than to maximise the contacts between the protein and the surface atoms. After a period of Brownian motion, the protein aligns in a way so the correct residues are in place to facilitate the anchoring event. The anchoring residues are polar uncharged, highlighting their importance at the initial stages of adsorption, and the interactions of SpA with Au (111) were driven by hydrophobicity, meaning it

has little effect on the interacting residues, which were mostly uncharged. The low adsorption specificity on gold has also been found by other authors (Heinz *et al.*, 2009, Feng *et al.*, 2011, Heinz *et al.*, 2008), and since hydrophobic Met33 is involved in the protein-gold interactions, this might indicate an important role for sulphur-gold interactions.

Fourthly, the conformational changes of SpA observed upon adsorption were related to local structural adjustments facilitated by the intrinsic flexibility between the  $\alpha$ -helix structural elements of the protein. However, it is to be noted that only the early stages of protein adsorption were assessed, so the long-term adsorption states might be different. This is particularly true for the adsorption onto the uncharged, hydrophilic model gold surface. However, for the adsorption onto the charge silica surfaces, it is worth noting that the electrostatics favour the adsorbed orientation of the protein with its long axis directed away from the surface plane, so that this is likely to be the long-term orientation.

Finally, these results indicate that adsorption to the negatively charged silica surface, as observed experimentally for SiNPs, is likely to produce favourable SpA adsorption that facilitates the binding of antibodies at the Fc region to functionalise the system. SpA not only adsorbs more readily, but the SpA also appears to need less amino acid ‘anchors’ on the negatively charged silica surface and it should be readily available to interact with the environment, and crucially keep the Fc binding regions free. Ionic strength also matters in the silica simulations as adsorption is driven more by electrostatic charge than hydrophobicity. The aforementioned results are, to some extent, transferable to other inorganic materials, and adsorption to other negatively charged NPs would similarly result in favourable functionalisation.

The intended approach was to use these studies as a basis to conjugate anti-SARS-CoV-2 antibodies to NPs in developing a new diagnostic for COVID-19. As mentioned previously, following the withdrawal of ‘The Antibody Company’ and the appointment of Alchemy Pharmatech as the new industrial partner, this route was not pursued, and the IN vaccine development route was pursued instead.

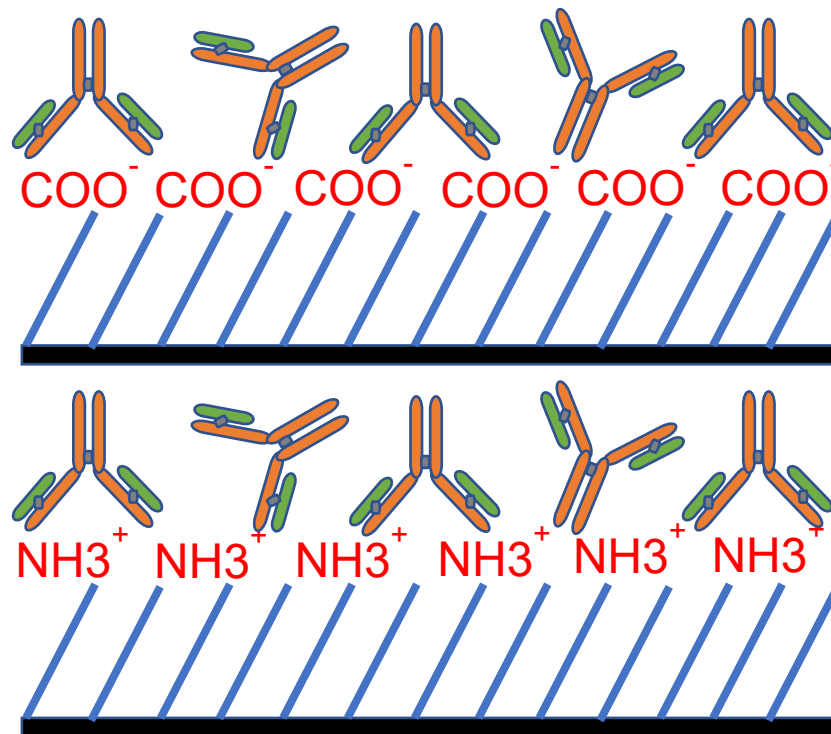
## Chapter Five: Model SARS-CoV-2 RBD Systems

*“The science of today is the technology of tomorrow”*

*Edward Teller*

## 5.1. Introduction

The surface chemistry of a material is an important aspect of protein-surface interactions, due to materials being hydrophobic or hydrophilic, and positive or negative. Engineering materials with the desired chemical properties can be achieved with the use of Self-assembled Monolayers (SAMs) (Almeida *et al.*, 2021, Latour, 2008, Ozboyaci *et al.*, 2016, Latour, 2014). SAMs are molecular formations of molecules formed on surfaces by adsorption (**Figure 5.1**); these molecules bind to the surface in an ordered way and are controllable for a variety of applications (Valkenier *et al.*, 2011). SAMs have been widely used in the past to study protein-surface interactions both experimentally and computationally, and have proven to be effective model surfaces (Liamas *et al.*, 2018, Farouq *et al.*, 2022). Antibody interaction was investigated on charged SAMs, with positively charged  $\text{NH}_2$ , and negatively terminated  $\text{COOH}$  SAMs utilised on a gold surface (Chen *et al.*, 2003). This is particularly relevant, as  $\text{COOH}$  SAM terminated NPs will also be used in this work.

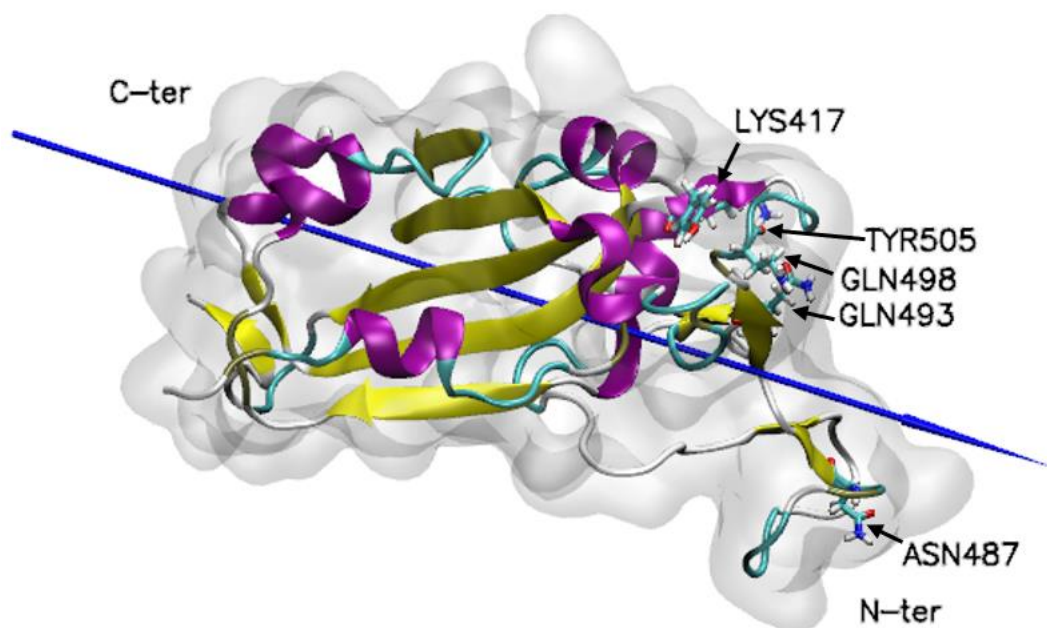


**Figure 5.1:** Diagram showing the possible adsorption of IgG1 onto two different SAMs on a gold surface. Figure modified from (Chen *et al.*, 2003).

The IgG1 and IgG2a antibodies were immobilised on SAMs, and further studied by Atomic Force Microscopy (AFM), secondary ion mass spectrometry and SPR. The difference in surface charge of COOH and NH<sub>2</sub> SAMs, and the higher dipole moment of the antibodies affected the ionic strength of protein/surface interactions, indicating the protein/surface interaction, which is driven by electrostatics, can be controlled by the type of SAMs on the surface (Chen *et al.*, 2003). The SPR experiments also showed a higher concentration of antibodies on the NH<sub>2</sub> SAMs than the COOH SAMs, indicating that antibodies interact preferentially with positively charged and hydrophilic surfaces (Chen *et al.*, 2003).

Furthermore, the effect of SAMs on the immobilisation of protein G from streptococcal bacteria with IgG from rat serum showed promising results (Yuan *et al.*, 2016). Using MD simulations, two thiols, 16-mercaptohexadecanoic acid (MHDA) and 11-mercapto-1-undecanol (MUO) were assembled into four different self-assembly systems with varying ratios, and the SAMs with the highest MUO ratio showed the best results (Yuan *et al.*, 2016). These results were also verified experimentally using a Quartz Crystal Microbalance (QCM) sensor, and the biggest shift of resonant frequency was observed for the SAMs with the highest MUO ratio (Yuan *et al.*, 2016), further indicating the MUO SAMs effectively immobilised protein G with IgG. The adsorption of BSA, lysozyme (LYZ) and rabbit IgG were previously studied with several SAMs ((HS(CH<sub>2</sub>)<sub>9</sub>CH<sub>3</sub>), (HS(CH<sub>2</sub>)<sub>11</sub>OH), (HS(CH<sub>2</sub>)<sub>10</sub>CHO) and (HS(CH<sub>2</sub>)<sub>15</sub>COOH)) using AFM. The IgG immobilised strongly on the aldehyde terminated surface primarily through covalent bonding (Wadu-Mesthrige *et al.*, 2000), and the adsorption with the COOH terminated SAMs was found to be electrostatic and unaffected by water on or around the SAMs layer. These properties could be attributed to the various conformations of IgG on the surface; the physical interactions are also affected by surface functionality and pH, which changes the coverage of the SAMs (Wadu-Mesthrige *et al.*, 2000). These can be modified by washing with a surfactant solution such as 1% (v/v) Tween, at the iso-electric point (IEP) (e.g. pH at which the molecule has no electrical charge), the molecules adsorbed onto the SAMs with 90% coverage, binding through hydrophobic interactions (Wadu-Mesthrige *et al.*, 2000).

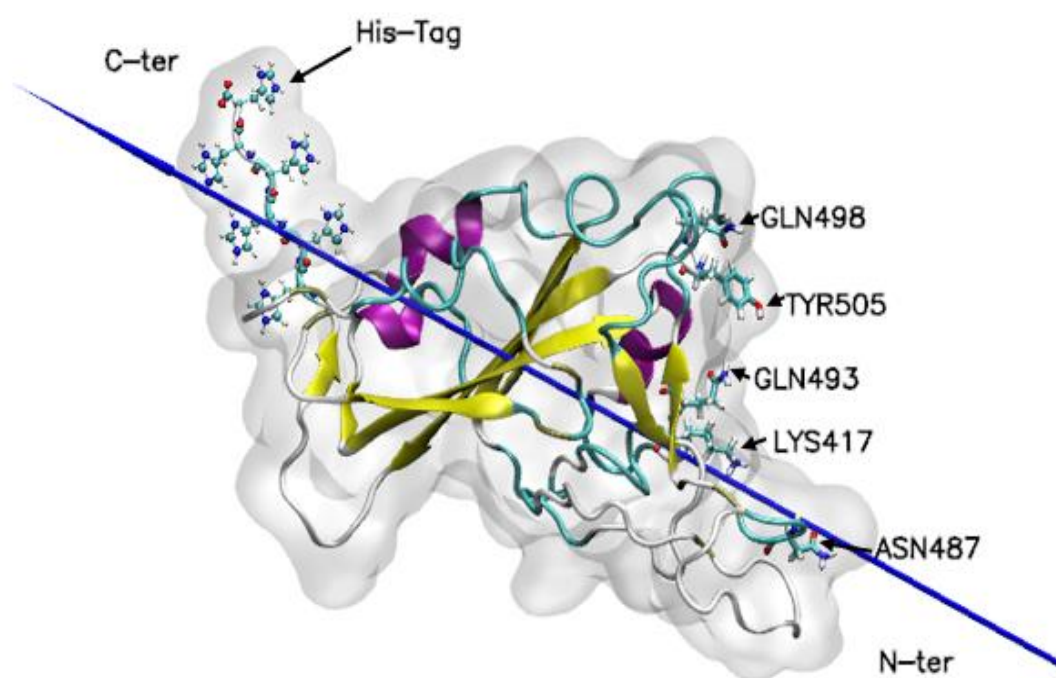
Investigating SAMs on NPs through experimental means or by MD simulations is important in assessing their influence in biomolecular interactions.



**Figure 5.2:** The S1 subunit structure (PDB: 7BWJ) illustrated using VMD 1.9.4 (Humphrey *et al.*, 1996). The protein is indicated as a ghost surface, while the secondary structural  $\alpha$ -helices are coloured purple, and the beta sheets are coloured yellow. The blue needle indicates the dipole moment. The key residues that interact with the ACE2 receptor, namely Lys417, Asn487, Gln493, Gln498 and Tyr505 are indicated by the ‘liquorice’ representation and coloured by atom type (carbon is cyan, nitrogen is blue, oxygen is red and hydrogen is white) (Humphrey *et al.*, 1996).

The S1 subunit of the S protein (**Figure 5.2**) binds to the ACE2 receptor through the Lys417 (positive, hydrophilic), Asn487 (neutral, hydrophilic), Gln493 (neutral, hydrophilic), Gln498 (neutral, hydrophilic) and Tyr505 (neutral, hydrophilic) residues (Veeramachaneni *et al.*, 2021). Therefore, it is important the protein adsorbs to the surface in a way to keep this region (RBD region) free. As established previously (see **Chapter 4**), MD simulations can provide molecular-scale insight into the interactions between biomolecules and inorganic materials, revealing details that would otherwise

be impossible to observe. There are several computational studies on the effect of surface charge, hydrophobicity, and ions on protein adsorption and electrostatic interactions play a key role in driving the proteins onto charged surfaces, where the adsorption takes place between charged surfaces and oppositely charged residues (Albers *et al.*, 2001, Singh *et al.*, 2016, Farouq *et al.*, 2022, Kubiak and Mulheran, 2009, Kubiak-Ossowska *et al.*, 2014). The ions also play a key role during adsorption on charged surfaces because they screen the electric field, which can promote or inhibit protein adsorption (Mulheran *et al.*, 2016).



**Figure 5.3:** The S1 subunit (PDB: 7BWJ), illustrated using VMD 1.9.4 (Humphrey *et al.*, 1996). The colour scheme is the same as Figure 5.2. Additionally, the histidine tag, added to the C terminal of the protein is shown as a CPK representation.

The aim of this chapter is to investigate the interactions of the S1 subunit, which contains the ACE2 binding RBD (see Section 2.1.2), with model inorganic NPs, and investigate how the S1 subunit binds to inorganic material surfaces, and if it binds in a way to keep the ACE2 binding region free. Keeping this region free is crucial for effective integration of these systems in designing a new vaccine, and adsorption is



studied on a model silica surface and a model COO<sup>-</sup> SAMs terminated silica surface. The simulations will be further assessed to establish: the adsorption stability of the S1 subunit on the model surfaces; the factors impacting protein stability; the influence of the histidine tag (His-Tag) on protein behaviour and adsorption. The S1 subunit modified with a His-Tag (**Figure 5.3**) is also being studied here due to its better availability experimentally.

## 5.2. Materials and Methods

### 5.2.1. Surface Models

**SiO<sub>2</sub>:** The model SiO<sub>2</sub> slab, created from an  $\alpha$ -cristobalite structure was modelled as ions fixed in space (Patwardhan *et al.*, 2012). An electric field induced through the simulation box (Kubiak-Ossowska *et al.*, 2013), means the electrostatic environment above the slab mimics that expected above a negatively charged silica surface. The slab dimension was 103 Å x 199 Å x 13 Å, with 17280 atoms, yielding two different faces: (i) an SiO<sub>2</sub> surface with siloxide groups at the top of the slab and (ii) undercoordinated Si species at the bottom. The Charmm-27 force-field parameters for the surface were used according to Patwardhan *et al.* (Emami *et al.*, 2014), and the SiO<sub>2</sub> surface with siloxide groups at the top mimics the negatively charged surface encountered experimentally at pH7 (Patwardhan *et al.*, 2012). The surface with undercoordinated Si species exposed mimics a positively charged surface, though this is a model only and not available experimentally.

**COO<sup>-</sup> Terminated SiO<sub>2</sub> surface:** The SAMs surface was constructed with two carboxyl (-COOH) slabs on opposing sides, with all the carboxyl molecules in their deprotonated (-COO<sup>-</sup>) state to achieve a homogeneous model negative surface. The molecules consisted of a backbone of four carbon molecules in addition to the COOH groups, and the broken C-C bonds were patched with hydrogen atoms to satisfy the valence requirements. The individual molecules were placed parallel to each other with a distance of 4.97 Å between them (Ulman *et al.*, 1989), and the slab contained 15,283 atoms with dimensions of 107 Å x 147 Å x 77 Å. The thickness of each surface was larger than the L-J cut-off distance of the VdW forces (12 Å), in order to prevent

interaction between the outer surface and the protein within the system water box. The first carbon atom (from the bottom) of every SAMs molecule was fixed in space, leaving the other three carbons on the backbone and the terminal functional groups free to move. The geometry and parameters for aspartic acid residue side chains were used to represent the COOH molecules.

### **5.2.2. MD Simulations of S1 Subunit**

The NAMD 3.0 package (Phillips *et al.*, 2020) was utilised along with the Charmm-27 force-field, and the simulation results were analysed with VMD 1.9.4 (Humphrey *et al.*, 1996). The simulation was performed in three stages following previously reported protocol (Kubiak-Ossowska *et al.*, 2016). The first stage involved water and ions being added to the simulation cell, that already contained the static protein as obtained from the PDB structure, followed by water and ion minimisation of 1000 steps, and a subsequent 100 ps run in the NPT ensemble with an integration time-step 1 fs, at a target temperature of 300K, and a pressure of 1 atm. The second stage simulated the complete system consisting of protein, water and ions through energy minimisation for 10,000 steps, followed by NPT equilibration for 300 ps. The final stage consisted of an initial 10 ns run, with a 2fs time-step at 300 K in the NVT ensemble, extended to give a 100ns production trajectory. PBC, along with the SHAKE algorithm, were used in the simulation and the L-J cut-off distance for the VdW interactions was set at 12 Å. PME summation was used to describe the electrostatic Coulomb interactions (Essmann *et al.*, 1995). The simulation setups of protein, water, ions and with the surfaces are described below.

### S1 Simulations in water

The S1 subunit, obtained from PDB: 7BWJ consists of 217 amino acids (1536 atoms), and a net protein charge at pH 7 of -2e. The structure also contains eight  $\alpha$ -helices and eleven  $\beta$ -sheets, with the ACE2 receptor binding residues located towards the N terminus. The protein was initially solvated in a rectangular box extending at least 12 Å (16821 waters) from the structure, and the TIP3P (Jorgensen *et al.*, 1983, Neria *et al.*, 1996) model was used describe the water molecules. The system was neutralised by adding NaCl salt at ionic strength  $2 \times 10^{-2}$  M (6 Na<sup>+</sup> and 8 Cl<sup>-</sup>), giving a system with 53428 atoms.

### SiO<sub>2</sub> Surface Simulations

The siloxide silica surface simulation system involved the S1 subunit being placed ~20 Å above the surface (the protein surface distance varied between 20-23 Å). The structure was solvated in a rectangular water box (TIP3P model) extending at least 40 Å in the z axis (~65781 water molecules), giving a system with ~216464 atoms. NaCl ions were added to shield both the siloxide and silicon undercoordinated surfaces (288 Na<sup>+</sup>, 286 Cl<sup>-</sup>). The net protein charge was -2e, so the ions added neutralised the system, as well as shielding the surfaces.

The silicon undercoordinated surface simulation system had the protein positioned ~22 Å above the surface (the protein surface distance varied between 22-24 Å), and was solvated in a rectangular water box (TIP3P model) extending at least 22 Å (~57270 water molecules) in the z axis. NaCl salt was added (288 Na<sup>+</sup>, 286 Cl<sup>-</sup>) to shield both surfaces, giving a system with ~190935 atoms.

### COOH terminated SiO<sub>2</sub> surface

The simulation with the SAMs terminated surface was initially tested at the same parameters used for simulations on the model silica surface. However, to improve the properties of the SAMs surface even further, the systems were computed at slightly different settings. The production trajectory was computed in the NPT ensemble (1.01325 bar atmospheric pressure, isotropic), with a timestep of 2fs at 300k. The protein was positioned ~25 Å above the surface (the protein surface distance varied

between 25-27 Å), and solvated in a rectangular water box (TIP3P model) extending at least 50 Å (~34921 water molecules) in the x axis. The system was neutralised and NaCl concentration was set to 0.2 mol/L, adding 1115 Na<sup>+</sup> ions and 131 Cl<sup>-</sup> ions, shielding both COO<sup>-</sup> surfaces and giving a system with ~120054 atoms.

### 5.2.3. MD Simulations of S1 Subunit with His-Tag

The same simulation setup used for the S1 subunit (See Section 5.2.2) was adapted for simulations of the S1 subunit with a His-Tag. The S1 subunit was modified with a His-Tag at the C terminus of the protein (See Figure 5.3) by the addition of six  $\alpha$ -carbon atoms, representing the addition of six histidine (positive, hydrophilic) residues. The simulation setups of protein, water, ions and with the surfaces are described below.

#### Simulations in Water at pH6

The crystal structure of the S1 subunit (Youn *et al.*, 2017) previously used in the simulations was modified with a His-Tag at the C terminus, and some residues were protonated to run the simulations at pH6 (Table 5.1). These simulations, where the S protein RBD was modified with a His-Tag, were computed at pH6 because the protonated His-Tag was then positively charged, thus enhancing the protein's ability to conjugate to negatively charged NPs and more likely to result in an optimum orientation of the conjugated protein for use in new therapeutics.

**Table 5.1:** A list of residues in the S1 subunit that were protonated to run the His-Tag modified S1 subunit simulations at pH6. The residue name changed to Hsp once protonated.

| Residue Type | Residue Number               |
|--------------|------------------------------|
| Asp          | 398, 406                     |
| His          | 519, 527, 529, 530, 531, 532 |

The final modified structure had 223 amino acids (1638 atoms), and a net protein charge at pH 6 of +11e. The protein was solvated in a rectangular water box extending at least 15 Å (40379 waters) from the structure, and the TIP3P (Jorgensen *et al.*, 1983,

Neria *et al.*, 1996) model was used describe the water molecules. The system was neutralised by adding NaCl salt at ionic strength  $2 \times 10^{-2}$  M (7 Na<sup>+</sup> and 18 Cl<sup>-</sup>), giving a system with 58887 atoms.

#### Simulations with Silica Surfaces at pH6

In the silica siloxide surface simulation, the protein was placed  $\sim 44$  Å above the surface (the protein surface distance varied between 44-50 Å), and solvated in a rectangular water box (TIP3P model) extending at least 40 Å in the z axis ( $\sim 65023$  water molecules), giving a system with  $\sim 214323$  atoms. NaCl ions (Na<sup>+</sup>: 277, Cl<sup>-</sup>: 288) were added to shield both surfaces.

In the silicon undercoordinated system, given the net charge and the influence of the His-Tag, the protein was positioned closer to the surface, with the His-Tag facing the positive silicon undercoordinated surface to encourage adsorption. The distance from the surface was  $\sim 22$  Å (the protein surface distance varied between 22-24 Å), and the system was solvated in a rectangular box (TIP3P model), extending at least 44 Å ( $\sim 77137$  waters) in the z axis. As the net protein charge was +11e, the ions neutralised the system as well as shielding the surfaces, so NaCl salt was added (277 Na<sup>+</sup>, 288 Cl<sup>-</sup>), giving a system with  $\sim 250665$  atoms.

#### COOH terminated SiO<sub>2</sub> surface pH6

The production trajectory was also computed in the NPT ensemble (1.01325 bar atmospheric pressure, isotropic), with a timestep of 2fs at 300k, compared to the NVT ensemble for the silica surface. The protein was positioned  $\sim 20$  Å above the surface (the protein surface distance varied between 20-23 Å), and solvated in a rectangular box (TIP3P model) extending at least 60 Å ( $\sim 36824$  water molecules) in the x axis. The system was neutralised and NaCl concentration was set to 0.2 mol/L adding 1113 Na<sup>+</sup> ions and 138 Cl<sup>-</sup> ions, shielding both COO<sup>-</sup> systems and giving a system with  $\sim 125864$  atoms.

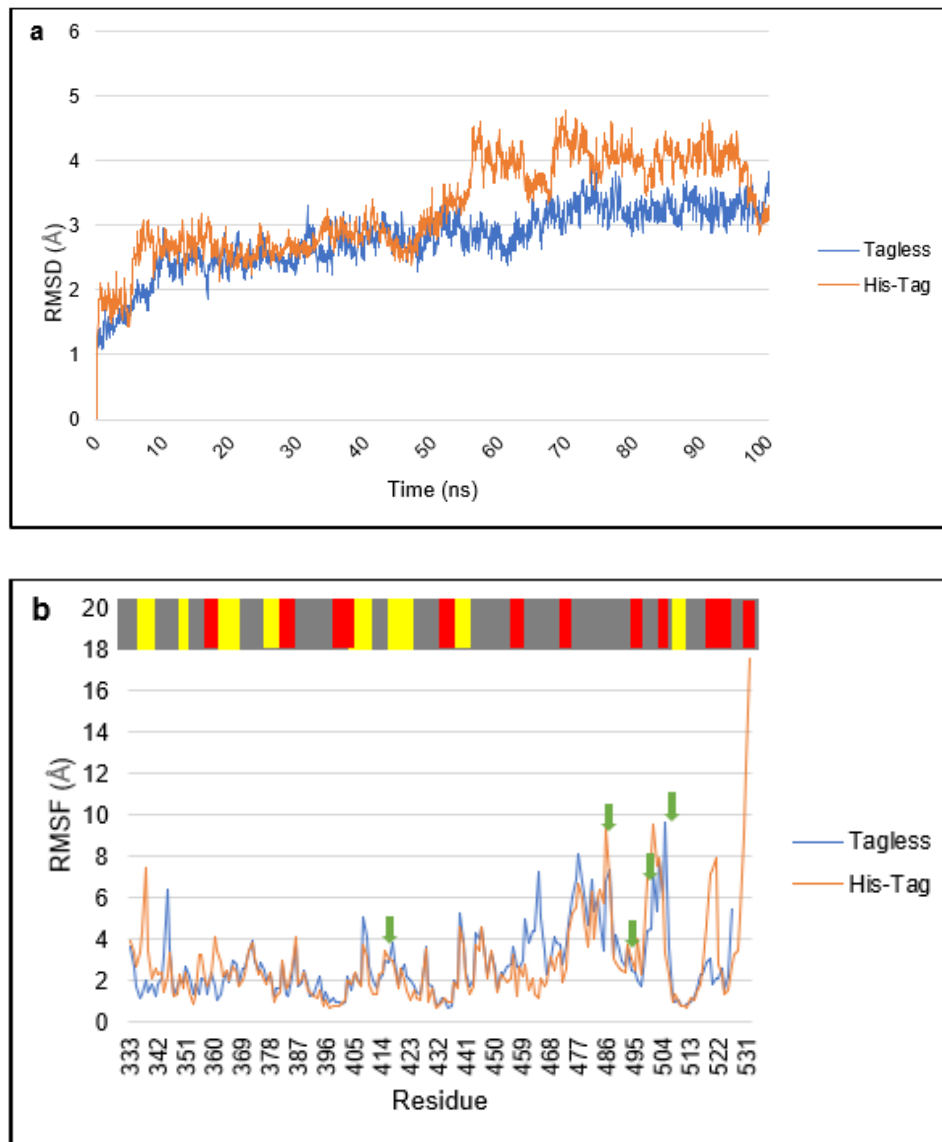
### 5.3. Results and Discussions

#### 5.3.1. Adsorption of the S1 Subunit and S1 Subunit with a His-Tag

##### Simulations in Water

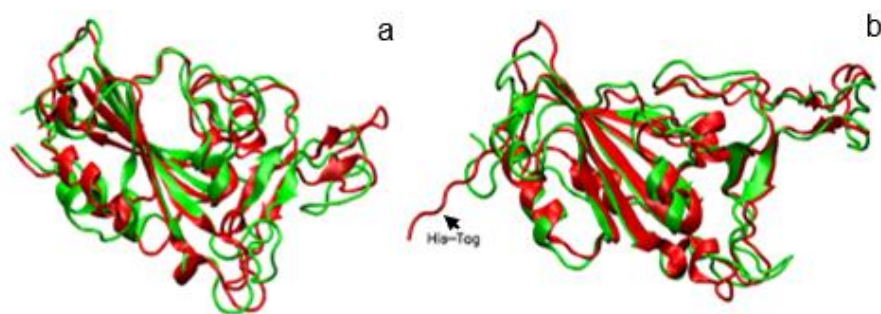
Protein adsorption is affected by several factors including surface charge and hydrophobicity; however, another important factor is the structural integrity of the protein. Therefore, the simulations in solution only need to be prepared for ensuring the stability of the protein within the used FF and the MD protocol employed. As mentioned previously, for successful binding with materials, the ACE2 binding region must be kept free, and to establish whether the fragment maintains its structural integrity in simulation, the protein was placed in a simulation box with water molecules and NaCl ions, with the computation of a 100 ns trajectory.

The RMSD for the tagless S1 subunit (tagless protein) is initially  $\sim 1.2$  Å, and the His-Tag modified S1 subunit (tagged protein) is initially  $\sim 2$  Å, indicating there is little deviation in the original protein 3D structure, in other words the protein is stable. However, as the simulation in water progresses, the situation changes around 55 ns of the trajectory. There is an increase just after 55ns (**Figure 5.4a**) for the tagged protein, which remains higher than the tagless protein for most of the remaining duration, increasing to  $\sim 4.8$  Å at 74ns, while the tagless protein increases to  $\sim 3.9$  Å at 79ns, indicating the introduction of the His-Tag affects the protein movements negatively, as it results in a decrease in stability. This shift after 55ns, when compared to the simulation from 0-55ns, could be attributed to the bending and twisting of the protein through the loops connecting the subsequent modules, as seen in the simulation trajectory and from the structure overlaps after 100ns (**Figure 5.5a**). The bends between subsequent modules may be greater as the simulation progresses, due to a lack of stabilisation coming from the remaining parts of the protein. For the tagged protein, the His-Tag is showing a particular tendency to flex as observed from the trajectory. This will naturally give a higher RMSD, and at the end of the simulation, the His-Tag visibly moves, changing its final position after 100ns relative to the original structure (**Figure 5.5b**).



**Figure 5.4:** The a) RMSD, b) Root mean square fluctuations (RMSF) of S protein RBD and tagged-S Protein RBD in the water simulations. The coloured ribbon at the top of the RMSF figure indicates the secondary structure of the protein:  $\beta$ -sheets (red) and  $\alpha$ -helices (yellow), while unstructured parts are shown in grey. The green arrows indicate the location of ACE2 binding residues. The His-Tag is at residues 527-532.

Despite the sudden increase, the RMSD curves for both the tagged and tagless proteins overall remained ~constant for the last 30ns of simulation, indicating the proteins maintained their structural integrity.



**Figure 5.5:** The structure overlaps after 100 ns simulation in water a) tagless protein, b) tagged protein. The original structure is indicated in red while the structure after 100ns is indicated in green, while the His-Tag is annotated.

The dipole moment for the tagless protein was 188.88 D fluctuating to 257.15 +/- 85 D as the simulation progressed. The dipole moment for the His-Tag modified protein was 779.61 D fluctuating to 715.69 +/- 158 D, the much larger dipole moment after 100ns could be attributed to vigorous fluctuations of the His-Tag. The Root Mean Square Fluctuations (RMSF), which measures the average deviation of a particle over time from a reference position, is ~3.1 Å for the Lys 417 (positive, hydrophilic) residue, ~3.2 Å for the Asn 487 (neutral, hydrophilic) residue, ~3.7 Å for the Gln 493 (neutral, hydrophilic) residue, and ~9 Å for the Tyr 505 (neutral, hydrophilic) residue for both proteins (**Figure 5.4b**). The RMSF values are ~9 Å for the Gln 498 (neutral, hydrophilic) residue (tagged protein), and ~7 Å (tagless protein). These are the ACE2 binding residues, and it is especially important to consider the RMSF for them as it is important this region is kept free, as well as possessing good conformational flexibility, which will enhance its use in therapeutics. The RMSF further shows fluctuations are generally small at the secondary structure regions, and the higher RMSF values generally occur at loop regions. The tagged protein generally maintains a higher RMSF than the tagless protein, especially at the His-Tag region, indicating certain regions have greater conformational flexibility in simulation, the higher RMSF could also be attributed to loop regions, which display greater movement during the simulation trajectory. Both proteins maintain an overall stable RMSD, and the structure overlaps (**Figure 5.5**) confirm the secondary structure of both structures

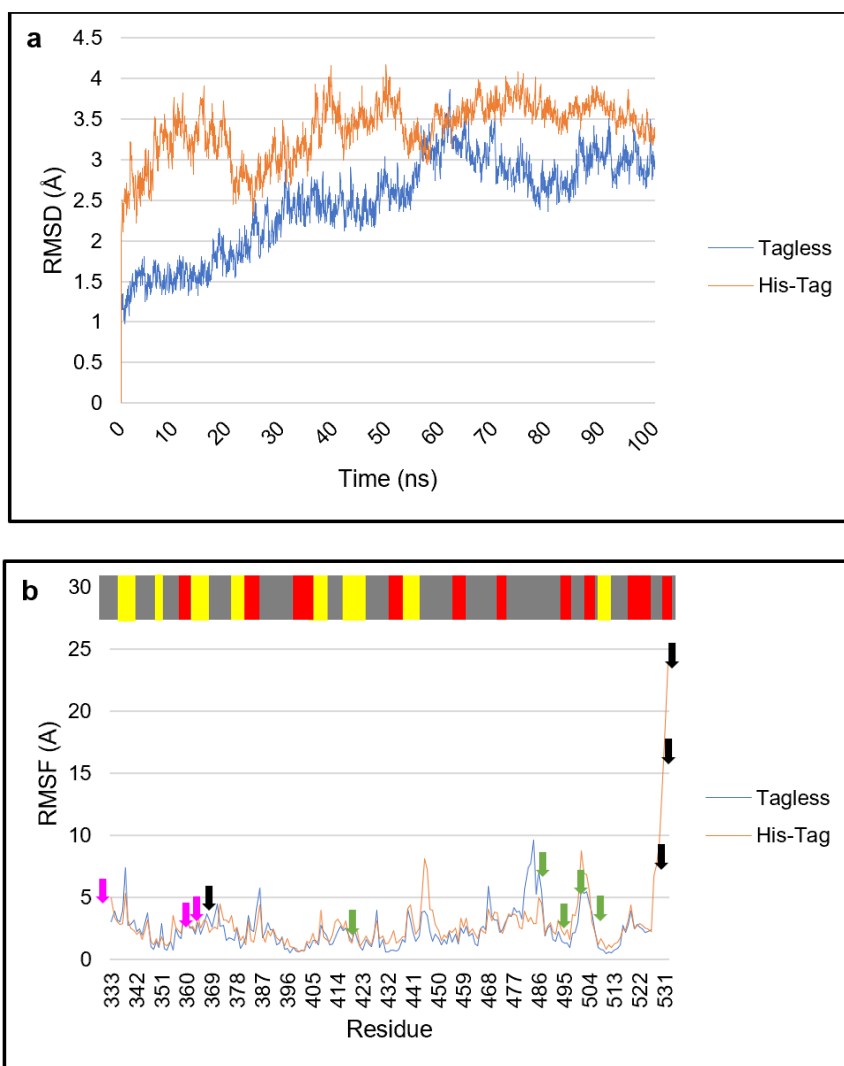


remains intact throughout simulation, meaning both models are stable to attempt adsorption on charged surfaces. However, the tagged protein is slightly less stable than the tagless protein (**Figure 5.5b**).

#### Tagless Protein Simulation on Negatively Charged Silica Surface

The two statistically independent trajectories obtained displayed similar behaviour of the protein described here. The tagless protein is overall negatively charged, meaning the electric field implemented in the model surface would direct it towards adsorption on the positive surface. However, despite its overall negative charge, the protein can adsorb on negatively charged surfaces. This is due to the attraction with positively charged regions in the protein, and these positively charged patches on the protein may be exposed as the protein rotates and diffuses in water (Lin *et al.*, 2014, Kubiak-Ossowska *et al.*, 2016). To promote the adsorption of negative protein onto negative surface, the electric field was screened by adding 286 Na<sup>+</sup> and 284 Cl<sup>-</sup> ions. The protein was placed in a side-on initial conformation, and the tagless protein undergoes Brownian motion in the first few ns of simulation. The RMSD increases steadily (**Figure 5.6a**), indicating a slight decrease in protein stability at this stage in simulation. The tagless protein ascends at 20ns and interacts with the ion/water layer at the surface, approaching the surface several times without adsorption, until 22.3ns, when the Asn 370 (neutral, hydrophilic) residue adsorbs to the surface in the first anchoring event. The first anchoring event is followed by the adsorption of the Asn 388 (neutral, hydrophilic) and Thr 333 (neutral, hydrophilic) residues adsorbing at 23.1ns and 24.6ns. The protein continues to diffuse on the surface, and the Asn 388 (neutral, hydrophilic) residue desorbs at 26.7ns, and re-adsorbs at 27.7ns, along with the first adsorption of the Val 367 (neutral, hydrophobic) residue. The RMSD increases as the protein adsorbs (**Figure 5.6a**) to the surface, indicating slight distortion of the protein structure upon adsorption, but overall good stability of the protein in its adsorbed state. The protein seems to be more stable when adsorbed to the surface, compared to the structure in water (**Figure 5.4a**), and the simulation trajectory seems

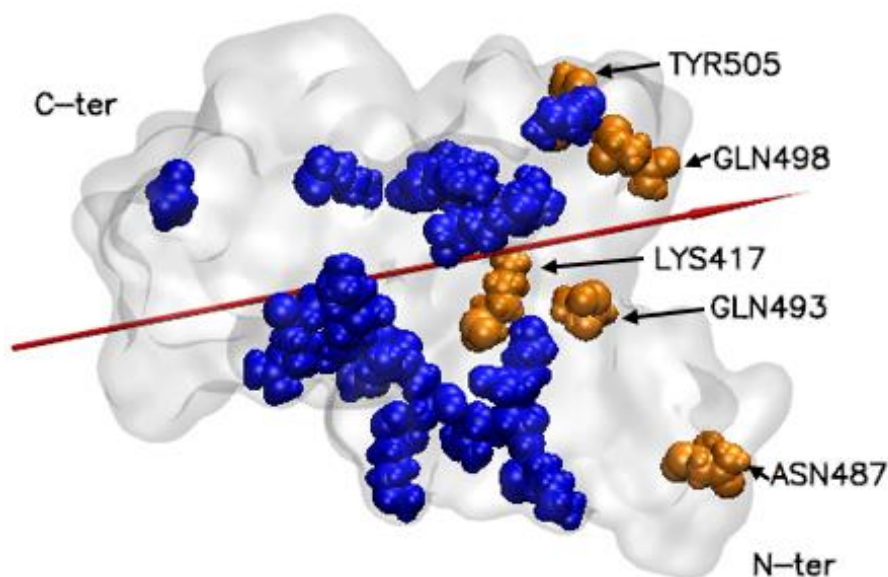
to indicate the protein seems to maintain its structural integrity. Though as the simulation proceeds, the protein seems to relax at the surface interface.



**Figure 5.6:** The a) RMSD, b) RMSF of S protein RBD and His-Tag S Protein RBD in the siloxide silica surface simulations. The colour scheme is the same as Figure 5.4. Additionally, the pink arrows represent the tagless protein adsorbing residues and the black arrows represent the tagged protein adsorbing residues.

These adsorptions are further followed by the Thr 385 (neutral, hydrophilic) residue reaching for the surface and adsorbing at 32.9ns, and the Asp 389 (negative, hydrophilic) residue, which adsorbs at 35.8ns. The Thr 333 (neutral, hydrophilic) residue, which was the first to interact with the surface, maintains this interaction with the surface and stays strongly bound, while the other residues desorb at 39.6ns. There are further changes in the RMSD at this point, meaning the final, stable adsorption state is not achieved and the protein tends to remain close to the surface, adjusting its structure and attempting to form stronger anchors to the surface. The protein freely diffuses on the surface, interacting with the ion/water layer and the Asp 389 (negative, hydrophilic) residue adsorbs again at 41.2ns. Shortly after at 47.7ns, the Val 362 (neutral, hydrophobic) residue also adsorbs to the surface.

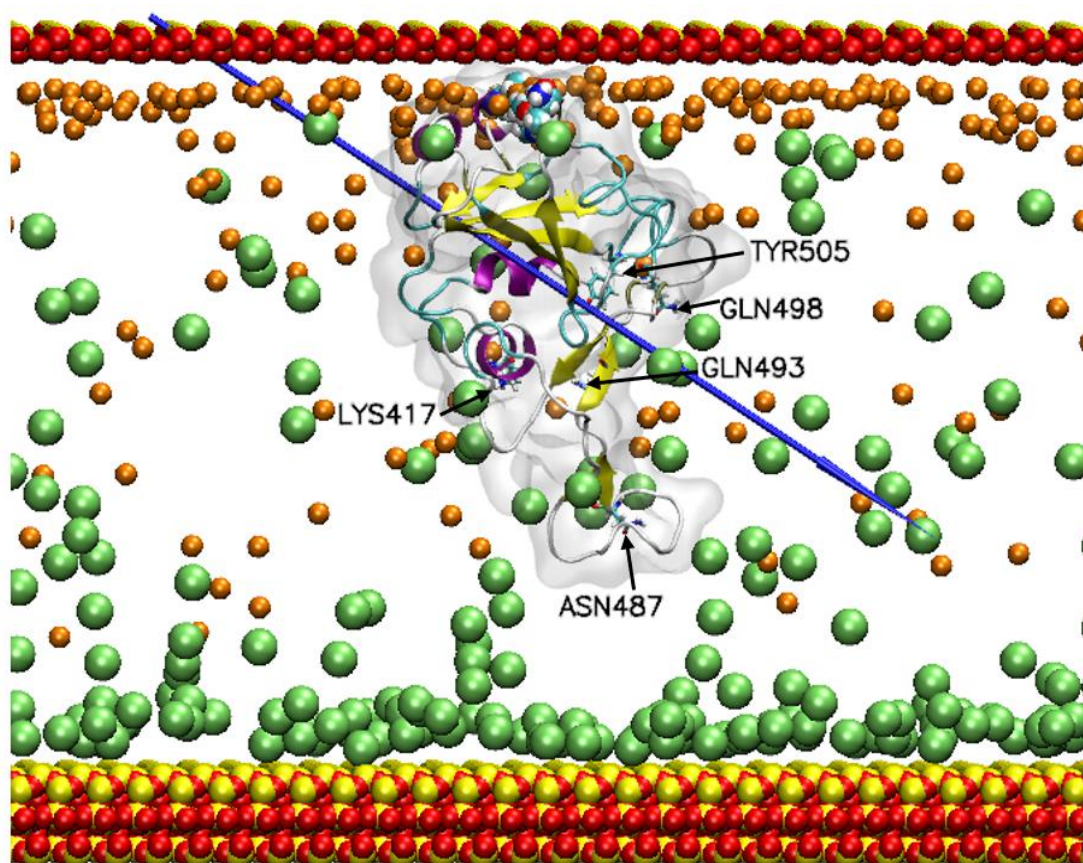
There seems to be a cluster of residues that are always present at the surface ion/water layer and the Thr 333 (neutral, hydrophilic) residue seems to form the strongest anchors to the surface for the duration of the simulation. Adsorption seems to be driven by hydrophilic/hydrophobic residues as opposed to charged residues, this results in non-specific movement of the protein, and when adsorption is achieved, it is weaker (Liamas *et al.*, 2018), which is why the residues desorb easily. The simulation events are consistent with the RMSD, which increases to  $\sim 3.7$  Å (**Figure 5.6a**) at 63ns, indicating the movements of the protein up to that point are unstable when compared with the starting point, and the RMSD increases steadily as the simulation progresses.



**Figure 5.7:** The S1 subunit shown as a ghost representation, and the positively charged hydrophilic lysine and arginine residues are shown as blue VdW representation. The ACE2 binding residues are shown as orange VdW representation. The red needle indicates the dipole moment, and water molecules are not shown for clarity.

All of the residues directed towards the surface are neutral, and the positive arginine and lysine residues, which would be expected to drive adsorption on negative surfaces are concentrated in the centre of the protein (**Figure 5.7**). The protein also has a hydrophilic core, and the surrounding sides seem to be soft and flexible with hydrophobic residues, with an irregular distribution of charged residues resulting in regions with varying partial charges. This is also an explanation for adsorption in the absence of positive residues, as the differently charged regions of the protein will interact with the target surfaces accordingly, resulting in a variety of conformations on adsorption. Furthermore, due to the electric field, positively charged residues are attracted towards the negative surface, and negatively charged residues are attracted towards the positive surface. Therefore, the protein may unfold when present in a strong field, as the strong opposing forces pull on the positive and negative residues. The atoms in the silica surfaces are also densely packed, and both the anchoring residues and ions are present at well-defined distances from the surface, which is

determined from the VdW volume of the atoms. The aforementioned observations also confirm electrostatic forces are the main driving force behind adsorption on the silica surfaces, as any adsorption of the protein is driven by the rapid movement of the residues. The protein remains close to the surface, and the Val 367 (neutral, hydrophobic) residue adsorbs to the surface at 75.6ns. The Thr 333 (neutral, hydrophilic) residue desorbs for the first time, along with the Asp 389 (negative, hydrophilic) and Val 362 (neutral, hydrophobic) residues.



**Figure 5.8:** Adsorption of the S1 subunit on oxygen rich surface. The protein colour scheme is same as Figure 5.2, and the outer layer of oxygen atoms in the silica model surface is shown as red spheres.  $\text{Cl}^-$  ions are shown as lime VdW spheres, and  $\text{Na}^+$  as orange. The adsorbing residues are also shown as VdW representation, and the ACE2 adsorbing residues are indicated by the black arrows. The blue needle indicates the dipole moment, and water molecules are not shown for clarity.

Generally, there is periodic interaction of the residues with the surface, and mostly the protein diffuses at the ion/water layer. The Thr 333 (neutral, hydrophilic) residue always maintains strong interactions with the surface, and the dipole moment is aligned towards the positive surface in this simulation. This indicates the adsorption events are driven by the electric field of the system, even though the protein seems to be influenced by other forces at times. In the final stable adsorption state after 100ns, the Thr 333 (neutral, hydrophilic), Val 362 (neutral, hydrophobic), and Val 367 (neutral, hydrophobic) residues are adsorbed to the surface (**Figure 5.8**). This also demonstrates adsorption to the siloxide-rich silica surface, as found experimentally (Patwardhan *et al.*, 2012). The tagless protein RMSD (**Figure 5.6a**) indicates the protein is the most stable in the first 50ns of simulation.

The RMSF is higher in the latter regions of the protein (**Figure 5.6b**), which is to be expected as that is where the ACE2 binding residues are located, and they would be expected to have higher conformational flexibility. For the adsorbing residues, the Thr 333 (neutral, hydrophilic) and Val 362 (neutral, hydrophobic) residues have values of  $\sim 3$  Å, and the Val 367 (neutral, hydrophobic) residue is  $\sim 4$  Å (**Figure 5.6b**). The adsorbing residues in this simulation are therefore not as conformationally flexible, indicating low affinity for the surface, this is also evidenced by the dipole moment of the tagless protein in simulation, which is aligned in the opposite direction, and wanting to pull the protein away from the surface. The ACE2 binding residues have RMSF values of  $\sim 3$  Å for the Lys 417 (positive, hydrophilic) residue,  $\sim 10$  Å for the Asn 487 (neutral, hydrophilic) residue,  $\sim 1.2$  Å for the Gln 493 (neutral, hydrophilic) residue,  $\sim 2$  Å for the Gln 498 (neutral, hydrophilic) residue and  $\sim 5$  Å for the Tyr 505 (neutral, hydrophilic) residue, indicating the Asn 487 (neutral, hydrophilic) residue is the most flexible in this simulation. Generally, the ACE2 binding residues seem to display higher conformational flexibility in the water simulation, when compared with the adsorption simulation of the protein on the negative silica surface (**Figure 5.4b**).

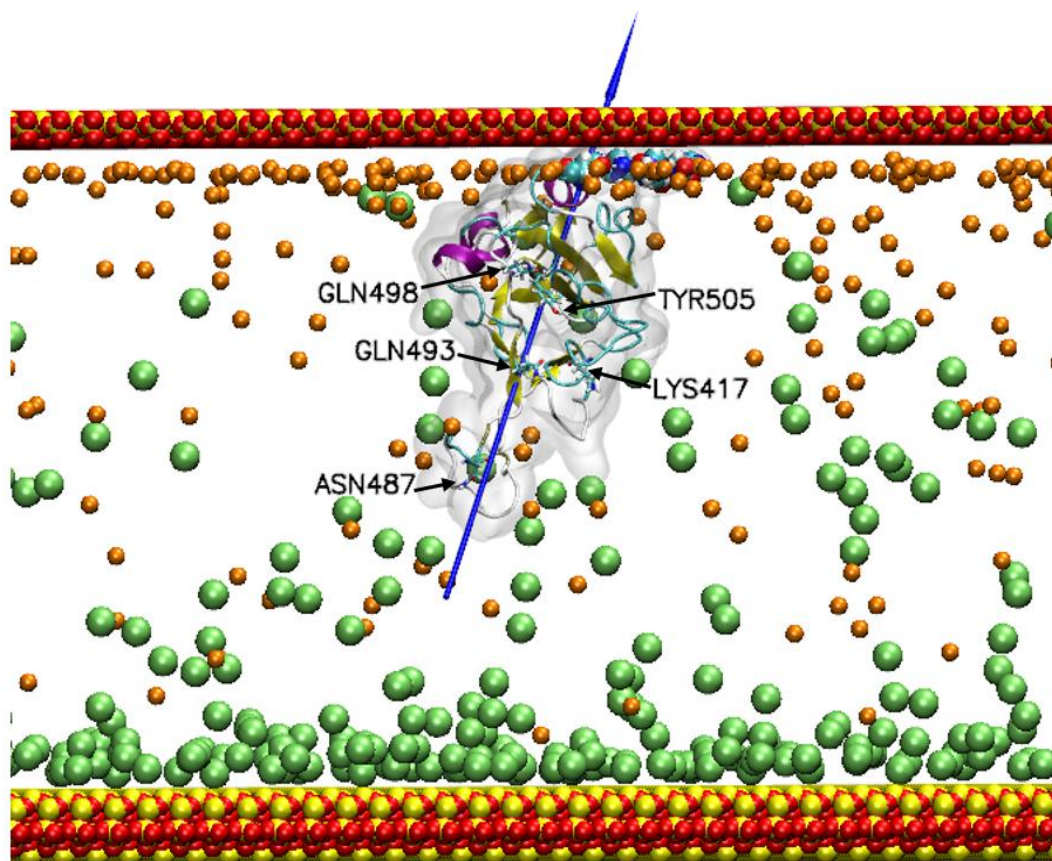
#### Tagged Protein Simulation on Negatively Charged Silica Surface

The two statistically independent trajectories obtained displayed similar, general behaviour of the protein described here, and identical to the tagless protein, the tagged

protein was placed on a side-on conformation, in the centre of the system to allow it to freely diffuse towards whichever surface. As the protein is overall positively charged, adsorption on the negative siloxide surface would be expected, and in the first few nanoseconds of simulation, the His-Tag on the C terminus of the protein flexes increasingly, and seems to cause the overall vigorous movements of the protein. This also corresponds to the higher RMSD of  $\sim 2.5$  Å (**Figure 5.6a**) when compared to  $\sim 1.3$  Å for the tagless protein. The Gly 504 (neutral, hydrophilic), residue starts moving towards the oxygen terminated siloxide surface at 12.6ns, and at 17ns, the protein freely diffuses, with the Thr 500 (neutral, hydrophilic) residue leading the protein. Interestingly, the Thr 500 (neutral, hydrophilic) residue was on the opposite side in the tagless protein simulation. The direction in which the protein moves changes, and this seems to be influenced by the His-Tag, as the vigorous movements of the His-Tag seem to drag the protein C terminus end to the opposite side. The RMSD increases, indicating a decrease in stability of the protein at this point in simulation. The protein diffuses in the bulk solution, and at 23.8ns, the Thr 500 (neutral, hydrophilic) residue this time descends, and the protein as a whole changes direction in which it moves. The His-Tag, which is very flexible in its movements, drags the protein, and leads the protein for adsorption on the negative siloxide surface. The Hsp 531 (positive, hydrophilic) side chain is the specific residue leading the charge.

The protein diffuses and gets close enough to the surface once it feels the electric field, there is rapid penetration of the water/ion layer and the first anchoring event occurs at 43.9ns by the Hsp 531 (positive, hydrophilic) residue. The Hsp 531 residue is joined by the Asn 370 (neutral, hydrophilic) and Hsp 529 residues at the ion/water layer. There is further adsorption of the Asn 370 (neutral, hydrophilic) residue at 48.6ns, and the Hsp 527 and Hsp 530 residues at 50.4ns. The RMSD for the tagged protein overlaps with the tagless protein until 63ns, averaging at  $\sim 3.3$  Å, indicating both proteins have a similar stability at this point. In the final stable adsorption state, the Hsp 530 (Hsp 531, Hsp 532) and Asn 370 (**Figure 5.9**) residues are adsorbed to the surface. The tagged protein seems to be less stable in this simulation when compared with the water simulation (**Figure 5.4a**) and tagless protein adsorbed to the negative surface (**Figure 5.6a**), this could be attributed to the positive His-Tag attraction to the

negative surface, which influences its aggressive movements. The adsorbing residues are followed by other His-Tag residues, Hsp 526 - 528, which do not interact with the surface, but interestingly, are there to support the adsorption of the other residues. Adsorption is driven by the positively charged His-Tag and the overall positive charge on the protein, as opposed to individually positively charged residues, which are concentrated in the centre of the protein (**Figure 5.7**).



**Figure 5.9:** Adsorption of His-Tag modified S1 subunit on oxygen rich silica surface. The colour scheme is same as Figure 5.8.

The RMSD for the tagged protein is  $\sim 3.5$  Å (**Figure 5.6a**) towards the end of simulation, indicating the protein is overall less stable compared to the tagless protein. The higher RMSD for the tagged protein is down to the vigorous movements of the His-Tag, which is the main difference between the movement of both proteins. During the course of this simulation, the dipole moment is aligned from the positive surface



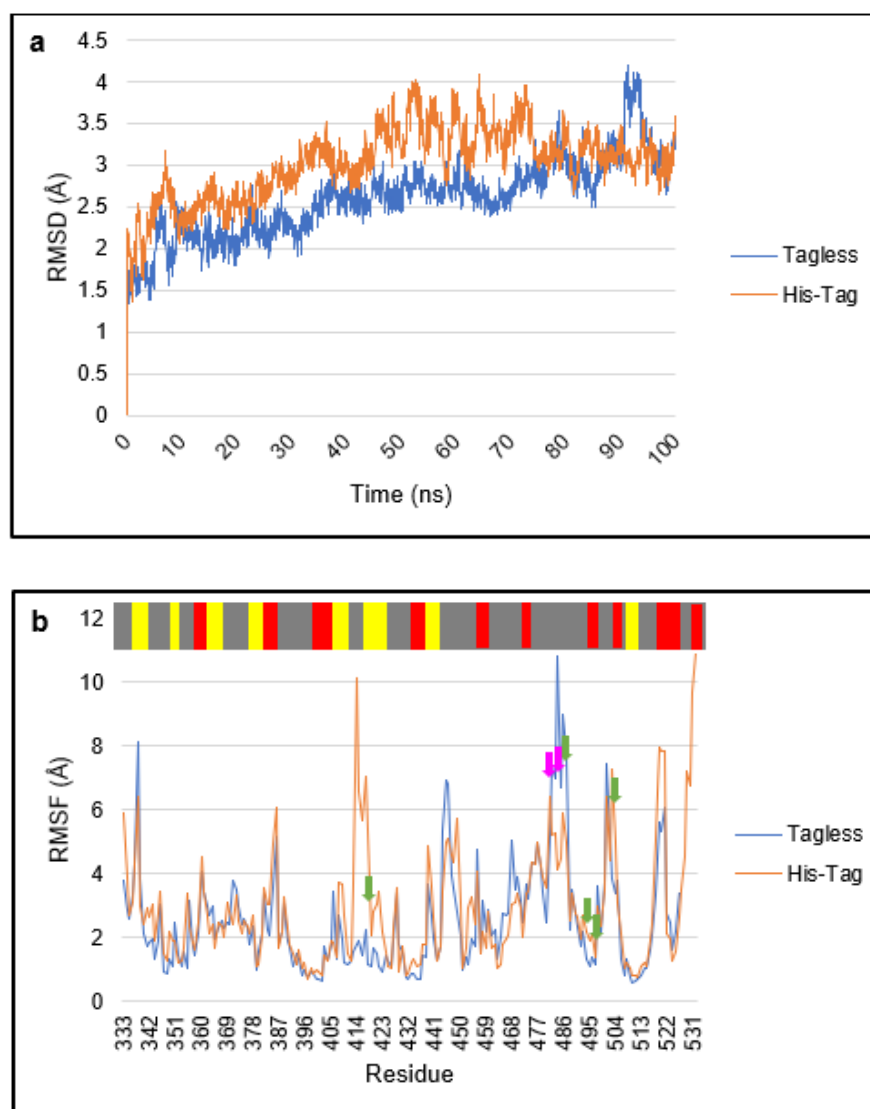
to negative surface, which is what would be expected, and is further evidence of protein affinity for the surface in this simulation. However, the dipole moment is relatively large, indicating that the His-Tag is expected to lead adsorption on this surface, which could be attributed to the large differences in partial charge between the negative surface and positive tagged protein.

The RMSF for the tagged protein is  $\sim 3$  Å for Asn 370, and  $\sim 24$  Å for Hsp 530, Hsp 531, and Hsp 532 (**Figure 5.6b**). The much higher RMSF when compared to the simulation in water (**Figure 5.4b**) would be expected as the tagged region flexes much more and displays higher conformational flexibility. The ACE2 binding residues have an RMSF of  $\sim 3$  Å for the Lys 417 (positive, hydrophilic) residue,  $\sim 5$  Å for the Asn 487 (neutral, hydrophilic) residue,  $\sim 2.5$  Å for the Gln 493 (neutral, hydrophilic) residue,  $\sim 7$  Å for the Gln 498 (neutral, hydrophilic) residue and  $\sim 8$  Å for the Tyr 505 (neutral, hydrophilic) residue, indicating the ACE2 binding residues overall have higher conformational flexibility in simulation when compared with the tagless protein (**Figure 5.6b**), which is a result of the more varied movements of the protein influenced by the His-Tag. Furthermore, the RMSF is higher for these regions of the proteins than in simulation in water (**Figure 5.4b**), indicating the difference a charged surface makes.

#### Tagless Protein Simulation on Positively Charged Silica Surface

The two statistically independent trajectories obtained displayed similar, general behaviour of the protein described here. Due to the polarising effect created by the charged surfaces, the  $\text{Na}^+$  and  $\text{Cl}^-$  ions were again driven to shield the oppositely charged surfaces, this also partially screens the force field beyond the Debye length. During the early stages of simulation, the protein rotates along its long axis to align its dipole moment in parallel with the electric field imposed by the charged surfaces. This, coupled with the overall negative charge on the tagless protein, drives the protein towards the positively charged silicon undercoordinated surface. The RMSD for the tagless protein is lower than that in the siloxide surface simulation,  $\sim 1.1$  Å, indicating better initial stability of the protein in this system. The first anchoring event is visible with the Glu 484 (negative, hydrophilic) residue, which adsorbs to the surface at 59ns.

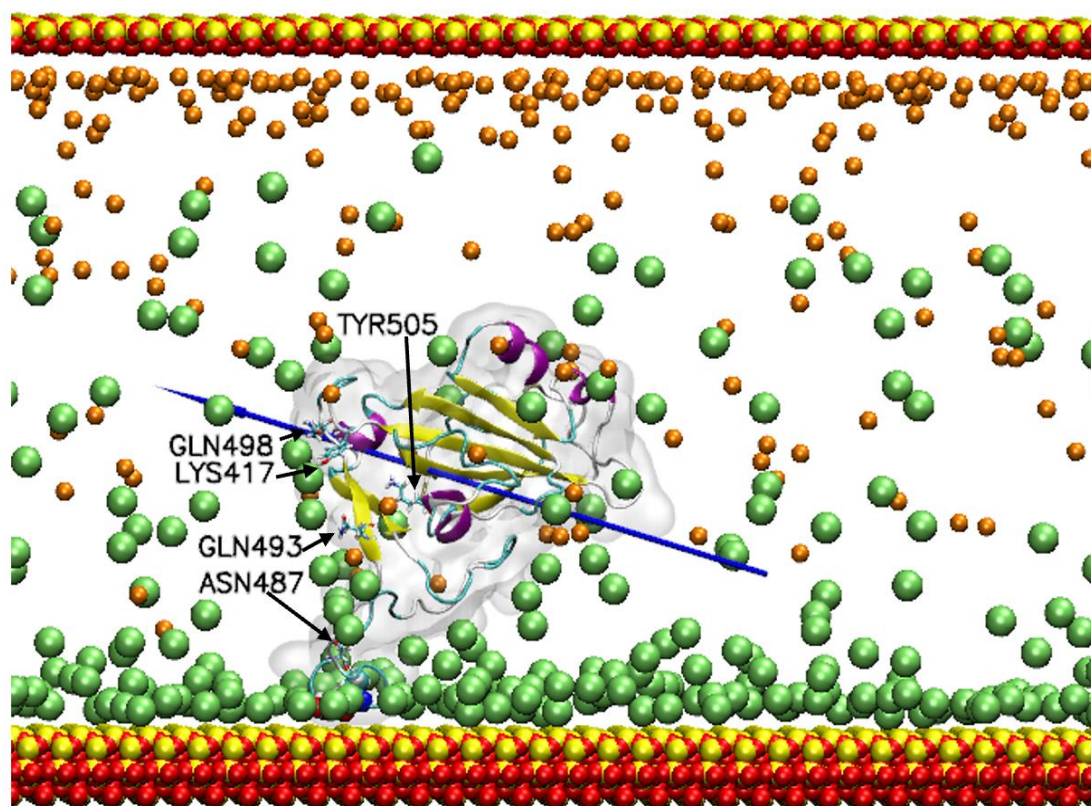
Interestingly, this first adsorption event of negative protein on positive silica surface occurs much later than it does on the negative siloxide surface. This is contrary to what would be expected, and highlights the importance of other factors such as shielding ions and the bulk system solution in driving adsorption. The RMSD increases to  $\sim 3$  Å at 61ns, pointing to the reduced stability of the protein in this conformation on the positive surface when compared to the water simulation (**Figure 5.4a**), and indicating a greater change in the protein structure upon adsorption. However, the protein seems to be more stable when compared to the simulation on the negative surface (**Figure 5.6a**). The shift in RMSD may also correspond to the adsorption of the Val 483 (neutral, hydrophobic) residue at 65ns in the same module, indicating a small adjustment of the structure, and then stabilisation of the protein as the RMSD decreases until 69ns (**Figure 5.10a**). The Glu 484 (negative, hydrophilic) residue has a stronger binding preference than the Val 483 (neutral, hydrophobic) residue, which is to be expected as negative residues will naturally attract to oppositely charged surfaces. The Val 483 (neutral, hydrophobic) and Glu 484 (negative, hydrophilic) residues desorb at 77ns, and the protein remains at the interface, interacting with the ion/water layer. The Glu 484 (negative, hydrophilic) residue re-adsorbs at 84ns, corresponding to an increase in RMSD up to  $\sim 3.5$  Å, and the protein seems particularly unstable when the Glu 484 (negative, hydrophilic) residue adsorbs.



**Figure 5.10:** The a) RMSD, b) RMSF of S protein RBD and tagged-S Protein RBD in the silica undercoordinated surface simulations. The colour scheme is the same as Figure 5.6.

The Val 483 (neutral, hydrophobic) residue also readsorbs at 88ns. The Glu and Val residues are consistently present at the interface, interacting with the ion/water layers and driving interactions with the surface. The Thr 478 (neutral, hydrophilic) residue adsorbs and desorbs at 95ns, this flash adsorption event corresponds to the RMSD observation that while the tagless protein RMSD was lower than the tagged protein for

the duration of simulation, it suddenly increases to  $\sim 4.1$  Å at 95ns. The RMSD then decreases, and both protein's RMSD overlap (**Figure 5.10a**) in the closing stages.



**Figure 5.11:** Adsorption of the S1 subunit on the silicon rich silica surface. The colour scheme is same as Figure 5.8.

At the end of the 100ns simulation, two residues adsorb to the surface: Glu 484 (negative, hydrophilic) and Val 483 (neutral, hydrophobic) (**Figure 5.11**). However, these residues adsorbed intermittently and this is not a stable adsorption, indicating a reluctance of the protein to adsorb to the positive surface when compared to the negative surface. The dipole moment of the tagless protein in simulation is also aligned in the opposite direction to the surface it adsorbed to, contrary to what would be expected, and shows the protein tends away from the surface. The RMSF (**Figure 5.10b**) for the adsorbing residues, Val 483 (neutral, hydrophobic) and Glu 484 (negative, hydrophilic) is  $\sim 7$  Å. The ACE2 binding residues have RMSF values of  $\sim 2$

Å for the Lys 417 (positive, hydrophilic) residue, ~11 Å for the Asn 487 (neutral, hydrophilic) residue, ~1 Å for the Gln 493 (neutral, hydrophilic) residue, ~6 Å for the Gln 498 (neutral, hydrophilic) residue and ~7 Å for the Tyr 505 (neutral, hydrophilic) residue, indicating the ACE2 binding residues overall have lower conformational flexibility when compared to simulation in water (**Figure 5.4b**), which may be explained by the overall movements of the protein in this simulation on the positive surface, which seem to be more reserved.

Although the protein adsorbs, this is not a representative model to guide development of new therapeutics as the protein tends to orient itself away from the surface, as indicated by the dipole moment and the observation that only the anchoring residues remain adsorbed in the final state. There do not seem to be any other residues showing a tendency to interact with the surface, which could be attributed to a strongly bound layer of water molecules on the undercoordinated-silicon silica surface, a layer which cannot be penetrated by every residue. The ACE2 binding residues are accessible from the side, except for the Asn 487 (neutral, hydrophilic) residue, which is sterically blocked. Furthermore, experimentally, most NPs are negatively charged, so even if all the ACE2 binding residues were free, this model is not an accurate representation of experiment. Nevertheless, these results indicate the possibility of such an adsorption.

#### Tagged Protein Simulation on Positively Charged Silica Surface

The two statistically independent trajectories obtained displayed similar, general behaviour of the protein described here. The tagged protein was positioned closer to the silicon undercoordinated surface, and rotated to move the His-Tag end towards the positive surface to encourage adsorption. The RMSD of ~2.1 Å is lower than that observed in the siloxide simulation (**Figure 5.10a**). The protein initially diffuses towards the undercoordinated silicon surface in the first stages of simulation, and at 33.5ns, the protein rotates and the His-Tag end shifts to the opposite side. The protein remains in the centre of the system and does not gravitate towards any one surface, this behaviour of the tagged protein is to be expected, as the positive His-Tag would naturally repel a positive surface, and it shows no affinity for the positive surface as the His-Tag, which would be readily attracted to negative surfaces, was placed on the

opposite end. The protein continues to diffuse freely, and at 57.2ns, rotates and turns on its side the other way, this event corresponds to an RMSD increase to  $\sim 4$  Å firstly at 57.2ns, and then at 76.8ns (**Figure 5.10a**), indicating lower stability of the protein at this stage in simulation. The protein seems to retain an RMSD similar or less stable than that in simulation in water (**Figure 5.4a**).

The RMSD for the tagged protein steadily decreases as the RMSD for the tagless protein increases, until they overlap, briefly separating at 85ns and the tagged protein is overall less stable than the tagless protein (**Figure 5.10a**). The RMSDs for the tagged protein on the negative and positive silica surfaces (**Figure 5.6a, Figure 5.10a**) are identical, indicating the His-Tag drives protein movements by vigorous movement in both simulations. After a 100ns trajectory, the protein is hovering in the centre. The RMSF data (**Figure 5.10b**) could be explained by the movement and flexing of the His-Tag observed in simulation. There are no adsorbing residues in this simulation, and the ACE2 binding residues have values of  $\sim 7$  Å for the Lys 417 (positive, hydrophilic) residue,  $\sim 3$  Å for the Asn 487 (neutral, hydrophilic) residue,  $\sim 2$  Å for the Gln 493 (neutral, hydrophilic) residue,  $\sim 3$  Å for the Gln 498 (neutral, hydrophilic) residue and  $\sim 5$  Å for the Tyr 505 (neutral, hydrophilic) residue, indicating the ACE2 binding residues have overall low conformational flexibility when compared to simulation of the protein in water and simulation of the tagged protein on the negative silica siloxide surface (**Figure 5.4b, Figure 5.6b**). This could also be attributed to the excessive flexing of the His-Tag, which although there is no adsorption of the tagged protein on the silicon undercoordinated surface, seems to be leading the protein movements, and the N terminus side of the protein with the ACE2 binding residues movement was much slower in comparison. As mentioned previously, the simulations on the silicon undercoordinated surface are not a representative model, so seeking protein adsorption on negative surfaces is a better model for experimental purposes.

The tagless protein adsorption to the positive surface could be due to two reasons. Firstly, the tagless protein was placed slightly closer to the surface at the initial configuration, therefore, it was easier to reach the surface. Secondly, the overall charge of the tagless protein is  $-2e$  whereas the tagged protein is  $+1e$ . A negatively charged protein will readily attract to a positive surface, although the tagless protein residues

that adsorbed are not negatively charged, further highlighting the role of overall protein charge or the presence of positive patches on the protein, to adsorption.

#### Tagless Protein Simulation on COOH SAMs Terminated Negatively Charged Silica Surface

The three statistically independent trajectories obtained displayed similar, general behaviour of the protein described here. The tagless protein was placed in the middle of the system, and despite the overall negative charge of the protein, it is hoped it can adsorb to the negative surface through the influence of partial charges on different residues. As with previous simulations, the concentration of NaCl was high enough to shield the surfaces, to attempt to facilitate adsorption, otherwise, the negative tagless protein would repel the negative surface. The protein diffuses freely and in the early stages of simulation, undergoes Brownian motion, slowly moving down and flexing above the surface. The RMSD increases from  $\sim 1$  Å (**Figure 5.12a**) to  $\sim 1.3$  Å at this point. The Gly 476 (neutral, hydrophilic) residue moves towards the surface at 11.08 ns, the Phe 486 (neutral, hydrophobic), Glu 484 (negative, hydrophilic) and Asn 487 (neutral, hydrophilic) residues, which are part of a combined cluster, move down towards the surface. The protein continues to diffuse just above the surface, and at 40.92 ns, this cluster region moves further down and at this point, it almost seems separate from the rest of the protein. The RMSD is identical at this point to the simulation of the protein in water (**Figure 5.4a**), which is understandable as the protein has not interacted with the surface at this stage. The protein movements just above the surface continue, and at 85.84 ns, the Ser 477 (neutral, hydrophilic) residue attempts adsorption to the surface via its side chain, followed closely by the Thr 478 (neutral, hydrophilic) residue. The RMSD (**Figure 5.12a**) is higher than the tagged protein after 50 ns, indicating the protein structure was more stable during the first 50 ns of simulation. It is however identical to the simulation in water (**Figure 5.4a**) for the duration of simulation, and in the simulation trajectory the protein is identical in its movements for both simulations. The trajectory was initially computed for 100 ns as with other simulations, and upon completion of 100 ns in this simulation, no adsorption of the protein was observed. The simulation was extended for another 100 ns, to see if the protein would adsorb, as it got very close to the surface within the 100 ns timescale.

The protein does not adsorb until 145.08 ns, when the first anchoring event occurs when the Gly 476 (neutral, hydrophilic) and Ala 475 (neutral, hydrophobic) residues adsorb to the surface. The adsorption of the residues does not seem strong or stable, as the protein movements are more vigorous than before and it looks to pull away. The weak adsorption is further evidenced by desorption of the protein at 161.24 ns, with the protein diffusing to just above surface once again. The N terminus side of the protein, with the ACE2 binding residues, is oriented towards the surface, and if a strong and stable adsorption to the surface was achieved, these residues would be blocked, rendering this model useless for our purposes.

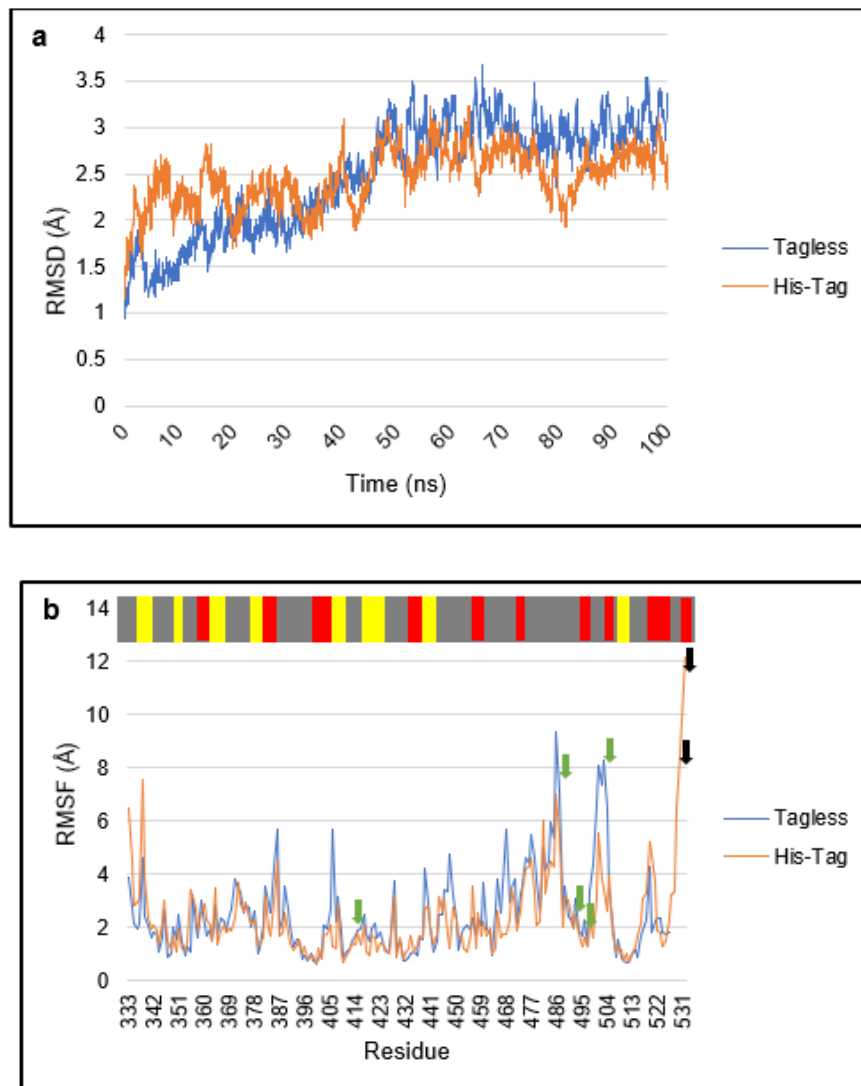
The tagless protein adsorbed in a stable state to the negative siloxide and positive silicon undercoordinated silica surfaces in a 100 ns timescale, only slightly diffusing on the surface. However, the tagless protein did not adsorb in a stable state to the SAMs terminated silica surface, only diffusing above the surface for most of the 200 ns trajectory. There is a reluctance of the protein to adsorb to the SAMs surface, and out of all the trajectories computed, 30% showed any kind of adsorption behaviour of the protein, when compared with 50% for the other silica surfaces. These observations further highlight the protein needs a His-Tag, which almost acts like a spacer arm, to adsorb to the SAMs terminated surface.

The RMSF (**Figure 5.12b**) for the briefly adsorbing residues, Ala 475 (neutral, hydrophobic) and Gly 476 (neutral, hydrophilic) is  $\sim 4$  Å. The RMSF for the ACE2 binding residues is  $\sim 1.8$  Å for the Lys 417 (positive, hydrophilic) residue,  $\sim 6.2$  Å for the Asn 487 (neutral, hydrophilic) residue,  $\sim 2$  Å for the Gln 493 (neutral, hydrophilic) residue,  $\sim 3.2$  Å for the Gln 498 (neutral, hydrophilic) residue and  $\sim 2$  Å for the Tyr 505 (neutral, hydrophilic) residue, indicating the ACE2 binding residues overall have low conformational flexibility in this simulation when compared to the tagless protein simulation in water (**Figure 5.4b**). These regions of the protein also seem to display lower conformational flexibility when compared to the silica surface simulations (**Figure 5.6b**, **Figure 5.10b**), this is another indication of the reluctance of the protein to adsorb, and consequently be utilised on the SAMs terminated surface.



### Tagged Protein Simulation on COOH SAMs Terminated Negatively Charged Silica Surface

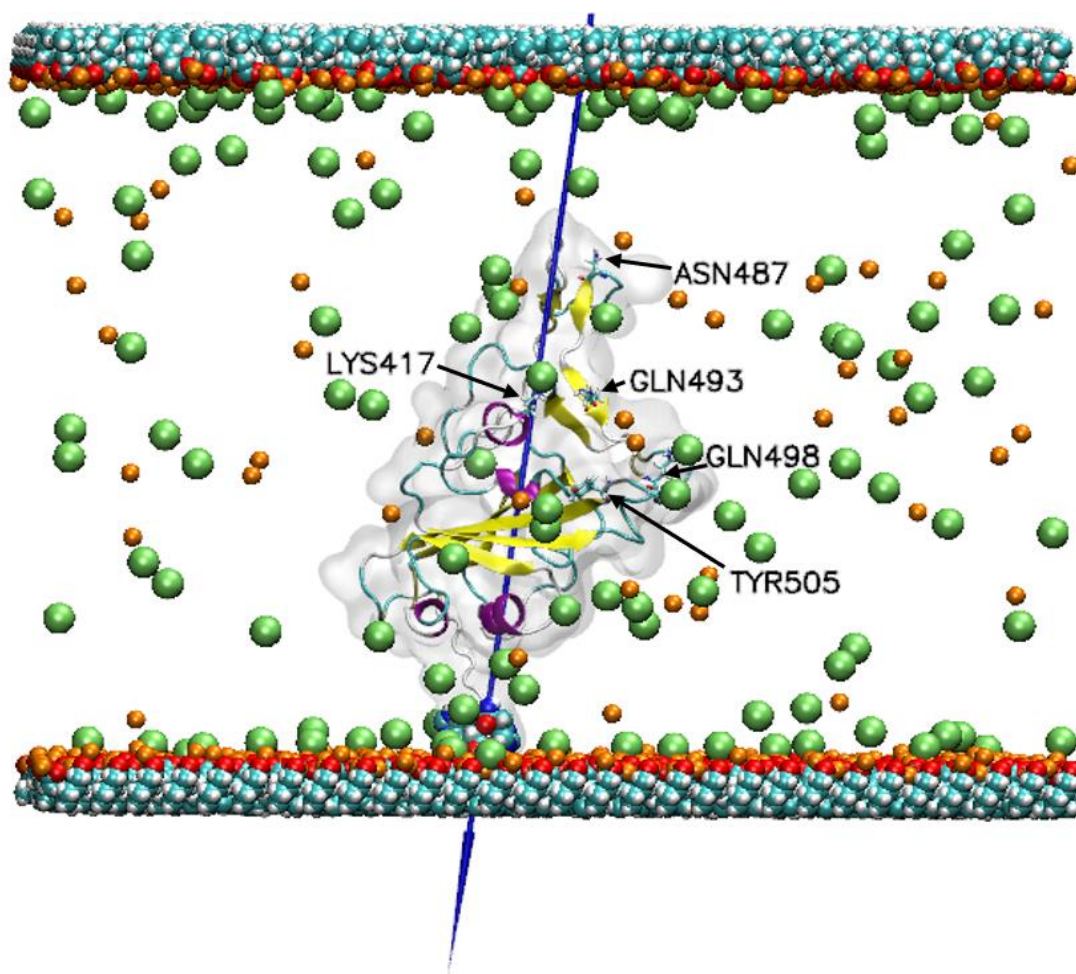
The three statistically independent trajectories obtained displayed similar, general behaviour of the protein described here. The tagged protein, which is overall positively charged, was placed in a side-on starting conformation, with the His-Tag facing the bottom negative surface. The RMSD is  $\sim 1.5$  Å (**Figure 5.12a**), indicating good initial stability, and there is flexing of the protein until 5.84ns, when the His-Tag reaches out for the surface at 7.28ns, driven by the Hsp 532 residue. The RMSD steadily increases at this point, up to 10ns, indicating instability of the protein as it intensifies in its movements.



**Figure 5.12:** The a) RMSD, b) RMSF of S protein RBD and His-Tag S Protein RBD in the SAMs terminated silica surface simulations. The colour scheme is the same as Figure 5.6.

The protein diffuses and slowly moves towards the negative surface, and the Hsp 532 residue adsorbs to the bottom surface, in the first anchoring event at 19.56 ns. The observation is consistent with a decrease in the RMSD, indicating good stability of the protein in this conformation, the RMSD is also identical to the protein in water (**Figure 5.4a**), indicating good stability on adsorption. Furthermore, even though the adsorption of positive residue on a negative surface is to be expected, the first

anchoring event occurs early in the simulation, earlier than the adsorption of the tagged protein on the silica siloxide surface, this indicates higher affinity of the tagged protein for the SAMs terminated surface, even though both surfaces are negative. The Hsp 531 residue also displays a particular tendency to move towards the negative surface, and adsorbs to the surface at 27.68ns. Interestingly, only two of the six His-Tag residues, Hsp 531 (and Hsp 532) adsorb to the surface and the other four His-Tag residues do not adsorb or tend towards the surface, and they are there to strengthen the adsorption of the others by providing a backbone. The protein freely diffuses on the surface, and at 38.08ns, the Hsp 532 residue desorbs, re-adsorbing at 47.12ns, and from that point, the Hsp 531 and Hsp 532 residues are present at the interface, leading the protein interactions with the surface. Protein adsorption seems easier on the SAMs surface than the pure silica surface, as the flexible SAMs molecules allow for easier adsorption. The protein is stable (**Figure 5.12a**), in this adsorbed state over the 100ns timescale, only freely diffusing on the surface. The ACE2 binding residues are also exposed to the bulk water in this simulation (**Figure 5.13**), indicating this model is a good representation in driving experimental integration of the protein in new therapeutics.



**Figure 5.13:** Adsorption of His-Tag modified S1 subunit on COOH terminated silica surface. The colour scheme is same as Figure 5.8.

After adsorption on the silica surfaces, the protein maintained good mobility, freely diffusing on the surface. However, despite a general diffusion of the protein, the anchoring residues in the SAMs terminated surface simulations were immobilised upon adsorption of the tagged protein. The lack of rigidity of the substrate in the SAMs surface has a role to play, as unlike the silica surface, where the atoms are fixed in space, the molecules that make up the SAMs terminated surface possess a degree of freedom. The SAMs terminated surface can therefore be considered as a ‘soft’ surface, which allows the anchoring residues to penetrate the SAMs molecules, create more bonds and inhibit their surface movement.

The increased mobility of the SAMs surfaces also allows the ions, water molecules and the anchoring residues to penetrate through the SAMs molecules. The immobility of the anchoring residues is further enhanced by the higher negative charge of the SAMs terminated surfaces as opposed to the silica surface, as when the residues are in contact with the charged SAMs surface, they develop an enhanced interaction that constrains their mobility. Furthermore, the SAMs surface has a combined layer of ions and water molecules strongly bound to the charged underlying substrate, and to anchor successfully, the residue has to compete with the water molecules and ions for the available free volume.

The greater charge of the SAMs surfaces also means the bound layer adsorbed more strongly to the substrate, and it was therefore difficult for the anchoring residues to initially replace some of the bound species and occupy a space on the surface. However, once this was done, it resulted in a smaller distance between the anchoring residue and the charged functional groups on the SAMs surface. This also gave stronger adhesion, reducing the mobility of the anchoring residue, and this phenomenon has also been observed previously (Liamas *et al.*, 2018). The extra ions in the SAMs systems could further strengthen the combined layer consisting of water molecules and ions bound on the surface substrate, which significantly reduces the possibility of further residues to adsorb. This is also an explanation for the adsorption of two residues and not more to the surface, as the barrier became very inaccessible as the simulation progressed, and the non-specific, slower movement of the protein fragment further prevented any subsequent adsorption.

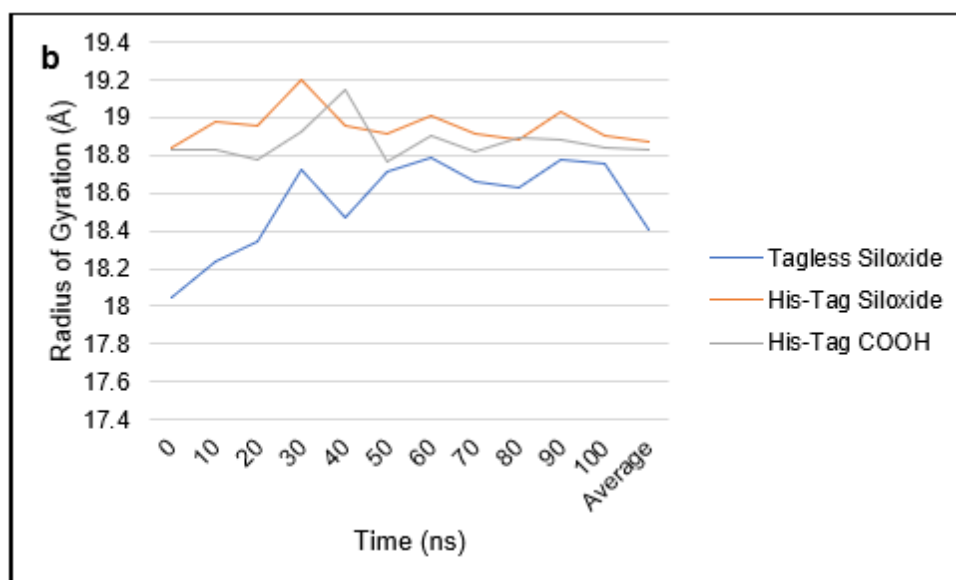
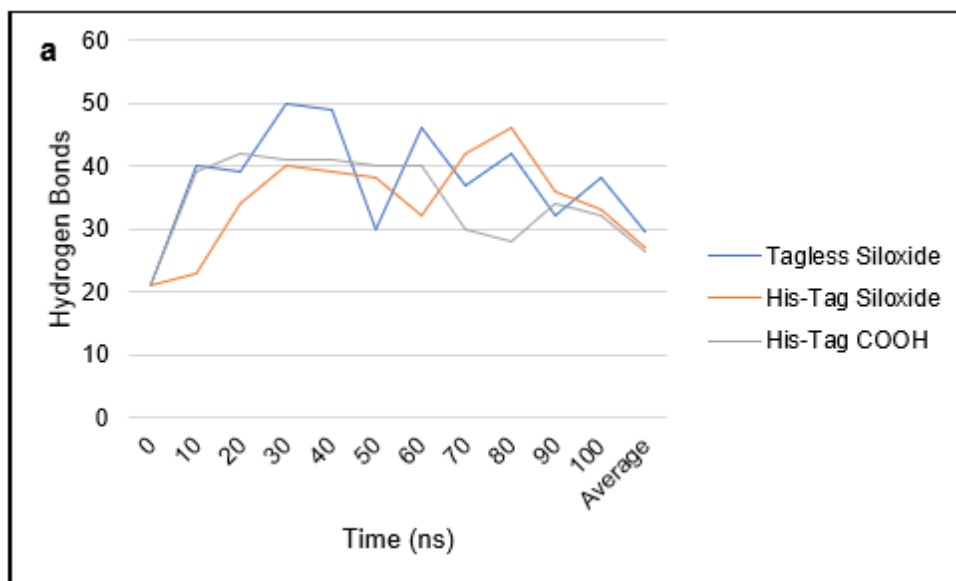
The RMSF (**Figure 5.12b**) is  $\sim 12$  Å for the His-Tag binding residues, indicating great flexibility of this region of the protein during simulation, this is consistent with observations from the trajectory. The ACE2 binding residues have RMSF values of  $\sim 1.7$  Å for the Lys 417 (positive, hydrophilic) residue,  $\sim 4.3$  Å for the Asn 487 (neutral, hydrophilic) residue,  $\sim 1.4$  Å for the Gln 493 (neutral, hydrophilic) residue,  $\sim 2.3$  Å for the Gln 498 (neutral, hydrophilic) residue and  $\sim 1$  Å for the Tyr 505 (neutral, hydrophilic) residue, indicating the ACE2 binding residues overall have low conformational flexibility in this simulation when compared to the protein in water (**Figure 5.4b**), even though all the ACE2 binding residues are free to bind to the ACE2

receptor. The ACE2 binding residues seem to have lower conformational flexibility in this simulation when compared to adsorption of the tagged protein on the silica siloxide surface (**Figure 5.6b**). This could be explained by the more vigorous movements of the protein, driven by the His-Tag on the siloxide surface, this is despite both surfaces being negative. This also highlights a general reluctance of the protein to adsorb to the SAMs terminated surface as even though the first anchoring event occurs earlier than adsorption on the siloxide surface, the Hsp 532 residue does desorb and re-adsorb, compared to consistent adsorption on the silica siloxide surface. The His-Tag has a significantly higher RMSF in adsorption of the tagged protein on the silica siloxide surface (**Figure 5.6b**) than it does for adsorption of the protein on the silica undercoordinated and SAMs terminated surfaces (**Figures 5.10b, Figure 5.12b**), this could again be explained by the much more vigorous movements of the His-Tag in simulation with the siloxide surface, where it reaches straight for the surface and adsorbs in a stable conformation. The movement of both the tagless and tagged proteins on the SAMs surface, when compared to the silica surfaces, is slower and the protein follows a non-specific trajectory, despite the adsorption of the tagged protein. The lack of adsorption of the tagless protein on the SAMs surface could also be influenced by the increased ion concentration, compared to the silica surface simulation. A higher concentration of ions slows down the rate of adsorption, providing the protein with more time to explore suitable adsorption positions, and in this simulation, it did not adsorb at all.

### **5.3.2. Further Discussion of Adsorption Simulations on Negative Surfaces**

The adsorption simulations on negative surfaces were further assessed for protein stability, and to establish their suitability in guiding the experimental work. The negative surface models were further analysed as they are realistic, and better representative of the protein binding to negative NPs experimentally. The following simulations were analysed: adsorption of the tagless protein on the siloxide surface, adsorption of the tagged protein on the siloxide surface and adsorption of the tagged protein on the COOH terminated surface. As established previously (see **Section 5.3.1**), the tagless protein did not adsorb on the SAMs surface in a stable state, even

though the simulation was extended for another 100ns, so that simulation is not considered here. A hydrogen bond is formed from an electrostatic attraction between a proton in one molecule, and an electronegative atom in the other (Vladilo and Hassanali, 2018, Herschlag and Pinney, 2018). Hydrogen bond formation between the protein itself is an important indicator for protein stability in simulation. The tagless protein, forms an average of ~29.5 (**Figure 5.14a**) intramolecular hydrogen bonds, in the adsorption simulation with the siloxide surface, and as the simulation progresses, the protein forms more hydrogen bonds and there are several fluctuations in the hydrogen bonding data, indicating the protein is more stable at some parts in the simulation than others. The protein forms over ~50 hydrogen bonds at 30ns (**Figure 5.14a**), at which point in the simulation trajectory, the protein is diffusing close to the surface, interacting with the ion/water layers at the interface. This observation is also particularly interesting as it shows protein stability is not always driven by adsorption, but sometimes by the residues interacting with the ion/water layers at the surface interface. The protein forms the most hydrogen bonds in this simulation, and this could also be attributed to the hydrophilic residues that are particularly active in this simulation. Hydrophilic residues are more hydrated than hydrophobic residues, and they will naturally form more hydrogen bonds.



**Figure 5.14:** The a) intramolecular Hydrogen Bonds, and b) Radius of Gyration every 10ns, and the average over 100ns for the tagless protein on siloxide silica surface, tagged protein siloxide silica surface and tagged protein COOH silica surface adsorption simulations.

The tagged protein forms an average of ~27 intramolecular hydrogen bonds in the siloxide surface simulation. As with the tagless protein on silica siloxide surface simulation, the hydrogen bonds formed between the protein increase as the simulation



progresses, and at 80ns, the protein forms ~46 hydrogen bonds (**Figure 5.14a**), at which point the His-Tag is adsorbed and the protein is diffusing on the surface, this peak could also correspond to the protein movements with the His-Tag, which is flexing and leading vigorous movements.

The tagged protein forms an average of ~26.5 intramolecular hydrogen bonds on adsorption to the SAMs surface, and as the simulation progresses, the number of hydrogen bonds it forms fluctuates greater than the other simulations (**Figure 5.14a**). The protein forms ~42 bonds at 20ns, which is the highest throughout the simulation, this observation corresponds to the absorption of the Hsp 532 residue on the surface. This means the protein is stable in this conformation, as the protein forms the most intramolecular hydrogen bonds at that point, and intramolecular hydrogen bonds are essential to the structure and stability of proteins. After this point, the hydrogen bonds formed decrease, indicating instability of the protein as the simulation progresses, the protein continues to diffuse on the surface in its adsorbed orientation, and 70ns onwards, the hydrogen bonds formed decrease further as the protein forms ~30 and ~28 hydrogen bonds at 70ns and 80ns.

The hydrogen bonding data for the adsorption simulations on negative surfaces concurs with the adsorbed residues in the final state (**Table 5.2**). The tagless siloxide and tagged SAMs simulations form the most hydrogen bonds, this is to be expected as both those simulations have more active hydrophilic residues when compared to the tagged siloxide simulation.

**Table 5.2:** A list of the adsorbed residues in the final adsorption state of each stable adsorption simulation on negative surfaces.

| <b>Simulation</b> | <b>Residues</b>                    |
|-------------------|------------------------------------|
| Tagless Siloxide  | Thr 333, Val 362, Val 367          |
| His-Tag Siloxide  | Hsp 530, Hsp 531, Hsp 532, Asn 370 |
| His-Tag COOH      | Hsp 531, Hsp 532                   |

The Radius of Gyration (RoG) is an imaginary distance from the axis of rotation to a point where the total mass of the body is concentrated, so the moment of inertia about the axis remains the same (ScienceTopia). In terms of proteins, this is the distribution

of atoms, which make up the mass body around its axis (Sneha and Doss, 2016). The RoG measures the compactness of a protein structure, and is an important measure to elucidate the stability of the protein in simulation along with the RMSD.  $\alpha$ -proteins, which are proteins with more  $\alpha$ -helices in their secondary structure, generally have higher RoG values, suggesting loose packing (Lobanov *et al.*, 2008). A lower RoG value corresponds to a shorter peptide chain and a more compact structure, this is commonly found in  $\beta$ -proteins, which have more  $\beta$ -sheets in their secondary structure (Lobanov *et al.*, 2008). The tagless protein siloxide surface simulation average RoG is  $\sim 18.4$  Å, and the protein is the most stable until 30 ns, when the RoG increases to  $\sim 18.7$  Å (**Figure 5.14b**). The increase could be attributed to the protein, which at this point in the trajectory, is fluctuating and may be relaxing. As the simulation progresses, the RoG further increases, and this data aligns with events observed in the trajectory at 60 ns, as the Phe 338 (neutral, hydrophobic) and Val 362 (neutral, hydrophobic) residues interact with the ion/water layers at the surface, causing changes in the protein structure. The protein maintains a RoG of  $\sim 18.7$  Å for the remainder of the simulation, and based on the average RoG, the protein structure seems to be the most compact from the three adsorption simulations on negative surfaces. The RoG data is also complemented by the RMSD data for this simulation (see **Figure 5.6a**), where the protein maintains an RMSD of  $\sim 2.4$  Å.

The tagged protein maintains a high RoG throughout the simulation in the silica siloxide surface simulation, with an average RoG of  $\sim 18.9$  Å. This fluctuates as the simulation progresses, and for the duration of simulation, the RoG remains higher than  $\sim 18.8$  Å. At 30 ns, there is a visibly higher RoG value of  $\sim 19.2$  Å, at which point in the simulation trajectory, the protein is close to the surface, and the His-Tag seems to be pulling the protein, which maybe an explanation for the higher RoG, as the protein unfolds. The RoG remains constant between  $\sim 18.8$ - $19$  Å for the remainder of the simulation, ending with an RoG of  $\sim 18.9$  Å, which is the highest from all simulations (**Figure 5.14b**). The RoG data also tells a different story about adsorption stability, indicating a decrease in protein structure compactness, while suggesting increased flexibility and unfolding of the protein. Therefore, the adsorbing residues (**Table 5.2**) are not as strongly bound to the surface, and they may desorb if the trajectory was to

be extended. The data are also consistent with the RMSD data for this simulation (see **Figure 5.6a**), where the protein maintains an RMSD of  $\sim 3.3$  Å throughout, which is a further indication of the protein modules changing their structure as the simulation progresses.

The tagged protein on the SAMs surface simulation has an average RoG of  $\sim 18.8$  Å. The highest RoG for this simulation is  $\sim 19$  Å at 40 ns. The RoG then decreases, and remains stable for the remainder of simulation, maintaining an average value of  $\sim 18.8$  Å (**Figure 5.14b**) and indicating good stability of the protein in its adsorbed state as the simulation progresses. The RoG data is similar to that of the tagged protein simulation on the siloxide surface, indicating the protein is more vigorous in its movements in these simulations than it is in the tagless protein simulation on the siloxide surface. The RoG data is further complemented by the RMSD data (see **Figure 5.12a**), which shows the protein maintains an RMSD of  $\sim 2.3$  Å during the course of simulation, and indicating good overall structural integrity.

#### **5.4. Conclusions**

This chapter assessed the behaviour of the S1 subunit of the SARS-CoV-2 S protein in simulation on different model surfaces, and to see what factors affect adsorption of the protein on the surface. In addition, the S1 subunit modified with a His-Tag was also simulated on the model surfaces to establish if the His-Tag had any effect on protein behaviour in simulation. Finally, the simulations were evaluated for protein adsorption, and whether the ACE2 binding residues were free, which will indicate the most suitable models to guide the experimental work. Analysis of the trajectories and the aforementioned data allows the following conclusions to be drawn:

- Simulations of the proteins with the negative silica siloxide surface showed anchoring for both tagged and tagless proteins was rapid and specific, and resulted in a ‘head-on’ final conformation. Simulations of the proteins with the positive silicon undercoordinated silica surfaces showed the tagless protein adsorbed, while the tagged protein was freely diffusing in the centre for the duration of simulation. Simulations of the proteins with the negative SAMs

surface showed the tagless protein moved non-specifically and did not adsorb, while the tagged protein was quick to adsorb.

- The His-Tag seems to play a crucial role in driving the S1 subunit towards the negative surfaces, and especially on the SAMs surface, acting like a spacer arm to drive adsorption on that surface.
- In all simulations except those on the model COOH SAM terminated silica surface, the tagged protein has lower structural integrity than the tagless protein, this could be attributed to the flexing of the His-Tag, which was prevalent in all simulations.
- Although the ACE2 binding residues were free in all adsorption simulations on negative surfaces, the aforementioned data show the adsorption simulations of the tagless protein on the silica siloxide and the tagged protein on the SAMs surface are the best models to guide the experimental work in the next chapter. This is because the protein binds to these surfaces in an ideal orientation, keeping the ACE2 binding residues free, for effective integration into the dry-powder IN vaccine formulation.

## Chapter Six: Dry-Powder Vaccine Formulation

*“An expert is a person who has made all the mistakes that can be made in a very narrow field”*

*Neils Bohr*

## 6.1. Introduction

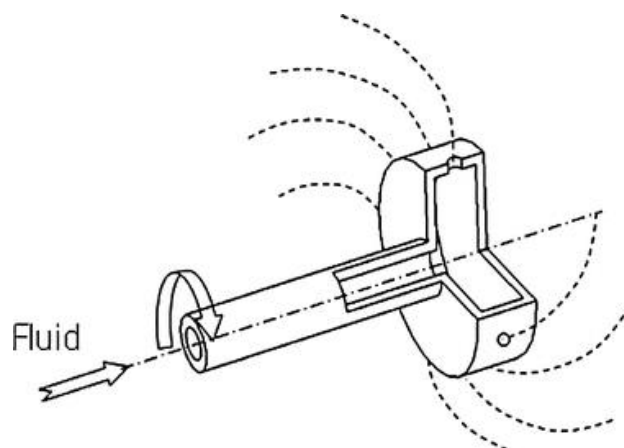
The initial response to the COVID-19 pandemic led to the development of several traditional vaccines, and although the initial vaccine roll-out was successful, there were several challenges that emerged (Sandmann and Jit, 2022). Firstly, COVID-19 is likely to be a virus we will live with, and new variants will emerge, which will need adaptation of current vaccines (Pather *et al.*, 2024). Secondly, many countries combine different vaccine products in their programmes, with this approach generating a robust immune response against COVID-19 (Rashedi *et al.*, 2022, Atmar *et al.*, 2022). Finally, with the current vaccines, the traditional challenges such as vaccine availability, geographical access and affordability remain (Galagali *et al.*, 2022), meaning there remains a need for alternative routes of vaccination. IN vaccines for COVID-19 (see section 1.5) have so far yielded mixed results, and there is not, as of yet, a dry-powder IN vaccine on the market, or undergoing clinical trials. As discussed previously (see section 2.2.2), SiNPs are promising for a variety of applications in drug delivery and nanomedicine due to their properties. The aim of this chapter is to formulate a dry powder vaccine formulation for IN delivery, targeting the RBD found in the S1 subunit of the S protein, by incorporating two variants of SiNPs in the formulation, COOH SiNPs and SiNPs.

## 6.2. Materials and Methods

### 6.2.1. Initial Spray Drying Runs

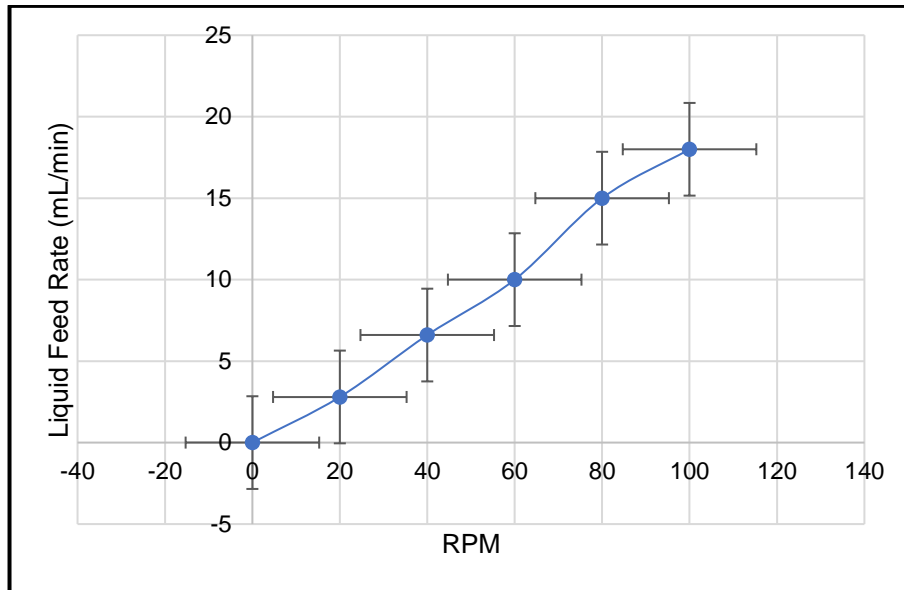
#### Rotary disk atomisers and spray dryer calibration

A rotary disk atomiser is a device which uses a high speed rotating mechanism to form a hollow spraying mechanism and atomise viscous, multicomponent liquids (Kuhnenn *et al.*, 2018). The rotating cup or disk uses centrifugal energy to force the liquid to exit the mechanism at high speed, producing the high speed essential for atomisation (Huang and Mujumdar, 2008).



**Figure 6.1:** The concept of rotary atomisation.

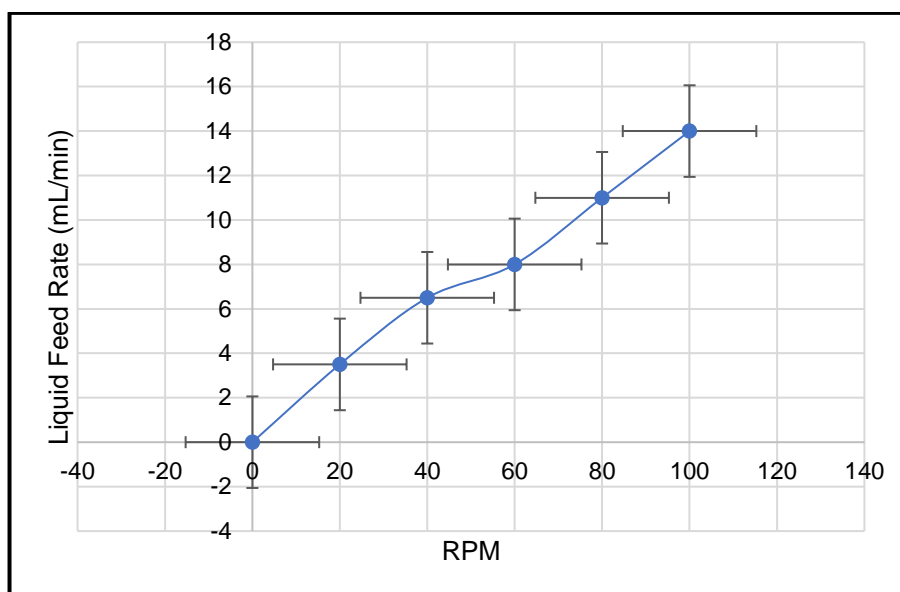
Rotary disk atomisers (**Figure 6.1**) are particularly important in spray drying as they allow the liquid sample to be fed into chamber at the optimum liquid feed rate for the required particle size (Huang and Mujumdar, 2008). The Buchi B-290 spray dryer was calibrated to give an indication of the rotations per minute (RPM) at every liquid feed level, and the liquid feed rate was tested at 20, 40, 60, 80 and 100 RPM before any spray-drying work. The spray dryer nozzle (see **chapter 3.3.1**) size was set at an outer diameter of 1.4mm with a nozzle tip of 0.5mm, and nitrogen was used as the preferred drying gas to air, this is because nitrogen allows organic solvents to be dried safely, as well as reducing oxidation in the final product.



**Figure 6.2:** The spray dryer calibration curve for the Buchi B290 mini spray dryer. This shows the liquid feed rate in relation to RPM count, which is particularly important for process control and optimisation.

The initial experiments used the tubing which gave the calibration curve shown in **Figure 6.2**. As the experimental work proceeded, this led to deterioration of the tubing, and for the experiments incorporating NPs, a new tubing was used for the spray dryer, which gave a new calibration curve (**Figure 6.3**). As evident, the new tubing has a slower liquid feed rate, which means it needs higher RPM to give the required feed rate for the experimental setup.





**Figure 6.3:** The calibration curve for the new tubing.

A full list of the materials used in this work is given in **Table 6.1**, and Alpha lactose monohydrate (LM) was used as the excipient. The aim was to spray dry it to a size of 20-25  $\mu\text{m}$ , which falls within the optimal particle size for nasal delivery (Degenhard *et al.*, 2015, Tiozzo Fasiolo *et al.*, 2018).

**Table 6.1:** A list of the materials used in the experimental work and their abbreviations.

| Material                             | CAS Number | Supplier                          | Abbreviation |
|--------------------------------------|------------|-----------------------------------|--------------|
| Alpha lactose monohydrate            | 599-81-1   | Sigma Aldrich, Massachusetts, USA | LM           |
| Ethanol                              | 64-1-5     | Sigma Aldrich, Massachusetts, USA | EtOH         |
| Silica nanoparticles                 | 7631-86-9  | Sigma Aldrich, Massachusetts, USA | SiNPs        |
| COOH terminated silica nanoparticles | 7631-86-9  | Glantreo Ltd, Cork, Ireland       | COOH SiNPs   |

The spray-drying parameters were modified from literature (Brennan *et al.*, 1971, Vickovic *et al.*, 2023, Arpagaus *et al.*, 2010, Wu *et al.*, 2014, Ke *et al.*, 2020), further research and modification of the parameters resulted in six parameter sets (PRM1-6, see **Table 6.2**) to trial. The spray-dryer inlet and outlet temperatures are complementary, and regulate the heat generated by the spray-dryer. This ultimately has an effect on final particle size. The liquid feed rate controls how much solution is fed into the spray-dryer at any one point, and a higher liquid feed rate means more solution is fed through, resulting in an increased droplet size. The rotameter is an indicator for spray gas flow, and the nozzle has a certain pressure drop, which increases with higher gas flow, meaning as the setting increases, there is higher gas flow and pressure. The aspirator pumps gas through the system, and the maximum rate of 100 has a gas flow rate of 35 m<sup>3</sup>/h. These parameters were all tested with LM only first to find the optimum conditions for obtaining the desired size, with 12g of LM weighed into 200 mL of distilled water and stirred at 50°C until clear. The process was repeated for all the parameters, and the apparatus was flushed with water in between runs.

**Table 6.2:** The spray-dryer parameters used in the first two cycles.

| PRM | Inlet Temp | Outlet Temp | Liquid feed rate | Rotameter Setting | Aspirator rate |
|-----|------------|-------------|------------------|-------------------|----------------|
| 1   | 120°C      | 57°C        | 15 mL/min        | 40mm              | 100            |
| 2   | 85°C       | 50-80°C     | 10 mL/min        | 40mm              | 100            |
| 3   | 170°C      | 87-93°C     | 6.6 mL/min       | 50mm              | 100            |
| 4   | 170°C      | 87-93°C     | 10 mL/min        | 45mm              | 100            |
| 5   | 150°C      | 40-90°C     | 15 mL/min        | 55mm              | 100            |
| 6   | 200°C      | 40-90°C     | 15 mL/min        | 25mm              | 100            |

### 6.2.2. DoE Spray Drying Parameters

From the initial trials and a literature search (Brennan *et al.*, 1971, Vickovic *et al.*, 2023, Arpagaus *et al.*, 2010, Wu *et al.*, 2014, Ke *et al.*, 2020), four factors were identified as factors of interest which affect the experimental set up, and these factors were set at two levels most likely to be effective (**Table 6.3**).

**Table 6.3:** The two levels of the four factors that have the most effect on the experimental spray drying set up.

|                           | <b>Low</b> | <b>High</b> |
|---------------------------|------------|-------------|
| <b>Rotameter Setting</b>  | 45mm       | 55mm        |
| <b>Outlet temperature</b> | 40°C       | 95°C        |
| <b>Inlet temperature</b>  | 195°C      | 220°C       |
| <b>Liquid feed rate</b>   | 6.6 mL/min | 10 mL/min   |

The two levels of the four factors identified (**Table 6.3**), were chosen as they are more likely to give the desired result by allowing the spray dryer to operate to the level required. The levels were used to form a  $2^{4-1}$  fractional factorial design, using the Minitab v19.0 software, entailing 8 total runs with no centre points (**Table 6.4**).

**Table 6.4:** The experimental runs obtained from running DoE in Minitab v19.0.

|          | <b>Rotameter Setting</b> | <b>Inlet Temperature</b> | <b>Outlet Temperature</b> | <b>Liquid Feed Rate</b> |
|----------|--------------------------|--------------------------|---------------------------|-------------------------|
| <b>1</b> | 55mm                     | 195°C                    | 40°C                      | 10 mL/min               |
| <b>2</b> | 55mm                     | 195°C                    | 95°C                      | 6.6 mL/min              |
| <b>3</b> | 55mm                     | 220°C                    | 95°C                      | 10 mL/min               |
| <b>4</b> | 45mm                     | 195°C                    | 95°C                      | 10 mL/min               |
| <b>5</b> | 45mm                     | 220°C                    | 95°C                      | 6.6 mL/min              |
| <b>6</b> | 45mm                     | 220°C                    | 40°C                      | 10 mL/min               |
| <b>7</b> | 55mm                     | 220°C                    | 40°C                      | 6.6 mL/min              |
| <b>8</b> | 45mm                     | 195°C                    | 40°C                      | 6.6 mL/min              |

The subsequent experimental runs used the parameters obtained from Minitab v19.0 (**Table 6.4**), and 19.9g of LM was mixed with 200 mL of distilled water, and stirred at 50°C until clear. LM was increased in these runs, as it may have a direct impact on particle size. In the run with SiNPs, 19.9g of LM and 0.0472g SiNPs were mixed with 200 mL of distilled water and stirred at 50°C until clear. The solution was further sonicated at 30°C for 30 minutes. The run with COOH SiNPs consisted of 19.9g LM and 0.0403g COOH SiNPs, mixed with 200 mL distilled water and stirred at 50°C until clear.

### **6.2.3. Mastersizer 3000**

The hydro medium volume dispersion unit, which is an automated sample dispersion unit used for the controlled, automated wet dispersion of samples for particle size analysis, was used to disperse the sample for size analysis in the Mastersizer 3000. EtOH, in which the sample was dispersed, was poured into the dispersing unit, and the LM samples were loaded until the sample obscuration reached 10%. The obscuration is a measure of the amount of light blocked or scattered by the particles, and gives an accurate measure of the concentration of particles within the Mastersizer 3000. The obscuration is advised to be between 10-20% for a wet dispersion unit (Malvern Panalytical, 2023). The sample was also stirred at 2000 RPM, and ultrasound (US) was applied to ensure there was no particle aggregation. US radiation, when applied to a sample, removes agglomerates, resulting in a more uniform sample. The Mastersizer 3000 takes six measurements of each sample, giving the average d10, d50 and d90.

### **6.2.4. Morphologi G3**

The LM samples were placed in the sample dispersion unit using the 7mm sample holder. The Morphologi G3 automatically disperses the sample on the glass slide and then analyses the sample objectively for particle size and shape. The particles are also separated into classes, allowing for easier data analysis. The sample classes were saved to the computer as an SOP to speed up subsequent tests.

### **6.2.5. SEM**

The samples were imaged using a Hitachi TM-4000 plus SEM. The standard specimen holder was used, with a gold sputter coating of 20.1nm. The SEM operated in BSE (see Section 3.3.2) mode, and the images were gathered at mode 2 with 10Kv accelerating voltage, at vacuum. All images for the LM samples were imaged at three magnifications, 100x, 200x, and 1000x. SiNPs and COOH SiNPs were imaged at 2,500x and 7000x magnifications.

### **6.2.6. ZP**

SiNPs and COOH SiNPs were prepared in a 0.2g/L solution with distilled water, followed by sonication at 30°C for 50 min. The solution pH was measured using a Mettler Toledo M800 pH probe. The ZP measurements were performed using a Malvern Zetasizer Nano ZS, with the solution placed in folded capillary zeta cells (Malvern Panalytical, 2013). The direction and velocity of the motion is a function of particle charge, the suspending medium, and the electric field strength. The equipment utilises the laser Doppler velocimetry (LDV) technique, and the particle velocity is then measured by observing the Doppler shift in the scattered light. The particle velocity is proportional to the electrical potential of the particle at the shear plane. Thus, this optical measurement of the particle motion under an applied field can be used to determine ZP.

### **6.2.7. DLS**

The same solution as prepared for the ZP measurement was used for the DLS measurement. The size of SiNPs was determined by DLS measurements using a Malvern zetasizer Nano ZS, which has a measurement range spanning from 0.6nm to 6µm. Non-invasive backscattering optics were used in this instrument, and each measurement was conducted three times with the average result taken.

## **6.3. Results and Discussion**

### **6.3.1. Initial Spray Drying Runs**

The initial spray drying runs utilised the parameters given in **Table 6.2**. The resulting samples showed visibly less product with PRM 6, where product waste occurred from adhesion to the sides of the spray-dryer chamber. This observation could be explained by the nitrogen gas pressure, which is crucial to the whole process. The nitrogen gas pressure at PRM 6 was low, therefore, the vaporised droplets were likely to be too big to dry, and instead adhered to the drying chamber. Furthermore, the sample for PRM 2 was wet, which could be explained by the low inlet temperature at those settings. Subsequently, the PRM 2 & 6 parameters were not used in subsequent runs. The

sample for PRM 3 yielded a much greater size than what would be expected, so guided by these observations, PRM 4 and PRM 5 seem to be the most promising spray-drying parameters, and more likely to yield the desired size. The samples were stored with a silica gel desiccant to prevent any moisture destroying the sample.

**Table 6.5:** Particle size data gathered from the Mastersizer 3000 from the initial runs.

| Sample       | d10                 | d50                 | d90                 |
|--------------|---------------------|---------------------|---------------------|
| PRM1 - US    | 4.38 $\mu\text{m}$  | 17.10 $\mu\text{m}$ | 36.92 $\mu\text{m}$ |
| PRM5 – US    | 8.88 $\mu\text{m}$  | 18.84 $\mu\text{m}$ | 31.92 $\mu\text{m}$ |
| PRM4 – No US | 19.20 $\mu\text{m}$ | 37.70 $\mu\text{m}$ | 70.28 $\mu\text{m}$ |

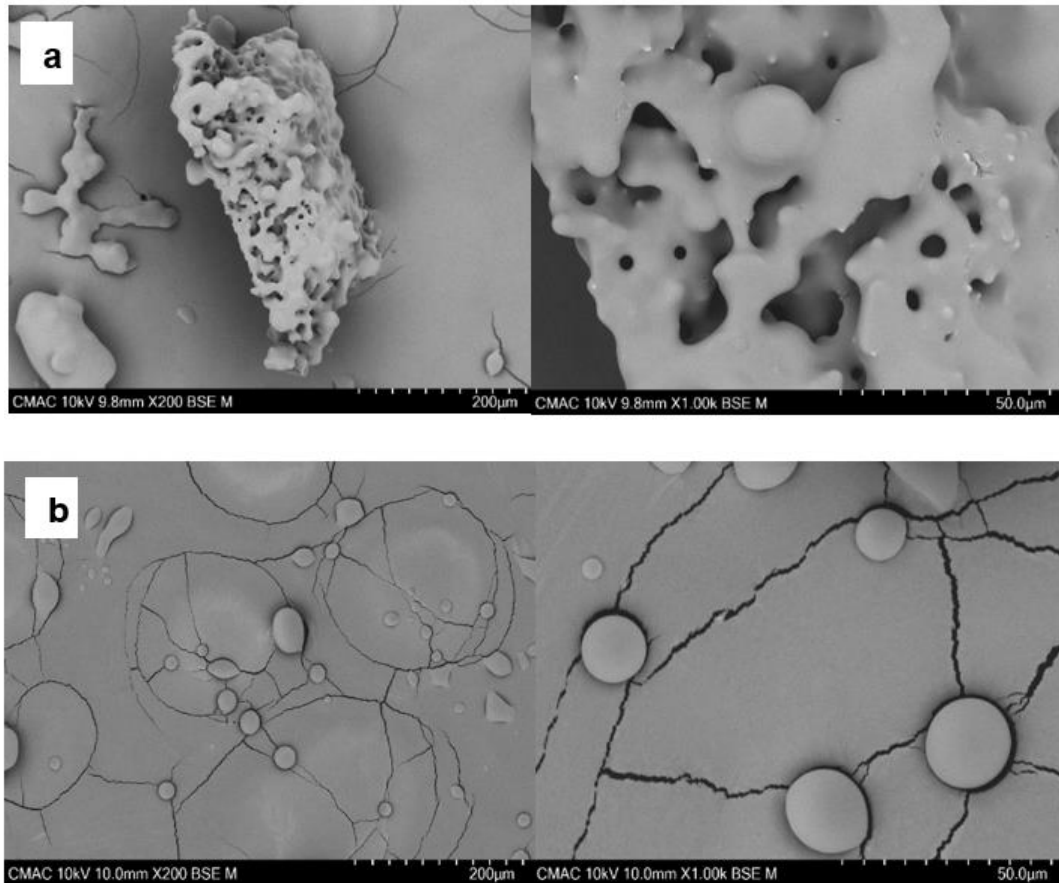
The data from the Mastersizer 3000 for the initial runs (**Table 6.5**) shows the three size distributions. The d10 distribution means 10% of the sample has particles of d10 size or below at, 50% for d50, and 90% for d90. These results highlight the importance of using US when preparing the sample for size analysis, as PRM 4 without US gives a higher average size. Overall though, the initial runs were test runs to establish if the spray-dryer was operational, to observe the effect of US on sample size measurement, and to determine which parameters were more likely to give the desired particle size. As PRM 2 and PRM 6 were eliminated, the experiments were repeated with the other parameters.

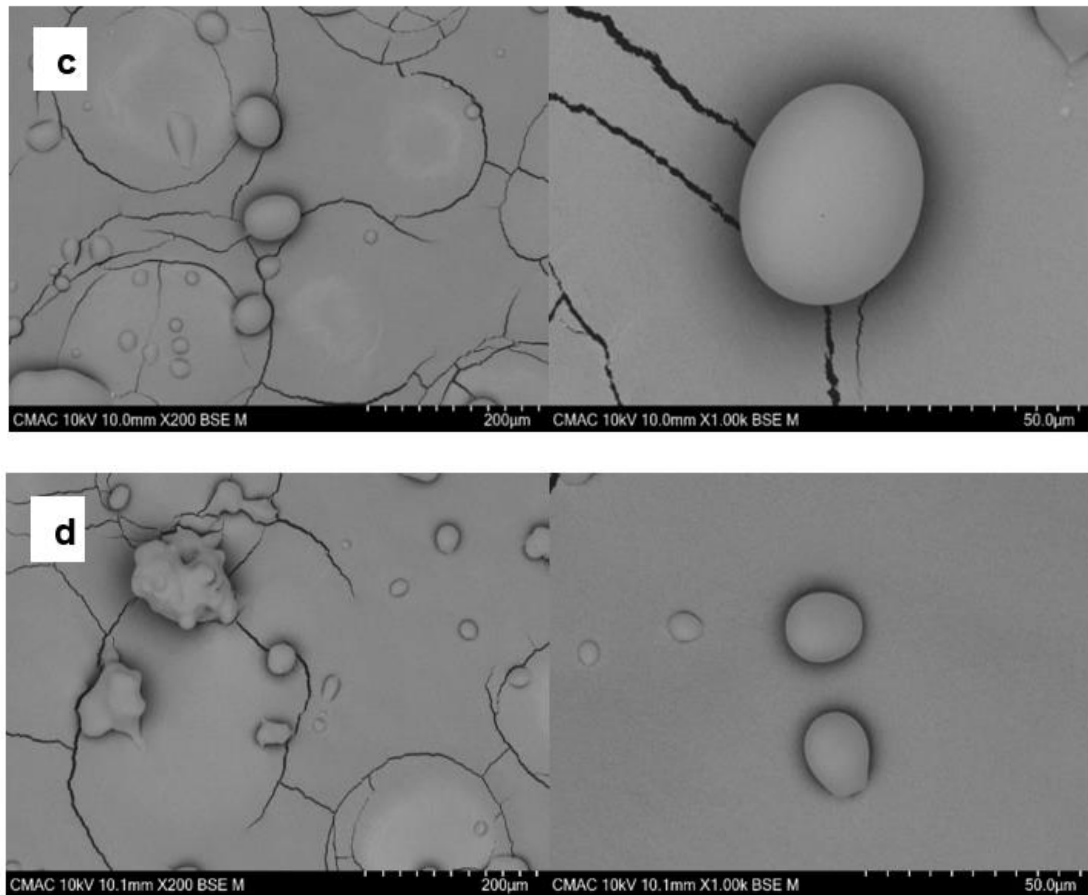
**Table 6.6:** Particle size data gathered from the Mastersizer 3000 from the second runs.

| Sample    | d10                 | d50                 | d90                 |
|-----------|---------------------|---------------------|---------------------|
| PRM1 - US | 51.48 $\mu\text{m}$ | 68.32 $\mu\text{m}$ | 90.03 $\mu\text{m}$ |
| PRM3 – US | 13.10 $\mu\text{m}$ | 54.25 $\mu\text{m}$ | 65.87 $\mu\text{m}$ |
| PRM4 – US | 7.53 $\mu\text{m}$  | 23.83 $\mu\text{m}$ | 48.01 $\mu\text{m}$ |
| PRM5 - US | 7.19 $\mu\text{m}$  | 20.28 $\mu\text{m}$ | 41.73 $\mu\text{m}$ |

The spray-drying runs were repeated at the parameters given in **Table 6.2**, and similar to the initial run, the results (**Table 6.6**) illustrate PRM 4 and PRM 5 as the most suitable parameters in obtaining the required particle size. A peculiar observation from these runs is that, although US was applied in the sample preparation, the samples at PRM 1 and PRM 3 had a significantly larger particle size. The sample for PRM 1 is

also notably clustered, with many interlinked particles, and little of the individual spherical particles that would be expected (**Figure 6.4a**). The observation is unusual, as smaller particles would be expected, given US should reduce the particle size, resulting in a narrower size distribution. The higher particle size for PRM 1 & PRM 5, when compared with the initial run (**Table 6.5**), could also be an indication of limitation of the Mastersizer 3000 instrument. The Mastersizer 3000 uses the laser diffraction technique, and the technique limitations such as uneven light scattering, or the inability to determine the exact size of some particles in a sample due to differences in wavelength maybe an explanation for the discrepancy between the results, and especially the very large particle size as seen with PRM 1 and PRM 3.





**Figure 6.4:** Images for A) PRM1, B) PRM3, C) PRM4, D) PRM5 for the second spray-drying runs. All images gathered from the Hitachi TM-4000- plus SEM.

SEM images for spray-dried LM samples are shown in **Figure 6.4**. The sample for PRM 1 (**Figure 6.4a**) seems to be composed of clustered aggregates of particles. Furthermore, these SEM samples seem to disappear under vacuum, and although the particle sizes for PRM 4 and 5 are an ideal size according to the Mastersizer 3000 data, the SEM images show the particles for the latter were still aggregated to an extent, and not giving the desired uniform, and spherical particles. The SEM image data shows PRM 3 and PRM 4 particles are spherical, and closest in shape to the requirement. Although the LM used was pharmaceutical grade, some spherical agglomerates were visible, indicating some degree of moisture in the original LM. Amorphous LM is often used in dry powder inhalations as a diluent, and although it is the most commonly used carrier as a flow aid, it facilitates the dose of the active ingredients to the lungs (Hebbink *et al.*, 2022, Janssen *et al.*, 2023). However, crystalline LM after spray-



drying could be a cause for concern, as it is more likely to absorb water in humid conditions, leading to wet samples (Afrassiabian and Saleh, 2020, Dominici *et al.*, 2022). This further reiterates the importance of optimising experimental conditions and processes in a way to ensure the resulting product is as dry and optimal as possible (Karas *et al.*, 2023).

**Table 6.7:** Particle size data gathered from the Morphologi G3 for the second runs.

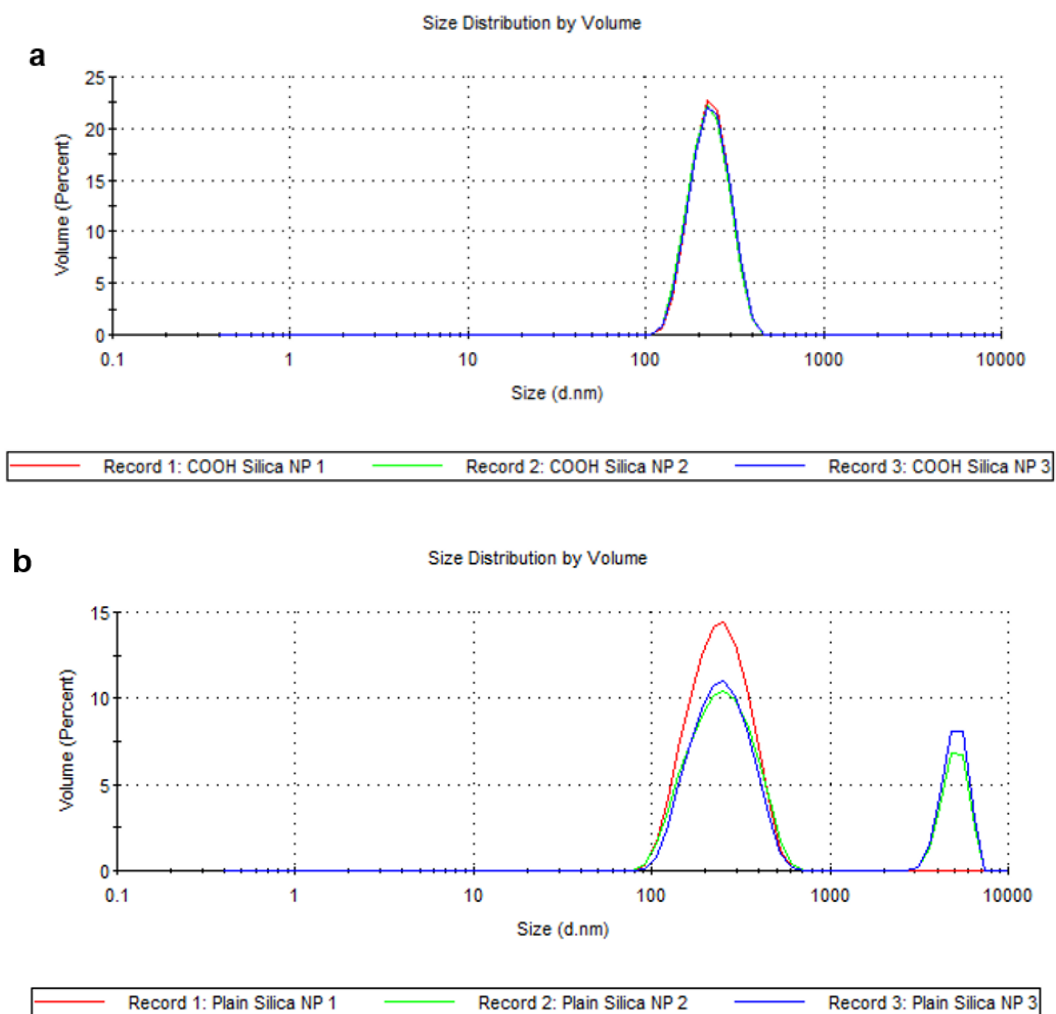
| Sample      | d10                | d50                 | d90                 |
|-------------|--------------------|---------------------|---------------------|
| <b>PRM1</b> | 5.12 $\mu\text{m}$ | 6.43 $\mu\text{m}$  | 9.63 $\mu\text{m}$  |
| <b>PRM3</b> | 4.83 $\mu\text{m}$ | 7.49 $\mu\text{m}$  | 10.93 $\mu\text{m}$ |
| <b>PRM4</b> | 1.66 $\mu\text{m}$ | 4.87 $\mu\text{m}$  | 9.06 $\mu\text{m}$  |
| <b>PRM5</b> | 6.75 $\mu\text{m}$ | 10.73 $\mu\text{m}$ | 16.79 $\mu\text{m}$ |

The samples for the subsequent second run were also evaluated in the Morphologi G3 and the results (**Table 6.7**) are a further indication that laser diffraction, and in particular the Mastersizer 3000, is not a reliable technique as it over inflates the particle size due to the intricacies of the diffraction process, and due to needing liquid sample. Furthermore, data from the Sympatec HELOS, gathered by Alchemy Pharmatech, was largely concurrent with that from the Morphologi G3. Therefore, the Morphologi G3 instrument was selected for use for subsequent size analysis, as it gives real-time images as well as size data of the sample, allowing for verification of the size measurements.

### **6.3.2. Further Production Runs Incorporating NPs**

#### Dynamic Light Scattering

The average size of both COOH SiNPs and the SiNPs, was around  $\sim 200\text{nm}$ , with a polydispersity index (PDI) of 0.006 and 0.157, respectively.

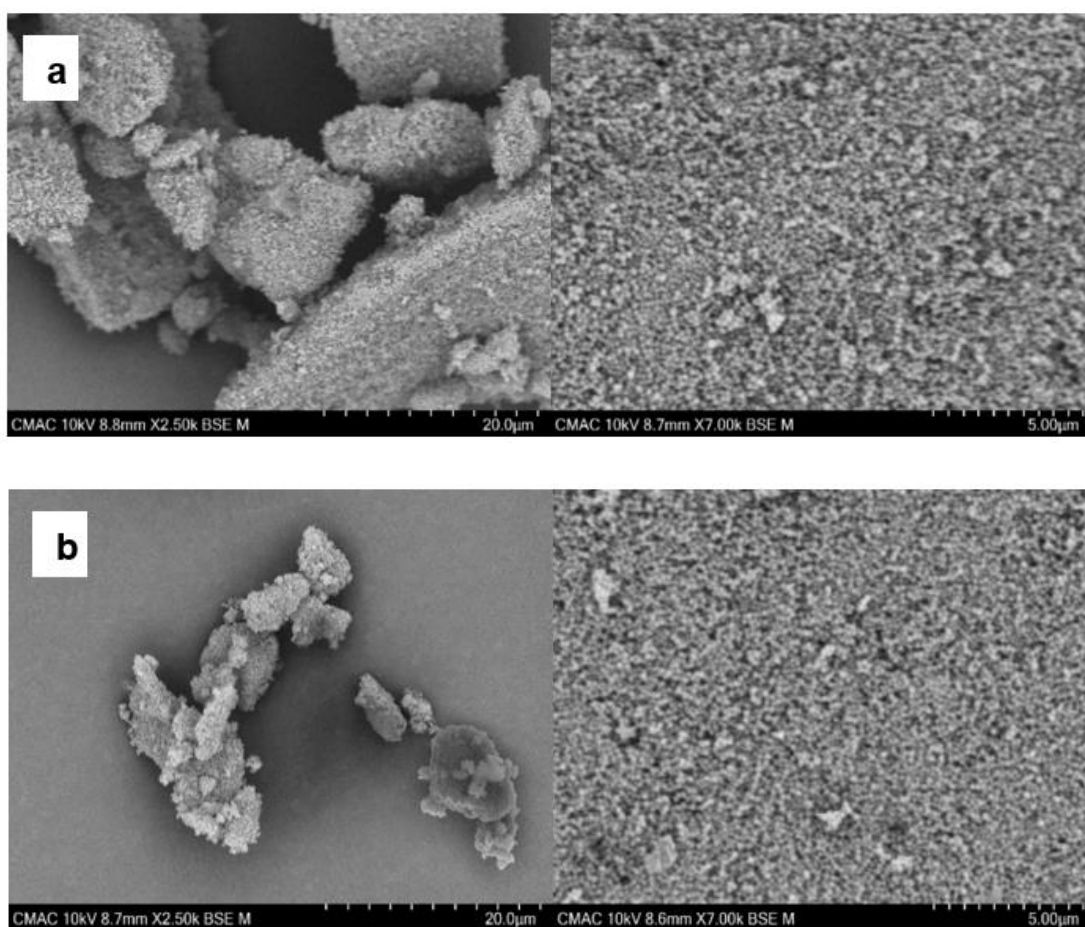


**Figure 6.5:** Size distribution of a) COOH SiNPs, b) SiNPs, measured by DLS.

The pH of the solution used in both the DLS and ZP measurements was 9 for the COOH SiNPs and 8.9 for SiNPs, meaning both solutions are mildly alkaline, and the pH may affect the properties (Fernando and Zhou, 2019), as well as the ZP (Fatfat *et al.*, 2023, Lu and Gao, 2010) of the NPs. The average size of the COOH SiNPs is ~200nm (**Figure 6.5a**), and the data has one uniform peak, indicating the sample was particularised without any impurities or aggregation of particles. Three measurements were taken, as standard for the equipment, and all three were within the required particle size range. The COOH SiNPs image data (**Figure 6.6a**), seems to be concurrent with the DLS data, as there are fewer smaller clumps of particles.

However, the size data for SiNPs (**Figure 6.5b**) gave two average peaks. The first peak, averaging at a size of ~200nm, is to be expected, and given the large average

area under the peak, indicates most of the particles in the sample were within the expected size range. The second peak at  $\sim 7500\text{nm}$  was unexpected, but could be attributed to several factors. The DLS measurements were taken three times, and in the first run, shown in red (**Figure 6.5b**) there is a greater % of particles at the required size. The second and third runs, shown in blue and green have fewer particles at the required size range and more at the larger particle size, this would generally not be expected.



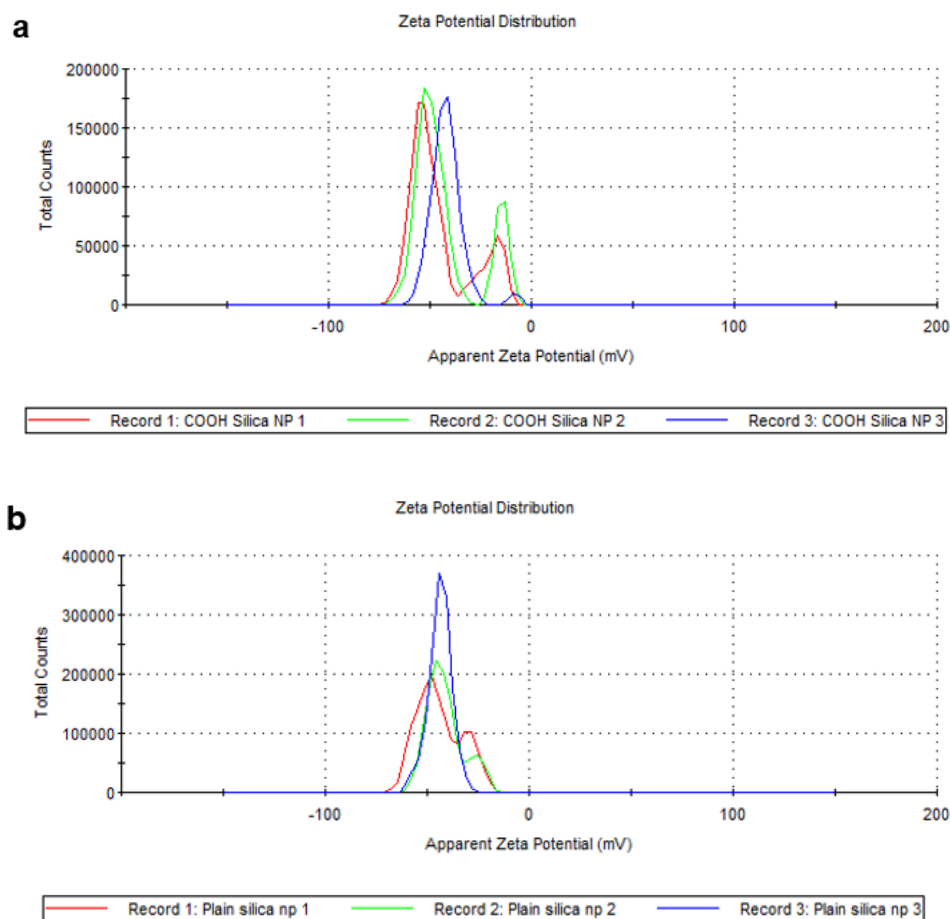
**Figure 6.6:** SEM images a) COOH SiNPs, b) SiNPs. All images gathered from the Hitachi TM-4000- plus SEM.

Firstly, aggregation may have a part to play, as the image (**Figure 6.6b**) shows there are some smaller clumps of particles, more than those seen with the COOH SiNPs. However, it is worth noting, the DLS data was obtained from a sample prepared in a

solution by sonicating, while the sample for the SEM images was the NPs in their pure powder form. It also seems like some of the aggregates may have failed to break down, as the size of the particles corresponding to the second peak is larger. Secondly, the second peak could be attributed to impurities in the sample, originating from very small particulates that are visible in the NPs in their raw form. Finally, the second peak for the SiNPs may be caused by some instrument limitation, giving a low scattering signal and causing differences in the measurements.

### Zeta Potential

The folded capillary zeta cells were used for both the ZP and DLS measurements.



**Figure 6.7:** Zeta potential data for a) COOH SiNPs, b) SiNPs, measured using the Malvern Nano ZS Zetasizer.

The ZP measurement data (**Figure 6.7**) shows both the NPs are strongly negative, at  $\sim -60$  mV. Therefore, both NPs are considered strongly anionic and tend to repel each other. Both NPs are stable and there will be no tendency for aggregation. There is however, deviation from the centre point at  $\sim -60$  mV, with the standard SiNPs fluctuating to  $\sim -50$  mV, this observation may be attributed to the pH of the solutions, which is higher than neutral pH. The NPs have negative ZP in their pure form, and when prepared in an alkaline solution, the particles tend to acquire more negative charge, this could account for the lower average ZP for COOH SiNPs. Additionally, there are two visible peaks for the COOH SiNPs, the larger peak is an average, and what would be expected of the ZP from the NPs. However, the smaller peak at  $\sim -15$  mV could correspond to the smaller particulates/visible aggregates present in the sample (**Figure 6.6a**). These particulates have a more positive ZP, meaning they will repel each other, with no tendency to aggregate. The ZP for stable particles should satisfy  $|Z| < -30$  mV or  $> +30$  mV (Honary and Zahir, 2013), and the SiNPs are moderately dispersed as they have a ZP of  $\sim -30$  mV for some of the particles in the sample, but most fall out of the range. The COOH SiNPs have a small quantity of NPs at a ZP of  $\sim -15$  mV, further indicating lower dispersion stability of these NPs. However, this observation for the COOH SiNPs does not match with the particle size data in **Figure 6.5a**, where there is one uniform size peak, indicating the ZP observed in the second peak for the COOH SiNPs sample may be due to other factors such as an impurity in the sample. There is also more deviation in both samples, which could be influenced by sample movements and different levels of interaction with the electrode.

The SiNPs and COOH SiNPs were imaged at much higher magnifications when compared to the spray-dried LM samples. This is because imaging them at the same magnifications as the LM samples did not show the individual NPs, as the NPs are significantly smaller than the spray-dried LM samples. The images (**Figure 6.6**) are therefore not as clear as those for the LM samples, but the spherical NPs are still clearly visible.

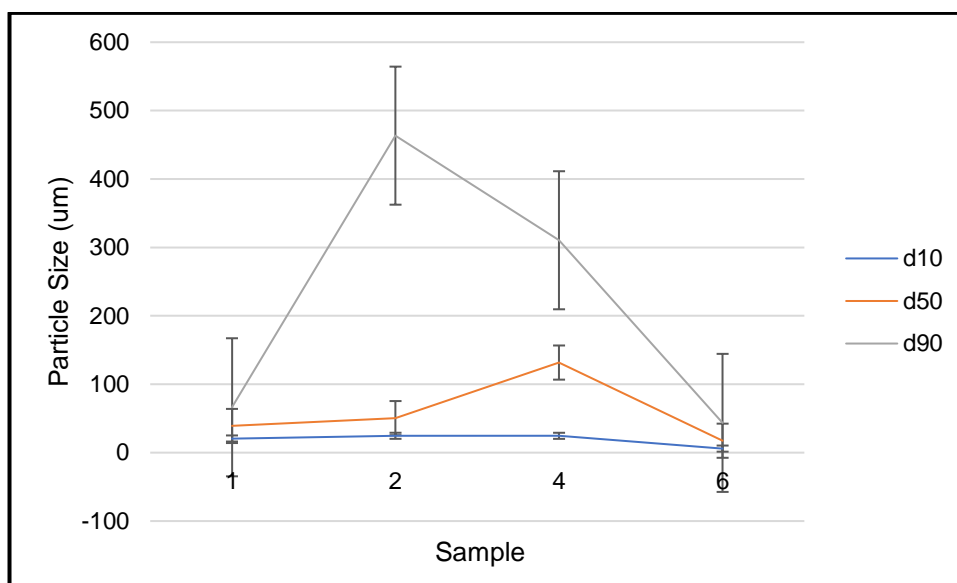
### Spray-drying

Given the mixed results obtained from the spray-drying runs so far, the factors affecting the experimental runs were evaluated. The humidity of the inlet air could be adjusted, in a way not to exceed the relative and absolute humidities, but to optimise the process. However, a literature search and pilot tests gave four main parameters that affect spray-drying runs (**Table 6.3**). These parameters were set at two levels most likely to give the desired outcome, and these were used to form a DoE in Minitab v19.0 (**Table 6.4**) giving eight experimental runs for subsequent runs on the spray-dryer.

The results from these experimental runs yielded four promising results that were close to the requirement of 20-25 micrometre lactose particle sizes. These were analysed using Morphologi G3 with the same method described before (**See Section 6.2.4**). The results (**Table 6.8**) show sample 4 has a significantly higher size than would be expected, and sample 6 is the closest to the required size of 20-25 micrometres. In this dataset, the d10 is within range for samples 1, 2 and 4. However, the d50 is the important parameter, and samples 1 and 6 are closest to the required particle size. Another observation from these runs was that although the exact parameters obtained from DoE were attempted to be implemented, the inlet and outlet temperatures were particularly difficult to regulate. This is because once the instrument heats up, it is difficult to cool it down to a low temperature. Subsequently, for the results in **Table 6.8**, the spray dryer maintained inlet temperatures of 196/196/198/225°C and outlet temperatures of 109/119/95/115°C. The other parameters were exactly the same as 1 (**Table 6.4**).

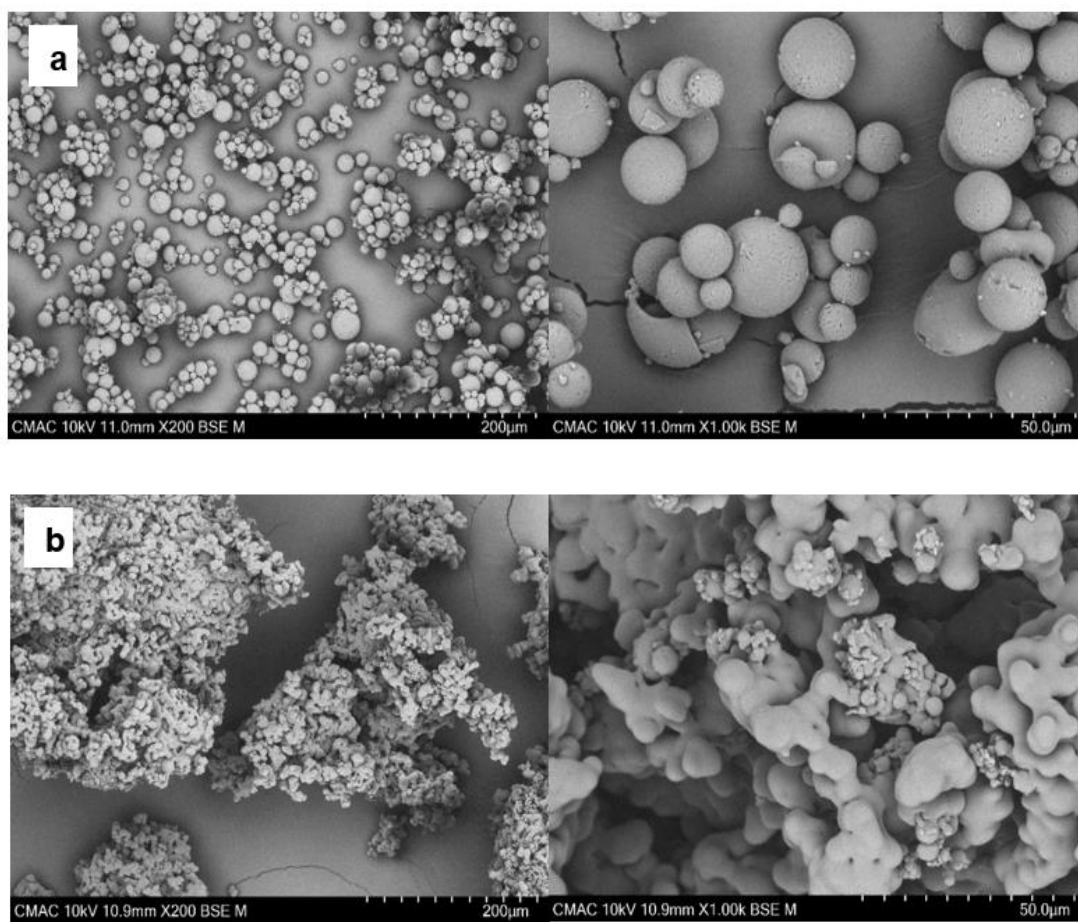
**Table 6.8:** Particle size data gathered from the Morphologi G3 from the third experimental runs using the spray-drying parameters obtained from DoE.

| <b>Sample</b> | <b>d10</b> | <b>d50</b> | <b>d90</b> |
|---------------|------------|------------|------------|
| <b>1</b>      | 20.72 µm   | 39.01 µm   | 66.33 µm   |
| <b>2</b>      | 24.66 µm   | 50.48 µm   | 463.4 µm   |
| <b>4</b>      | 24.62 µm   | 131.7 µm   | 310.5 µm   |
| <b>6</b>      | 5.92 µm    | 17.45 µm   | 43.51 µm   |



**Figure 6.8:** Particle size data for samples 1,2,4 and 6 from the third experimental runs. The standard error bars indicate the uncertainty of the data. All data gathered from the Morphologi G3.

To confirm the conclusions and visualise the samples, samples 1 and 6, which were the closest to the required size range, were imaged with SEM using the methodology described in **Section 6.2.5**. As seen in **Figure 6.9**, sample 1 is a uniform powder, giving the spherical particles as would be expected. However, many of the particles are small and there are many shells of what appear to be damaged particles. Furthermore, the images do not agree with the size data given by the Morphologi G3, which seems to be significantly larger. This discrepancy in the data could be explained by the Morphologi G3 analysing clumps of particles as opposed to individual particles. As the DoE parameters only resulted in one sample with particles of the required size, an ANOVA statistical analysis was not done.



**Figure 6.9:** Images for a) 1, b) 6. All images gathered from the Hitachi TM-4000- plus SEM.

The images for sample 6 are clumps of aggregated particles, some of which appear to have merged and melted during the process. Going by the above data, the spray-drying parameters for sample 1 were used for further runs, as despite the bigger size from the Morphologi G3 data, the SEM images show good size and distribution of the particles, the particles are also mostly uniform and spherical as would be expected.

Similar to the previous runs using DoE parameters (**Table 6.4**), even though the spray drying parameters for sample 1 were employed in the production runs incorporating NPs, it was difficult to obtain a spray-dryer inlet temperature of 195°C and an outlet temperature of 40°C. The instrument gets very hot and regulating the temperature is challenging, this was despite feeding water initially to cool the instrument. Subsequently, in the production runs with SiNPs and COOH SiNPs, the spray dryer



maintained inlet temperatures of 196/195°C, and outlet temperatures of 121/115°C. The nitrogen gas flow rate and liquid feed rate was the same as that in the parameters obtained from DoE.

The spray-drying run with LM and SiNPs, which was carried out by the technician due to my worsening mobility problems, resulted in a lower yield than expected due to operator error. The sample collection pot of the spray dryer was incorrectly secured, which resulted in the loss of some sample during the process.

#### **6.4. Conclusions**

This chapter attempted to create a vaccine formulation using spray-dried spherical lactose particles with NPs, and the SARS-CoV-2 S protein RBD. The work started by the testing of ideal spray-drying parameters and subsequent analysis of the samples with several different particle sizing and imaging techniques. This was followed by integration of the LM with NPs. Given the work completed above, the following conclusions can be drawn:

- Spray drying the particles to obtain spherical particles as planned is challenging, and many times, the spheres break. It is therefore important to modify the spray drying parameters, to ensure maximum product yield, while obtaining uniform, spherical particles. This is also an indication of how challenging it is to develop dry-powder vaccines, and maybe an explanation for why there is not one currently on the market.
- Despite the challenges though, LM was successfully spray-dried to the required size for a dry-powder IN vaccine formulation.
- Going by the particle size and ZP data, both SiNPs and COOH SiNPs seem suitable for integration with the S1 subunit.
- The use of DoE in this component of the project showed DoE although helpful, is not a complete solution, and there is still a bit of trial and error involved with fine-tuning parameters.

- The work conducted in this chapter is not a proof of concept by immunisation for COVID-19, but work towards the development of a product that maybe relevant for a future viral threat.

## Chapter Seven: Conclusions & Perspectives

*“We feel that even if all scientific questions be answered, the problems of life have still not been touched at all”*

*Ludwig Wittgenstein*

## 7.1. Scope for IN Vaccines

Many vaccines are on the market that have effectively prevented or eradicated infectious diseases globally (Zhu *et al.*, 2014). There are several different types of conventional vaccines (see **Section 1.1**), but they come with the problems associated with conventional vaccines and vaccine programmes (see **Section 1.3**). Therefore, it is important to research and develop new alternatives. Dry-powder IN vaccines show much promise in the field of new vaccine development, with the aforementioned advantages (allow easy administration/self-administration, non-invasive) over conventional vaccines (see **Sections 1.3 and 1.4**) improving vaccine uptake and the delivery of vaccine programmes, enhancing overall patient care. Vaccine development, particularly IN vaccine development, is a dynamic process filled with both challenges and progress, and progress has been made with regards to overcoming stability and efficacy issues. This is illustrated by the popularity of FluMist Quadrivalent (Nigel, 2016, FluMist Quadrivalent, 2022), which reported a 72% vaccine effectiveness among children aged between 2-17 in the UK during the 2021/2022 influenza season, and recently got licensed in Japan (Clinical Trials Arena, 2023). Furthermore, MannKind corporation and TechnoVax Inc have created a powder formulation of a virus-like particle Influenza vaccine for intrapulmonary self-delivery by inhalation. This ‘inhaled vaccine powder’ for influenza is shelf-stable and self-inhaled (Smutney *et al.*, 2014, TechnoVax, 2023). These developments are a promising sign for the future of IN vaccines, and an indication that we are not too far away from having a dry-powder IN vaccine on the market as a competitive challenger to conventional vaccines.

## 7.2. Development of a Dry-Powder IN Vaccine for COVID-19

The work in this thesis started by using MD simulations to study the interactions of SpA with model inorganic materials, to establish the suitability of these models in driving the development of new diagnostics (see **Chapter 4**). Given the workplan change, it was decided not to pursue the SpA/antibody conjugation route for the

development of new diagnostics, and focus instead on the development of a dry-powder IN vaccine formulation (see **Chapter 3**).

From the literature (see **Chapter 2**), several target antigens for the SARS-CoV-2 virus were identified (see **Chapter 2.1.2**). The S protein, which has been chosen as the target protein in most COVID-19 vaccine applications (Antonopoulou and Athanassakis, 2022), was also used here and it will need further study with different NPs, to establish the most effective adjuvants for new therapeutic applications. Many current vaccines use aluminium salts, as they remain at the site of injection, and initiate a stronger immune response against the antigen (Awate *et al.*, 2013). However, aluminium salts can cause pain and inflammation at the site of administration, and even accumulate in the brain (Skrastina *et al.*, 2014, Gherardi *et al.*, 2015). In this study, SiNPs were used as an adjuvant for the S1 subunit of the S protein, as they are biocompatible, chemically stable and show low cytotoxicity (Han *et al.*, 2011, Huang *et al.*, 2022b). The S1 subunit with and without a His-Tag, were both studied here, to establish the effect of the His-Tag (if any) on protein behaviour with model SiNPs (see **Chapter 5**). The targeting of the RBD region was made possible by simulations of the model proteins in water, ensuring the protein maintained its structural integrity and the RBD region remained intact for therapeutic application (see **Chapter 5.3.1, Figure 5.5**).

The MD studies showed the SARS-CoV-2 S1 subunit interacted with model negative SiNPs, while keeping the ACE2 binding residues free (see **Chapter 5.3.1, Figure 5.8**). The S1 subunit with a His-Tag interacted similarly with model COOH SiNPs, with the His-Tag appearing to play a crucial role (see **Chapter 5.3.1, Figure 5.13**). These studies were used to guide the experimental work, where the development of a dry-powder IN vaccine formulation was initiated (see **Chapter 6**). The size of the SiNPs and COOH SiNPs, measured by DLS (see **Chapter 6.3.2, Figure 6.5**), was ~200nm, indicating the SiNPs are big enough for the S1 subunit (Kianpour *et al.*, 2022, Guerrini *et al.*, 2022, NewsMedical, 2021). The S1 subunit with a His-Tag is positively charged, and as such it would be expected to effectively decorate the negative SiNPs, which have a ZP of approximately ~-60mV as found by ZP measurements (see **Chapter 6.3.2, Figure 6.7**). The excipient, LM was also spray-dried to the required size between 20-25 micrometres (see **Chapter 6.3.2, Figure 6.9**).

My medical condition did impact aspects of the laboratory work, so I was unable to complete the work to the level planned. Therefore, the work in this component is targeted towards product development, and I have an image of what the final formulation and proof of concept vaccine would look like.

### **7.3. Future Directions: Proof of Concept Dry-Powder IN Vaccine**

This project has initiated dry-powder IN vaccine formulation development, and further continuation of the project, if it was pursued for COVID-19, may involve the following steps. Further spray-drying runs would be conducted with SiNPs, COOH SiNPs and LM, this would be done in a way to ensure the NPs are integrated into the LM particles, while maintaining the desired particle size (20-25 micrometres). Then, the S1 subunit of the SARS-CoV-2 S protein would be adsorbed to the NPs to make the complete dry-powder IN vaccine formulation, all while ensuring the NPs and protein are encapsulated in the correctly sized LM particles.

The complete dry-powder formulation would then undergo a variety of stability tests, ensuring the stability of the formulation in different storage/transport conditions. The residual moisture would be measured by Karl Fischer titrations (Huyge *et al.*, 2012, Veazey *et al.*, 2011, Lakeh *et al.*, 2020). The complete formulation would also be tested for amorphism and crystallinity, which could be done using DSC (Huyge *et al.*, 2012). Final tests would involve measurement of dry dispersion properties, to ensure all particles are uniform and of the required size. This could be carried out using the Morphologi G3 (see **Chapter 3.3.2**), or other particle size instruments.

Dependent on how the aforementioned tests go, if the SiNPs are found to be ineffective, further work could also involve simulation of the RBD protein with different model NPs, to establish if the protein maintains structural integrity and the suitability with different NPs. The above steps would need to be repeated with different NPs experimentally if necessary. The next stage would involve further testing of the complete dry-powder formulation with the Naltos nasal delivery device, ensuring it performs as planned, and giving a proof of concept vaccine ready for pre-clinical tests.

The vaccine would initially be administered to animals, human cell cultures and tissues to decide its efficacy and determine the effective dosage (Shegokar, 2020, AIMST University). Once safety of the vaccines is confirmed in humans, the vaccine will progress to the clinical development phase. Phase 1 trials would involve administration of the vaccine to a small number of healthy volunteers in order to assess its efficacy (Chen *et al.*, 2017b, AIMST University), and a positive phase 1 trial will see the vaccine progress to phase 2, where actual COVID-19 patients would be chosen at random from a larger group to receive either the vaccine or a placebo (any other substance that looks identical to the vaccine, but has no chemical effect) (Van Norman, 2019, AIMST University). A successful phase 2 trial will see progress to phase 3, where a much larger group will randomly receive the vaccine or a placebo (Umscheid *et al.*, 2011). The much larger group is representative of the population the vaccine is intended for, making it is easier to detect side effects, and showing whether the vaccine is safer or more effective than current treatments (Umscheid *et al.*, 2011, AIMST University).

After passing phase 1, 2 and 3 clinical trials, the vaccine would have to undergo a regulatory approval process by health boards such as MHRA and FDA. The health boards will assess the safety and reliability of the vaccine, as well as the benefits outweighing the risks to the patient (Klamer *et al.*, 2022, AIMST University). After regulatory approval, the vaccine would need continual monitoring of the production process, and for any adverse effects to ensure it is as safe and effective as possible (Lee *et al.*, 2020, AIMST University). Traditionally, these combined stages could take anywhere between 21-25 years. However, modern research methods incorporating MD simulations (**see Chapter 3.2**), where target antigens can be studied *in silico* for their efficacy with different materials, have significantly expedited the process.

SARS-CoV-2 was used a model in this study due to its relevance at the time, and it was shown for the first time that the model S protein RBD and S protein RBD with a His-Tag interact preferentially with model SiNPs, opening up a host of possibilities for IN vaccine design. However, the work completed in this project could allow design of an IN vaccine targeting any viral threat, and future work is not limited to SARS-CoV-2. Needless to say, much work is still to be done before a dry-powder IN vaccine,

that can be a viable alternative to conventional vaccines, is approved and readily available on the market.



## Bibliography

*“Nothing in life is to be feared, it is only to be understood. Now is the time to understand more, so that we may fear less”*

*Marie Curie*

- AABY, P., NETEA, M. G. & BENN, C. S. 2023. Beneficial non-specific effects of live vaccines against COVID-19 and other unrelated infections. *Lancet Infect Dis*, 23, e34-e42.
- AFRASSIABIAN, Z. & SALEH, K. 2020. Caking of anhydrous lactose powder owing to phase transition and solid-state hydration under humid conditions: From microscopic to bulk behavior. *Powder Technology*, 363, 488-499.
- AIMSTUNIVERSITY. *Five Stages of Vaccine Development* [Online]. Available: <https://aimst.edu.my/event-news/5-stages-vaccine-development/> [Accessed 17/11/23].
- AL QARAGHULI, M. M., KUBIAK-OSSOWSKA, K. & MULHERAN, P. A. 2018. Thinking outside the Laboratory: Analyses of Antibody Structure and Dynamics within Different Solvent Environments in Molecular Dynamics (MD) Simulations. *Antibodies (Basel, Switzerland)*, 7, 21.
- ALBERS, W. M., VIKHOLM, I., VIITALA, T. & PELTONEN, J. 2001. Chapter 1 - INTERFACIAL AND MATERIALS ASPECTS OF THE IMMOBILIZATION OF BIOMOLECULES ONTO SOLID SURFACES. In: NALWA, H. S. (ed.) *Handbook of Surfaces and Interfaces of Materials*. Burlington: Academic Press.
- ALMEIDA, F. C. L., SANCHES, K., PINHEIRO-AGUIAR, R., ALMEIDA, V. S. & CARUSO, I. P. 2021. Protein Surface Interactions—Theoretical and Experimental Studies. *Frontiers in Molecular Biosciences*, 8.
- ALONSO, D. O. V. & DAGGETT, V. 2000. Staphylococcal protein A: Unfolding pathways, unfolded states, and differences between the B and E domains. *Proceedings of the National Academy of Sciences*, 97, 133.
- AMERICANPHARMACEUTICALREVIEW. *Morphologi G3 Particle Characterization from Malvern Panalytical* [Online]. Available: <https://www.americanpharmaceuticalreview.com/25604-Pharmaceutical-Particle-Size-Analyzers/12040056-Morphologi-G3-Particle-Characterization/> [Accessed 8th August 2022].
- ANAND, P. & STAHEL, V. P. 2021. The safety of Covid-19 mRNA vaccines: a review. *Patient Safety in Surgery*, 15, 20.
- ANDERSEN, K. G., RAMBAUT, A., LIPKIN, W. I., HOLMES, E. C. & GARRY, R. F. 2020. The proximal origin of SARS-CoV-2. *Nat Med*.
- ANDERSON, E. J. & WEBER, S. G. 2004. Rotavirus infection in adults. *Lancet Infect Dis*, 4, 91-9.
- ANGELO, M. G., DAVID, M. P., ZIMA, J., BARIL, L., DUBIN, G., ARELLANO, F. & STRUYF, F. 2014. Pooled analysis of large and long-term safety data from the human papillomavirus-16/18-AS04-adjuvanted vaccine clinical trial programme. *Pharmacoepidemiol Drug Saf*, 23, 466-79.
- ANGSANTIKUL, P., FANG, R. H. & ZHANG, L. 2018. Toxoid Vaccination against Bacterial Infection Using Cell Membrane-Coated Nanoparticles. *Bioconjug Chem*, 29, 604-612.
- ANTONOPOULOU, T. & ATHANASSAKIS, I. 2022. SARS-CoV-2 immunogenicity: Is S protein the best target for vaccination? *Vaccine*, 40, 3093-3095.
- ANTOSIEWICZ, J. M. & DŁUGOSZ, M. 2020. Constant-pH Brownian Dynamics Simulations of a Protein near a Charged Surface. *ACS Omega*, 5, 30282-30298.
- APTER, D., WHEELER, C. M., PAAVONEN, J., CASTELLSAGUÉ, X., GARLAND, S. M., SKINNER, S. R., NAUD, P., SALMERÓN, J., CHOW, S. N., KITCHENER, H. C., TEIXEIRA, J. C., JAISAMRARN, U., LIMSON, G., SZAREWSKI, A., ROMANOWSKI, B., AOKI, F. Y., SCHWARZ, T. F., POPPE, W. A., BOSCH, F. X., MINDEL, A., DE SUTTER, P., HARDT, K.,

- ZAHAF, T., DESCAMPS, D., STRUYF, F., LEHTINEN, M. & DUBIN, G. 2015. Efficacy of human papillomavirus 16 and 18 (HPV-16/18) AS04-adjuvanted vaccine against cervical infection and precancer in young women: final event-driven analysis of the randomized, double-blind PATRICIA trial. *Clin Vaccine Immunol*, 22, 361-73.
- ARANGO DUQUE, G. & DESCOTEAUX, A. 2014. Macrophage Cytokines: Involvement in Immunity and Infectious Diseases. *Frontiers in Immunology*, 5.
- ARASHKIA, A., JALILVAND, S., MOHAJEL, N., AFCHANGI, A., AZADMANESH, K., SALEHI-VAZIRI, M., FAZLALIPOUR, M., POURIAYEVALI, M. H., JALALI, T., MOUSAVI NASAB, S. D., ROOHVAND, F., SHOJA, Z. & FOR THE, S. C.-R. R. T. O. P. I. O. I. 2021. Severe acute respiratory syndrome-coronavirus-2 spike (S) protein based vaccine candidates: State of the art and future prospects. *Reviews in Medical Virology*, 31, e2183.
- AREVALO, C. P., BOLTON, M. J., LE SAGE, V., YE, N., FUREY, C., MURAMATSU, H., ALAMEH, M.-G., PARDI, N., DRAPEAU, E. M., PARKHOUSE, K., GARRETSON, T., MORRIS, J. S., MONCLA, L. H., TAM, Y. K., FAN, S. H. Y., LAKDAWALA, S. S., WEISSMAN, D. & HENSLEY, S. E. 2022. A multivalent nucleoside-modified mRNA vaccine against all known influenza virus subtypes. *Science*, 378, 899-904.
- ARPAGAU, C., SCHAFROTH, N. & MEURI, M. 2010. Laboratory scale spray-drying of lactose: A review. *BUCHI Brochure*.
- ARVIN, A. M., FINK, K., SCHMID, M. A., CATHCART, A., SPREAFICO, R., HAVENAR-DAUGHTON, C., LANZAVECCHIA, A., CORTI, D. & VIRGIN, H. W. 2020. A perspective on potential antibody-dependent enhancement of SARS-CoV-2. *Nature*, 584, 353-363.
- ASQ. *What is Design of Experiments (DoE)?* [Online]. Available: <https://asq.org/quality-resources/design-of-experiments> [Accessed 11/5/23].
- ATKINS, P. & DE PAULA, J. 2006. *Atkins' Physical Chemistry*, Oxford University Press.
- ATMAR, R. L., BERNSTEIN, D. I., HARRO, C. D., AL-IBRAHIM, M. S., CHEN, W. H., FERREIRA, J., ESTES, M. K., GRAHAM, D. Y., OPEKUN, A. R., RICHARDSON, C. & MENDELMAN, P. M. 2011. Norovirus vaccine against experimental human Norwalk Virus illness. *N Engl J Med*, 365, 2178-87.
- ATMAR, R. L., LYKE, K. E., DEMING, M. E., JACKSON, L. A., BRANCHE, A. R., EL SAHLY, H. M., ROSTAD, C. A., MARTIN, J. M., JOHNSTON, C., RUPP, R. E., MULLIGAN, M. J., BRADY, R. C., FRENCK, R. W., JR., BÄCKER, M., KOTTKAMP, A. C., BABU, T. M., RAJAKUMAR, K., EDUPUGANTI, S., DOBRZYNSKI, D., COLER, R. N., POSAVAD, C. M., ARCHER, J. I., CRANDON, S., NAYAK, S. U., SZYDLO, D., ZEMANEK, J. A., DOMINGUEZ ISLAS, C. P., BROWN, E. R., SUTHAR, M. S., MCELRATH, M. J., MCDERMOTT, A. B., O'CONNELL, S. E., MONTEFIORI, D. C., EATON, A., NEUZIL, K. M., STEPHENS, D. S., ROBERTS, P. C. & BEIGEL, J. H. 2022. Homologous and Heterologous Covid-19 Booster Vaccinations. *N Engl J Med*, 386, 1046-1057.
- AVOLIO, E., CARRABBA, M., MILLIGAN, R., KAVANAGH WILLIAMSON, M., BELTRAMI, A. P., GUPTA, K., ELVERS, K. T., GAMEZ, M., FOSTER, R. R., GILLESPIE, K., HAMILTON, F., ARNOLD, D., BERGER, I., DAVIDSON, A. D., HILL, D., CAPUTO, M. & MADEDDU, P. 2021. The SARS-CoV-2 Spike protein disrupts human cardiac pericytes function through CD147 receptor-mediated signalling: a potential non-infective mechanism of COVID-19 microvascular disease. *Clin Sci (Lond)*, 135, 2667-2689.
- AWATE, S., BABIUK, L. A. & MUTWIRI, G. 2013. Mechanisms of action of adjuvants. *Front Immunol*, 4, 114.

- BABICHEVA, R. I., SEMENOV, A. S., SHCHERBININ, S. A., KORZNIKOVA, E. A., KUDREYKO, A. A., VIVEGANANTHAN, P., ZHOU, K. & DMITRIEV, S. V. 2022. Effect of the stiffness of interparticle bonds on properties of delocalized nonlinear vibrational modes in an fcc lattice. *Physical Review E*, 105, 064204.
- BADEN, L. R., EL SAHLY, H. M., ESSINK, B., KOTLOFF, K., FREY, S., NOVAK, R., DIEMERT, D., SPECTOR, S. A., ROUPHAEL, N., CREECH, C. B., MCGETTIGAN, J., KHETAN, S., SEGALL, N., SOLIS, J., BROSZ, A., FIERRO, C., SCHWARTZ, H., NEUZIL, K., COREY, L., GILBERT, P., JANES, H., FOLLMANN, D., MAROVICH, M., MASCOLA, J., POLAKOWSKI, L., LEDGERWOOD, J., GRAHAM, B. S., BENNETT, H., PAJON, R., KNIGHTLY, C., LEAV, B., DENG, W., ZHOU, H., HAN, S., IVARSSON, M., MILLER, J. & ZAKS, T. 2020. Efficacy and Safety of the mRNA-1273 SARS-CoV-2 Vaccine. *New England Journal of Medicine*, 384, 403-416.
- BALLESTEROS-BRIONES, M. C., SILVA-PILIPICH, N., HERRADOR-CAÑETE, G., VANRELL, L. & SMERDOU, C. 2020. A new generation of vaccines based on alphavirus self-amplifying RNA. *Current opinion in virology*, 44, 145-153.
- BANKAMP, B., FONTANA, J. M., BELLINI, W. J. & ROTA, P. A. 2008. Adaptation to cell culture induces functional differences in measles virus proteins. *Virology Journal*, 5, 129.
- BARHOUM, A., GARCÍA-BETANCOURT, M. L., RAHIER, H. & VAN ASSCHE, G. 2018. Chapter 9 - Physicochemical characterization of nanomaterials: polymorph, composition, wettability, and thermal stability. In: BARHOUM, A. & MAKHLOUF, A. S. H. (eds.) *Emerging Applications of Nanoparticles and Architecture Nanostructures*. Elsevier.
- BARTELS, D. A., JOHNSON, R., BAYOR, M. T., AINOOSON, G. K., OSSEI, P. P. S., ETUAFUL, R. K. & BUAMAH, R. 2021. Formulation of Suppositories of Alum Produced from Bauxite Waste in Ghana for the Treatment of Hemorrhoid. *The Scientific World Journal*, 2021, 6667562.
- BECKER, S., FRANKEL, M. B., SCHNEEWIND, O. & MISSIAKAS, D. 2014. Release of protein A from the cell wall of *Staphylococcus aureus*. *Proceedings of the National Academy of Sciences*, 111, 1574.
- BERNASCONI, V., NORLING, K., GRIBONIKA, I., ONG, L. C., BURAZEROVIC, S., PARVEEN, N., SCHÖN, K., STENSSON, A., BALLY, M., LARSON, G., HÖÖK, F. & LYCKE, N. 2021. A vaccine combination of lipid nanoparticles and a cholera toxin adjuvant derivative greatly improves lung protection against influenza virus infection. *Mucosal Immunol*, 14, 523-536.
- BERNSTEIN, D. I., SMITH, V. E., SHERWOOD, J. R., SCHIFF, G. M., SANDER, D. S., DEFEUDIS, D., SPRIGGS, D. R. & WARD, R. L. 1998. Safety and immunogenicity of live, attenuated human rotavirus vaccine 89-12. *Vaccine*, 16, 381-7.
- BHARATBIOTECH. 2022. *COVID-19 Vaccine ChAd36-SARS-CoV-2-S (Recombinant)* [Online]. Available: <https://www.bharatbiotech.com/images/incovacc/incovacc-factsheet.pdf> [Accessed 8/2/2023].
- BLAKNEY, A. 2021. The next generation of RNA vaccines: self-amplifying RNA. *The Biochemist*, 43, 14-17.
- BLAMEY, J. M., FISCHER, F., MEYER, H.-P., SARMIENTO, F. & ZINN, M. 2017. Chapter 14 - Enzymatic Biocatalysis in Chemical Transformations: A Promising and Emerging Field in Green Chemistry Practice. In: BRAHMACHARI, G. (ed.) *Biotechnology of Microbial Enzymes*. Academic Press.
- BLOOM, K., VAN DEN BERG, F. & ARBUTHNOT, P. 2021. Self-amplifying RNA vaccines for infectious diseases. *Gene Therapy*, 28, 117-129.

- BORMASHENKO, E. 2020. What Is Temperature? Modern Outlook on the Concept of Temperature. *Entropy (Basel)*, 22.
- BOTH, E. M., BOOM, R. M. & SCHUTYSER, M. A. I. 2020. Particle morphology and powder properties during spray drying of maltodextrin and whey protein mixtures. *Powder Technology*, 363, 519-524.
- BOZZO, P., NARDUCCI, A. & EINARSON, A. 2011. Vaccination during pregnancy. *Can Fam Physician*, 57, 555-7.
- BRAUN, E., GILMER, J., MAYES, H. B., MOBLEY, D. L., MONROE, J. I., PRASAD, S. & ZUCKERMAN, D. M. 2019. Best Practices for Foundations in Molecular Simulations [Article v1.0]. *Living J Comput Mol Sci*, 1.
- BRENNAN, J. G., HERRERA, J. & JOWITT, R. 1971. A study of some of the factors affecting the spray drying of concentrated orange juice, on a laboratory scale. *International Journal of Food Science & Technology*, 6, 295-307.
- BRESME, F., LEHLE, H. & OETTEL, M. 2009. Solvent-mediated interactions between nanoparticles at fluid interfaces. *The Journal of Chemical Physics*, 130, 214711.
- BREWER, J. M., CONACHER, M., HUNTER, C. A., MOHRS, M., BROMBACHER, F. & ALEXANDER, J. 1999. Aluminium hydroxide adjuvant initiates strong antigen-specific Th2 responses in the absence of IL-4- or IL-13-mediated signaling. *J Immunol*, 163, 6448-54.
- BREWER, K. D., WEIR, G. M., DUDE, I., DAVIS, C., PARSONS, C., PENWELL, A., RAJAGOPALAN, R., SAMMATUR, L., BOWEN, C. V. & STANFORD, M. M. 2018. Unique depot formed by an oil based vaccine facilitates active antigen uptake and provides effective tumour control. *Journal of Biomedical Science*, 25, 7.
- BUGLAK, A. A. & KONONOV, A. I. 2020. Comparative study of gold and silver interactions with amino acids and nucleobases. *RSC Advances*, 10, 34149-34160.
- BULLOCK, J., RIZVI, S. A. A., SALEH, A. M., AHMED, S. S., DO, D. P., ANSARI, R. A. & AHMED, J. 2018. Rheumatoid Arthritis: A Brief Overview of the Treatment. *Medical principles and practice : international journal of the Kuwait University, Health Science Centre*, 27, 501-507.
- BURGESS, T. H., MURRAY, C. K., BAVARO, M. F., LANDRUM, M. L., O'BRYAN, T. A., ROSAS, J. G., CAMMARATA, S. M., MARTIN, N. J., EWING, D., RAVIPRAKASH, K., MOR, D., ZELL, E. R., WILKINS, K. J. & MILLAR, E. V. 2015. Self-administration of intranasal influenza vaccine: Immunogenicity and volunteer acceptance. *Vaccine*, 33, 3894-9.
- BÜCKER, M., FLORES OROZCO, A., UNDORF, S. & KEMNA, A. 2019. On the Role of Stern- and Diffuse-Layer Polarization Mechanisms in Porous Media. *Journal of Geophysical Research: Solid Earth*, 124, 5656-5677.
- CAO, Z., YU, Q., XUE, H., CHENG, G. & JIANG, S. 2010. Nanoparticles for Drug Delivery Prepared from Amphiphilic PLGA Zwitterionic Block Copolymers with Sharp Contrast in Polarity between Two Blocks. *Angewandte Chemie International Edition*, 49, 3771-3776.
- CAO-MILÁN, R. & LIZ-MARZÁN, L. M. 2014. Gold nanoparticle conjugates: recent advances toward clinical applications. *Expert Opin Drug Deliv*, 11, 741-52.
- CASEY, K., ITEEN, A., NICOLINI, R. & AUTEN, J. 2020. COVID-19 pneumonia with hemoptysis: Acute segmental pulmonary emboli associated with novel coronavirus infection. *Am J Emerg Med*, 38, 1544.e1-1544.e3.
- CENTREFORDISEASECONTROLANDPREVENTION. 2022. *Adjuvants and Vaccines* [Online]. Available: <https://www.cdc.gov/vaccinesafety/concerns/adjuvants.html> [Accessed 22/03/2023].

- CHAVDA, V. P., VORA, L. K., PANDYA, A. K. & PATRAVALE, V. B. 2021. Intranasal vaccines for SARS-CoV-2: From challenges to potential in COVID-19 management. *Drug Discovery Today*.
- CHEATHAM, T. E., III, MILLER, J. L., FOX, T., DARDEN, T. A. & KOLLMAN, P. A. 1995. Molecular Dynamics Simulations on Solvated Biomolecular Systems: The Particle Mesh Ewald Method Leads to Stable Trajectories of DNA, RNA, and Proteins. *Journal of the American Chemical Society*, 117, 4193-4194.
- CHELLASAMY, G., KIRIYANTHAN, R. M., GOVINDARAJU, S., RADHA, A. & YUN, K. 2021. Chapter 14 - Recent trends in the development of vaccine technologies to combat pandemic outbreaks and challenges. In: VISWANATH, B. (ed.) *Pandemic Outbreaks in the 21st Century*. Academic Press.
- CHEN, B., TIAN, E.-K., HE, B., TIAN, L., HAN, R., WANG, S., XIANG, Q., ZHANG, S., EL ARNAOUT, T. & CHENG, W. 2020. Overview of lethal human coronaviruses. *Signal Transduction and Targeted Therapy*, 5, 89.
- CHEN, N., WEI, M., SUN, Y., LI, F., PEI, H., LI, X., SU, S., HE, Y., WANG, L., SHI, J., FAN, C. & HUANG, Q. 2014. Self-assembly of poly-adenine-tailed CpG oligonucleotide-gold nanoparticle nanoconjugates with immunostimulatory activity. *Small*, 10, 368-75.
- CHEN, Q., LIU, W., WANG, W., THOMAS, J. C. & SHEN, J. 2017a. Particle sizing by the Fraunhofer diffraction method based on an approximate non-negatively constrained Chin-Shifrin algorithm. *Powder Technology*, 317, 95-103.
- CHEN, S., LIU, L., ZHOU, J. & JIANG, S. 2003. Controlling Antibody Orientation on Charged Self-Assembled Monolayers. *Langmuir*, 19, 2859-2864.
- CHEN, S. C., SINAI, N., BEDARIDA, G., GREGORIO, M. A., EMANUEL, E. & GRADY, C. 2017b. Phase 1 healthy volunteer willingness to participate and enrollment preferences. *Clin Trials*, 14, 537-546.
- CHEN, W. C., BAILY, J. E., CORSELLI, M., DÍAZ, M. E., SUN, B., XIANG, G., GRAY, G. A., HUARD, J. & PÉAULT, B. 2015. Human myocardial pericytes: multipotent mesodermal precursors exhibiting cardiac specificity. *Stem Cells*, 33, 557-73.
- CHEN, X., SUN, Y., MISSIAKAS, D. & SCHNEEWIND, O. 2019. Staphylococcus aureus Decolonization of Mice With Monoclonal Antibody Neutralizing Protein A. *The Journal of infectious diseases*, 219, 884-888.
- CICCOTTI, G. & RYCKAERT, J. P. 1986. Molecular dynamics simulation of rigid molecules. *Computer Physics Reports*, 4, 346-392.
- CLIFTON YOUNG, J. 1996. BLOCKING, REPLICATION, AND RANDOMIZATION—THE KEY TO EFFECTIVE EXPERIMENTATION: A CASE STUDY. *Quality Engineering*, 9, 269-277.
- CLINICALGATE. 2015. *Rectal and vaginal drug delivery* [Online]. Available: <https://clinicalgate.com/rectal-and-vaginal-drug-delivery/> [Accessed 20/6/2022].
- CLINICALTRIALSARENA. 2021. *Moderna initiates Phase III trial of cytomegalovirus vaccine candidate* [Online]. Available: <https://www.clinicaltrialsarena.com/news/moderna-trial-cytomegalovirus-vaccine/> [Accessed 20/2/2023].
- CLINICALTRIALSARENA. 2023. *Success of FluMist Quadrivalent in UK unlikely to be matched in Japan* [Online]. Available: <https://www.clinicaltrialsarena.com/comment/success-flumist-uk-japan/?cf-view> [Accessed 23/10/23].
- COFFMAN, R. L., SHER, A. & SEDER, R. A. 2010. Vaccine adjuvants: putting innate immunity to work. *Immunity*, 33, 492-503.

- COMPCHEMS. 2022. *Molecular Dynamics: Ensembles* [Online]. Available: <https://www.compchems.com/molecular-dynamics-ensembles/#the-microcanonical-ensemble-nve> [Accessed 4/5/2023].
- CUCINOTTA, D. & VANELLI, M. 2020. WHO Declares COVID-19 a Pandemic. *Acta Biomed*, 91, 157-160.
- CZITROM, V. 1999. One-Factor-at-a-Time versus Designed Experiments. *The American Statistician*, 53, 126-131.
- DANIEL, S., ANA COLETTE, M., VITOR, S., JOSÉ DOMINGOS, S., MARIA, H. F. & PEDRO, S. G. 2017. Spray Drying: An Overview. In: ROSARIO, P. & TERESA, M. (eds.) *Biomaterials*. Rijeka: IntechOpen.
- DARAEI, H., ETEMADI, A., KOUHI, M., ALIMIRZALU, S. & AKBARZADEH, A. 2016. Application of liposomes in medicine and drug delivery. *Artificial Cells, Nanomedicine, and Biotechnology*, 44, 381-391.
- DAS, M. K., ARORA, N. K., MATHEW, T., VYAS, B., DEVI, S. K. & YADAV, A. 2020. Temperature integrity and exposure of vaccines to suboptimal temperatures in cold chain devices at different levels in three states of India. *Trop Dis Travel Med Vaccines*, 6, 8.
- DEGENHARD, M., GERALT, W. & MATTHIAS, B. 2015. Intranasal Drug Administration — An Attractive Delivery Route for Some Drugs. In: OMBOON, V. & SULEIMAN, O. (eds.) *Drug Discovery and Development*. Rijeka: IntechOpen.
- DENG, S., LIANG, H., CHEN, P., LI, Y., LI, Z., FAN, S., WU, K., LI, X., CHEN, W., QIN, Y., YI, L. & CHEN, J. 2022. Viral Vector Vaccine Development and Application during the COVID-19 Pandemic. *Microorganisms*, 10.
- DIDIERLAURENT, A. M., MOREL, S., LOCKMAN, L., GIANNINI, S. L., BISTEAU, M., CARLSEN, H., KIELLAND, A., VOSTERS, O., VANDERHEYDE, N., SCHIAVETTI, F., LAROCQUE, D., VAN MECHELEN, M. & GARÇON, N. 2009. AS04, an Aluminum Salt- and TLR4 Agonist-Based Adjuvant System, Induces a Transient Localized Innate Immune Response Leading to Enhanced Adaptive Immunity. *The Journal of Immunology*, 183, 6186.
- DOMINICI, S., MARESCOTTI, F., SANMARTIN, C., MACALUSO, M., TAGLIERI, I., VENTURI, F., ZINNAI, A. & FACIONI, M. S. 2022. Lactose: Characteristics, Food and Drug-Related Applications, and Its Possible Substitutions in Meeting the Needs of People with Lactose Intolerance. *Foods*, 11.
- DUMPA, N., GOEL, K., GUO, Y., MCFALL, H., PILLAI, A. R., SHUKLA, A., REPKA, M. A. & MURTHY, S. N. 2019. Stability of Vaccines. *AAPS PharmSciTech*, 20, 42.
- DURRANT, J. D. & MCCAMMON, J. A. 2011. Molecular dynamics simulations and drug discovery. *BMC Biology*, 9, 71.
- DYAKIN, V. V. & UVERSKY, V. N. 2022. Arrow of Time, Entropy, and Protein Folding: Holistic View on Biochirality. *International Journal of Molecular Sciences* [Online], 23.
- DYKMAN, L. A. & KHLEBTSOV, N. G. 2017. Immunological properties of gold nanoparticles. *Chemical Science*, 8, 1719-1735.
- DYKMAN, L. A., STAROVEROV, S. A., FOMIN, A. S., KHANADEV, V. A., KHLEBTSOV, B. N. & BOGATYREV, V. A. 2018. Gold nanoparticles as an adjuvant: Influence of size, shape, and technique of combination with CpG on antibody production. *International Immunopharmacology*, 54, 163-168.
- D'AMICO, C., FONTANA, F., CHENG, R. & SANTOS, H. A. 2021. Development of vaccine formulations: past, present, and future. *Drug Delivery and Translational Research*, 11, 353-372.

- EISENBARTH, S. C., COLEGIO, O. R., O'CONNOR, W., SUTTERWALA, F. S. & FLAVELL, R. A. 2008. Crucial role for the Nalp3 inflammasome in the immunostimulatory properties of aluminium adjuvants. *Nature*, 453, 1122-6.
- EL RIDI, R. & TALLIMA, H. 2017. Physiological functions and pathogenic potential of uric acid: A review. *J Adv Res*, 8, 487-493.
- EL-KAMARY, S. S., PASETTI, M. F., MENDELMAN, P. M., FREY, S. E., BERNSTEIN, D. I., TREANOR, J. J., FERREIRA, J., CHEN, W. H., SUBLETT, R., RICHARDSON, C., BARGATZE, R. F., SZTEIN, M. B. & TACKET, C. O. 2010. Adjuvanted intranasal Norwalk virus-like particle vaccine elicits antibodies and antibody-secreting cells that express homing receptors for mucosal and peripheral lymphoid tissues. *J Infect Dis*, 202, 1649-58.
- EMAMI, F. S., PUDDU, V., BERRY, R. J., VARSHNEY, V., PATWARDHAN, S. V., PERRY, C. C. & HEINZ, H. 2014. Force Field and a Surface Model Database for Silica to Simulate Interfacial Properties in Atomic Resolution. *Chemistry of Materials*, 26, 2647-2658.
- ERDŐ, F., BORS, L. A., FARKAS, D., BAJZA, Á. & GIZURARSON, S. 2018. Evaluation of intranasal delivery route of drug administration for brain targeting. *Brain Research Bulletin*, 143, 155-170.
- ERIKSSON, A. M., SCHÖN, K. M. & LYCKE, N. Y. 2004. The cholera toxin-derived CTA1-DD vaccine adjuvant administered intranasally does not cause inflammation or accumulate in the nervous tissues. *J Immunol*, 173, 3310-9.
- ESSINK, B., CHU, L., SEGER, W., BARRANCO, E., LE CAM, N., BENNETT, H., FAUGHNAN, V., PAJON, R., PAILA, Y. D., BOLLMAN, B., WANG, S., DOOLEY, J., KALIDINDI, S. & LEAV, B. 2023. The safety and immunogenicity of two Zika virus mRNA vaccine candidates in healthy flavivirus baseline seropositive and seronegative adults: the results of two randomised, placebo-controlled, dose-ranging, phase 1 clinical trials. *The Lancet Infectious Diseases*.
- ESSMANN, U., PERERA, L., BERKOWITZ, M. L., DARDEN, T., LEE, H. & PEDERSEN, L. G. 1995. A smooth particle mesh Ewald method. *The Journal of Chemical Physics*, 103, 8577-8593.
- ESTEPHAN, Z. G., SCHLENOFF, P. S. & SCHLENOFF, J. B. 2011. Zwitteration as an alternative to PEGylation. *Langmuir*, 27, 6794-800.
- FAHRNI, M. L., ISMAIL, I. A.-N., REFI, D. M., ALMEMAN, A., YAAKOB, N. C., SAMAN, K. M., MANSOR, N. F., NOORDIN, N. & BABAR, Z.-U.-D. 2022. Management of COVID-19 vaccines cold chain logistics: a scoping review. *Journal of Pharmaceutical Policy and Practice*, 15, 16.
- FALSEY, A. R., SOBIESZCZYK, M. E., HIRSCH, I., SPROULE, S., ROBB, M. L., COREY, L., NEUZIL, K. M., HAHN, W., HUNT, J., MULLIGAN, M. J., MCEVOY, C., DEJESUS, E., HASSMAN, M., LITTLE, S. J., PAHUD, B. A., DURBIN, A., PICKRELL, P., DAAR, E. S., BUSH, L., SOLIS, J., CARR, Q. O., OYEDELE, T., BUCHBINDER, S., COWDEN, J., VARGAS, S. L., GUERREROS BENAVIDES, A., CALL, R., KEEFER, M. C., KIRKPATRICK, B. D., PULLMAN, J., TONG, T., BREWINSKI ISAACS, M., BENKESER, D., JANES, H. E., NASON, M. C., GREEN, J. A., KELLY, E. J., MAASKE, J., MUELLER, N., SHOEMAKER, K., TAKAS, T., MARSHALL, R. P., PANGALOS, M. N., VILLAFANA, T. & GONZALEZ-LOPEZ, A. 2021. Phase 3 Safety and Efficacy of AZD1222 (ChAdOx1 nCoV-19) Covid-19 Vaccine. *New England Journal of Medicine*, 385, 2348-2360.
- FARAFONOV, V. G., VINOKUROV, A. A. & BARKANOV, S. V. 2011. Electrostatic solution and rayleigh approximation for small nonspherical particles in a spheroidal basis. *Optics and Spectroscopy*, 111, 980-992.



- FAROUQ, M. A. H., AL QARAGHULI, M. M., KUBIAK-OSSOWSKA, K., FERRO, V. A. & MULHERAN, P. A. 2021. Biomolecular interactions with nanoparticles: applications for coronavirus disease 2019. *Current Opinion in Colloid & Interface Science*, 54, 101461.
- FAROUQ, M. A. H., KUBIAK-OSSOWSKA, K., AL QARAGHULI, M. M., FERRO, V. A. & MULHERAN, P. A. 2022. Functionalisation of Inorganic Material Surfaces with Staphylococcus Protein A: A Molecular Dynamics Study. *International Journal of Molecular Sciences* [Online], 23.
- FATFAT, Z., KARAM, M., MAATOUK, B., FAHS, D. & GALI-MUHTASIB, H. 2023. Chapter 7 - Nanoliposomes as safe and efficient drug delivery nanovesicles. In: NAYAK, A. K., HASNAIN, M. S., LAHA, B. & MAITI, S. (eds.) *Advanced and Modern Approaches for Drug Delivery*. Academic Press.
- FEECO. *Co-Current vs Counter Current Drying* [Online]. Available: <https://feeco.com/co-current-vs-counter-current-drying/#:~:text=Counter%2Dcurrent%20dryers%20are%20often,exhaust%20gas%20temperature%20remains%20high>. [Accessed 18/4/2024].
- FELLER, S. E., ZHANG, Y., PASTOR, R. W. & BROOKS, B. R. 1995. Constant pressure molecular dynamics simulation: The Langevin piston method. *The Journal of Chemical Physics*, 103, 4613-4621.
- FENG, J., PANDEY, R. B., BERRY, R. J., FARMER, B. L., NAIK, R. R. & HEINZ, H. 2011. Adsorption mechanism of single amino acid and surfactant molecules to Au {111} surfaces in aqueous solution: design rules for metal-binding molecules. *Soft Matter*, 7, 2113-2120.
- FERNANDO, I. & ZHOU, Y. 2019. Impact of pH on the stability, dissolution and aggregation kinetics of silver nanoparticles. *Chemosphere*, 216, 297-305.
- FERRUCCI, P. F., PALA, L., CONFORTI, F. & COCOROCCHIO, E. 2021. Talimogene Laherparepvec (T-VEC): An Intralesional Cancer Immunotherapy for Advanced Melanoma. *Cancers* [Online], 13.
- FLUMISTQUADRIVALENT. 2022. *Nasal Spray Flu Vaccine* [Online]. Available: <https://www.flumistquadrivalent.com/> [Accessed 27/7/23].
- FORTPIED, J., WAUTERS, F., ROCHART, C., HERMAND, P., HOET, B., MONIOTTE, N. & VOJTEK, I. 2018. Stability of an aluminum salt-adjuvanted protein D-conjugated pneumococcal vaccine after exposure to subzero temperatures. *Hum Vaccin Immunother*, 14, 1243-1250.
- FRANCHI, L. & NÚÑEZ, G. 2008. The Nlrp3 inflammasome is critical for aluminium hydroxide-mediated IL-1beta secretion but dispensable for adjuvant activity. *European journal of immunology*, 38, 2085-2089.
- FREEMAN, D., LAMBE, S., YU, L. M., FREEMAN, J., CHADWICK, A., VACCARI, C., WAITE, F., ROSEBROCK, L., PETIT, A., VANDERSLOTT, S., LEWANDOWSKY, S., LARKIN, M., INNOCENTI, S., MCSHANE, H., POLLARD, A. J. & LOE, B. S. 2021. Injection fears and COVID-19 vaccine hesitancy. *Psychol Med*, 1-11.
- FREYTAG, L. C. & CLEMENTS, J. D. 2015. Chapter 61 - Mucosal Adjuvants: New Developments and Challenges. In: MESTECKY, J., STROBER, W., RUSSELL, M. W., KELSALL, B. L., CHEROUTRE, H. & LAMBRECHT, B. N. (eds.) *Mucosal Immunology (Fourth Edition)*. Boston: Academic Press.
- FU, P. P., XIA, Q., HWANG, H.-M., RAY, P. C. & YU, H. 2014. Mechanisms of nanotoxicity: Generation of reactive oxygen species. *Journal of Food and Drug Analysis*, 22, 64-75.

- FU, Y., ZHAO, J., WEI, X., HAN, P., YANG, L., REN, T., ZHAN, S. & LI, L. 2022. Effectiveness and Cost-Effectiveness of Inactivated Vaccine to Address COVID-19 Pandemic in China: Evidence From Randomized Control Trials and Real-World Studies. *Front Public Health*, 10, 917732.
- FUJIMURA, R. 2022. *Without COVID-19 vaccines, death toll would be much higher: Pfizer analysis* [Online]. Available: <https://abcnews.go.com/Health/covid-19-vaccines-death-toll-higher-pfizer-analysis/story?id=84741599> [Accessed 26/07/2022].
- FURST, D., FELSON, D., THOREN, G., GENDREAU, R. M. & FOR THE PROSORBA TRIAL, I. 2000. Immunoabsorption for the Treatment of Rheumatoid Arthritis: Final Results of a Randomized Trial. *Therapeutic Apheresis*, 4, 363-373.
- GADADE, D. D. & PEKAMWAR, S. S. 2020. Cyclodextrin Based Nanoparticles for Drug Delivery and Theranostics. *Adv Pharm Bull*, 10, 166-183.
- GALAGALI, P. M., KINIKAR, A. A. & KUMAR, V. S. 2022. Vaccine Hesitancy: Obstacles and Challenges. *Curr Pediatr Rep*, 10, 241-248.
- GAO, H., SHI, W. & FREUND, L. B. 2005. Mechanics of receptor-mediated endocytosis. *Proceedings of the National Academy of Sciences of the United States of America*, 102, 9469.
- GARRIDO, P. F., CALVELO, M., BLANCO-GONZÁLEZ, A., VELEIRO, U., SUÁREZ, F., CONDE, D., CABEZÓN, A., PIÑEIRO, Á. & GARCIA-FANDINO, R. 2020. The Lord of the NanoRings: Cyclodextrins and the battle against SARS-CoV-2. *International Journal of Pharmaceutics*, 588, 119689.
- GASPAR, F. 2014. *Spray Drying In The Pharmaceutical Industry* [Online]. EuropeanPharmaceuticalReview. Available: <https://www.europeanpharmaceuticalreview.com/article/27768/spray-drying-pharmaceutical-industry/> [Accessed].
- GAVI. *What are viral vector-based vaccines and how could they be used against COVID-19?* [Online]. Available: <https://www.gavi.org/vaccineswork/what-are-viral-vector-based-vaccines-and-how-could-they-be-used-against-covid-19> [Accessed 28th July 2022].
- GEISSHÜSLER, S., SCHINEIS, P., LANGER, L., WÄCKERLE-MEN, Y., LEROUX, J.-C., HALIN, C., VOGEL-KINDGEN, S., JOHANSEN, P. & GANDER, B. 2022. Amphiphilic Cyclodextrin-Based Nanoparticulate Vaccines Can Trigger T-Cell Immune Responses. *Advanced NanoBiomed Research*, 2, 2100082.
- GELPERINA, S., KISICH, K., ISEMAN, M. D. & HEIFETS, L. 2005. The potential advantages of nanoparticle drug delivery systems in chemotherapy of tuberculosis. *American journal of respiratory and critical care medicine*, 172, 1487-1490.
- GEMMA, E., PIERGIUSEPPE, V. & COSTANTINO, E. 2017. Staphylococcal Protein A as a Pharmacological Treatment for Autoimmune Disorders. *Journal of Autoimmune Disorders*, 3.
- GHASEMIYEH, P. & MOHAMMADI-SAMANI, S. 2018. Solid lipid nanoparticles and nanostructured lipid carriers as novel drug delivery systems: applications, advantages and disadvantages. *Res Pharm Sci*, 13, 288-303.
- GHERARDI, R. K., EIDI, H., CRÉPEAUX, G., AUTHIER, F. J. & CADUSSEAU, J. 2015. Biopersistence and brain translocation of aluminum adjuvants of vaccines. *Front Neurol*, 6, 4.
- GOHEL, M., PARIKH, R. K., NAGORI, S. A., GANDHI, A. V., SHROFF, M. S., PATEL, P. K., GANDHI, C. S., PATEL, V., BHAGAT, N. Y., POPTANI, S. D., KHARADI, S. R., PANDYA, R. & PATEL, T. C. 2009. Spray drying: A review. *Pharmaceutical Reviews*, 7.

- GOLDING, C. G., LAMBOO, L. L., BENIAC, D. R. & BOOTH, T. F. 2016. The scanning electron microscope in microbiology and diagnosis of infectious disease. *Scientific Reports*, 6, 26516.
- GOODSWEN, S. J., KENNEDY, P. J. & ELLIS, J. T. 2023. A state-of-the-art methodology for high-throughput in silico vaccine discovery against protozoan parasites and exemplified with discovered candidates for *Toxoplasma gondii*. *Scientific Reports*, 13, 8243.
- GRAILLE, M., STURA, E. A., CORPER, A. L., SUTTON, B. J., TAUSSIG, M. J., CHARBONNIER, J. B. & SILVERMAN, G. J. 2000. Crystal structure of a *Staphylococcus aureus* protein A domain complexed with the Fab fragment of a human IgM antibody: structural basis for recognition of B-cell receptors and superantigen activity. *Proceedings of the National Academy of Sciences of the United States of America*, 97, 5399-5404.
- GRANOFF, D. M., PELTON, S. & HARRISON, L. H. 2013. 21 - Meningococcal vaccines. In: PLOTKIN, S. A., ORENSTEIN, W. A. & OFFIT, P. A. (eds.) *Vaccines (Sixth Edition)*. London: W.B. Saunders.
- GROTTESE, A., BEŠKER, N., EMERSON, A., MANELFI, C., BECCARI, A. R., FRIGERIO, F., LINDAHL, E., CERCHIA, C. & TALARICO, C. 2020. Computational Studies of SARS-CoV-2 3CLpro: Insights from MD Simulations. *International journal of molecular sciences*, 21, 5346.
- GSK. 2009a. *Pandemic (H1N1) 2009 Influenza Update: Experience of GSK's H1N1 adjuvanted vaccine, Pandemrix™, and preliminary paediatric results* [Online]. Available: [https://web.archive.org/web/20091029160027/http://www.gsk.com/media/pressreleases/2009/2009\\_pressrelease\\_10116.htm](https://web.archive.org/web/20091029160027/http://www.gsk.com/media/pressreleases/2009/2009_pressrelease_10116.htm) [Accessed 04/12/2022].
- GSK. 2009b. *Pandemic (H1N1) 2009 Influenza Update: Results from second clinical trial of GSK's H1N1 adjuvanted vaccine confirm immune response and tolerability* [Online]. Available: [https://web.archive.org/web/20091031103005/http://www.gsk.com/media/pressreleases/2009/2009\\_pressrelease\\_10111.htm](https://web.archive.org/web/20091031103005/http://www.gsk.com/media/pressreleases/2009/2009_pressrelease_10111.htm) [Accessed 04/12/2022].
- GUERRINI, G., MAGRÌ, D., GIORIA, S., MEDAGLINI, D. & CALZOLAI, L. 2022. Characterization of nanoparticles-based vaccines for COVID-19. *Nature Nanotechnology*, 17, 570-576.
- GUI, M., LIU, X., GUO, D., ZHANG, Z., YIN, C.-C., CHEN, Y. & XIANG, Y. 2017. Electron microscopy studies of the coronavirus ribonucleoprotein complex. *Protein & Cell*, 8.
- GUVENCH, O. & MACKERELL, A. D. 2008. Comparison of Protein Force Fields for Molecular Dynamics Simulations. In: KUKOL, A. (ed.) *Molecular Modeling of Proteins*. Totowa, NJ: Humana Press.
- HADFIELD, T. L., MCEVOY, P., POLOTSKY, Y., TZINSERLING, V. A. & YAKOVLEV, A. A. 2000. The Pathology of Diphtheria. *The Journal of Infectious Diseases*, 181, S116-S120.
- HAN, B., GUO, J., ABRAHALEY, T., QIN, L., WANG, L., ZHENG, Y., LI, B., LIU, D., YAO, H., YANG, J., LI, C., XI, Z. & YANG, X. 2011. Adverse Effect of Nano-Silicon Dioxide on Lung Function of Rats with or without Ovalbumin Immunization. *PLOS ONE*, 6, e17236.
- HANLEY, B., NARESH, K. N., ROUFOSSE, C., NICHOLSON, A. G., WEIR, J., COOKE, G. S., THURSZ, M., MANOUSOU, P., CORBETT, R., GOLDIN, R., AL-SARRAJ, S., ABDOLRASOULI, A., SWANN, O. C., BAILLON, L., PENN, R., BARCLAY, W. S., VIOLA, P. & OSBORN, M. 2020. Histopathological findings and viral tropism in UK patients with severe fatal COVID-19: a post-mortem study. *The Lancet Microbe*, 1, e245-e253.

- HANLEY, K. A. 2011. The double-edged sword: How evolution can make or break a live-attenuated virus vaccine. *Evolution (N Y)*, 4, 635-643.
- HARRISON, R. L. 2010. Introduction To Monte Carlo Simulation. *AIP Conf Proc*, 1204, 17-21.
- HARVEY, W. T., CARABELLI, A. M., JACKSON, B., GUPTA, R. K., THOMSON, E. C., HARRISON, E. M., LUDDEN, C., REEVE, R., RAMBAUT, A., PEACOCK, S. J., ROBERTSON, D. L. & CONSORTIUM, C.-G. U. 2021. SARS-CoV-2 variants, spike mutations and immune escape. *Nature Reviews Microbiology*, 19, 409-424.
- HASSANZADEH, P. 2020. Nanotheranostics against COVID-19: From multivalent to immune-targeted materials. *Journal of Controlled Release*, 328, 112-126.
- HE, P., ZOU, Y. & HU, Z. 2015. Advances in aluminum hydroxide-based adjuvant research and its mechanism. *Hum Vaccin Immunother*, 11, 477-88.
- HEBBINK, G. A., JASPERS, M., PETERS, H. J. W. & DICKHOFF, B. H. J. 2022. Recent developments in lactose blend formulations for carrier-based dry powder inhalation. *Advanced Drug Delivery Reviews*, 189, 114527.
- HEIDARY, M., KAVIAR, V. H., SHIRANI, M., GHANAVATI, R., MOTAHAR, M., SHOLEH, M., GHAHRAMANPOUR, H. & KHOSHNOOD, S. 2022. A Comprehensive Review of the Protein Subunit Vaccines Against COVID-19. *Front Microbiol*, 13, 927306.
- HEINZ, H., FARMER, B. L., PANDEY, R. B., SLOCIK, J. M., PATNAIK, S. S., PACHTER, R. & NAIK, R. R. 2009. Nature of Molecular Interactions of Peptides with Gold, Palladium, and Pd-Au Bimetal Surfaces in Aqueous Solution. *Journal of the American Chemical Society*, 131, 9704-9714.
- HEINZ, H., VAIA, R. A., FARMER, B. L. & NAIK, R. R. 2008. Accurate Simulation of Surfaces and Interfaces of Face-Centered Cubic Metals Using 12-6 and 9-6 Lennard-Jones Potentials. *The Journal of Physical Chemistry C*, 112, 17281-17290.
- HENRIQUES, P., FORTUNA, A. & DOKTOROVOVÁ, S. 2022. Spray dried powders for nasal delivery: Process and formulation considerations. *European Journal of Pharmaceutics and Biopharmaceutics*, 176, 1-20.
- HERSCHLAG, D. & PINNEY, M. M. 2018. Hydrogen Bonds: Simple after All? *Biochemistry*, 57, 3338-3352.
- HLADY, V. V. & BUIJS, J. 1996. Protein adsorption on solid surfaces. *Current opinion in biotechnology*, 7, 72-77.
- HO, B. K., THOMAS, A. & BRASSEUR, R. 2003. Revisiting the Ramachandran plot: hard-sphere repulsion, electrostatics, and H-bonding in the alpha-helix. *Protein Sci*, 12, 2508-22.
- HOFFMAN, W., LAKKIS, F. G. & CHALASANI, G. 2016. B Cells, Antibodies, and More. *Clinical Journal of the American Society of Nephrology*, 11, 137.
- HOGENESCH, H. 2002. Mechanisms of stimulation of the immune response by aluminum adjuvants. *Vaccine*, 20 Suppl 3, S34-9.
- HOGENESCH, H. 2013. Mechanism of Immunopotential and Safety of Aluminum Adjuvants. *Frontiers in Immunology*, 3.
- HOLLINGSWORTH, S. A. & DROR, R. O. 2018. Molecular Dynamics Simulation for All. *Neuron*, 99, 1129-1143.
- HOMAYUN, B., LIN, X. & CHOI, H.-J. 2019. Challenges and Recent Progress in Oral Drug Delivery Systems for Biopharmaceuticals. *Pharmaceutics*, 11, 129.
- HONARY, S. & ZAHIR, F. 2013. Effect of Zeta Potential on the Properties of Nano-Drug Delivery Systems - A Review (Part 1). *Tropical Journal of Pharmaceutical Research*, 12.

- HOOFT, R. W. W., SANDER, C. & VRIEND, G. 1997. Objectively judging the quality of a protein structure from a Ramachandran plot. *Bioinformatics*, 13, 425-430.
- HOSPITAL, A., GOÑI, J. R., OROZCO, M. & GELPÍ, J. L. 2015. Molecular dynamics simulations: advances and applications. *Advances and applications in bioinformatics and chemistry : AABC*, 8, 37-47.
- HU, B., GUO, H., ZHOU, P. & SHI, Z.-L. 2021. Characteristics of SARS-CoV-2 and COVID-19. *Nature Reviews Microbiology*, 19, 141-154.
- HUANG, B., LIU, F.-F., DONG, X.-Y. & SUN, Y. 2011. Molecular Mechanism of the Affinity Interactions between Protein A and Human Immunoglobulin G1 Revealed by Molecular Simulations. *The Journal of Physical Chemistry B*, 115, 4168-4176.
- HUANG, L. X. & MUJUMDAR, A. S. 2008. The Effect of Rotary Disk Atomizer RPM on Particle Size Distribution in a Semi-Industrial Spray Dryer. *Drying Technology*, 26, 1319-1325.
- HUANG, M., ZHANG, M., ZHU, H., DU, X. & WANG, J. 2022a. Mucosal vaccine delivery: A focus on the breakthrough of specific barriers. *Acta Pharmaceutica Sinica B*, 12, 3456-3474.
- HUANG, Y., LI, P., ZHAO, R., ZHAO, L., LIU, J., PENG, S., FU, X., WANG, X., LUO, R., WANG, R. & ZHANG, Z. 2022b. Silica nanoparticles: Biomedical applications and toxicity. *Biomedicine & Pharmacotherapy*, 151, 113053.
- HUGHES, Z. E., KOCHANDRA, R. & WALSH, T. R. 2017. Facet-Specific Adsorption of Tripeptides at Aqueous Au Interfaces: Open Questions in Reconciling Experiment and Simulation. *Langmuir*, 33, 3742-3754.
- HUMPHREY, W., DALKE, A. & SCHULTEN, K. 1996. VMD: Visual molecular dynamics. *Journal of Molecular Graphics*, 14, 33-38.
- HUYGE, K., VAN REETH, K., DE BEER, T., LANDMAN, W. J., VAN ECK, J. H., REMON, J. P. & VERVAET, C. 2012. Suitability of differently formulated dry powder Newcastle disease vaccines for mass vaccination of poultry. *Eur J Pharm Biopharm*, 80, 649-56.
- HÜNENBERGER, P. H. 2005. Thermostat Algorithms for Molecular Dynamics Simulations. In: DR. HOLM, C. & PROF. DR. KREMER, K. (eds.) *Advanced Computer Simulation: Approaches for Soft Matter Sciences I*. Berlin, Heidelberg: Springer Berlin Heidelberg.
- IDRISS, H. T. & NAISMITH, J. H. 2000. TNF alpha and the TNF receptor superfamily: structure-function relationship(s). *Microsc Res Tech*, 50, 184-95.
- ILANGOVAN, U., TON-THAT, H., IWAHARA, J., SCHNEEWIND, O. & CLUBB, R. T. 2001. Structure of sortase, the transpeptidase that anchors proteins to the cell wall of *Staphylococcus aureus*. *Proceedings of the National Academy of Sciences*, 98, 6056-6061.
- IMIG, J. D. 2022. SARS-CoV-2 spike protein causes cardiovascular disease independent of viral infection. *Clin Sci (Lond)*, 136, 431-434.
- INTRAVACC. 2022. *Intravacc launches phase I clinical trial of Avacc® 10, an intranasal subunit booster vaccine for SARS-CoV-2* [Online]. Available: <https://www.intravacc.nl/blog/intravacc-launches-phase-i-clinical-trial-of-avaccr-10> [Accessed 19/1/24].
- IZADI, S. & ONUFRIEV, A. V. 2016. Accuracy limit of rigid 3-point water models. *J Chem Phys*, 145, 074501.
- JANKOVIC, A., CHAUDHARY, G. & GOIA, F. 2021. Designing the design of experiments (DOE) – An investigation on the influence of different factorial designs on the characterization of complex systems. *Energy and Buildings*, 250, 111298.

- JANSSEN, P. H. M., BISHARAT, L. M. N. & BASTIAANSEN, M. 2023. Complexities related to the amorphous content of lactose carriers. *Int J Pharm X*. © 2023 The Authors. Published by Elsevier B.V.
- Jl, Q., PELLENQ, R. J. M. & VAN VLIET, K. J. 2012. Comparison of computational water models for simulation of calcium–silicate–hydrate. *Computational Materials Science*, 53, 234-240.
- JIAO, J. & ZHANG, L. 2019. Influence of Intranasal Drugs on Human Nasal Mucociliary Clearance and Ciliary Beat Frequency. *Allergy Asthma Immunol Res*, 11, 306-319.
- JORGENSEN, W. L., CHANDRASEKHAR, J., MADURA, J. D., IMPEY, R. W. & KLEIN, M. L. 1983. Comparison of simple potential functions for simulating liquid water. *The Journal of Chemical Physics*, 79, 926-935.
- JOSEPH, E. & SINGHVI, G. 2019. Chapter 4 - Multifunctional nanocrystals for cancer therapy: a potential nanocarrier. In: GRUMEZESCU, A. M. (ed.) *Nanomaterials for Drug Delivery and Therapy*. William Andrew Publishing.
- JULIÁN, Q., ANA, N., GELMY, C. & JOHN, R. 2017. Vegetable Proteins: Non-sensitizing Encapsulation Agents for Bioactive Compounds. In: SEYYED SHAMSADIN, A. (ed.) *Allergen*. Rijeka: IntechOpen.
- KAFETZIS, K. N., PAPALAMPROU, N., MCNULTY, E., THONG, K. X., SATO, Y., MIRONOV, A., PUROHIT, A., WELSBY, P. J., HARASHIMA, H., YU-WAI-MAN, C. & TAGALAKIS, A. D. 2023. The Effect of Cryoprotectants and Storage Conditions on the Transfection Efficiency, Stability, and Safety of Lipid-Based Nanoparticles for mRNA and DNA Delivery. *Advanced Healthcare Materials*, n/a, 2203022.
- KANOKUDOM, S., ASSAWAKOSRI, S., SUNTRONWONG, N., AUPHIMAI, C., NILYANIMIT, P., VICHAIWATTANA, P., THONGMEE, T., YORSAENG, R., SRIMUAN, D., THATSANATORN, T., KLINFUENG, S., SUDHINARASET, N., WANLAPAKORN, N., HONSAWEK, S. & POOVORAWAN, Y. 2022. Safety and Immunogenicity of the Third Booster Dose with Inactivated, Viral Vector, and mRNA COVID-19 Vaccines in Fully Immunized Healthy Adults with Inactivated Vaccine. *Vaccines (Basel)*, 10.
- KARAS, J., PAVLOKOVÁ, S., HOŘAVOVÁ, H. & GAJDZIOK, J. 2023. Optimization of Spray Drying Process Parameters for the Preparation of Inhalable Mannitol-Based Microparticles Using a Box-Behnken Experimental Design. *Pharmaceutics* [Online], 15.
- KARTOGLU, U. H., MOORE, K. L. & LLOYD, J. S. 2020. Logistical challenges for potential SARS-CoV-2 vaccine and a call to research institutions, developers and manufacturers. *Vaccine*, 38, 5393-5395.
- KE, W. R., CHANG, R. Y. K., KWOK, P. C. L., CHEN, D. & CHAN, H. K. 2020. Spray drying lactose from organic solvent suspensions for aerosol delivery to the lungs. *Int J Pharm*, 591, 119984.
- KHAN, I., SAEED, K. & KHAN, I. 2019. Nanoparticles: Properties, applications and toxicities. *Arabian Journal of Chemistry*, 12, 908-931.
- KHANDELWAL, N., KAUR, G., CHAUBEY, K. K., SINGH, P., SHARMA, S., TIWARI, A., SINGH, S. V. & KUMAR, N. 2014. Silver nanoparticles impair Peste des petits ruminants virus replication. *Virus Res*, 190, 1-7.
- KHARLAMOV, A. N., TYURNINA, A. E., VESELOVA, V. S., KOVTUN, O. P., SHUR, V. Y. & GABINSKY, J. L. 2015. Silica-gold nanoparticles for atheroprotective management of plaques: results of the NANOM-FIM trial. *Nanoscale*, 7, 8003-15.

- KHATOON, S., HAN, H. S., LEE, M., LEE, H., JUNG, D.-W., THAMBI, T., IKRAM, M., KANG, Y. M., YI, G.-R. & PARK, J. H. 2016. Zwitterionic mesoporous nanoparticles with a bioresponsive gatekeeper for cancer therapy. *Acta Biomaterialia*, 40, 282-292.
- KIANPOUR, M., AKBARIAN, M. & UVERSKY, V. N. 2022. Nanoparticles for Coronavirus Control. *Nanomaterials (Basel)*, 12.
- KIM, J., YEOM, M., LEE, T., KIM, H.-O., NA, W., KANG, A., LIM, J.-W., PARK, G., PARK, C., SONG, D. & HAAM, S. 2020. Porous gold nanoparticles for attenuating infectivity of influenza A virus. *Journal of Nanobiotechnology*, 18, 54.
- KIM, J.-H., KIM, H., CHOI, Y., LEE, D. S., KIM, J. & YI, G.-R. 2017. Colloidal Mesoporous Silica Nanoparticles as Strong Adhesives for Hydrogels and Biological Tissues. *ACS Applied Materials & Interfaces*, 9, 31469-31477.
- KLAMER, T. A., LINSCHOTEN, M. & ASSELBERGS, F. W. 2022. The benefit of vaccination against COVID-19 outweighs the potential risk of myocarditis and pericarditis. *Neth Heart J*, 30, 190-197.
- KOBAYASHI, S. D. & DELEO, F. R. 2013. Staphylococcus aureus protein A promotes immune suppression. *mBio*, 4, e00764.
- KOOL, M., PÉTRILLI, V., DE SMEDT, T., ROLAZ, A., HAMMAD, H., VAN NIMWEGEN, M., BERGEN, I. M., CASTILLO, R., LAMBRECHT, B. N. & TSCHOPP, J. 2008a. Cutting edge: alum adjuvant stimulates inflammatory dendritic cells through activation of the NALP3 inflammasome. *J Immunol*, 181, 3755-9.
- KOOL, M., SOULLIÉ, T., VAN NIMWEGEN, M., WILLART, M. A., MUSKENS, F., JUNG, S., HOOGSTEDEN, H. C., HAMMAD, H. & LAMBRECHT, B. N. 2008b. Alum adjuvant boosts adaptive immunity by inducing uric acid and activating inflammatory dendritic cells. *J Exp Med*, 205, 869-82.
- KOVACS, J. M., MANT, C. T. & HODGES, R. S. 2006. Determination of intrinsic hydrophilicity/hydrophobicity of amino acid side chains in peptides in the absence of nearest-neighbor or conformational effects. *Peptide Science*, 84, 283-297.
- KUBIAK, K. & MULHERAN, P. A. 2009. Molecular Dynamics Simulations of Hen Egg White Lysozyme Adsorption at a Charged Solid Surface. *The Journal of Physical Chemistry B*, 113, 12189-12200.
- KUBIAK-OSSOWSKA, K., BURLEY, G., PATWARDHAN, S. V. & MULHERAN, P. A. 2013. Spontaneous Membrane-Translocating Peptide Adsorption at Silica Surfaces: A Molecular Dynamics Study. *The Journal of Physical Chemistry B*, 117, 14666-14675.
- KUBIAK-OSSOWSKA, K., JACHIMSKA, B. & MULHERAN, P. A. 2016. How Negatively Charged Proteins Adsorb to Negatively Charged Surfaces: A Molecular Dynamics Study of BSA Adsorption on Silica. *The Journal of Physical Chemistry B*, 120, 10463-10468.
- KUBIAK-OSSOWSKA, K. & MULHERAN, P. A. 2012. Protein Diffusion and Long-Term Adsorption States at Charged Solid Surfaces. *Langmuir*, 28, 15577-15585.
- KUBIAK-OSSOWSKA, K., MULHERAN, P. A. & NOWAK, W. 2014. Fibronectin Module FNIII9 Adsorption at Contrasting Solid Model Surfaces Studied by Atomistic Molecular Dynamics. *The Journal of Physical Chemistry B*, 118, 9900-9908.
- KUEHNERT, M. J. & CARDO, D. M. 2000. Infections Associated with Health-care Personnel: Vaccine-preventable Diseases and Bloodborne Pathogens. *Curr Infect Dis Rep*, 2, 475-483.
- KUFAREVA, I. & ABAGYAN, R. 2012. Methods of protein structure comparison. *Methods Mol Biol*, 857, 231-57.

- KUHNHENN, M., JOENSEN, T. V., RECK, M., ROISMAN, I. V. & TROPEA, C. 2018. Study of the internal flow in a rotary atomizer and its influence on the properties of the resulting spray. *International Journal of Multiphase Flow*, 100, 30-40.
- KUMRU, O. S., JOSHI, S. B., SMITH, D. E., MIDDAGH, C. R., PRUSIK, T. & VOLKIN, D. B. 2014. Vaccine instability in the cold chain: Mechanisms, analysis and formulation strategies. *Biologicals*, 42, 237-259.
- LAKEH, M. A., KARIMVAND, S. K., KHOSHAYAND, M. R. & ABDOLLAHI, H. 2020. Analysis of residual moisture in a freeze-dried sample drug using a multivariate fitting regression model. *Microchemical Journal*, 154, 104516.
- LAM, S. D., BORDIN, N., WAMAN, V. P., SCHOLLES, H. M., ASHFORD, P., SEN, N., VAN DORP, L., RAUER, C., DAWSON, N. L., PANG, C. S. M., ABBASIAN, M., SILLITOE, I., EDWARDS, S. J. L., FRATERNALI, F., LEES, J. G., SANTINI, J. M. & ORENGO, C. A. 2020. SARS-CoV-2 spike protein predicted to form complexes with host receptor protein orthologues from a broad range of mammals. *Scientific Reports*, 10, 16471.
- LAN, J., GE, J., YU, J., SHAN, S., ZHOU, H., FAN, S., ZHANG, Q., SHI, X., WANG, Q., ZHANG, L. & WANG, X. 2020. Structure of the SARS-CoV-2 spike receptor-binding domain bound to the ACE2 receptor. *Nature*, 581, 215-220.
- LAROCCA, C. & SCHLOM, J. 2011. Viral vector-based therapeutic cancer vaccines. *Cancer J*, 17, 359-71.
- LATOURE, R. A. 2008. Molecular simulation of protein-surface interactions: benefits, problems, solutions, and future directions. *Biointerphases*, 3, Fc2-12.
- LATOURE, R. A. 2014. Perspectives on the simulation of protein-surface interactions using empirical force field methods. *Colloids Surf B Biointerfaces*, 124, 25-37.
- LE TALLEC, D., DOUCET, D., ELOUAHABI, A., HARVENGT, P., DESCHUYTENEER, M. & DESCHAMPS, M. 2009. Cervarix, the GSK HPV-16/HPV-18 AS04-adjuvanted cervical cancer vaccine, demonstrates stability upon long-term storage and under simulated cold chain break conditions. *Hum Vaccin*, 5, 467-74.
- LEE, G. M., ROMERO, J. R. & BELL, B. P. 2020. Postapproval Vaccine Safety Surveillance for COVID-19 Vaccines in the US. *JAMA*, 324, 1937-1938.
- LEE, H. G., KANG, S. & LEE, J. S. 2021. Binding characteristics of staphylococcal protein A and streptococcal protein G for fragment crystallizable portion of human immunoglobulin G. *Computational and structural biotechnology journal*, 19, 3372-3383.
- LEHMAN, S. E., MORRIS, A. S., MUELLER, P. S., SALEM, A. K., GRASSIAN, V. H. & LARSEN, S. C. 2016. Silica Nanoparticle-Generated ROS as a Predictor of Cellular Toxicity: Mechanistic Insights and Safety by Design. *Environmental science. Nano*, 3, 56-66.
- LI, J., LIU, Q., LIU, J., WU, X., LEI, Y., LI, S., ZHAO, D., LI, Z., LUO, L., PENG, S., OU, Y., YANG, H., JIN, J., LI, Y. & PENG, Y. 2022. An mRNA-based rabies vaccine induces strong protective immune responses in mice and dogs. *Virology Journal*, 19, 184.
- LI, Y.-D., CHI, W.-Y., SU, J.-H., FERRALL, L., HUNG, C.-F. & WU, T. C. 2020. Coronavirus vaccine development: from SARS and MERS to COVID-19. *Journal of Biomedical Science*, 27, 104.
- LIAMAS, E., KUBIAK-OSSOWSKA, K., BLACK, R. A., THOMAS, O. R. T., ZHANG, Z. J. & MULHERAN, P. A. 2018. Adsorption of Fibronectin Fragment on Surfaces Using Fully Atomistic Molecular Dynamics Simulations. *International Journal of Molecular Sciences* [Online], 19.
- LIANG, T. J. 2009. Hepatitis B: the virus and disease. *Hepatology*, 49, S13-21.



- LIKHACHEV, I. V., BALABAEV, N. K. & GALZITSKAYA, O. V. 2016. Available Instruments for Analyzing Molecular Dynamics Trajectories. *Open Biochem J*, 10, 1-11.
- LIN, J. H., CHANG, H. Y., KAO, W. L., LIN, K. Y., LIAO, H. Y., YOU, Y. W., KUO, Y. T., KUO, D. Y., CHU, K. J., CHU, Y. H. & SHYUE, J. J. 2014. Effect of Surface Potential on Extracellular Matrix Protein Adsorption. *Langmuir*, 30, 10328-10335.
- LIU, D. X., LIANG, J. Q. & FUNG, T. S. 2021. Human Coronavirus-229E, -OC43, -NL63, and -HKU1 (Coronaviridae). *Encyclopedia of Virology*. Copyright © 2021 Elsevier Ltd. All rights reserved.
- LIU, H., CHEN, F., SUN, H., LI, D. & HOU, T. 2017. Improving the Efficiency of Non-equilibrium Sampling in the Aqueous Environment via Implicit-Solvent Simulations. *Journal of Chemical Theory and Computation*, 13, 1827-1836.
- LIU, S., HALLER, E., HORAK, J., BRANDSTETTER, M., HEUSER, T. & LÄMMERHOFER, M. 2019. Protein A- and Protein G-gold nanoparticle bioconjugates as nano-immunoaffinity platform for human IgG depletion in plasma and antibody extraction from cell culture supernatant. *Talanta*, 194, 664-672.
- LLOYD, J., LYDON, P., OUHICHI, R. & ZAFFRAN, M. 2015. Reducing the loss of vaccines from accidental freezing in the cold chain: the experience of continuous temperature monitoring in Tunisia. *Vaccine*, 33, 902-7.
- LOBANOV, M., BOGATYREVA, N. S. & GALZITSKAIA, O. V. 2008. [Radius of gyration is indicator of compactness of protein structure]. *Mol Biol (Mosk)*, 42, 701-6.
- LOPEZ, S. M. C., SATO, A. I. & CHATTERJEE, A. 2023. Chapter 56 - Vaccines: An overview. In: BAGCHI, D., DAS, A. & DOWNS, B. W. (eds.) *Viral, Parasitic, Bacterial, and Fungal Infections*. Academic Press.
- LOUTEN, J. 2016. Chapter 8 - Vaccines, Antivirals, and the Beneficial Uses of Viruses. In: LOUTEN, J. (ed.) *Essential Human Virology*. Boston: Academic Press.
- LU, G. W. & GAO, P. 2010. CHAPTER 3 - Emulsions and Microemulsions for Topical and Transdermal Drug Delivery. In: KULKARNI, V. S. (ed.) *Handbook of Non-Invasive Drug Delivery Systems*. Boston: William Andrew Publishing.
- LU, J., LIONG, M., ZINK, J. I. & TAMANOI, F. 2007. Mesoporous Silica Nanoparticles as a Delivery System for Hydrophobic Anticancer Drugs. *Small*, 3, 1341-1346.
- LÓPEZ-VILLELLAS, L., KJELGAARD MIKKELSEN, C. C., GALANO-FRUTOS, J. J., MARCO-SOLA, S., ALASTRUEY-BENEDÉ, J., IBÁÑEZ, P., MORETÓ, M., SANCHO, J. & GARCÍA-RISUEÑO, P. 2023. Accurate and efficient constrained molecular dynamics of polymers using Newton's method and special purpose code. *Computer Physics Communications*, 288, 108742.
- LÖFGREN, A., AHLKRONA, J. & HELANOW, C. 2022. Increasing stable time-step sizes of the free-surface problem arising in ice-sheet simulations. *Journal of Computational Physics: X*, 16, 100114.
- MACARTHUR, M. W. & THORNTON, J. M. 1991. Influence of proline residues on protein conformation. *J Mol Biol*, 218, 397-412.
- MAHASE, E. 2020a. Covid-19: Moderna vaccine is nearly 95% effective, trial involving high risk and elderly people shows. *BMJ*, 371, m4471.
- MAHASE, E. 2020b. Covid-19: Pfizer and BioNTech submit vaccine for US authorisation. *BMJ*, 371, m4552.
- MALVERNANALYTICAL. 2010. *Dynamic Light Scattering: An Introduction in 30 Minutes* [Online]. Available: <https://www.malvernanalytical.com/de/learn/knowledge-center/technical-notes/tn101104dynamiclightscatteringintroduction> [Accessed 10/5/23].

- MALVERNANALYTICAL. 2013. *DTS1070 Folded Capillary Cell* [Online]. Available: <https://www.malvernpanalytical.com/kr/learn/knowledge-center/technical-notes/tn130904dts1070foldedcapillarycell> [Accessed 13/9/23].
- MALVERNANALYTICAL. 2021. *Morphologi G3* [Online]. Available: <https://www.malvernpanalytical.com/en/support/product-support/morphologi-range/morphologi-g3> [Accessed 01/12/2022].
- MALVERNANALYTICAL. 2023. *Mastersizer 3000 User Manual* [Online]. Available: <https://www.montana.edu/eal-lres/documents/Mastersizer-3000-user-manual-English-MAN0474-2-1.pdf> [Accessed 7/8/23].
- MANDELL, L. A. 2012. 297 - Streptococcus Pneumoniae Infections. In: GOLDMAN, L. & SCHAFER, A. I. (eds.) *Goldman's Cecil Medicine (Twenty Fourth Edition)*. Philadelphia: W.B. Saunders.
- MANTIS, N. J., ROL, N. & CORTHÉSY, B. 2011. Secretory IgA's complex roles in immunity and mucosal homeostasis in the gut. *Mucosal Immunology*, 4, 603-611.
- MARRACK, P., MCKEE, A. S. & MUNKS, M. W. 2009. Towards an understanding of the adjuvant action of aluminium. *Nature reviews. Immunology*, 9, 287-293.
- MARTYNA, G. J., TOBIAS, D. J. & KLEIN, M. L. 1994. Constant pressure molecular dynamics algorithms. *The Journal of Chemical Physics*, 101, 4177-4189.
- MATHÉ, C., DEVINEAU, S., AUDE, J.-C., LAGNIEL, G., CHÉDIN, S., LEGROS, V., MATHON, M.-H., RENAULT, J.-P., PIN, S., BOULARD, Y. & LABARRE, J. 2013. Structural Determinants for Protein adsorption/non-adsorption to Silica Surface. *PLOS ONE*, 8, e81346.
- MCKAY, P. F., HU, K., BLAKNEY, A. K., SAMNUAN, K., BROWN, J. C., PENN, R., ZHOU, J., BOUTON, C. R., ROGERS, P., POLRA, K., LIN, P. J. C., BARBOSA, C., TAM, Y. K., BARCLAY, W. S. & SHATTOCK, R. J. 2020. Self-amplifying RNA SARS-CoV-2 lipid nanoparticle vaccine candidate induces high neutralizing antibody titers in mice. *Nature Communications*, 11, 3523.
- MEHNDIRATTA, M. M., MEHNDIRATTA, P. & PANDE, R. 2014. Poliomyelitis: historical facts, epidemiology, and current challenges in eradication. *Neurohospitalist*, 4, 223-9.
- MEOLA, T. R., ABUHELWA, A. Y., JOYCE, P., CLIFTON, P. & PRESTIDGE, C. A. 2021. A safety, tolerability, and pharmacokinetic study of a novel simvastatin silica-lipid hybrid formulation in healthy male participants. *Drug Deliv Transl Res*, 11, 1261-1272.
- MERAD, M. & MARTIN, J. C. 2020. Pathological inflammation in patients with COVID-19: a key role for monocytes and macrophages. *Nat Rev Immunol*, 20, 355-362.
- MICROTRAC. *Mie Scattering & Mie Theory* [Online]. Available: <https://www.microtrac.com/knowledge/mie-scattering-mie-theory/> [Accessed 14/11/23].
- MILLER, A. M. 2011. Role of IL-33 in inflammation and disease. *Journal of inflammation (London, England)*, 8, 22-22.
- MILLER, E., ANDREWS, N., STELLITANO, L., STOWE, J., WINSTONE, A. M., SHNEERSON, J. & VERITY, C. 2013. Risk of narcolepsy in children and young people receiving AS03 adjuvanted pandemic A/H1N1 2009 influenza vaccine: retrospective analysis. *BMJ : British Medical Journal*, 346, f794.
- MILLS, K. H., COSGROVE, C., MCNEELA, E. A., SEXTON, A., GIEMZA, R., JABBAL-GILL, I., CHURCH, A., LIN, W., ILLUM, L., PODDA, A., RAPPUOLI, R., PIZZA, M., GRIFFIN, G. E. & LEWIS, D. J. 2003. Protective levels of diphtheria-neutralizing antibody induced in healthy volunteers by unilateral priming-boosting intranasal immunization

- associated with restricted ipsilateral mucosal secretory immunoglobulin a. *Infect Immun*, 71, 726-32.
- MISHRA, A. & RATHORE, A. S. 2021. RNA dependent RNA polymerase (RdRp) as a drug target for SARS-CoV2. *J Biomol Struct Dyn*, 1-13.
- MITCHELL, M. J., BILLINGSLEY, M. M., HALEY, R. M., WECHSLER, M. E., PEPPAS, N. A. & LANGER, R. 2021. Engineering precision nanoparticles for drug delivery. *Nature Reviews Drug Discovery*, 20, 101-124.
- MOHAMED ISA, E. D., AHMAD, H., ABDUL RAHMAN, M. B. & GILL, M. R. 2021. Progress in Mesoporous Silica Nanoparticles as Drug Delivery Agents for Cancer Treatment. *Pharmaceutics*, 13.
- MOHAN, S. V., HEMALATHA, M., KOPPERI, H., RANJITH, I. & KUMAR, A. K. 2021. SARS-CoV-2 in environmental perspective: Occurrence, persistence, surveillance, inactivation and challenges. *Chemical Engineering Journal*, 405, 126893.
- MOLLICA, V., RIZZO, A. & MASSARI, F. 2020. The pivotal role of TMPRSS2 in coronavirus disease 2019 and prostate cancer. *Future oncology (London, England)*, 16, 2029-2033.
- MOSHREF JAVADI, M., TAGHDISI HOSSEINZADEH, M., SOLEIMANI, N. & ROMMASI, F. 2022. Evaluating the immunogenicity of gold nanoparticles conjugated RBD with Freund's adjuvant as a potential vaccine against SARS-CoV-2. *Microb Pathog*, 170, 105687.
- MOYNAN, D., O'RIORDAN, R., O'CONNOR, R. & MERRY, C. 2018. Tetanus - A Rare But Real Threat. *IDCases*, 12, 16-17.
- MSI. 1998. *Molecular Dynamics* [Online]. Available: [http://www.chem.cmu.edu/courses/09-560/docs/msi/ffbsim/5\\_Dynamics.html#470244](http://www.chem.cmu.edu/courses/09-560/docs/msi/ffbsim/5_Dynamics.html#470244) [Accessed 4/5/2023].
- MULHERAN, P. A., CONNELL, D. J. & KUBIAK-OSSOWSKA, K. 2016. Steering protein adsorption at charged surfaces: electric fields and ionic screening. *RSC Advances*, 6, 73709-73716.
- MÜCKSCH, C. & URBASSEK, H. M. 2014. Enhancing protein adsorption simulations by using accelerated molecular dynamics. *PLoS One*, 8, e64883.
- MÜLLER, I., HARTMANN, D., OERTEL, J., KECK, C. M. & EICHLER, H. 2015. Static image analysis as new approach for the characterization of tumor cell lysate used in dendritic cell vaccine preparation. *Transfus Med Hemother*, 42, 122-8.
- NANDIYANTO, A. B. D., KIM, S.-G., ISKANDAR, F. & OKUYAMA, K. 2009. Synthesis of spherical mesoporous silica nanoparticles with nanometer-size controllable pores and outer diameters. *Microporous and Mesoporous Materials*, 120, 447-453.
- NANOMEDIC. 2021. *Why is the timestep so important?* [Online]. Available: <https://nanomedic.org/why-is-the-time-step-so-important/> [Accessed 9/5/23].
- NATIONALINSTITUTE OF ALLERGY AND INFECTIOUS DISEASES. 2022. *Coronaviruses* [Online]. Available: <https://www.niaid.nih.gov/diseases-conditions/coronaviruses> [Accessed 22/03/2023].
- NAVEGANTES, K. C., DE SOUZA GOMES, R., PEREIRA, P. A. T., CZAIKOSKI, P. G., AZEVEDO, C. H. M. & MONTEIRO, M. C. 2017. Immune modulation of some autoimmune diseases: the critical role of macrophages and neutrophils in the innate and adaptive immunity. *Journal of translational medicine*, 15, 36-36.
- NAYAK, S. K. 2020. Inhibition of S-protein RBD and hACE2 Interaction for Control of SARSCoV-2 Infection (COVID-19). *Mini Rev Med Chem*.
- NERIA, E., FISCHER, S. & KARPLUS, M. 1996. Simulation of activation free energies in molecular systems. *The Journal of Chemical Physics*, 105, 1902-1921.

- NEWSMEDICAL. 2021. *The Size of SARS-CoV-2 and its Implications* [Online]. Available: <https://www.news-medical.net/health/The-Size-of-SARS-CoV-2-Compared-to-Other-Things.aspx#:~:text=Upon%20analysis%20of%20negative%2Dstained,50%20nm%20to%20140%20nm.> [Accessed 5/12/23].
- NIGEL, H. 2016. UK stands by nasal flu vaccine for children as US doctors are told to stop using it. *BMJ*, 353, i3546.
- NIIKURA, K., MATSUNAGA, T., SUZUKI, T., KOBAYASHI, S., YAMAGUCHI, H., ORBA, Y., KAWAGUCHI, A., HASEGAWA, H., KAJINO, K., NINOMIYA, T., IJIRO, K. & SAWA, H. 2013. Gold Nanoparticles as a Vaccine Platform: Influence of Size and Shape on Immunological Responses in Vitro and in Vivo. *ACS Nano*, 7, 3926-3938.
- NOBBMANN, U., MORFESIS, A., BILLICA, J. & GERTIG, K. 2010. *The Role of Zeta Potential in the Optimization of Water Treatment*.
- NOHYNEK, H., JOKINEN, J., PARTINEN, M., VAARALA, O., KIRJAVAINEN, T., SUNDMAN, J., HIMANEN, S. L., HUBLIN, C., JULKUNEN, I., OLSÉN, P., SAARENPÄÄ-HEIKKILÄ, O. & KILPI, T. 2012. AS03 adjuvanted AH1N1 vaccine associated with an abrupt increase in the incidence of childhood narcolepsy in Finland. *PLoS One*, 7, e33536.
- OGANDO, N. S., ZEVENHOVEN-DOBBE, J. C., VAN DER MEER, Y., BREDENBEEK, P. J., POSTHUMA, C. C. & SNIJDER, E. J. 2020. The Enzymatic Activity of the nsp14 Exoribonuclease Is Critical for Replication of MERS-CoV and SARS-CoV-2. *Journal of Virology*, 94, e01246-20.
- OH, J. Y., KIM, H. S., PALANIKUMAR, L., GO, E. M., JANA, B., PARK, S. A., KIM, H. Y., KIM, K., SEO, J. K., KWAK, S. K., KIM, C., KANG, S. & RYU, J.-H. 2018. Cloaking nanoparticles with protein corona shield for targeted drug delivery. *Nature Communications*, 9, 4548.
- OUYANG, L., SHAIK, R., XU, R., ZHANG, G. & ZHE, J. 2021. Mapping Surface Charge Distribution of Single-Cell via Charged Nanoparticle. *Cells*, 10.
- OZBOYACI, M., KOKH, D. B., CORNI, S. & WADE, R. C. 2016. Modeling and simulation of protein–surface interactions: achievements and challenges. *Quarterly Reviews of Biophysics*, 49, e4.
- PAL, S., RAMKUMAR, B., JUGADE, S., RAO, A., NAIK, A., CHAKRABORTY, B. & VARMA, M. M. 2020. Effect of single nanoparticle-nanopore interaction strength on ionic current modulation. *Sens Actuators B Chem*, 325.
- PALAFOX-HERNANDEZ, J. P., TANG, Z., HUGHES, Z. E., LI, Y., SWIHART, M. T., PRASAD, P. N., WALSH, T. R. & KNECHT, M. R. 2014. Comparative Study of Materials-Binding Peptide Interactions with Gold and Silver Surfaces and Nanostructures: A Thermodynamic Basis for Biological Selectivity of Inorganic Materials. *Chemistry of Materials*, 26, 4960-4969.
- PARDI, N., HOGAN, M. J., PORTER, F. W. & WEISSMAN, D. 2018. mRNA vaccines — a new era in vaccinology. *Nature Reviews Drug Discovery*, 17, 261-279.
- PASQUA, L., LEGGIO, A., SISI, D., ANDÒ, S. & MORELLI, C. 2016. Mesoporous Silica Nanoparticles in Cancer Therapy: Relevance of the Targeting Function. *Mini Rev Med Chem*, 16, 743-53.
- PATEL, C. N., KUMAR, S. P., PANDYA, H. A. & RAWAL, R. M. 2020. Identification of potential inhibitors of coronavirus hemagglutinin-esterase using molecular docking, molecular dynamics simulation and binding free energy calculation. *Mol Divers*, 1-13.

- PATHER, S., MUIK, A., RIZZI, R. & MENSA, F. 2024. Developing variant-adapted COVID-19 vaccines to improve protection against Omicron and other recent variants: a plain language summary. *Expert Rev Vaccines*, 23, 463-466.
- PATIL, V. M., SINGHAL, S. & MASAND, N. 2020. A systematic review on use of aminoquinolines for the therapeutic management of COVID-19: Efficacy, safety and clinical trials. *Life Sciences*, 254, 117775.
- PATWARDHAN, S. V., EMAMI, F. S., BERRY, R. J., JONES, S. E., NAIK, R. R., DESCHAUME, O., HEINZ, H. & PERRY, C. C. 2012. Chemistry of Aqueous Silica Nanoparticle Surfaces and the Mechanism of Selective Peptide Adsorption. *Journal of the American Chemical Society*, 134, 6244-6256.
- PEARSON, L.-A., GREEN, C. J., LIN, D., PETIT, A.-P., GRAY, D. W., COWLING, V. H. & FORDYCE, E. A. F. 2021. Development of a High-Throughput Screening Assay to Identify Inhibitors of the SARS-CoV-2 Guanine-N7-Methyltransferase Using RapidFire Mass Spectrometry. *SLAS DISCOVERY: Advancing the Science of Drug Discovery*, 24725552211000652.
- PENNA, M. J., MIJAJLOVIC, M. & BIGGS, M. J. 2014. Molecular-Level Understanding of Protein Adsorption at the Interface between Water and a Strongly Interacting Uncharged Solid Surface. *Journal of the American Chemical Society*, 136, 5323-5331.
- PHILLIPS, E., PENATE-MEDINA, O., ZANZONICO, P. B., CARVAJAL, R. D., MOHAN, P., YE, Y., HUMM, J., GÖNEN, M., KALAIGIAN, H., SCHÖDER, H., STRAUSS, H. W., LARSON, S. M., WIESNER, U. & BRADBURY, M. S. 2014. Clinical translation of an ultrasmall inorganic optical-PET imaging nanoparticle probe. *Sci Transl Med*, 6, 260ra149.
- PHILLIPS, J. C., BRAUN, R., WANG, W., GUMBART, J., TAJKHORSHID, E., VILLA, E., CHIPOT, C., SKEEL, R. D., KALÉ, L. & SCHULTEN, K. 2005. Scalable molecular dynamics with NAMD. *J Comput Chem*, 26, 1781-802.
- PHILLIPS, J. C., HARDY, D. J., MAIA, J. D. C., STONE, J. E., RIBEIRO, J. V., BERNARDI, R. C., BUCH, R., FIORIN, G., HÉNIN, J., JIANG, W., MCGREEVY, R., MELO, M. C. R., RADAK, B. K., SKEEL, R. D., SINGHARROY, A., WANG, Y., ROUX, B., AKSIMENTIEV, A., LUTHEY-SCHULTEN, Z., KALÉ, L. V., SCHULTEN, K., CHIPOT, C. & TAJKHORSHID, E. 2020. Scalable molecular dynamics on CPU and GPU architectures with NAMD. *J Chem Phys*, 153, 044130.
- PIÑÓN-BALDERRAMA, C. I., LEYVA-PORRAS, C., TERÁN-FIGUEROA, Y., ESPINOSA-SOLÍS, V., ÁLVAREZ-SALAS, C. & SAAVEDRA-LEOS, M. Z. 2020. Encapsulation of Active Ingredients in Food Industry by Spray-Drying and Nano Spray-Drying Technologies. *Processes* [Online], 8.
- POLACK, F. P., THOMAS, S. J., KITCHIN, N., ABSALON, J., GURTMAN, A., LOCKHART, S., PEREZ, J. L., PÉREZ MARC, G., MOREIRA, E. D., ZERBINI, C., BAILEY, R., SWANSON, K. A., ROYCHOUDHURY, S., KOURY, K., LI, P., KALINA, W. V., COOPER, D., FRENCK, R. W., HAMMITT, L. L., TÜRECI, Ö., NELL, H., SCHAEFER, A., ÜNAL, S., TRESNAN, D. B., MATHER, S., DORMITZER, P. R., ŞAHİN, U., JANSEN, K. U. & GRUBER, W. C. 2020. Safety and Efficacy of the BNT162b2 mRNA Covid-19 Vaccine. *New England Journal of Medicine*, 383, 2603-2615.
- POLLARD, A. J. & BIJKER, E. M. 2021. A guide to vaccinology: from basic principles to new developments. *Nature Reviews Immunology*, 21, 83-100.
- PULENDRAN, B., S. ARUNACHALAM, P. & O'HAGAN, D. T. 2021. Emerging concepts in the science of vaccine adjuvants. *Nature Reviews Drug Discovery*, 20, 454-475.

- QIN, S., TANG, X., CHEN, Y., CHEN, K., FAN, N., XIAO, W., ZHENG, Q., LI, G., TENG, Y., WU, M. & SONG, X. 2022. mRNA-based therapeutics: powerful and versatile tools to combat diseases. *Signal Transduct Target Ther*, 7, 166.
- RAMACHANDRAN, G. N., RAMAKRISHNAN, C. & SASISEKHARAN, V. 1963. Stereochemistry of polypeptide chain configurations. *J Mol Biol*, 7, 95-9.
- RAMEZANPOUR, M., LEUNG, S. S. W., DELGADO-MAGNERO, K. H., BASHE, B. Y. M., THEWALT, J. & TIELEMAN, D. P. 2016. Computational and experimental approaches for investigating nanoparticle-based drug delivery systems. *Biochimica et Biophysica Acta (BBA) - Biomembranes*, 1858, 1688-1709.
- RAMOS, H. 2019. Development of a new Runge-Kutta method and its economical implementation. *Computational and Mathematical Methods*, 1, e1016.
- RAMOS, H. & VIGO-AGUIAR, J. 2007. A fourth-order Runge–Kutta method based on BDF-type Chebyshev approximations. *Journal of Computational and Applied Mathematics*, 204, 124-136.
- RAMVIKAS, M., ARUMUGAM, M., CHAKRABARTI, S. R. & JAGANATHAN, K. S. 2017. Nasal Vaccine Delivery. *Micro and Nanotechnology in Vaccine Development*. Copyright © 2017 Elsevier Inc. All rights reserved.
- RASHEDI, R., SAMIEEFAR, N., MASOUMI, N., MOHSENI, S. & REZAEI, N. 2022. COVID-19 vaccines mix-and-match: The concept, the efficacy and the doubts. *J Med Virol*, 94, 1294-1299.
- RAWAL, S. U. & PATEL, M. M. 2018. Chapter 2 - Lipid nanoparticulate systems: Modern versatile drug carriers. In: GRUMEZESCU, A. M. (ed.) *Lipid Nanocarriers for Drug Targeting*. William Andrew Publishing.
- REICHMUTH, A. M., OBERLI, M. A., JAKLENEC, A., LANGER, R. & BLANKSCHTEIN, D. 2016. mRNA vaccine delivery using lipid nanoparticles. *Ther Deliv*, 7, 319-34.
- REILLY, A. M. & TKATCHENKO, A. 2015. van der Waals dispersion interactions in molecular materials: beyond pairwise additivity. *Chemical Science*, 6, 3289-3301.
- ROSA, S. S., PRAZERES, D. M. F., AZEVEDO, A. M. & MARQUES, M. P. C. 2021. mRNA vaccines manufacturing: Challenges and bottlenecks. *Vaccine*, 39, 2190-2200.
- ROY, I., OHULCHANSKY, T. Y., PUDAVAR, H. E., BERGEY, E. J., OSEROFF, A. R., MORGAN, J., DOUGHERTY, T. J. & PRASAD, P. N. 2003. Ceramic-Based Nanoparticles Entrapping Water-Insoluble Photosensitizing Anticancer Drugs: A Novel Drug–Carrier System for Photodynamic Therapy. *Journal of the American Chemical Society*, 125, 7860-7865.
- RYBCZYNSKA, M., BAUDRY, J. & KLAUS, E. 2020. The impact of frost-damage on the quality and quantity of the secreted antigen-specific IgG repertoire. *Vaccine*, 38, 5337-5342.
- RYCKAERT, J.-P., CICCOTTI, G. & BERENDSEN, H. J. C. 1977. Numerical integration of the cartesian equations of motion of a system with constraints: molecular dynamics of n-alkanes. *Journal of Computational Physics*, 23, 327-341.
- SAIKIA, J., MOHAMMADPOUR, R., YAZDIMAMAGHANI, M., NORTHRUP, H., HLADY, V. & GHANDEHARI, H. 2018. Silica Nanoparticle-Endothelial Interaction: Uptake and Effect on Platelet Adhesion under Flow Conditions. *ACS Appl Bio Mater*, 1, 1620-1627.
- SALK, J. E. 1953. Studies in human subjects on active immunization against poliomyelitis. I. A preliminary report of experiments in progress. *J Am Med Assoc*, 151, 1081-98.
- SANCHEZ-GUZMAN, D., LE GUEN, P., VILLERET, B., SOLA, N., LE BORGNE, R., GUYARD, A., KEMMEL, A., CRESTANI, B., SALLENAVE, J. M. & GARCIA-VERDUGO, I. 2019. Silver

- nanoparticle-adjuvanted vaccine protects against lethal influenza infection through inducing BALT and IgA-mediated mucosal immunity. *Biomaterials*, 217, 119308.
- SANDMANN, F. G. & JIT, M. 2022. Rapid COVID-19 vaccine rollout: immense success but challenges ahead. *Lancet Infect Dis*, 22, 302-304.
- SASAKI, E., ASANUMA, H., MOMOSE, H., FURUHATA, K., MIZUKAMI, T. & HAMAGUCHI, I. 2021. Nasal alum-adjuvanted vaccine promotes IL-33 release from alveolar epithelial cells that elicits IgA production via type 2 immune responses. *PLOS Pathogens*, 17, e1009890.
- SCHOEMAN, D. & FIELDING, B. C. 2019. Coronavirus envelope protein: current knowledge. *Virology Journal*, 16, 69.
- SCIENCETOPIA. *Radius of Gyration* [Online]. Available: <https://www.sciencetopia.net/physics/radius-gyration> [Accessed 15/11/23].
- SEINFELD, J. H. & PANDIS, S. N. 2006. *Atmospheric Chemistry and Physics: From Air Pollution to Climate Change*, Wiley.
- SELVARAJ, C., DINESH, D. C., PANWAR, U., ABHIRAMI, R., BOURA, E. & SINGH, S. K. 2020. Structure-based virtual screening and molecular dynamics simulation of SARS-CoV-2 Guanine-N7 methyltransferase (nsp14) for identifying antiviral inhibitors against COVID-19. *Journal of Biomolecular Structure and Dynamics*, 1-12.
- SERPOOSHAN, V., MAHMOUDI, M., ZHAO, M., WEI, K., SIVANESAN, S., MOTAMEDCHABOKI, K., MALKOVSKIY, A. V., GLADSTONE, A. B., COHEN, J. E., YANG, P. C., RAJADAS, J., BERNSTEIN, D., WOO, Y. J. & RUIZ-LOZANO, P. 2015. Protein Corona Influences Cell-Biomaterial Interactions in Nanostructured Tissue Engineering Scaffolds. *Advanced functional materials*, 25, 4379-4389.
- SHEGOKAR, R. 2020. Chapter 2 - Preclinical testing—Understanding the basics first. In: SHEGOKAR, R. (ed.) *Drug Delivery Aspects*. Elsevier.
- SHIM, S. & YOO, H. S. 2020. The Application of Mucoadhesive Chitosan Nanoparticles in Nasal Drug Delivery. *Mar Drugs*, 18.
- SHIN, D., MUKHERJEE, R., GREWE, D., BOJKOVA, D., BAEK, K., BHATTACHARYA, A., SCHULZ, L., WIDERA, M., MEHDIPOUR, A. R., TASCHER, G., GEURINK, P. P., WILHELM, A., VAN DER HEDEN VAN NOORT, G. J., OVAA, H., MÜLLER, S., KNOBELOCH, K.-P., RAJALINGAM, K., SCHULMAN, B. A., CINATL, J., HUMMER, G., CIESEK, S. & DIKIC, I. 2020. Papain-like protease regulates SARS-CoV-2 viral spread and innate immunity. *Nature*.
- SIMULEON. 2021. *Implicit vs explicit finite element analysis: when to use which?* [Online]. Available: <https://info.simuleon.com/blog/implicit-vs-explicit-finite-element-analysis> [Accessed 22/12/2022].
- SINGH, R. & SONI, R. K. 2019. Chapter 11 - Laser-Induced Heating Synthesis of Hybrid Nanoparticles. In: MOHAPATRA, S., NGUYEN, T. A. & NGUYEN-TRI, P. (eds.) *Noble Metal-Metal Oxide Hybrid Nanoparticles*. Woodhead Publishing.
- SINGH, T., RÜHE, J. & BIESALSKI, M. 2016. Biocompatibility of Microsystems. *Reference Module in Materials Science and Materials Engineering*. Elsevier.
- SKRASTINA, D., PETROVSKIS, I., LIEKNINA, I., BOGANS, J., RENHOFA, R., OSE, V., DISHLERS, A., DEKHTYAR, Y. & PUMPENS, P. 2014. Silica nanoparticles as the adjuvant for the immunisation of mice using hepatitis B core virus-like particles. *PLoS One*, 9, e114006.
- SLOMSKI, A. 2022. Intranasal COVID-19 Vaccine Disappointing in First-in-Human Trial. *JAMA*, 328, 2003-2003.

- SLOWING, II, WU, C. W., VIVERO-ESCOTO, J. L. & LIN, V. S. 2009. Mesoporous silica nanoparticles for reducing hemolytic activity towards mammalian red blood cells. *Small*, 5, 57-62.
- SMUTNEY, C. C., LEONE-BAY, A., GALARZA, J. M., MUNOZ, H., MARTIN, G. R. & GRANT, M. L. 2014. *Inhalable vaccine compositions and methods*.
- SNEHA, P. & DOSS, C. G. P. 2016. Molecular Dynamics: New Frontier in Personalized Medicine. *Advances in protein chemistry and structural biology*, 102, 181-224.
- SONG, Y., WANG, Y., THAKUR, R., MEIDAN, V. M. & MICHNIAK, B. 2004. Mucosal drug delivery: membranes, methodologies, and applications. *Crit Rev Ther Drug Carrier Syst*, 21, 195-256.
- SPORTELLI, M. C., IZZI, M., KUKUSHKINA, E. A., HOSSAIN, S. I., PICCA, R. A., DITARANTO, N. & CIOFFI, N. 2020. Can Nanotechnology and Materials Science Help the Fight against SARS-CoV-2? *Nanomaterials (Basel)*, 10.
- STETEFELD, J., MCKENNA, S. A. & PATEL, T. R. 2016. Dynamic light scattering: a practical guide and applications in biomedical sciences. *Biophys Rev*, 8, 409-427.
- STROUD, A., LEUTY, G., MURATORE, C., DEROSA, P. A. & BERRY, R. 2019. Molecular dynamics simulation of the interaction of HLL peptide and 2D materials with individual residue resolution. *Computational Materials Science*, 169, 109112.
- SUBHASISH, S. 2020. Silver Nanoparticles with Bronchodilators through Nebulisation to Treat Covid 19 Patients. *Journal of Current Medical Research and Opinion*, 3, 449-450.
- SUHOBOKOV, A. 2007. Application of Monte Carlo simulation methods in risk management. *Journal of Business Economics and Management*, 8, 165-168.
- SWOPE, W. C., ANDERSEN, H. C., BERENS, P. H. & WILSON, K. R. 1982. A computer simulation method for the calculation of equilibrium constants for the formation of physical clusters of molecules: Application to small water clusters. *The Journal of Chemical Physics*, 76, 637-649.
- SYAMA, K., JAKUBEK, Z. J., CHEN, S., ZAIFMAN, J., TAM, Y. Y. C. & ZOU, S. 2022. Development of lipid nanoparticles and liposomes reference materials (II): cytotoxic profiles. *Scientific Reports*, 12, 18071.
- SYMPATEC. *Dynamic Light Scattering* [Online]. Available: [https://www.sympatec.com/en/particle-measurement/glossary/dynamic-light-scattering/#:~:text=The%20Stokes%2DEinstein%20equation%20establishes,kB%20is%20the%20Boltzmann%20constant](https://www.sympatec.com/en/particle-measurement/glossary/dynamic-light-scattering/#:~:text=The%20Stokes%2DEinstein%20equation%20establishes,kB%20is%20the%20Boltzmann%20constant.). [Accessed 12/5/23].
- SYMPATEC. *Laser Diffraction* [Online]. Available: <https://www.sympatec.com/en/particle-measurement/sensors/laser-diffraction/> [Accessed 01/12/2022].
- TABISH, T. A. & HAMBLIN, M. R. 2020. Multivalent nanomedicines to treat COVID-19: A slow train coming. *Nano Today*, 35, 100962.
- TAN, A., ESKANDAR, N. G., RAO, S. & PRESTIDGE, C. A. 2014. First in man bioavailability and tolerability studies of a silica-lipid hybrid (Lipoceramic) formulation: a Phase I study with ibuprofen. *Drug Deliv Transl Res*, 4, 212-21.
- TAVANTI, F., PEDONE, A., MATTEINI, P. & MENZIANI, M. C. 2017. Computational Insight into the Interaction of Cytochrome C with Wet and PVP-Coated Ag Surfaces. *The Journal of Physical Chemistry B*, 121, 9532-9540.
- TECHNOVAX. 2023. *Our Pipeline* [Online]. Available: <https://www.technovax.com/pipeline-1> [Accessed 23/10/23].



- THAKKAR, S. G., RUWONA, T. B., WILLIAMS, R. O. & CUI, Z. 2017. The immunogenicity of thin-film freeze-dried, aluminum salt-adjuvanted vaccine when exposed to different temperatures. *Human Vaccines & Immunotherapeutics*, 13, 936-946.
- THAKKAR, S. G., WARNKEN, Z. N., ALZHRANI, R. F., VALDES, S. A., ALDAYEL, A. M., XU, H., WILLIAMS, R. O., 3RD & CUI, Z. 2018a. Intranasal immunization with aluminum salt-adjuvanted dry powder vaccine. *J Control Release*, 292, 111-118.
- THAKKAR, S. G., XU, H., LI, X. & CUI, Z. 2018b. Uric acid and the vaccine adjuvant activity of aluminium (oxy)hydroxide nanoparticles. *Journal of drug targeting*, 26, 474-480.
- THALHAUSER, S., PETERHOFF, D., WAGNER, R. & BREUNIG, M. 2020. Presentation of HIV-1 Envelope Trimers on the Surface of Silica Nanoparticles. *Journal of Pharmaceutical Sciences*, 109, 911-921.
- THEORETICALANDCOMPUTATIONALBIOPHYSICSGROUP. *Non-bonded Interactions* [Online]. Available: <https://www.ks.uiuc.edu/Research/namd/2.10b2/ug/node23.html> [Accessed 9/5/23].
- THEORETICALANDCOMPUTATIONALBIOPHYSICSGROUP. *VMD - Visual Molecular Dynamics* [Online]. Available: <https://www.ks.uiuc.edu/Research/vmd/> [Accessed 9/5/23].
- THEORETICALANDCOMPUTATIONALBIOPHYSICSGROUP. 2002. *NAMD User's Guide* [Online]. Available: <http://www.ks.uiuc.edu/Research/namd/2.7/ug/> [Accessed 12/5/23].
- THEORETICALANDCOMPUTATIONALBIOPHYSICSGROUP. 2013. *Current NAMD Feature Summary* [Online]. Available: <http://www.ks.uiuc.edu/Research/namd/features.html> [Accessed 29/03/2023].
- THERMOFISHER. 2019. *What is SEM? Scanning Electron Microscopy Explained* [Online]. Available: <https://www.thermofisher.com/blog/materials/what-is-sem-scanning-electron-microscopy-explained/> [Accessed 01/12/2022].
- THIELMANN, A., PUTH, M.-T., KERSTING, C., PORZ, J. & WELTERMANN, B. 2019. Vaccine cold chain in general practices: A prospective study in 75 refrigerators (Keep Cool study). *PLOS ONE*, 14, e0224972.
- TIOZZO FASIOLO, L., MANNIELLO, M. D., TRATTA, E., BUTTINI, F., ROSSI, A., SONVICO, F., BORTOLOTTI, F., RUSSO, P. & COLOMBO, G. 2018. Opportunity and challenges of nasal powders: Drug formulation and delivery. *Eur J Pharm Sci*, 113, 2-17.
- TORRESI, J. & KOLLARITSCH, H. 2013. 12 - Special Adult Travel Vaccines: Yellow Fever, Meningococcal, Japanese Encephalitis, TBE, Rabies, Polio, Cholera. In: KEYSTONE, J. S., FREEDMAN, D. O., KOZARSKY, P. E., CONNOR, B. A. & NOTHDURFT, H. D. (eds.) *Travel Medicine (Third Edition)*. London: Elsevier.
- TREUEL, L. & NIENHAUS, G. U. 2012. Toward a molecular understanding of nanoparticle-protein interactions. *Biophysical reviews*, 4, 137-147.
- TRUEMAN, R. E., LAGO DOMINGUES, E., EMMETT, S. N., MURRAY, M. W. & ROUTH, A. F. 2012. Auto-stratification in drying colloidal dispersions: A diffusive model. *Journal of Colloid and Interface Science*, 377, 207-212.
- ULANOVA, M., TARKOWSKI, A., HAHN-ZORIC, M. & HANSON, L. A. 2001. The Common vaccine adjuvant aluminum hydroxide up-regulates accessory properties of human monocytes via an interleukin-4-dependent mechanism. *Infection and immunity*, 69, 1151-1159.
- ULMAN, A., EILERS, J. E. & TILLMAN, N. 1989. Packing and molecular orientation of alkanethiol monolayers on gold surfaces. *Langmuir*, 5, 1147-1152.
- UMSCHEID, C. A., MARGOLIS, D. J. & GROSSMAN, C. E. 2011. Key concepts of clinical trials: a narrative review. *Postgrad Med*, 123, 194-204.

- UNIVERSITYOFOXFORD. 2021. *Vaccine for treating cancer made possible using Oxford COVID vaccine technology* [Online]. Available: <https://www.ox.ac.uk/news/2021-09-03-vaccine-treating-cancer-made-possible-using-oxford-covid-vaccine-technology-0> [Accessed 20/2/2023].
- UNIVERSITYOFOXFORD. 2022. *Intranasal COVID-19 vaccine candidate's clinical data highlights need for further development of nasal spray vaccines* [Online]. Available: <https://www.ox.ac.uk/news/2022-10-11-intranasal-covid-19-vaccine-candidate-s-clinical-data-highlights-need-further> [Accessed 19/01/24].
- VALKENIER, H., HUISMAN, E. H., VAN HAL, P. A., DE LEEUW, D. M., CHIECHI, R. C. & HUMMELEN, J. C. 2011. Formation of High-Quality Self-Assembled Monolayers of Conjugated Dithiols on Gold: Base Matters. *Journal of the American Chemical Society*, 133, 4930-4939.
- VAN NORMAN, G. A. 2019. Phase II Trials in Drug Development and Adaptive Trial Design. *JACC Basic Transl Sci*, 4, 428-437.
- VANOMMESLAEGHE, K., HATCHER, E., ACHARYA, C., KUNDU, S., ZHONG, S., SHIM, J., DARIAN, E., GUVENCH, O., LOPES, P., VOROBYOV, I. & MACKERELL, A. D., JR. 2010. CHARMM general force field: A force field for drug-like molecules compatible with the CHARMM all-atom additive biological force fields. *J Comput Chem*, 31, 671-90.
- VAN GUNSTEREN, W. F., DAURA, X., HANSEN, N., MARK, A. E., OOSTENBRINK, C., RINIKER, S. & SMITH, L. J. 2018. Validation of Molecular Simulation: An Overview of Issues. *Angewandte Chemie International Edition*, 57, 884-902.
- VEAZEY, R. L., BOCKHORN, B., GOLDING, R. & WU, A. 2011. Evaluation of a humidity-measuring instrument for the determination of water in spray-dried flavour powders. *Flavour and Fragrance Journal*, 26, 116-121.
- VEERAMACHANENI, G. K., THUNUGUNTLA, V., BOBBILLAPATI, J. & BONDILI, J. S. 2021. Structural and simulation analysis of hotspot residues interactions of SARS-CoV 2 with human ACE2 receptor. *J Biomol Struct Dyn*, 39, 4015-4025.
- VEERAMACHANENI, G. K., THUNUGUNTLA, V. B. S. C., BOBBILLAPATI, J. & BONDILI, J. S. 2020. Structural and simulation analysis of hotspot residues interactions of SARS-CoV 2 with human ACE2 receptor. *Journal of Biomolecular Structure and Dynamics*, 1-11.
- VERLET, L. 1967. Computer "Experiments" on Classical Fluids. I. Thermodynamical Properties of Lennard-Jones Molecules. *Physical Review*, 159, 98-103.
- VICKOVIC, D., PEDERSEN, S. J., AHRNÉ, L. & HOUGAARD, A. B. 2023. Effects of lactic acid concentration and spray drying conditions on stickiness of acidified skim milk powder. *International Journal of Dairy Technology*, 76, 266-275.
- VLADILLO, G. & HASSANALI, A. 2018. Hydrogen Bonds and Life in the Universe. *Life (Basel)*, 8.
- VOX. 2021. *Here's how Covid-19 ranks among the worst plagues in history* [Online]. Available: <https://www.vox.com/future-perfect/21539483/covid-19-black-death-plagues-in-history> [Accessed 15/2/2023].
- WADU-MESTHRIGE, K., AMRO, N. A. & LIU, G.-Y. 2000. Immobilization of proteins on self-assembled monolayers. *Scanning*, 22, 380-388.
- WANG, F., KREAM, R. M. & STEFANO, G. B. 2020. An Evidence Based Perspective on mRNA-SARS-CoV-2 Vaccine Development. *Medical science monitor : international medical journal of experimental and clinical research*, 26, e924700-e924700.
- WANG, J., ZHU, R., GAO, B., WU, B., LI, K., SUN, X., LIU, H. & WANG, S. 2014. The enhanced immune response of hepatitis B virus DNA vaccine using SiO<sub>2</sub>@LDH nanoparticles as an adjuvant. *Biomaterials*, 35, 466-78.

- WANG, M., BUIST, G. & VAN DIJL, J. M. 2022. Staphylococcus aureus cell wall maintenance – the multifaceted roles of peptidoglycan hydrolases in bacterial growth, fitness, and virulence. *FEMS Microbiology Reviews*, 46, fuac025.
- WATANABE, Y., MENDONÇA, L., ALLEN, E. R., HOWE, A., LEE, M., ALLEN, J. D., CHAWLA, H., PULIDO, D., DONNELLAN, F., DAVIES, H., ULASZEWSKA, M., BELIJ-RAMMERSTORFER, S., MORRIS, S., KREBS, A.-S., DEJNIRATTISAI, W., MONGKOLSAPAYA, J., SUPASA, P., SCREATON, G. R., GREEN, C. M., LAMBE, T., ZHANG, P., GILBERT, S. C. & CRISPIN, M. 2021. Native-like SARS-CoV-2 spike glycoprotein expressed by ChAdOx1 nCoV-19/AZD1222 vaccine. *bioRxiv*, 2021.01.15.426463.
- WEI, C., WAN, L., YAN, Q., WANG, X., ZHANG, J., YANG, X., ZHANG, Y., FAN, C., LI, D., DENG, Y., SUN, J., GONG, J., WANG, Y., LI, J., YANG, H., LI, H., ZHANG, Z., WANG, R., DU, P., ZONG, Y., YIN, F., ZHANG, W., WANG, N., PENG, Y., LIN, H., FENG, J., QIN, C., CHEN, W., GAO, Q., ZHANG, R., CAO, Y. & ZHONG, H. 2020. HDL-scavenger receptor B type 1 facilitates SARS-CoV-2 entry. *Nat Metab*.
- WEINER, G. J., LIU, H. M., WOOLDRIDGE, J. E., DAHLE, C. E. & KRIEG, A. M. 1997. Immunostimulatory oligodeoxynucleotides containing the CpG motif are effective as immune adjuvants in tumor antigen immunization. *Proc Natl Acad Sci U S A*, 94, 10833-7.
- WEISSMAN, S. A. & ANDERSON, N. G. 2015. Design of Experiments (DoE) and Process Optimization. A Review of Recent Publications. *Organic Process Research & Development*, 19, 1605-1633.
- WEN, Z. S., XU, Y. L., ZOU, X. T. & XU, Z. R. 2011. Chitosan nanoparticles act as an adjuvant to promote both Th1 and Th2 immune responses induced by ovalbumin in mice. *Mar Drugs*, 9, 1038-1055.
- WINGER, M., TRZESNIAK, D., BARON, R. & VAN GUNSTEREN, W. F. 2009. On using a too large integration time step in molecular dynamics simulations of coarse-grained molecular models. *Physical Chemistry Chemical Physics*, 11, 1934-1941.
- WORLD ECONOMIC FORUM. 2021. *mRNA vaccines - here's everything you need to know* [Online]. Available: <https://www.weforum.org/agenda/2021/07/everything-you-need-to-know-about-mrna-vaccines/> [Accessed 20/2/2023].
- WORLD HEALTH ORGANISATION. 2019. *Immunization* [Online]. Available: <https://www.who.int/news-room/facts-in-pictures/detail/immunization> [Accessed 17/6/2022 2022].
- WORLD HEALTH ORGANISATION. 2020. *How do vaccines work?* [Online]. Available: <https://www.who.int/news-room/feature-stories/detail/how-do-vaccines-work> [Accessed 3/10/23].
- WU, F., ZHAO, S., YU, B., CHEN, Y.-M., WANG, W., SONG, Z.-G., HU, Y., TAO, Z.-W., TIAN, J.-H., PEI, Y.-Y., YUAN, M.-L., ZHANG, Y.-L., DAI, F.-H., LIU, Y., WANG, Q.-M., ZHENG, J.-J., XU, L., HOLMES, E. C. & ZHANG, Y.-Z. 2020. A new coronavirus associated with human respiratory disease in China. *Nature*, 579, 265-269.
- WU, L., MIAO, X., SHAN, Z., HUANG, Y., LI, L., PAN, X., YAO, Q., LI, G. & WU, C. 2014. Studies on the spray dried lactose as carrier for dry powder inhalation. *Asian Journal of Pharmaceutical Sciences*, 9, 336-341.
- XIA, T., KOVOCHICH, M., LIONG, M., MENG, H., KABEHIE, S., GEORGE, S., ZINK, J. I. & NEL, A. E. 2009. Polyethyleneimine Coating Enhances the Cellular Uptake of Mesoporous Silica Nanoparticles and Allows Safe Delivery of siRNA and DNA Constructs. *ACS Nano*, 3, 3273-3286.

- XU, Y., TANG, H., LIU, J. H., WANG, H. & LIU, Y. 2013. Evaluation of the adjuvant effect of silver nanoparticles both in vitro and in vivo. *Toxicol Lett*, 219, 42-8.
- YADAV, D. K., YADAV, N. & KHURANA, S. M. P. 2014. Chapter 26 - Vaccines: Present Status and Applications. In: VERMA, A. S. & SINGH, A. (eds.) *Animal Biotechnology*. San Diego: Academic Press.
- YEE, S., TAN, C. S., KHAN, A., LEE, K. S., GOH, B. H. & MING, L. C. 2021. SARS-COV-2 as an artificial creation: scientific arguments and counterarguments. *J Med Life*, 14, 118-120.
- YEH, Y. C., CRERAN, B. & ROTELLO, V. M. 2012. Gold nanoparticles: preparation, properties, and applications in bionanotechnology. *Nanoscale*, 4, 1871-80.
- YORK, D. M., DARDEN, T. A. & PEDERSEN, L. G. 1993. The effect of long-range electrostatic interactions in simulations of macromolecular crystals: A comparison of the Ewald and truncated list methods. *The Journal of Chemical Physics*, 99, 8345-8348.
- YOUN, S.-J., KWON, N.-Y., LEE, J. H., KIM, J. H., CHOI, J., LEE, H. & LEE, J.-O. 2017. Construction of novel repeat proteins with rigid and predictable structures using a shared helix method. *Scientific Reports*, 7, 2595.
- YUAN, Y. J., CHEN, Q. & LI, J. 2016. QCM-based immunosensor for determining immunoglobulin G. *RSC Advances*, 6, 40336-40342.
- ZANONI, D. K., STAMBUK, H. E., MADAJEWSKI, B., MONTERO, P. H., MATSUURA, D., BUSAM, K. J., MA, K., TURKER, M. Z., SEQUEIRA, S., GONEN, M., ZANZONICO, P., WIESNER, U., BRADBURY, M. S. & PATEL, S. G. 2021. Use of Ultrasmall Core-Shell Fluorescent Silica Nanoparticles for Image-Guided Sentinel Lymph Node Biopsy in Head and Neck Melanoma: A Nonrandomized Clinical Trial. *JAMA Netw Open*, 4, e211936.
- ZHANG, H. & GAO, X. D. 2017. Nanodelivery systems for enhancing the immunostimulatory effect of CpG oligodeoxynucleotides. *Mater Sci Eng C Mater Biol Appl*, 70, 935-946.
- ZHAO, Y., SUN, X., ZHANG, G., TREWYN, B. G., SLOWING, I. I. & LIN, V. S. Y. 2011. Interaction of Mesoporous Silica Nanoparticles with Human Red Blood Cell Membranes: Size and Surface Effects. *ACS Nano*, 5, 1366-1375.
- ZHENG, T., CHERUBIN, P., CILENTI, L., TETER, K. & HUO, Q. 2016. A simple and fast method to study the hydrodynamic size difference of protein disulfide isomerase in oxidized and reduced form using gold nanoparticles and dynamic light scattering. *Analyst*, 141, 934-938.
- ZHOU, H.-X. & PANG, X. 2018. Electrostatic Interactions in Protein Structure, Folding, Binding, and Condensation. *Chemical reviews*, 118, 1691-1741.
- ZHU, M., WANG, R. & NIE, G. 2014. Applications of nanomaterials as vaccine adjuvants. *Hum Vaccin Immunother*, 10, 2761-74.
- ZONG, Y., BICE, T. W., TON-THAT, H., SCHNEEWIND, O. & NARAYANA, S. V. 2004. Crystal structures of Staphylococcus aureus sortase A and its substrate complex. *J Biol Chem*, 279, 31383-9.

## Appendix

*“Progress is made by trial and failure; the failures are generally a hundred times more numerous than the successes, yet they are left unchronicled”*

*William Ramsay*

<https://www.sciencedirect.com/science/article/pii/S1359029421000455?via%3Dihub>

<https://www.mdpi.com/1422-0067/23/9/4832>

<https://www.mdpi.com/1422-0067/23/11/6078>